論文 / 著書情報
Article / Book Information

題目(和文)	液状化により発生する側方流動地盤中の地盤と杭の相互作用
Title(English)	Soil-pile interaction in liquefaction-induced lateral spreading of soils
著者(和文)	高橋章浩
Author(English)	Akihiro Takahashi
出典(和文)	学位:博士(工学), 学位授与機関:東京工業大学, 報告番号:乙第3591号, 授与年月日:2002年3月31日, 学位の種別:論文博士, 審査員:
Citation(English)	Degree:Doctor (Engineering), Conferring organization: Tokyo Institute of Technology, Report number:乙第3591号, Conferred date:2002/3/31, Degree Type:Thesis doctor, Examiner:
学位種別(和文)	博士論文
Type(English)	Doctoral Thesis

Soil–pile interaction in liquefaction-induced lateral spreading of soils

TAKAHASHI Akihiro

DISSERTATION

submitted in partial fulfillment of the requirements for the degree of

DOCTOR OF ENGINEERING

at

TOKYO INSTITUTE OF TECHNOLOGY

2002

Synopsis

Detailed investigations on pile foundations damaged in past earthquakes reveal only consequent breakage to the piles. Analyses of the transient events that cause the damage are needed to understand the overall performance of the pile foundation. In this dissertation, soil–pile interaction in liquefaction-induced lateral spreading of soils is investigated through physical model tests and numerical analyses.

To make clear piled structure behavior in liquefaction-induced lateral spreading of soils due to earthquake, shaking table tests are conducted in a geotechnical centrifuge. The targeted structure is a pile-supported wharf damaged in the 1995 Hyogo-ken Nambu Earthquake at Takahama, Kobe. While there are very few quantitative field data of pile foundation responses during earthquakes, the permanent deformations observed in the centrifuge tests agree well with post hoc site investigation results. Pile deformation mechanisms associated with earthquake motion are also determined.

Soil–pile interactions in liquefied and non-liquefied soils are individually investigated by pile loading tests with newly developed apparatuses. In liquefied sand, when a relative displacement between pile and soil is imposed, only the soil adjacent to the pile is strained during a shaking, resulting in small lateral resistance. Even in liquefied sand, the pore water migration rate in relation to the loading rate of the pile plays a key role in mobilization of the lateral resistance of the pile.

As damage to piles was mainly found in the sites where liquefaction took place, particularly when large lateral movement of liquefied soil overlaid by non-liquefied soil occurred, evaluation of non-liquefied soil–pile interaction is also important. Centrifuge model tests on piles subjected to strong seismic ground motion in quasi-static conditions are conducted for non-liquefied sand. The test results reveal remarkable sensitivity of the pile response to differences in the seismic ground motion mode.

Based on the results of these physical model tests, pile modeling methods using three-dimensional finite element analysis are proposed which consider (1) a pile volume effect on soil–pile interaction and (2) slippage between the pile surface and adjacent soils. The pile modeling methods are applied to simulations of the centrifuge model tests and perform well for the soil–pile interaction problems. In order to evaluate soil–pile interaction in terms of p–y relations that are usually used in the practical design, the relations were calculated from the finite element analysis results and compared with those in practical design codes in Japan.

Acknowledgments

I would like to express my gratitude to the many people who encouraged and assisted me in conducting the research projects on which my dissertation is based. I also wish to thank all who have made the Geotechnical Engineering Group at Tokyo Institute of Technology a pleasant group to do research with.

I am grateful to Professor Osamu Kusakabe for his constant encouragement and guidance. His knowledge of global trends, as well as his suggestions on how to tackle a problem guided me towards my research goals.

I am thankful to Professor Hideki Ohta for his advice and encouragement. His logical ideas and detailed knowledge in the theoretical soil behavior modeling motivated me to study the numerical modeling of dynamic soil–structure interactions.

Gratitude is also due to Professors Kazuhiko Kawashima and Kohji Tokimatsu for their valuable suggestions.

I wish to express gratitude to Associate Professors Jiro Kuwano and Jiro Takemura. They have advised me and always had open doors for discussion not only on the research but also on any problem I encountered ever since I joined the group.

I am thankful to former Research Associates, Dr Ichizo Kobayashi of Kajima Corporation and Dr Masayuki Koda of Railway Technical Research Institute, for their advice and encouragement, and for their friendship. Dr Kobayashi gave me advice on the theoretical soil behavior modeling. Dr Koda and I often had discussion on our researches and others, and sometimes struggled with the faulty centrifuge far into the night.

Mr. Sakae Seki, Technician of the department, deserves credit for his help to maintain the laboratory.

I wish to acknowledge former research students, Mr. Yoshitaka Kawaguchi of Tokyo Gas Company and Mr. Atsushi Mizoguchi of West Japan Railway Company, and current research students, Messrs Yasuyuki Arai, Akihiro Suzuki and Atsushi Yano, for doing the physical model tests in this dissertation.

I am grateful to doctoral students, Messrs Kazuya Itoh and Jun Izawa, for relieving me of much of my duties so that I could focus on completing this dissertation.

I acknowledge the funding for the projects in this dissertation provided by the Japan Association for Steel Pipe Piles, the Ministry of Education, Culture, Sports, Science and Technology, Japan (Special Expenses for Promoting Advanced Research, 1997), and the Japan Society for the Promotion of Science (Grant-in-Aid for Encouragement of Young Scientists, No.12750442). I would also like to express my gratitude to the Department of Civil Engineering for financially supporting the young researchers.

Lastly, I am grateful to my wife, Naoko, for her constant encouragement and putting up with my often-unusual working hours.

Contents

List of Figures

List of Tables

Chapter 1

Introduction

1.1 Background and objectives of research

The 1995 Hyogo-ken Nambu Earthquake caused severe damage to port facilities and structures near the waterfront. In reclaimed land areas, quay walls moved towards the sea and large ground movement took place due to liquefaction of the walls' foundation and backfill. As a result, many pile foundations near the waterfront were damaged not only near the top of the piles but also at middle to lower portions of the piles (e.g. Matsui & Oda, 1996; Fujii *et al.*, 1998). Detailed observations of damage to the pile foundations after the earthquake revealed that the damage occurred at depths other than the pile heads, particularly near an interface between liquefied and non-liquefied soils. Even far from the waterfront, many piles showed similar damage (Tokimatsu & Asaka, 1998), and some of them were damaged even without any superstructures (Ohtsu *et al.*, 1997).

These detailed investigations reveal only consequent damage to the piles. Analyses of the transient events that cause the damage are needed to understand the overall performance of the pile foundation. After the Kobe Earthquake, in order to evaluate the seismic performance of the piles, many researchers have experimentally and analytically investigated the effects of large lateral soil movements on the failure and deformation of the piles, especially effects resulting from liquefaction-induced lateral spreading of soil.

In physical modeling, in order to examine the seismic performance of the piles, a shaking table is usually used to simulate the ground motion during an earthquake. However, it is very difficult to pick out the dominant factors in soil–pile interactions from such shaking table test results, as the actual pile behavior observed is complicated and affected by several factors such as the inertial effect from the superstructure, the dynamic response of the soils, the lateral movement of the soils, and so on.

In numerical modeling, several approaches have been developed for dynamic response analysis and pseudo-static analysis of the pile foundations. One of the simple methods is a framed structure analysis subjected to soil movements through soil–pile interaction springs. The soil–pile interaction is modeled using one-dimensional non-linear empirical p–y springs involving three-dimensional effects in soil–pile interaction. The most complex and accurate method is a three-dimensional finite element analysis having capability of soil–structure coupled analysis, though there are still difficulties in modeling of the soil–structure interface.

There are many unexplained factors affecting soil–pile interaction during an earthquake. Therefore, this dissertation investigates soil–pile interaction in liquefaction-induced lateral spreading of

soils. The objectives of the research presented in this dissertation are:

1. To understand piled structure behavior in liquefaction-induced lateral spreading of soils through dynamic centrifuge model tests. A targeted piled structure is a pile-supported wharf damaged in the 1995 Hyogoken-Nambu Earthquake at Takahama, Kobe.
2. To measure the lateral resistance of piles in liquefied soil. Loading tests are conducted using a newly developed pile loading system having the capability of applying horizontal cyclic vibrations to the pile during an earthquake and allowing the observation of deformation of the liquefying sand surrounding the pile.
3. To propose an experimental method to evaluate the performance of piles subjected to several types of large non-liquefied soil movements. The results of non-liquefied soil movements dominate the pile deformation; damage of piles was mainly found in sites where liquefaction took place, particularly when a large lateral movement of liquefied soil overlaid by non-liquefied soil occurred. Accordingly, evaluation of non-liquefied soil–pile interaction is important for the assessment of pile performance in liquefaction-induced lateral spreading of soils.
4. To propose pile modeling methods in a three-dimensional finite element analysis considering (1) a pile volume effect on soil–pile interaction and (2) a slippage between pile surface and adjacent soils.

1.2 Organization of the dissertation

This dissertation consists of seven chapters:

Chap. 1: *Introduction* – includes background and objectives of the research and an organization of the dissertation.

Chap. 2: *Liquefaction–induced large displacement of pile-supported wharf* – presents dynamic centrifuge model test results on a pile-supported wharf. Discusses the pile-failure mechanism, the effects of liquefaction in the backfill and underlying sand layer on the permanent deformation of the wharf during earthquakes, and the dynamic interaction between piled deck and caisson through an approach bridge.

Chap. 3: *Lateral resistance of piles in liquefied soil* – the lateral resistance of piles in liquefying soil is directly measured by a newly developed testing apparatus. The new pile loading system has the capability of applying horizontal cyclic vibrations to the pile during a shaking and allowing the observation of deformation of the liquefying sand surrounding the pile.

Chap. 4: *Soil–pile interaction in large soil deformation* – details of a newly developed active type shear box are described. Centrifuge model test results on soil–pile interaction in large soil movement are presented.

Chap. 5: *Numerical modeling of waterfront structure during earthquake* – describes the governing equations for dynamic porous solid–pore fluid interaction and a constitutive model proposed by Hashiguchi *et al.* (1996, 1998). The sensitivity of each parameter of the constitutive model on soil behavior is examined. A simulation of centrifuge model test on a caisson type quay wall subjected to backfill liquefaction is conducted to examine the applicability of the newly developed analysis code to liquefaction problems.

Chap. 6: *Evaluation of soil–pile interaction in large soil movement* – pile modeling methods in three-dimensional finite element analysis are proposed, considering the pile volume effect on soil–pile interaction and the slippage between the pile surface and the adjacent soils. Performance of the pile modeling methods is verified by the centrifuge model test simulations presented in Chapters two and four.

Chap. 7: *Conclusions* – includes a summary of the dissertation and its findings.

Chapter 2

Liquefaction–induced large displacement of pile-supported wharf

2.1 Damage of pile-supported structures due to liquefaction in waterfront

One of the major sources of earthquake-induced damage to port facilities is liquefaction of saturated loose sandy soils. This type of soil often prevails at waterfronts and marine environments. The significant liquefaction and associated ground movement and waterfront structure damage have not only occurred under very strong earthquakes like the 1995 Hyogo-ken Nambu Earthquake, but also under moderate levels of earthquake motion in past earthquakes (Technical council on lifeline earthquake engineering of ASCE, 1998). For instance, port facilities experienced severe damage due to liquefaction at the Port of Oakland and the Port of San Francisco during the 1989 Loma Prieta Earthquake in USA, although recorded peak horizontal accelerations at those locations were 0.29g and 0.15g, respectively.

Seismic performances of retaining structures at ports have been influenced by liquefaction of adjacent backfills and underlying soils. The liquefaction of surrounding soil has caused substantial lateral movement, tilting, overturning, and settlement of the structures. With respect to earthquakes in Japan, quay walls have shown large deformations at Ni'igata (1964), Tokachi-Oki (1968), Kushiro-Oki (1993), Kobe (1995) and others. Especially in the 1995 Hyogo-ken Nambu Earthquake, quay walls moved several meters seaward, and many piled structures were damaged (Hamada *et al.*, 1996; Great Hanshin Earthquake investigation committee of JGS, 1996; Port and Harbour Research Institute, 1997). Figure 2.1 shows permanent displacements of the quay walls in Port Island and Rokko Island (Inagaki *et al.*, 1996). Distributions of permanent horizontal ground surface displacement are shown in Fig. 2.2 (Ishihara et al., 1996; Hamada & Wakamatsu, 1998). These large displacements of the quay walls caused lateral spreading/lateral flow of ground behind the walls.

2.1.1 Piled structures at waterfronts

Near waterfronts many pile-supported structures, especially pile-supported buildings, had pile damage without severe damage to their superstructures. During the lateral spreading of liquefied soil, the covering non-liquefied soil, i.e. the soil layer above the water table, moves seaward together with the liquefied soil. Pile foundations located in such a lateral spreading ground were investigated, and detailed observations revealed that the damage to the piles occurred at depths other than the pile heads,

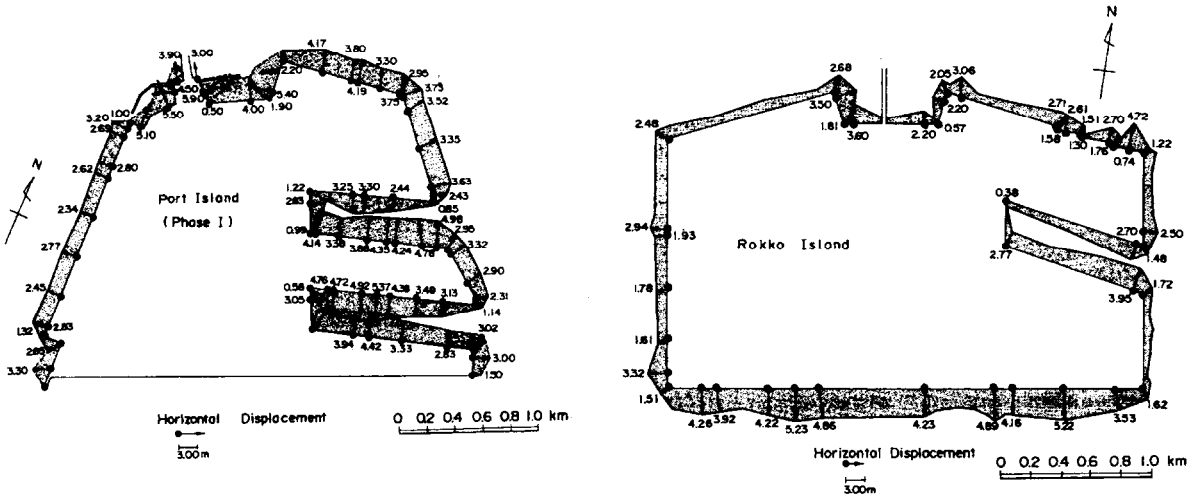

(a) Horizontal displacement

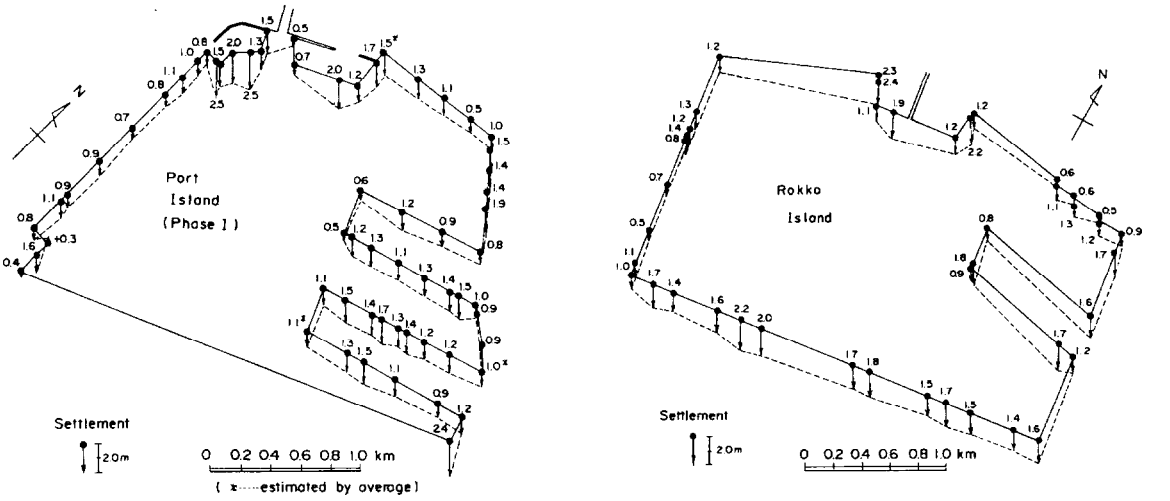

(b) Vertical displacement

Figure 2.1: Permanent horizontal and vertical displacements of quay walls at Port Island and Rokko Island (after Inagaki *et al.*, 1996).

particularly near the interface between the liquefied and non-liquefied soils. Figure 2.3(a) shows typical examples of observed cracks along the piles supporting the expressway piers (using the bore-hole television system). Near the interface between liquefied and non-liquefied soils, a significant curvature will be demanded to a pile due to the difference in soil stiffness, i.e. the lateral resistance of the pile drastically changes along the pile length. It was considered that the cracks shown in the figure were caused by the large curvature demands. Observed deformation of the building piles just behind the quay wall is illustrated in Fig. 2.3(b). Tokimatsu & Asaka (1998) concluded that the failure and deformation patterns of piles in the lateral spread zone vary with distance from the waterfront due to the variation of lateral ground movements.

Not only the piles behind the quay walls, but also those in front of the wall were damaged in past earthquakes. For instance, the 1989 Loma Prieta Earthquake caused damage to the wharves at the

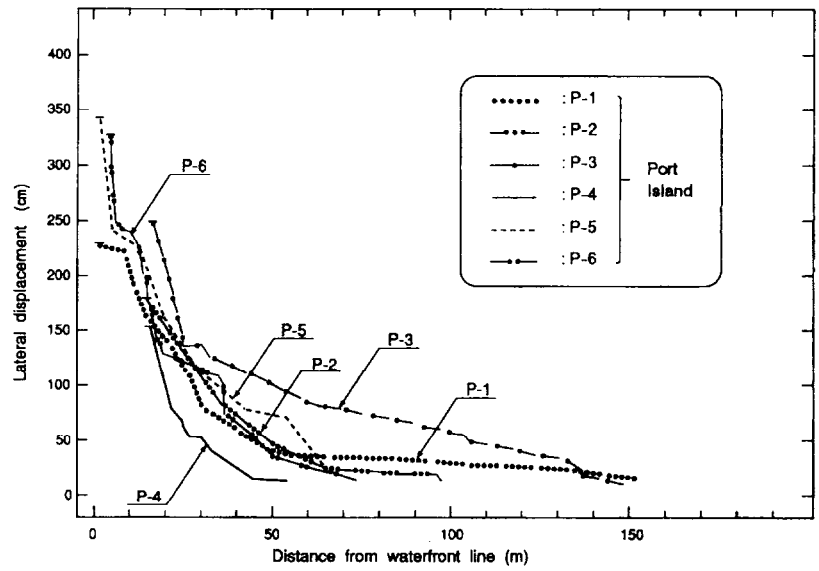

(a) after Ishihara *et al.*, 1996

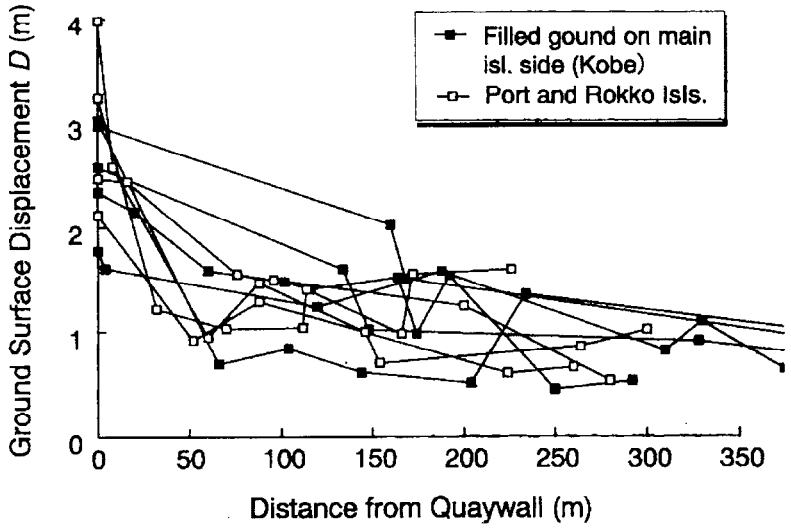

(b) after Hamada & Wakamatsu, 1998

Figure 2.2: Distributions of permanent horizontal displacement of ground surface (after Ishihara *et al.*, 1996; Hamada & Wakamatsu, 1998).

port of Oakland (Technical council on lifeline earthquake engineering of ASCE, 1998). There were four damaged areas that had pile-supported wharves, i.e. the Seventh Street Terminal, the Matson Terminal, the APL Terminal, and the Howard Terminal. All of the piles of the decks were installed into rock dikes. Dredged sands and silty sands were filled behind the dikes.

A deck of the Seventh Street Terminal wharf was a ballasted cast-in-place concrete slab, and it was supported by vertical piles in six rows and battered piles in one row. The wharf was constructed

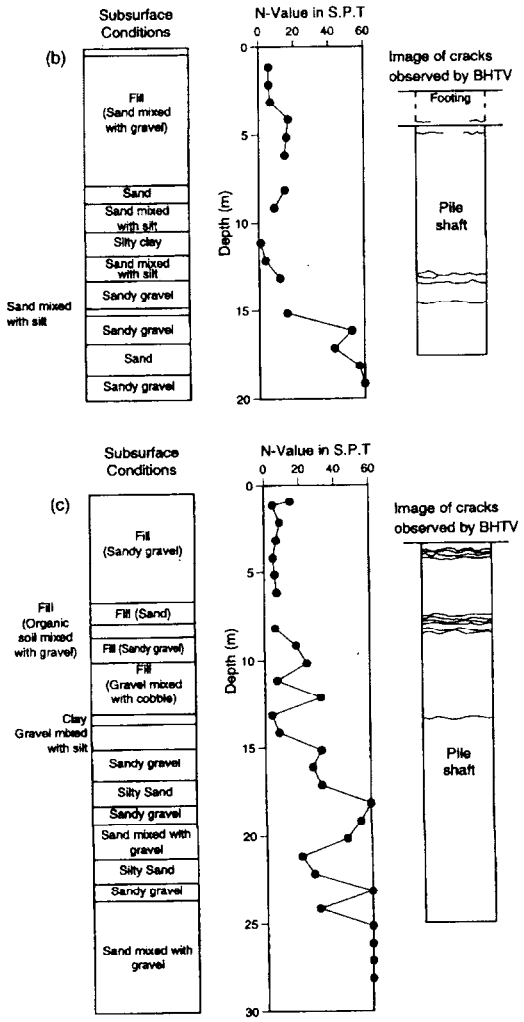

(a) Piers in the Harbor highway of the Hanshin Expressway (after Matsui & Oda, 1996).

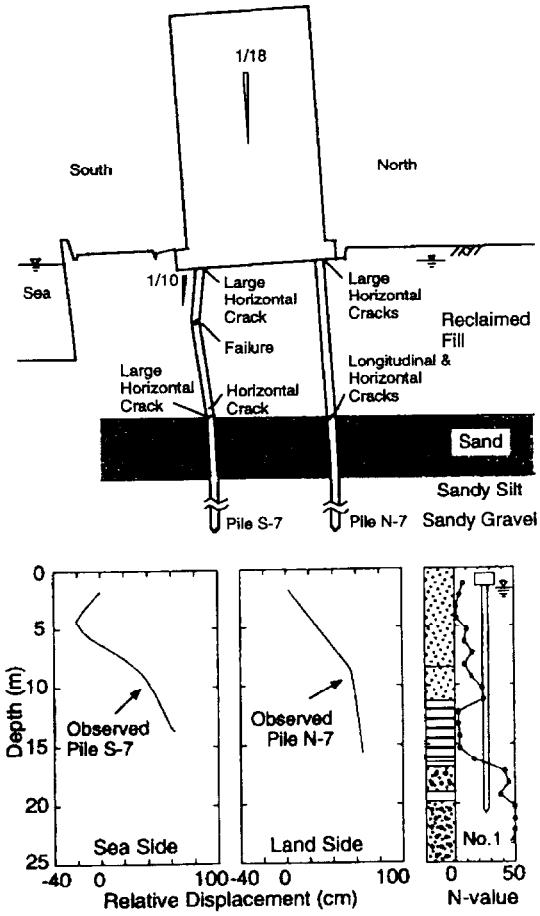

(b) Kobe University of Mercantile Marine Building located just behind quay wall (after Tokimatsu & Asaka, 1998 & Tokimatsu, 1999).

Figure 2.3: Observed cracks along pile foundations with associated soil profiles (after Matsui & Oda, 1996, Tokimatsu & Asaka, 1998).

in 1968. A cross section of the Seventh Street Terminal wharf is shown in Fig. 2.4 (Egan *et al.*, 1992). The hydraulic sand fill and the upper 1.5m of the dense native sand in the figure could have experienced liquefaction and the wharf moved 0.3m seaward during the Loma Prieta Earthquake. Most of the battered piles were cracked or fractured, though the vertical piles and the deck suffered only minor damage.

On the other hand, the Howard Terminal was seismically designed in 1981 to perform as a ductile moment-resisting frame. The deck of the wharf was a cast-in-place concrete slab without ballast, and it was supported by vertical pre-stressed concrete piles. Although the lateral movement of the dike was almost the same as that at the Seventh Street, there was no serious damage to the piles.

Several piers and wharves were damaged during the 1995 Hyogo-ken Nambu (Kobe) Earthquake (Matsui & Oda, 1996; Japan Association for Steel Pipe Piles, 1995; Minami *et al.*, 1997; Takahashi

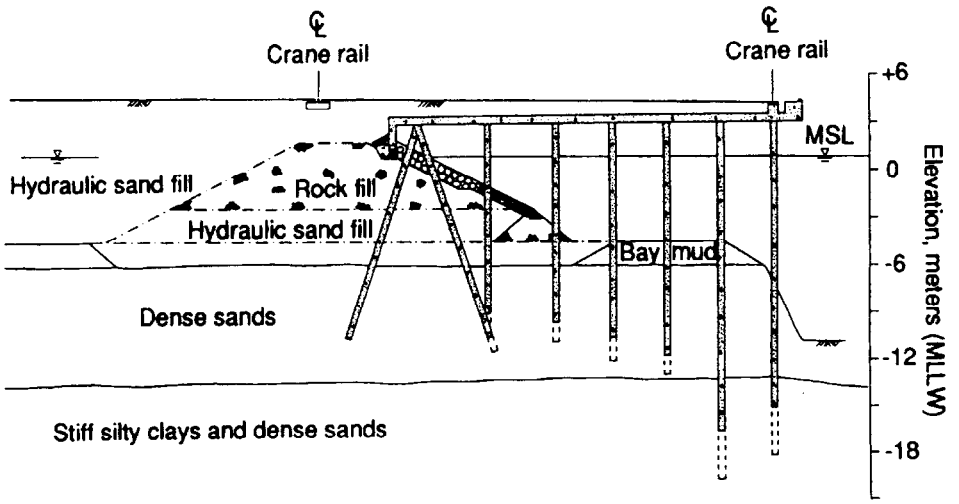

Figure 2.4: Wharf cross section at the time of the 1989 Loma Prieta Earthquake (after Egan *et al.*, 1992).

et al., 1997; Sugano *et al.*, 1998; Nishizawa *et al.*, 1998). One of the damaged piers was constructed at Sumiyoshihama-cho, Higashinada, Kobe in 1969. Front and plan views of the pier are shown in Fig. 2.5. Permanent deformation of the pier is illustrated in Fig. 2.6. The pier was supported by vertical steel pipe piles of diameter (ϕ) 558.8mm, thickness (t) 9.5mm, and batter steel pipe piles of ϕ =609.6mm or 711.2mm, and t=9.5mm. The design horizontal seismic coefficient was 0.15. Caissons behind the deck moved 1.5m seawards, and the large bending of the piles occurred around liquefiable replaced sand.

A wharf supported by vertical steel pipe piles was also damaged at Takahama in Kobe (Minami *et al.*, 1997; Takahashi *et al.*, 1997). Detailed observations on the Takahama Wharf will be described in the following section.

2.1.2 Damage of the Takahama Wharf in Kobe

In the 1995 Hyogo-ken Nambu Earthquake, the wharf supported on vertical piles moved 1.3 to 1.7m toward the sea at Takahama in Kobe (Minami *et al.*, 1997; Takahashi *et al.*, 1997). The Takahama Wharf was constructed in front of stacked gravity type caissons made of concrete cellular blocks as shown in Fig. 2.7. The wharf was constructed on a firm foundation deposit that consists of alternating layers of Pleistocene clay and sandy gravel. The caissons were installed on a layer of loose sand layer about 2m thick, and hydraulically backfilled with the decomposed granite, *masado*. (Minami *et al.* (1997) considered both these loose sandy soils to be liquefiable.) The concrete deck of the wharf was supported by three rows of steel pipe piles with a diameter of 700mm and connected to the top caisson with approach bridges. Thicknesses of the steel pipe piles were 10, 12 and 14mm from sea-side to land-side, respectively. The piles of the deck penetrated the sand layer into the bearing strata consisting of gravel and Pleistocene clay layers. The rubble mound was constructed on the sand layers in order to increase lateral resistance of the deck against shiploads.

After the Hyogo-ken Nambu Earthquake, a detailed investigation on the damaged wharf was car-

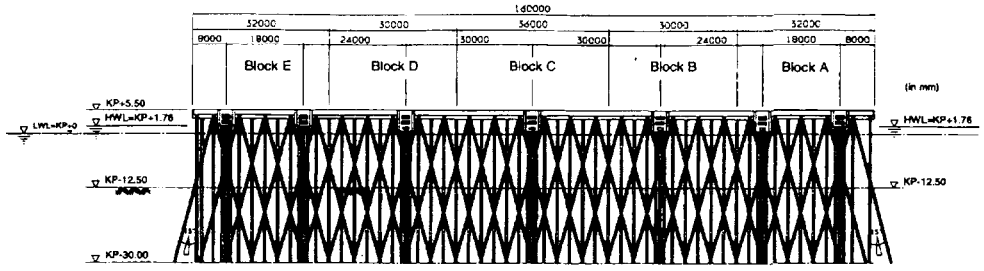

Fig. 1. Front view of the pier

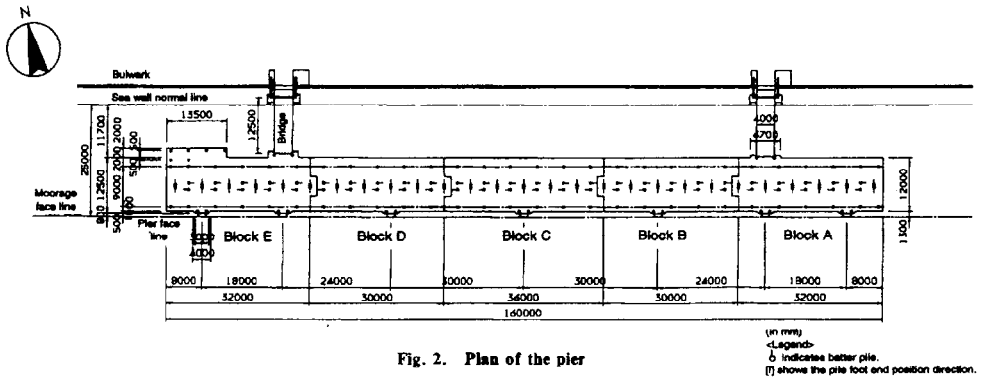

Fig. 2. Plan of the pier

Figure 2.5: Front and plan views of pier at Sumiyoshihama (after Nishizawa et al, 1998).

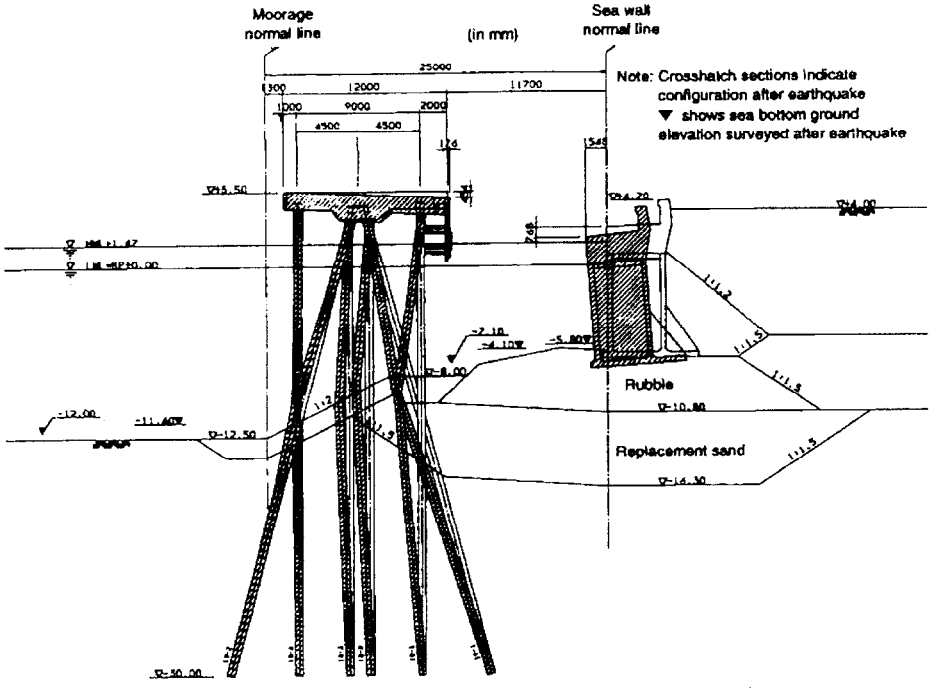

Figure 2.6: Side view of pier at Sumiyoshihama (after Nishizawa et al, 1998).

ried out, including post-mortem observations of the piles. Figure 2.8 shows the plan view of the Takahama Wharf and the location where the detailed investigation was conducted. Permanent displacements of the rubble mound were measured by divers at five locations at intervals of 5m and are illustrated in Fig. 2.9. Clear failures with buckling were observed in the removed piles as shown in Fig. 2.10. Large deformations took place at the top, near the deck of the wharf, and at the interface between the rubble mound and the liquefiable sand layer, as shown in Fig. 2.7. Also, several cracks were found on the approach bridges and the connection points between the bridges and the deck of the wharf. Figure 2.11 shows the locations where the large deformations, including the buckling failures, were observed at the top of the piles.

2.1.3 Physical model tests on pile-supported wharf

Using shaking tables in geotechnical centrifuges as well as ordinary shaking tables, many researchers have experimentally investigated the effects of the large lateral soil movement – especially liquefaction-induced lateral spreading of soil – on the failure and deformation of the piles on slopes and behind the quay walls (e.g. Abdoun & Dobry, 1998; Horikoshi *et al.*, 1998; Satoh *et al.*, 1998). However, only a limited number of shaking table tests have been carried out for pile-supported wharves. Other than the centrifuge tests that the author performed (Takahashi *et al.*, 1998a, 1998b, 1999a & 1999b; Takemura *et al.*, 1998), Iai & Sugano (1999) and McCullough *et al.* (2001a, 2001b) have conducted shaking table tests in 1g field at the Port and Harbour Research Institute and in a centrifuge at the University

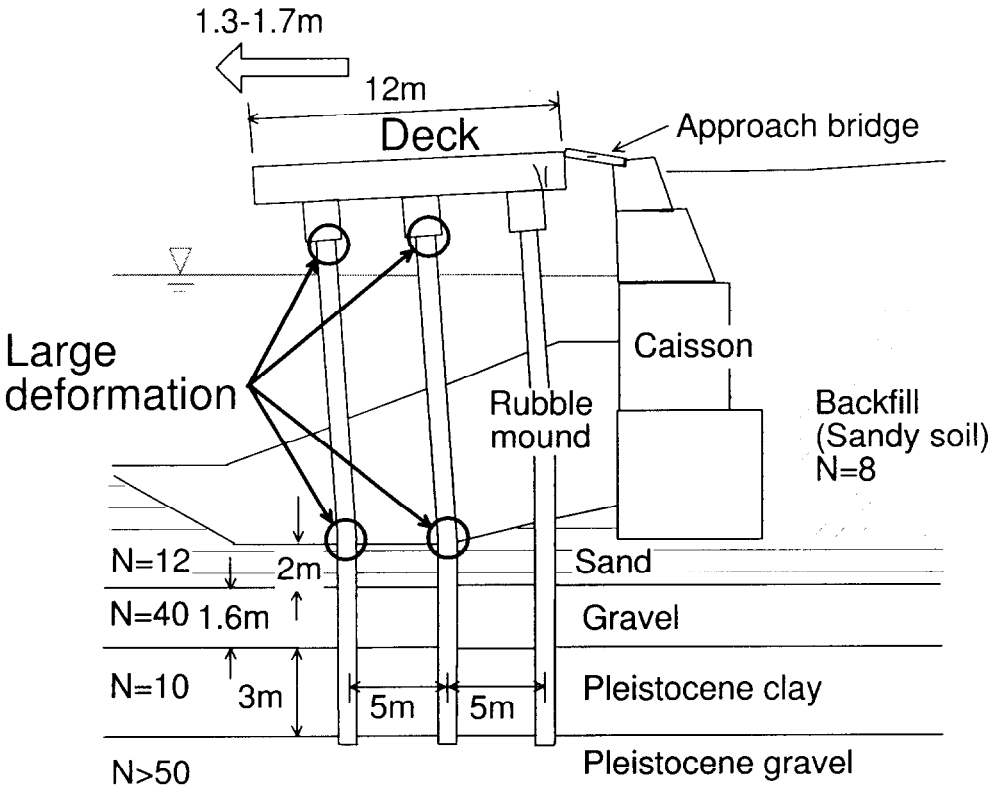

Figure 2.7: Cross section of damaged wharf at Takahama, Kobe.

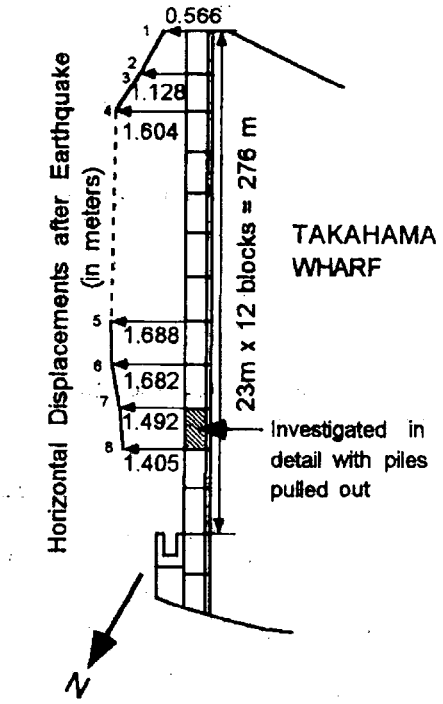

Figure 2.8: Plan view of the Takahama Wharf (after Iai & Sugano, 1999)

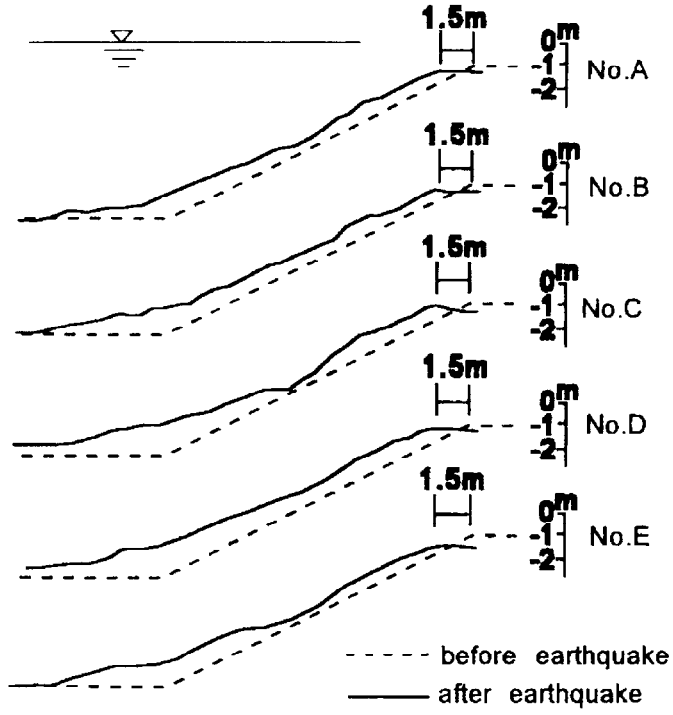

Figure 2.9: Displacements of rubble mound at the Takahama Wharf (after Iai & Sugano, 1999)

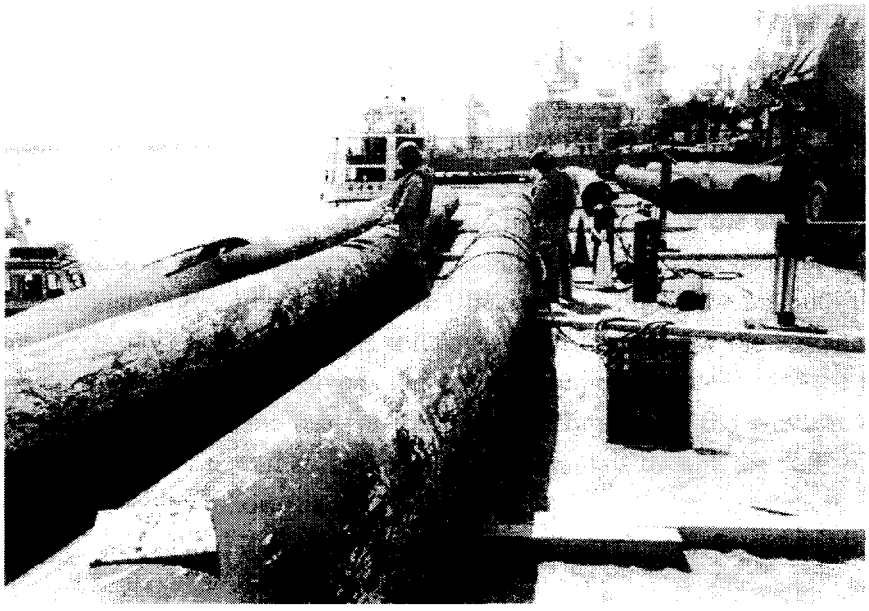

Figure 2.10: Failure of piles at Takahama (after Japan Association for Steel Pipe Piles, 1997)

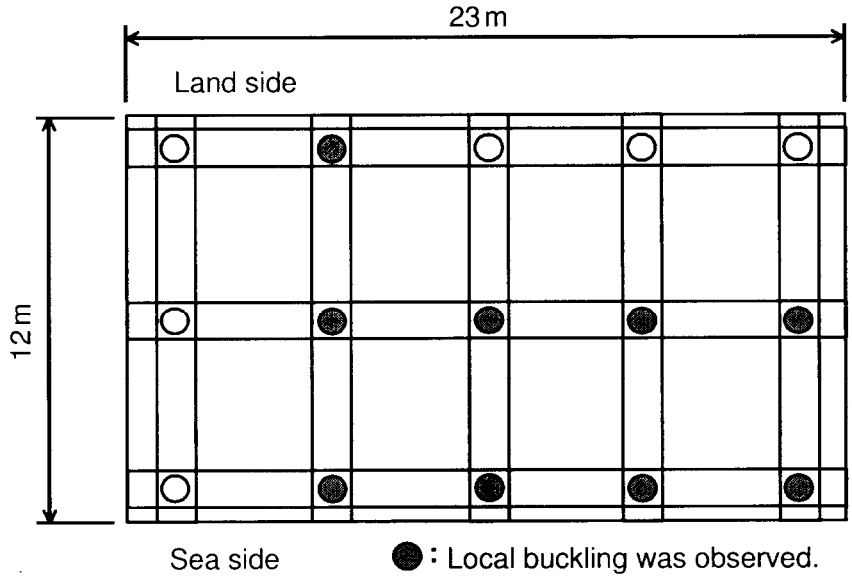

Figure 2.11: Plan view of deck with positions of buckling failure of pile at Takahama (after Minami *et al.*, 1997).

of California at Davis, respectively. Model setups for their tests are shown in Fig. 2.12. The former was intended to simulate the Takahama Wharf during the Kobe Earthquake, and the geometry of the latter was based on typical pile-supported wharves at western US ports.

Figure 2.13 shows time histories of the accelerations, displacements, and excess pore water pressures in a 1g shaking table test in the prototype scale. The size of the specimen box, which had a longitudinal length of 4m, was larger than those in the other ordinary shaking table tests in 1g. The wharf was scaled down to 1/15 of the actual wharf. The similitude, i.e. the scaling law, proposed by Iai (1989) was adopted in these tests. In order to convert the $1/\lambda$ scale model's values into full scale, the time, length, displacement, acceleration, stress, and strain were multiplied by factors of $\lambda^{0.75}$, λ, $\lambda^{1.5}$, λ, λ, and $\lambda^{0.5}$, respectively. The wharf gradually moved seaward as the rubble mound earth pressure acting on the land-side pile increased with shaking. The piles of the deck behaved as *passive pile* due to the lateral displacement gap between the rubble mound and the bearing stratum.

Bending moment distributions of the piles are illustrated in Fig. 2.14 for both the tests. Large bending moments were observed at the soft soil layers. In the test for the Takahama Wharf, the buckling locations observed in the prototype piles coincided approximately with the locations of the maximum bending moments. In the test for the typical geometry of the western US ports, large bending moments were also observed at the levels of the soft clay, though the soft soil layer beneath the rock dike was improved by mixing cement into the soil.

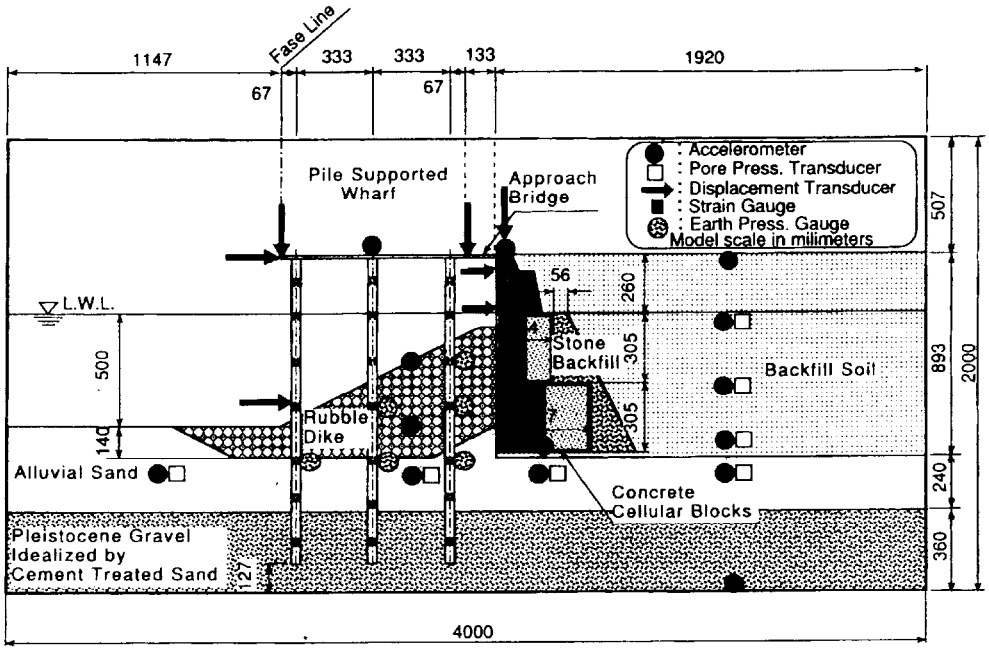

(a) For 1g shaking table test (after Iai & Sugano, 1999).

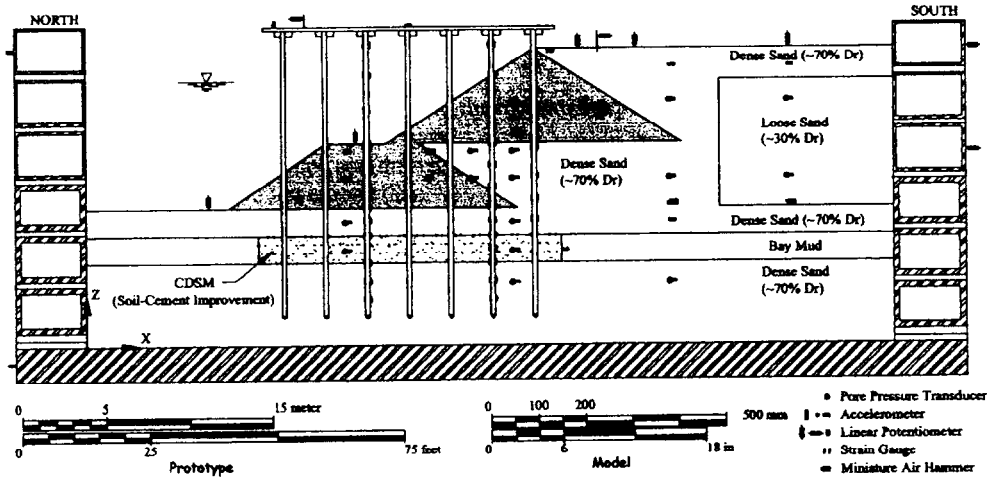

(b) For centrifuge model test (after McCullough *et al.*, 2001a).

Figure 2.12: Model setups for shaking table test (after Iai & Sugano, 1999, McCullough *et al.*, 2001a).

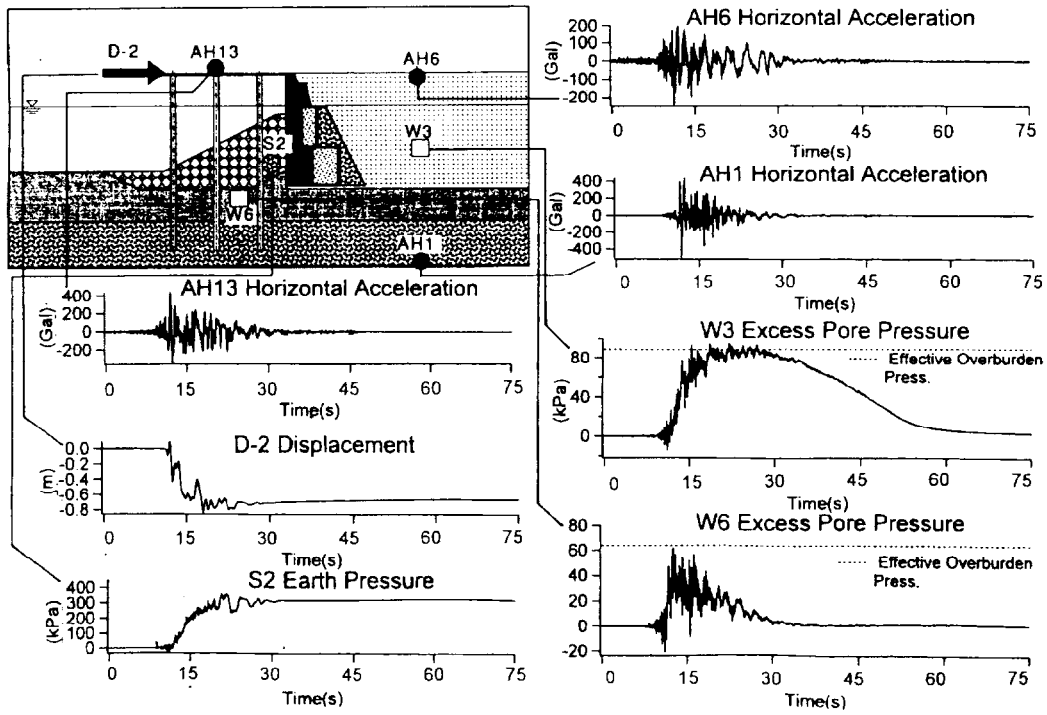

Figure 2.13: Time histories of the wharf response in 1g shaking table test in the prototype scale (after Iai & Sugano, 1999).

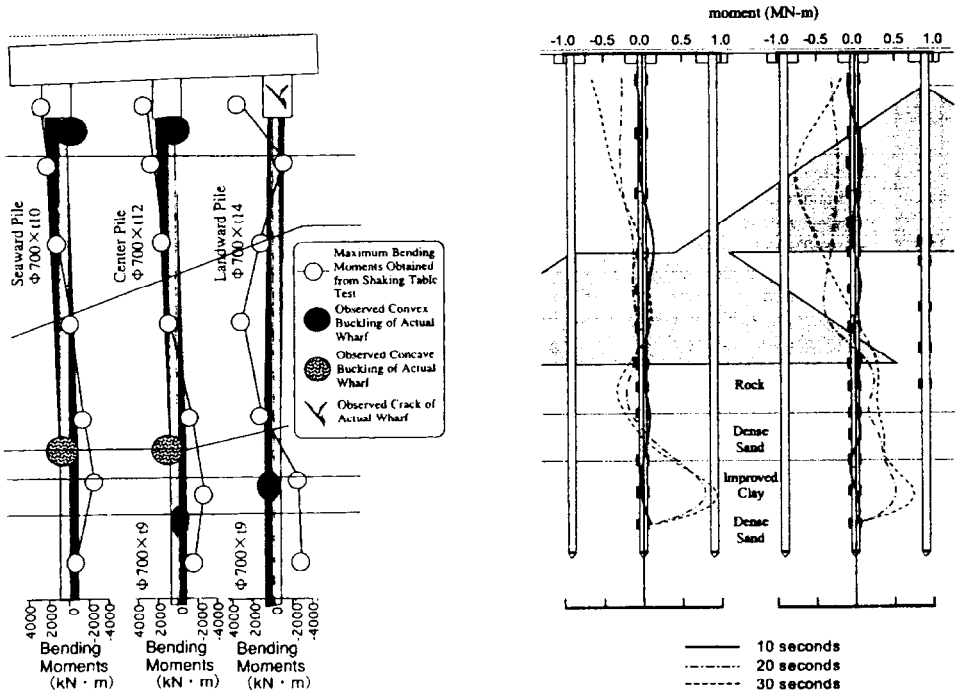

(a) In 1g shaking table test in prototype scale (after Iai & Sugano, 1999).

(b) In centrifuge test (after McCullough *et al.*, 2001a).

Figure 2.14: Bending moment distributions of pile just after shaking (after Iai & Sugano, 1999, McCullough *et al.*, 2001a).

2.2 Motivations for centrifuge model tests

Detailed investigations have been conducted for the wharves damaged in the earthquakes. However, many questions remain, i.e., pile-failure mechanism, effects of liquefaction in backfill and sand layer on permanent deformation of the wharf, and dynamic interaction between deck and caisson through the approach bridge. In order to examine wharf response during an earthquake, the author has carried out physical model tests using a geotechnical centrifuge (Takahashi *et al.*, 1998a, 1998b, 1999a & 1999b; Takemura *et al.*, 1998).

2.3 Test procedures and conditions

The centrifuge used in the tests was the Tokyo Tech Mark II Centrifuge (Takemura *et al.* 1989, cf. Appendix A). The model setup used in this study is shown in Fig. 2.15. An aluminum model container was used with inner sizes of 450mm in width, 150mm in breadth, and 250mm in height. The inner side of the container was coated with alumite. The front face of the container was a transparent window which enabled observation of the model's ground deformation. Rubber sheets 10mm thick were placed at both sides of the container to absorb stress waves from the side boundaries.

Due to the limitations of the container size and a 50g allowable centrifuge acceleration for shaking test, prototype scales of all dimensions of the model were reduced to half those of the site, and some simplifications were introduced in modeling the caissons and soil layers. The model deck consisted of an aluminum deck weighing 0.42kg and 9 piles rigidly fixed to the deck. The pile spacing ratio s/d=6.7, as shown in Fig. 2.16. The piles were steel tubes having an outside diameter of 7mm, a thickness of 0.14mm, and a total length of 200 or 220mm. Properties of the model pile are listed in Table 2.1. Strain gauges were instrumented inside each pile at 9 different levels. However, due to a limited number of data acquisition channels, data from only three or four gauges for each pile were used, as shown in Fig. 2.15. Though the *open-end* pipe pile was used for the easier pile driving in the site, the tip of the model pipe pile was *closed*, since in-situ soil plug lengths were uncertain. The

Table 2.1: Properties of model pile.

Young's modulus, E (GPa)	1.90×10^2
Yield strength, σ_Y (MPa)	2.00×10^2
Pile radius, r (mm)	3.50
Thickness of pipe, t (mm)	0.14
Moment of inertia, I (mm^4)	17.8
Area, A (mm^2)	3.02
Bending moment at yield, M_Y (N.m)	1.05
Bending strain at yield, ε_{bY} (μ)	1.05×10^3
Axial force at yield, N_Y (N)	6.03×10^2
Axial strain at yield, ε_{aY} (μ)	1.05×10^3
Euler's critical load, P_{cr} (N)	$1.67 \times 10^{3*}$

$* \; P_{cr} = \frac{\pi EI}{2L^2}$ (for a member fixed on one end), where L=100mm for the pile in the sea-side row.

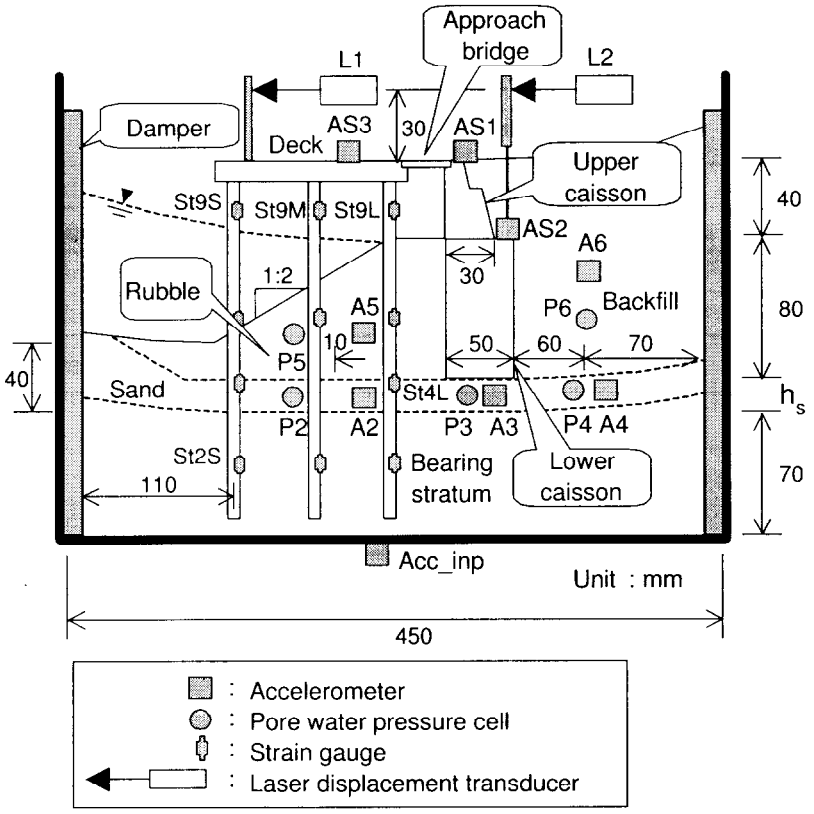

Figure 2.15: Model setup for centrifuge tests.

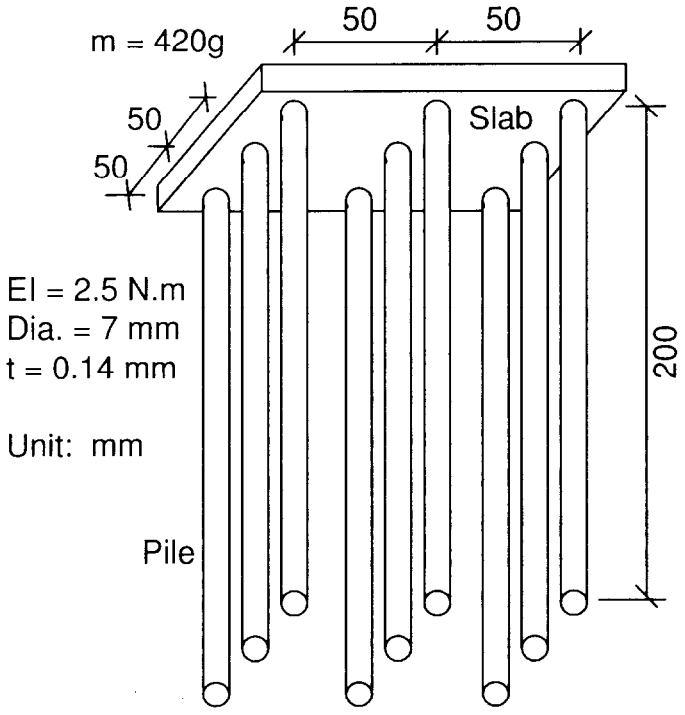

Figure 2.16: Detail of a model deck.

Table 2.2: Material properties of soils used in the Takahama Wharf series.

	Material	D_{50} (mm)	D_r (%)	Hydraulic conductivity* (m/sec)
Liquefiable sand layer	Toyoura sand	0.19	50	5×10^{-4}
Non-liquefiable sand layer	Silica sand No.3	1.2	75	5×10^{-3}
Rubble mound	Quartz sand	3.1	30	7×10^{-2}
Bearing stratum	Silica sand No.3	1.2	80	5×10^{-3}

*: Fresh water was used as pore fluid to measure the hydraulic conductivities.

Table 2.3: Test conditions in the Takahama Wharf series.

Case	Input motion	Deck	Approach bridge	Backfill	Sand layer under rubble (Thickness h_s(mm))
PW1	Kobe P.I.	Yes	Yes	○	○ (20)
PW2	Sinusoidal	Yes	Yes	○	○ (20)
PW3	Sinusoidal	No	No	○	○ (20)
PW4	Sinusoidal	Yes	Yes	○	× (20)
PW5	Sinusoidal	Yes	Yes	×	○ (20)
PW6	Sinusoidal	Yes	No	○	○ (20)
PW7	Sinusoidal	Yes	Yes	○	○ (40)

○ : Liquefiable, × : Non-liquefiable

piles of the deck were installed in three different soil layers; (1) a bottom dense sand bearing stratum corresponding to the gravel and Pleistocene clay at the Kobe site, (2) a saturated loose liquefiable sand layer, and (3) a top rubble mound. These soils were prepared by air pluviation. The basic properties of the soils used in the tests are summarized in Table 2.2. Aluminum gravity type caissons were placed between the rubble mound and the backfill. The unit weight of the caissons was 2.5kN/m^3. An approach bridge made of aluminum was placed between the deck and the caisson to transmit only compressive axial load. The bridge was placed in notches on the deck and the upper caisson. Higher viscosity fluid was usually used as pore fluid to avoid conflict with the scaling laws associated with the time of dynamic events and the seepage in centrifuge tests (Sakemi *et al.*, 1995, cf. Appendix B). Sand layers were saturated with a methyl-cellulose-base solution (Hiro-oka *et al.* 1995) which has a viscosity 50 times higher than that of water under a negative pressure of about 98kPa in a large tank by applying a vacuum. Ground water level was set at a depth of 40mm from the backfill surface in all the tests. Japanese noodles *somen* were placed between the model ground and the transparent window as markers to observe deformation of the ground.

Table 2.3 gives the test conditions. In case PW1, a shaking test was conducted under 50g by applying the earthquake motion recorded at Kobe Port Island in 1995 to the shaking table (Fig. 2.17).

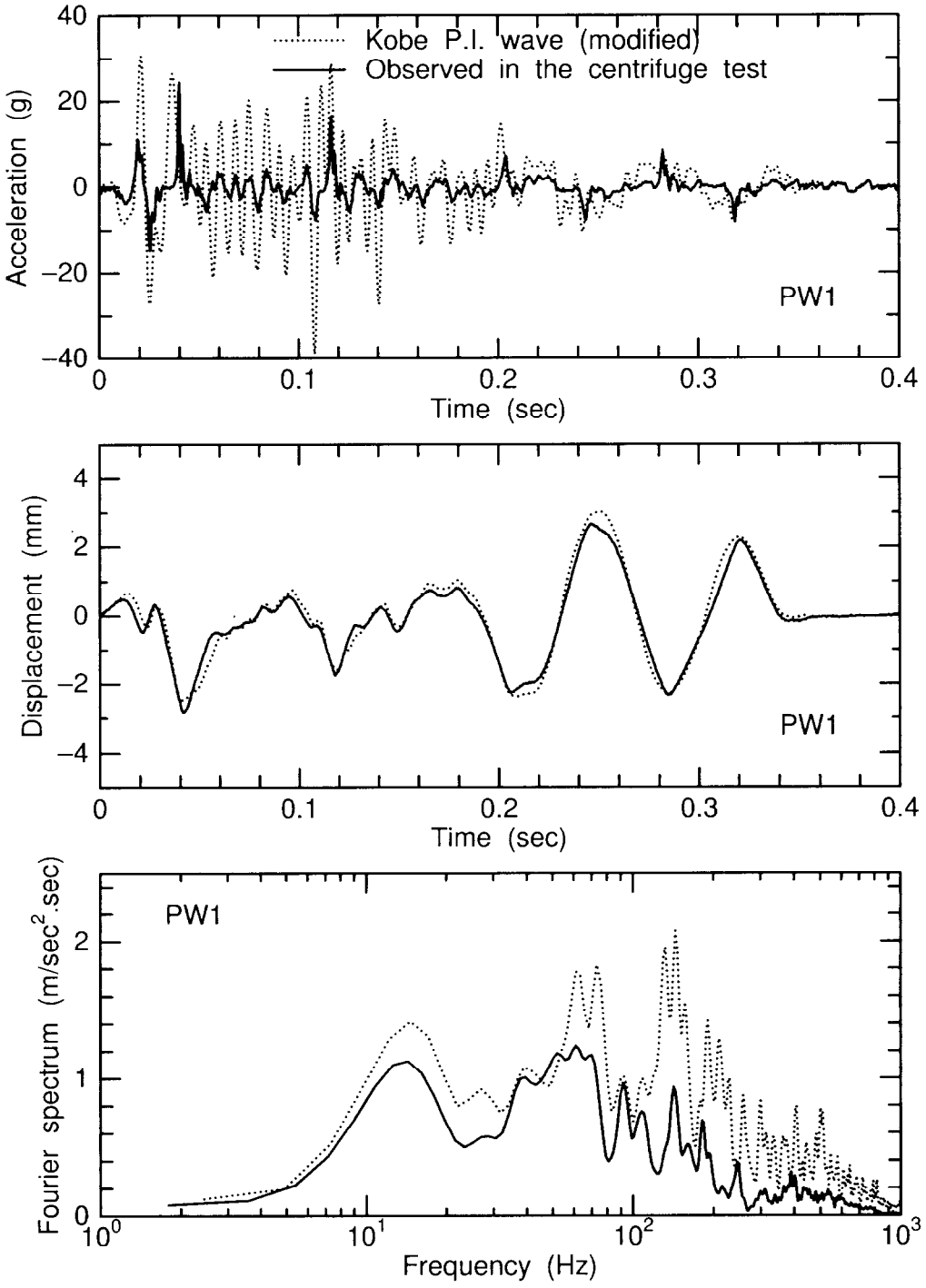

Figure 2.17: Time history of input wave for the Kobe Port Island.

This wave was recorded at a depth of 83m from the ground level, the same stratum as the bearing stratum for the wharf. As the wharf faced at an angle of 20 degrees to the north, the input motion was calculated using the NS- and EW-oriented ground accelerations. In the figure the input signal to the shaker was plotted with a dotted line, and the recorded motion of the table was plotted with a solid

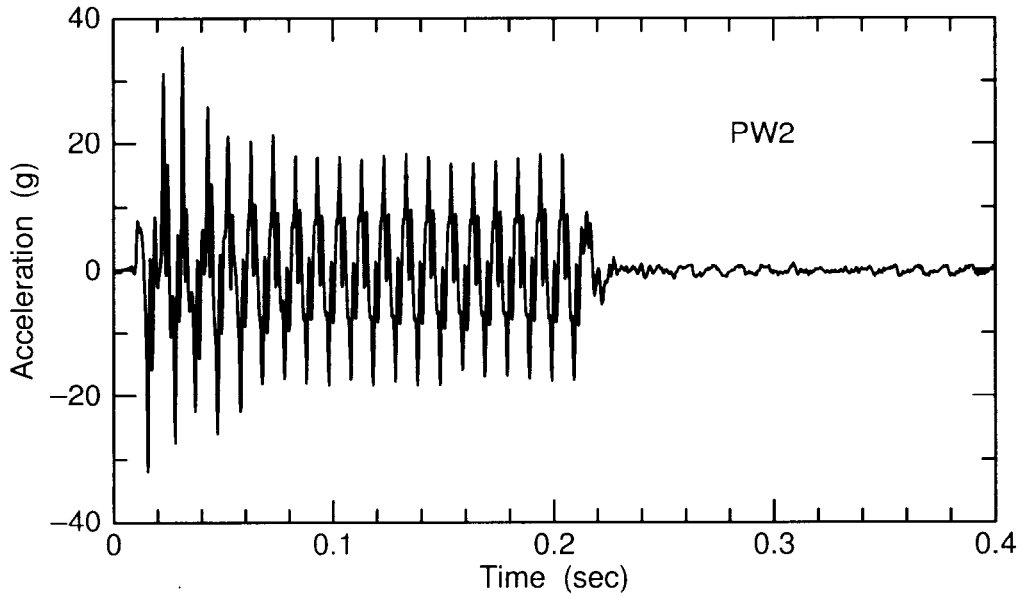

Figure 2.18: Time history of input sinusoidal waves.

line. As shown in Fig. 2.17, the strong ground motion like the Hyogo-ken Nambu Earthquake could not be obtained in the simulation by the shaker used, although the differences in the displacement time history and the Fourier spectrum were not large. Hence, in cases PW2 through PW7, 20 sinusoidal waves with a frequency of 100Hz (2Hz in the prototype scale) were applied which approximated the spectral peaks of the recorded wave at Kobe P.I. (around 1.4 and 2.8Hz). Typical time histories of the input sinusoidal waves are given in Fig. 2.18.

Besides PW1 and PW2, which simulate the conditions of the Kobe site, five additional tests were conducted. The stabilizing effect of the deck piles on the lateral spreading of soils was addressed in PW3 using a model without a deck. In PW4 and PW5, to gain further insight into the effect of liquefaction on the large deformation of the wharf, the liquefiable sand layers under the rubble mound and behind the caisson were replaced by higher hydraulic conductivity silica sand to avoid liquefaction. The effect of the approach bridge on a dynamic interaction between the deck and the caisson will be discussed in a comparison between PW6 and PW2. In PW7, the thickness h_s of the liquefiable sand layer under the rubble was twice as large as that in PW1 and PW2. In order to align the embedded length of the pile into the bearing stratum in all the cases, piles with lengths of 220mm were used in PW7.

Due to the limited number of data acquisition channels, the number of sensor-placed points were varied according to the test case as summarized in Table 2.4. Displacements of the deck and the lower caisson were measured by laser displacement transducers. These displacements were not measured directly on structures but at targets 30mm above the surface of the deck as shown in Fig. 2.15.

Table 2.4: Placed accelerometers and pore pressure transducers in shaking table tests.

Case \ Sensor location	A2	A3	A4	A5	A6	AS1	AS2	AS3	P1	P2	P3	P4	P5	P6
PW1, 2, 4, 5, 6 & 7	○	×	×	○	○	○	○	○	○	○	○	○	×	×
PW3	○	○	○	○	○	○	○	×	○	○	○	○	○	○

2.4 Simulation of the Takahama Wharf damaged in the 1995 Hyogo-ken Nambu Earthquake

Figure 2.19 shows observed excess pore water pressures at cell locations P2 & P4 and accelerations at meter location A6 in cases PW1 and PW2. The effective over burden pressures, σ'_{v0}, are also plotted in the figure. In case PW1 the excess pore water pressure at P2 almost reached a value of 80% of its σ'_{v0} at two peaks in the input wave, i.e., at 0.04 and 0.12 seconds, but no clear liquefaction was observed in this case. In PW2, the pore pressure at P2, located in the liquefiable sand layers, reached σ'_{v0} and leveled off, showing liquefaction at an early stage of the shaking. Although excess pore water pressure at P6 was not recorded in PW2, the backfill was seen to be liquefied, considering that the acceleration response at A6 was remarkably attenuated with shaking in PW2, and the pore pressure at P6 in PW3 reached its σ'_{v0} as shown in Fig. 2.20. The pore water pressure response in the rubble in PW3 is also shown in Fig. 2.20. As the rubble had a higher hydraulic conductivity compared to the liquefiable sand layer, accumulation of the excess pore water pressure at P6 in PW3 was very small. Taking this into account, the decrease in stiffness and strength of the rubble mound was thought to be small in PW2.

A photo taken just after shaking in PW2 is shown in Fig. 2.21, and the observed permanent deformation of the model ground in PW2 are also shown in Fig. 2.22. The noodle markers that can be seen in Fig. 2.21 were placed vertically on the ground before the tests. The structures moved laterally seaward, and a large horizontal displacement gap was observed between the rubble mound and the bearing stratum. Permanent deformation of the model ground in PW1 was essentially the same as that observed in PW2, although the displacement was smaller than that in PW2.

Figure 2.23 illustrates observed lateral displacements of the deck and the lower caisson. It should be noted that the displacements shown in the figure were not measured directly at those structures but at targets 30mm above the surface of the deck as shown in Fig. 2.15. Regarding the plot of the lower caisson (dotted line in Fig. 2.23), the laser displacement transducer went out of its measurable range as the target surface defected its laser reflection. It is apparent from the figure that the caisson and the deck moved together in the early stages of the shaking. Displacements of the caisson, however, became larger than that of the deck, which may have been caused by the relatively large tilting of the caisson. In PW1, permanent displacements of the structures were smaller than those in PW2. Two large fluctuations were observed, corresponding to the peaks of input acceleration. The structures gradually moved with time, and no substantial displacement took place after the shaking in PW2. This result suggests that not only deterioration of the soil strength due to liquefaction but also the continuous cyclic force had substantial effects on the accumulation of the deck displacement.

For case PW2, the strain on the piles at various depths was measured, and the values recorded

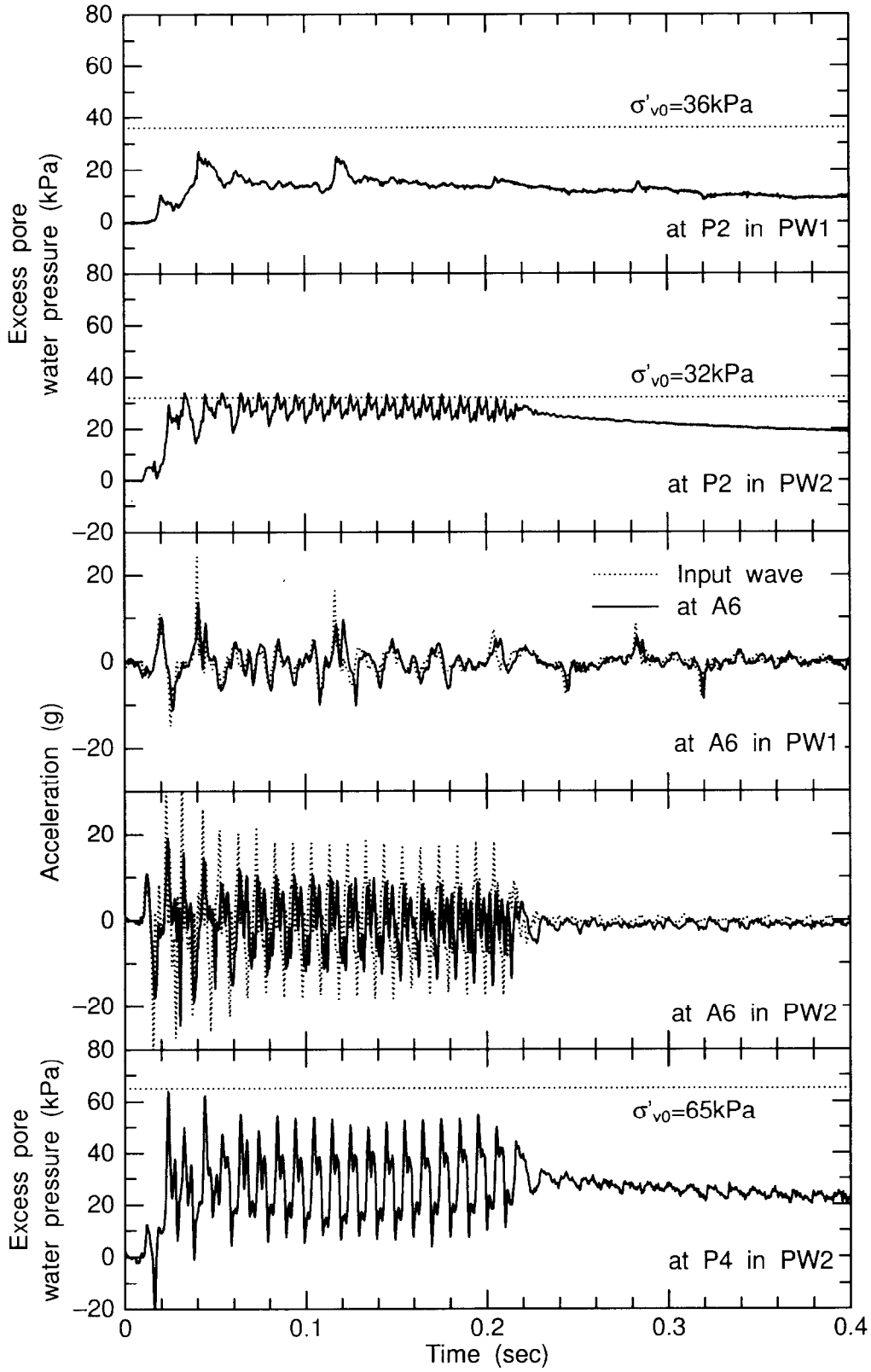

Figure 2.19: Time histories of excess pore water pressure at the sand layer, P2 & P4, and acceleration at the backfill, A6, in PW1 & 2.

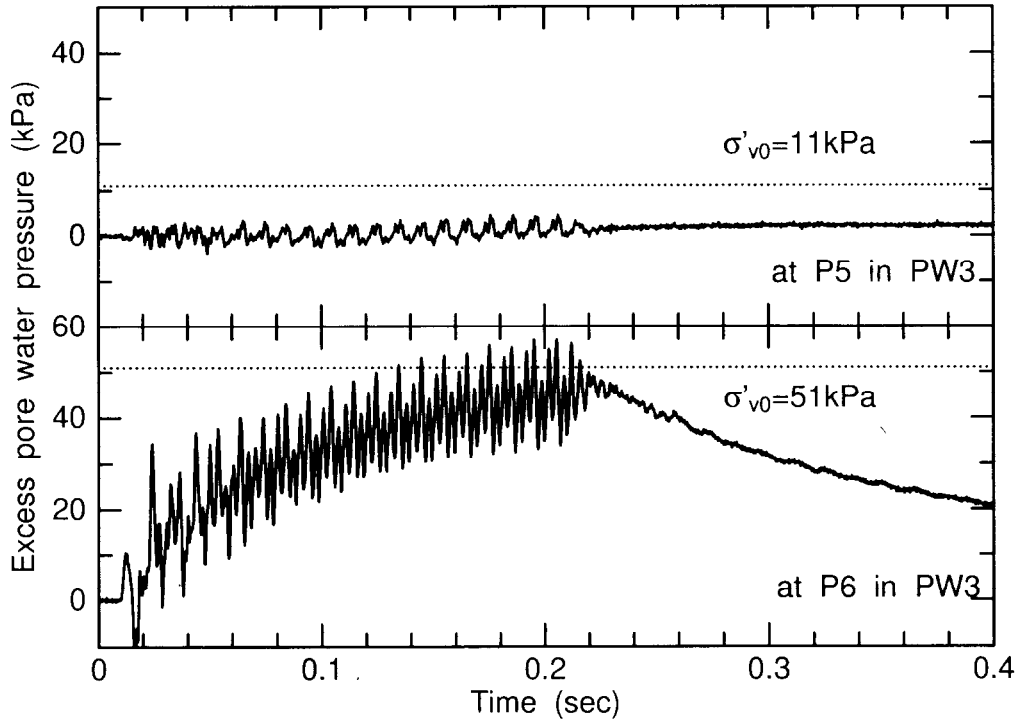

Figure 2.20: Time histories of excess pore water pressure at the rubble mound, P5, and at the backfill, P6, in PW3.

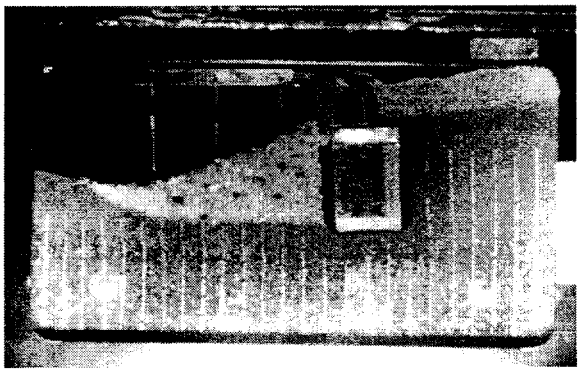

Figure 2.21: Photo taken just after shaking in PW2.

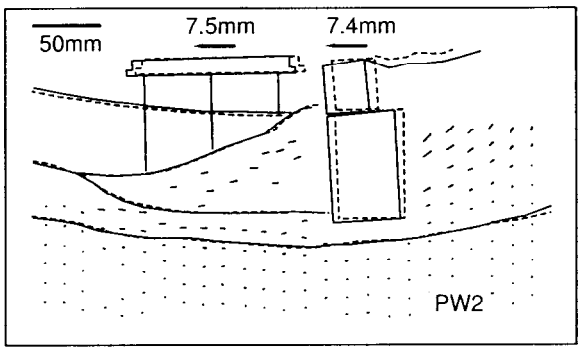

Figure 2.22: Observed deformation of model ground in PW2.

just after the shaking are shown in Fig. 2.24. Also for case PW2 the variation of strains measured at the top of the sea side pile (St9S), at the land-side pile (St9L), and at the lower point of the land-side pile in the bearing stratum just below the sand layer (St2L) are illustrated in Fig. 2.25. As strain gauges were put only on the right inside of the piles, outputs from them include strains caused by axial tension or compression as well as bending. However, the variation of the axial strain was very small compared to the measured strain on the right side of the pile, as shown in Fig. 2.25. The measured strain on the right side of the pile would be nearly equal to the bending strain of the pile. Negative

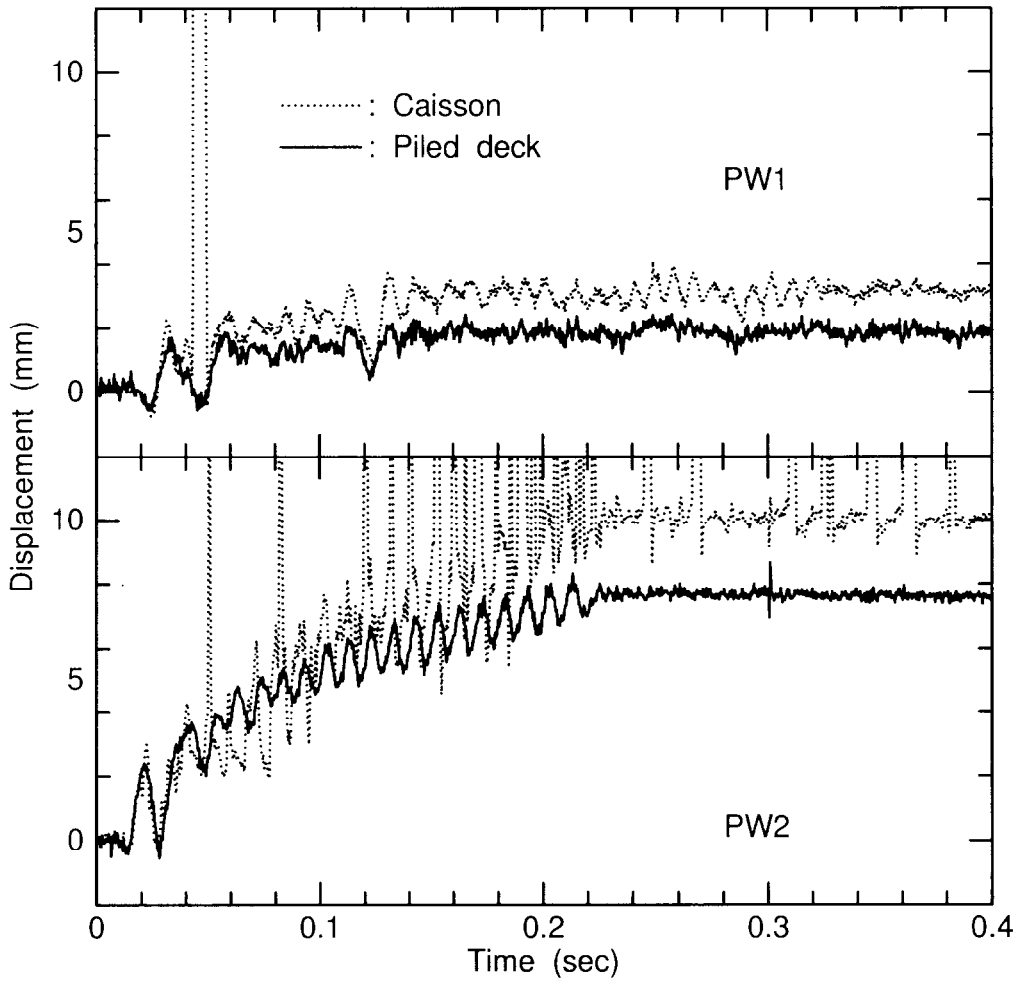

Figure 2.23: Time histories of displacements of deck and caisson in PW1 & 2.

values in the figure represent compression on the right side of the pile. As shown in this figure, a very large negative strain appeared at the top of the piles, and large positive values were measured in the bearing stratum just below the sand layer, also evident in Fig. 2.24. These points agree with the locations of large pile deformation observed at the Kobe site as illustrated in Figs. 2.7 and 2.11. All indications support the conclusion that the centrifuge model tests can reliably show us the failure mode or mechanism of the wharf at the actual site. The strain on the piles changed sign in the sand layer irrespective of the pile row. This fact represents that the inflection points in the piles deflection existed at this level, and there was large relative displacement between the rubble mound and the bearing stratum as shown in Fig. 2.22. The deck moved seaward as a result of lateral movement of the rubble mound and behaved as a *passive pile*.

Regarding the amplitudes and accumulations of strain on the pile, the strains observed at St9S & St9L are larger than that at St2L, especially in the early stage of shaking. Both the larger amplitude and the larger permanent strain at the top of the piles suggest that the large deformation at the pile top initiated the failure of the deck pile before that at the lower portion of the pile around the sand layer

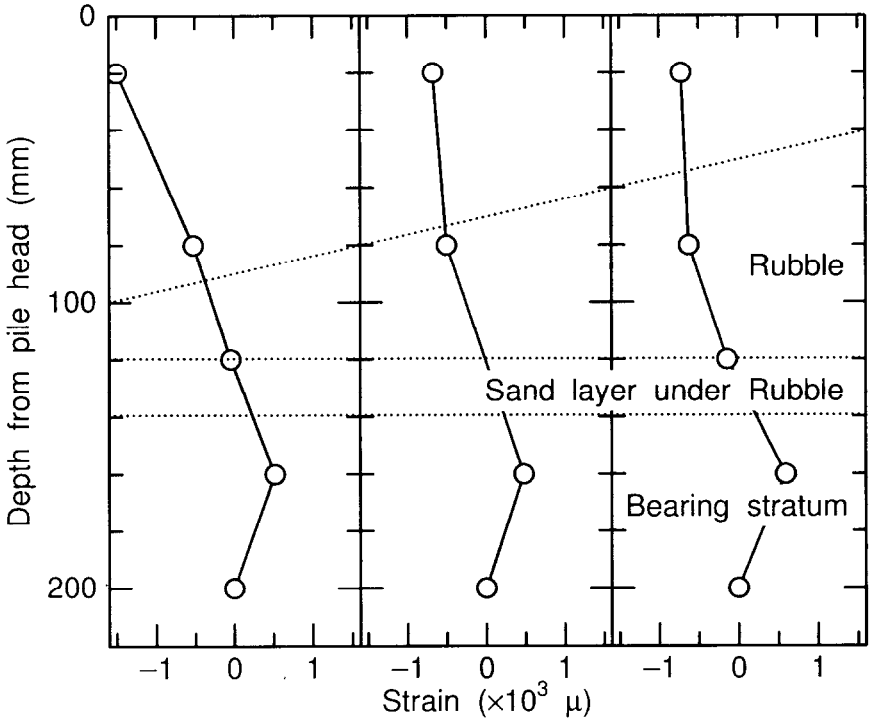

Figure 2.24: Permanent strain distributions of pile in PW2.

under the rubble mound. According to the results of a beam structure analysis of the deck subjected to rubble mound movements through soil springs by Minami *et al.* (1997), the structure hinging initially occurred at the heads of the sea-side and the land-side piles and at the lower portion which corresponded to the depth of the liquefiable layer of the middle pile, and then the hinging came to the lower portion of the sea-side and the land-side piles. The centrifuge test results agree with their analysis results as a whole, although there are minor differences in the middle pile response. Further discussion on the failure process of the piles of the deck will be made in Chapter 6 in comparison with the numerical analysis results. In the following sections, effects of several factors on the permanent deformation of the wharf will be discussed.

2.5 Effects of several factors on permanent deformation of wharf

2.5.1 Deck–caisson interaction through approach bridge

The wharf deck in this study was connected to the caisson by the approach bridge. As mentioned in Section 2.1.2, cracks were found on the approach bridges and the land-side of the deck. These cracks were seen to be caused by clashing between the bridge and the deck. Though the impact was not enough to collapse the deck, the interaction between the deck and the caisson through the approach bridge might increase the damage to the wharf. In order to examine effects of the approach bridge on the permanent deformation of the wharf, a centrifuge test result without the approach bridge (PW6) will be compared with a test with the bridge (PW2).

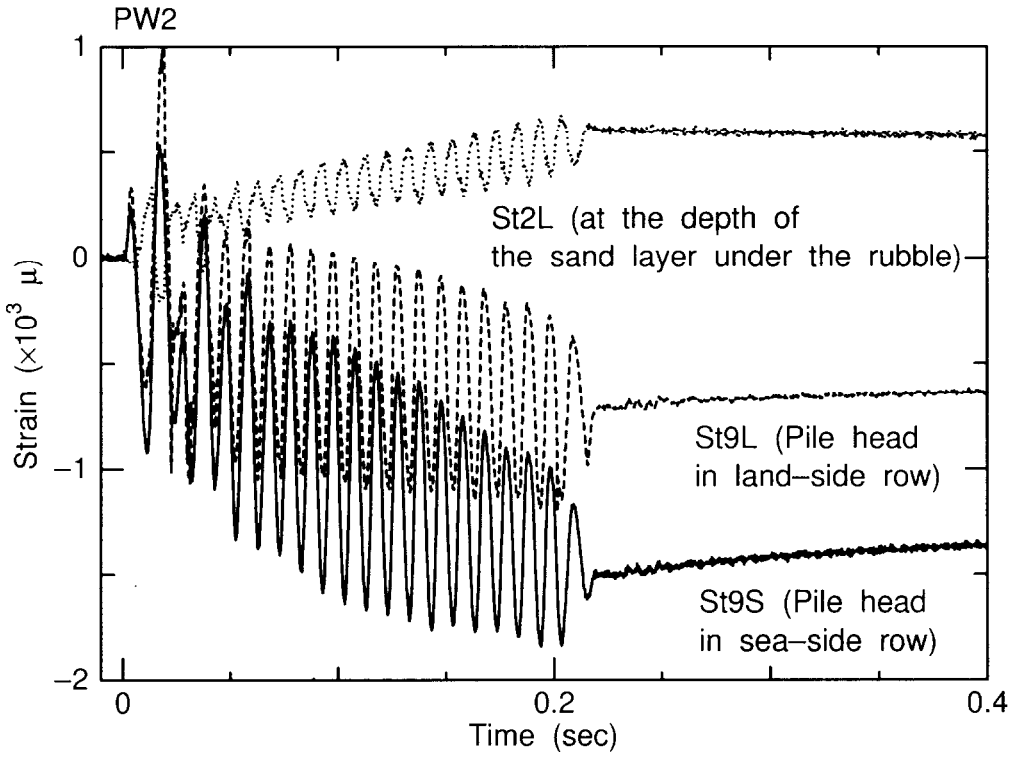

(a) Variations of strain in land-side row.

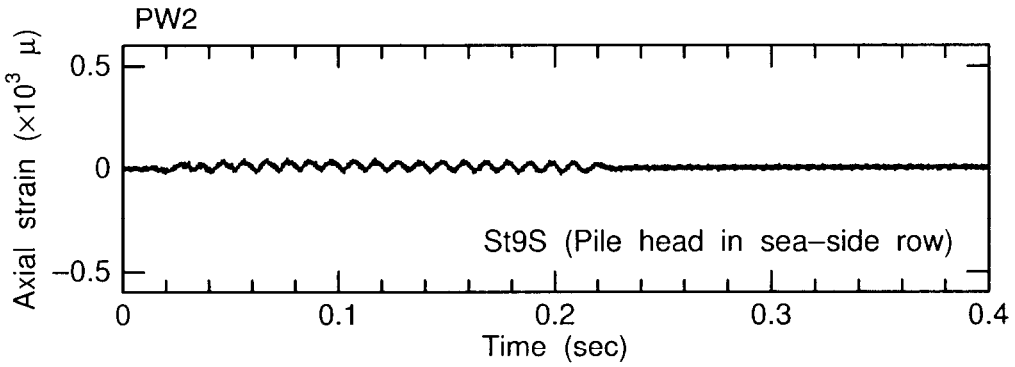

(b) Variation of axial strain at the top of pile.

Figure 2.25: Time histories of the strain of pile in PW2.

Observed displacements of the deck in PW2 and PW6 are shown in Fig. 2.26. Comparing the results in PW2 and PW6, the velocity of the deck in PW6 was smaller than that in PW2, resulting the smaller permanent displacement. Accelerations observed at the deck of the deck in PW2 and PW6 are compared in Fig. 2.27. Acceleration in the seaward direction is taken as positive in the figure. In PW2, clear spikes can be seen in the positive peaks where the deck moved landward. This implies that the movement of the deck of the wharf landward was prevented by the caisson through the approach bridge, and a large horizontal force was applied from the caisson. It can be expected that the approach bridge accelerated the seaward movement of the wharf.

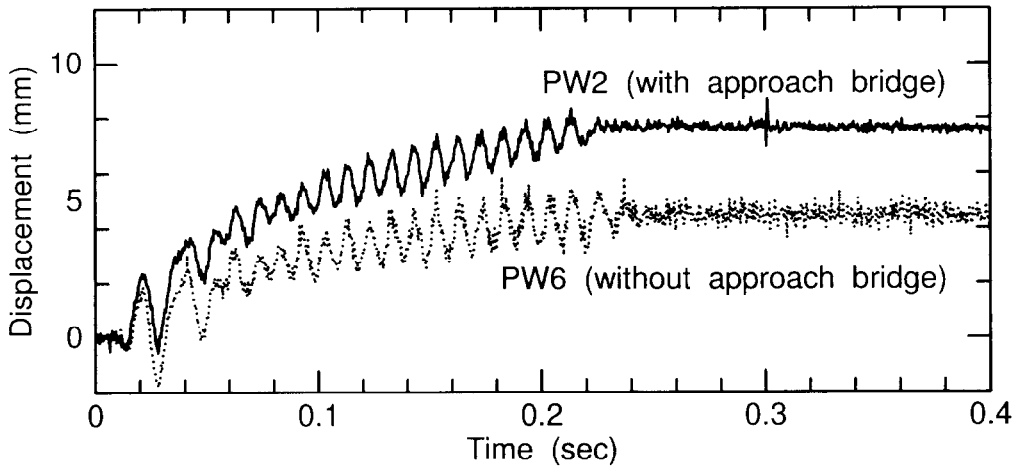

Figure 2.26: Time histories of displacement of deck in PW2 & 6.

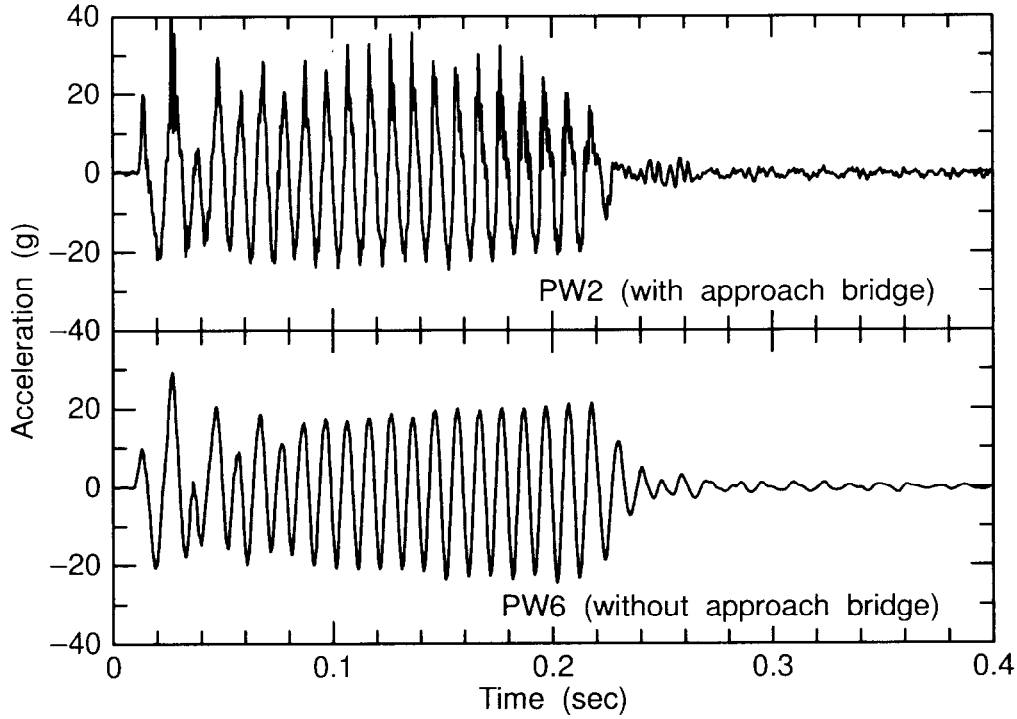

Figure 2.27: Acceleration time histories of deck in PW2 & 6.

2.5.2 Stabilizing effect of piles

A row of piles is sometimes used for stabilization of a moving slope, i.e. a landslide. This stabilizing effect of the row of piles might have a potential for preventing the movement of the rubble mound and/or the caisson in this study. Figure 2.28 shows permanent lateral displacements of the rubble mound and the sand layer under the rubble in PW2 and PW3. These displacements were the horizontal

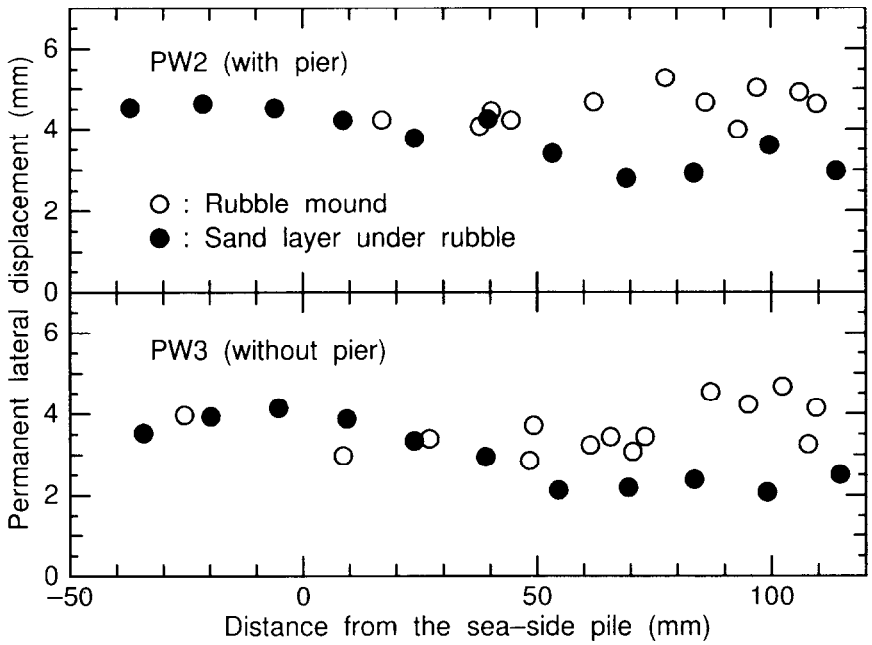

Figure 2.28: Permanent lateral displacements of rubble mound and sand layer under rubble in PW2 & 3.

movements of the noodle targets placed between the transparent window of the container and the model grounds. Regarding the pile spacing of the deck, the movement of the front side of the model ground corresponded to that at the center of the pile space. Although obtained data are scattered, the displacement distributions of the rubble and the sand layer are nearly the same, and no remarkable difference can be seen since the pile spacing ratio was relatively larger than that of the other piled structures.

2.5.3 Liquefaction of sand layers

Liquefaction of the sand layers undoubtedly affected the permanent deformation of the wharf. Although this fact can be qualitatively accepted, how the liquefaction of the sand layers quantitatively affects performance of the wharf is unknown. In order to examine the liquefaction effects on the wharf performance, in PW4 and PW5 the liquefiable sand layer under the rubble mound (PW4) and behind the caisson (PW5) were replaced by higher hydraulic conductivity silica sand to avoid liquefaction. The density of the replaced soil was adjusted to that of the original liquefiable layer. In PW7, the thickness (h_s) of the liquefiable sand layer under the rubble was twice as large as that in PW1 and PW2.

Observed excess pore water pressures at P2 in PW4 and at P4 in PW5 and acceleration at A6 in PW5 are illustrated in Fig. 2.29. Responses of pore pressures and acceleration in PW2 are plotted in dotted lines for the sake of comparison. Although excess pore water pressures at P2 in PW4 and at P4 in PW5 (where the liquefiable sand was replaced by high hydraulic conductivity sand) showed almost the same responses as those in PW2 in the early stages, quick dissipation of pore pressures was observed. Such dissipation was not marked in the other tests. The amplitude of the acceleration at A6 remained constant with the shaking in PW5, while the acceleration response was remarkably

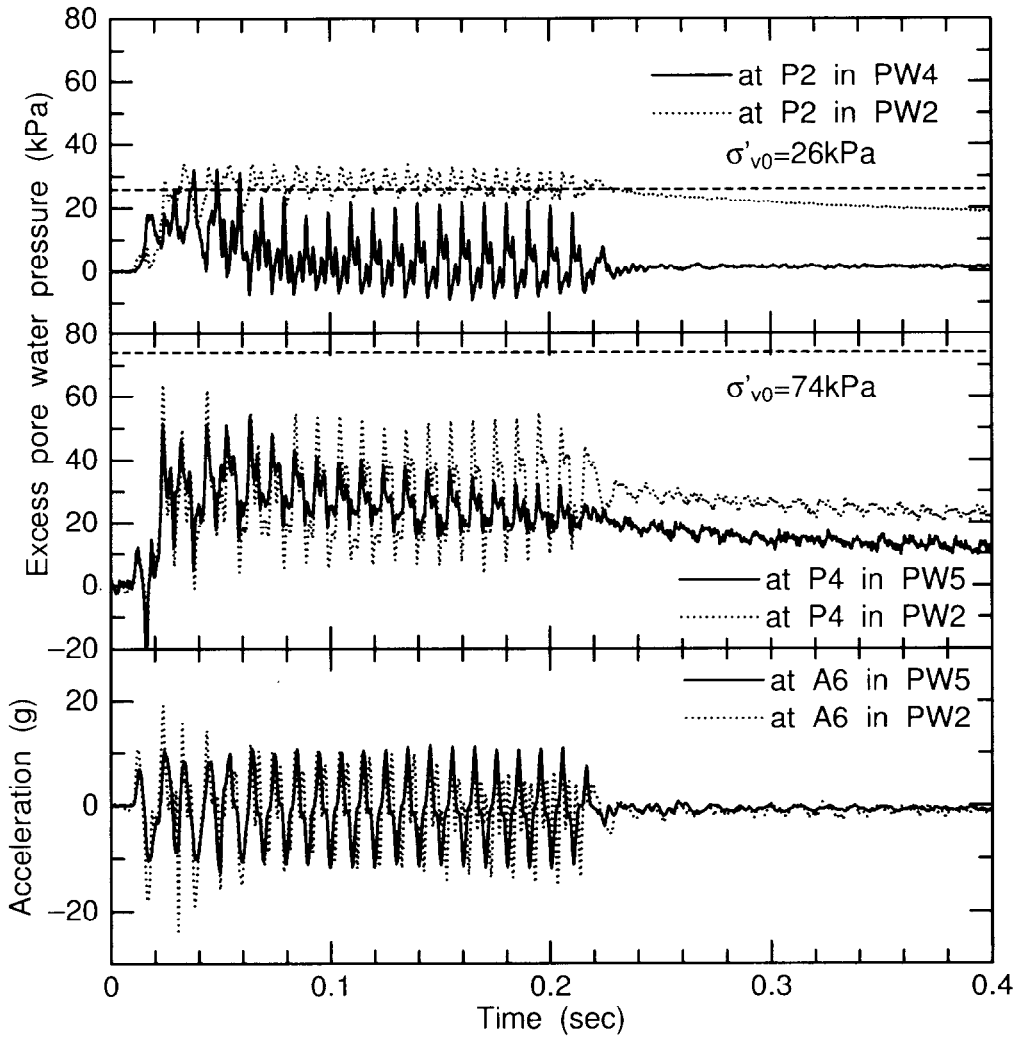

Figure 2.29: Time histories of excess pore water pressure at P2 in PW4 and at P4 in PW5 and acceleration at A6 in PW5.

attenuated in PW2. These facts show that the replacement of the liquefiable soil performed well as a countermeasure.

Observed horizontal displacements of the lower caisson and the deck in PW2, PW4, PW5 & PW7 are shown in Fig. 2.30. In the early stage of the shaking, the responses of the deck and the caisson were almost the same and they moved together in all the cases. Except in PW7, the displacements of the caisson, however, became larger than that of the deck, which may be caused by the relatively large tilting of the caisson, as previously explained. In PW7, the tilting of the caisson was small, and the horizontal displacement of the deck and the caisson was almost the same, as shown in Fig. 2.31.

Displacements of the deck and the caisson in PW4 and PW5 were smaller than those in PW2. Comparing the results in PW4 and PW5, the velocity of the structures in PW4 decreased at earlier stages than in PW5, resulting in smaller displacements. Under these test conditions, it can be concluded that the liquefaction at the sand layer beneath the rubble mound and caisson has more marked

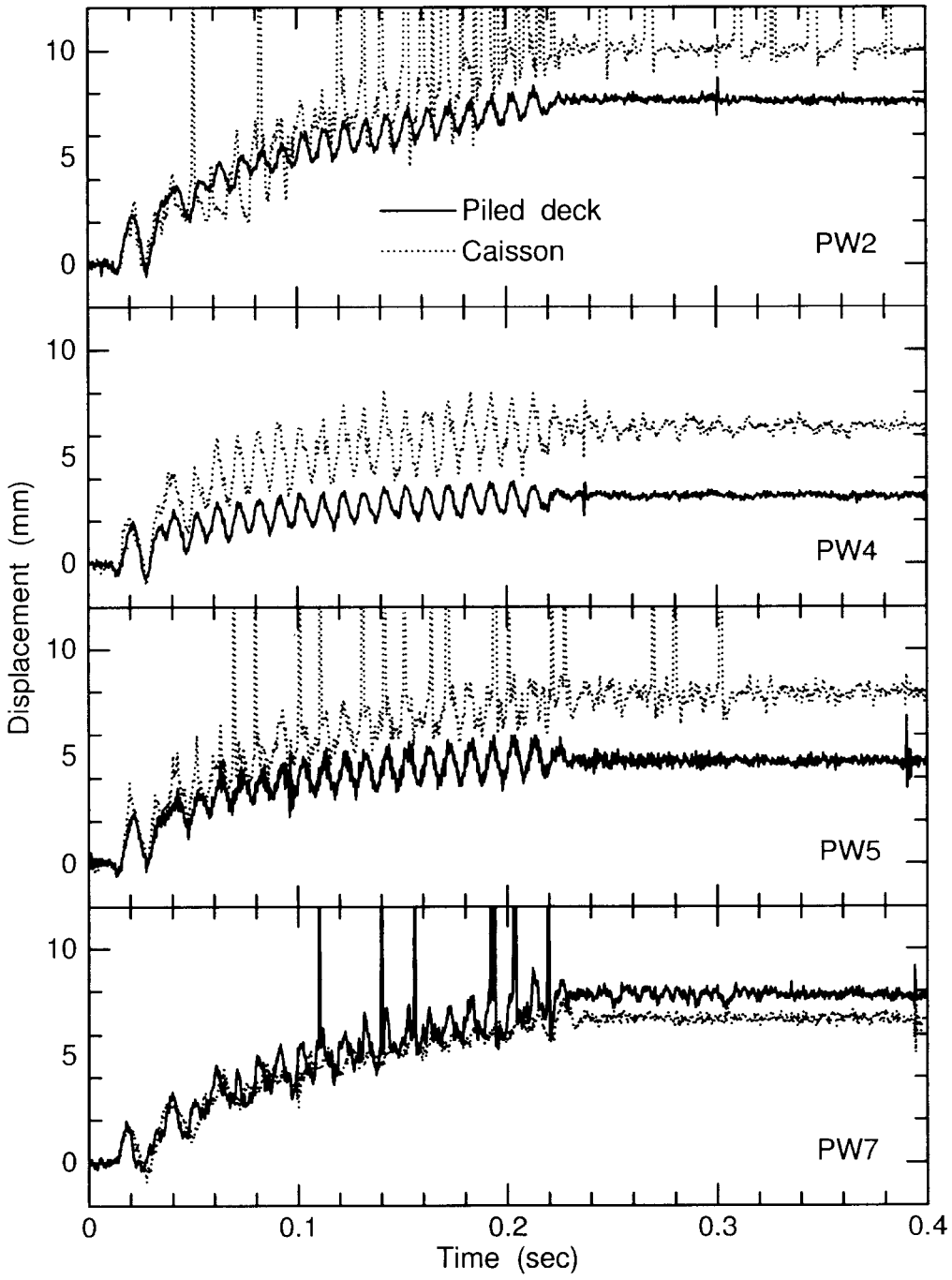

Figure 2.30: Time histories of deck and lower caisson in PW2, 4, 5 & 7.

effects on the movement of the structures than that at the backfill.

Observed deformations of the model ground due to the shaking in PW2, PW4, PW5 and PW7 are shown in Figure 2.31. The horizontal displacement gap between the rubble mound and the bearing stratum was remarkably smaller in PW4 than the other cases. Considering the fact that liquefaction took place in the sand layer between these two layers except in PW4, as shown in Fig. 2.29, it can

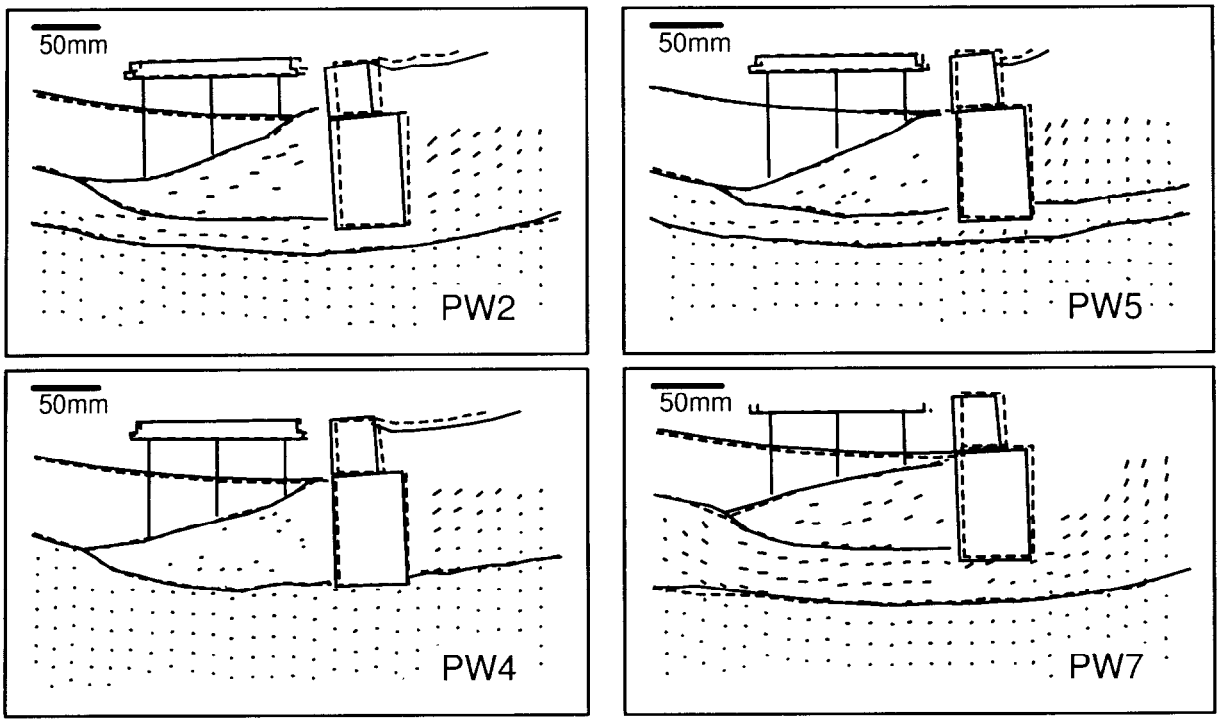

Figure 2.31: Permanent deformations of model ground in PW2, 4, 5 & 7.

be said that even the thin sand layer under the rubble mound, i.e. 1–2m in these model tests and at Takahama, had a significant effect on the displacement of the rubble mound and caisson. Regarding the difference in the thickness of the liquefiable sand layer under the rubble, significant settlement of the caisson and squeezing of the sand layer between the two non-liquefiable layers were observed in PW7, while in PW2 displacement of the rubble mound was larger than that of the sand layer, and no large settlement was observed. This result indicates that variation of the thickness of the sand layer under the rubble mound causes a change of deformation mode of the ground and structures.

Permanent displacements of the rubble mound and the sand layer under the rubble around the deck are plotted against the permanent displacement of the deck in Fig. 2.32. These displacements were measured from photos taken before and after the shaking. Within the test conditions of this study, the displacement of the deck is proportional to that of the rubble mound. This implies that the deformation of the stiff rubble mound dominated the displacement of deck.

The change of the deformation mode of the ground and the structures can also be seen in Fig. 2.32 and Fig. 2.30. The displacement of the caisson became larger than that of the deck in PW2, reflecting the relatively large tilting of the caisson, while in PW7 the tilting of the caisson was small, and horizontal displacements of the deck and the caisson were almost the same, resulting in a small permanent horizontal displacement. Though the thicker liquefiable sand layer made the movement of the overlaying non-liquefiable layer easier, it also made the settlement of the caisson larger. Due to the larger settlement of the caisson, its tilting might have been attenuated, resulting in smaller horizontal displacements of the rubble mound and the deck. Regarding the facts mentioned above, the thicker liquefiable sand layer does not necessarily make the permanent displacement of the deck larger.

The measured strain on the piles just after the shaking in PW2, PW4, PW5 and PW7 are shown

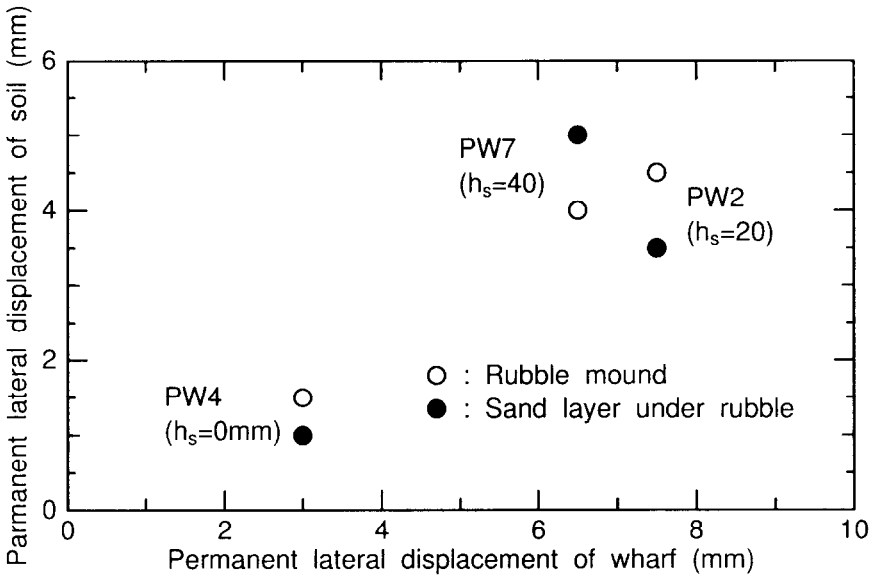

Figure 2.32: Permanent lateral displacements of rubble mound and sand layer under rubble against displacement of deck in PW2, 4 & 7.

in Fig. 2.33. In PW2, PW5 and PW7, the strain value changed its sign around the sand layer under the rubble. This fact represents that the inflection points in the pile deflection existed at this portion, and there were large relative displacements between the rubble mound and the bearing stratum, as shown in Fig. 2.31. The strain distribution in PW5 was almost the same in shape as PW2, but smaller in magnitude. By replacing the backfill with high hydraulic conductivity material to prevent liquefaction, the permanent displacement of the rubble mound as well as the strain on the pile can be reduced. Improvement of the backfill against liquefaction can be an effective countermeasure to prevent the failure of the deck. In case PW4 where the sand layer located under the rubble mound was replaced, the inflection points of the pile deflection were located around the surface of the rubble mound. This confirms that there was no relative displacement between the rubble mound and the bearing stratum. Strains at the pile top in PW4 are smaller than those in the other cases. It can be concluded that improvement of the sand layer under the rubble mound is more effective for reducing the lateral spreading of the ground and preventing the large deformation of piles than improvement of the backfill.

2.6 Summary

In this chapter, centrifuge model tests were carried out to investigate the dynamic behavior of the pile-supported wharf, focusing on the pile-failure mechanism, the effects of liquefaction in the backfill and the sand layer on permanent deformation of the wharf during earthquakes, and the dynamic interaction between the wharf deck and the caisson through the approach bridge. The targeted piled structure was the pile-supported wharf damaged in the 1995 Hyogoken-Nambu Earthquake at Takahama, Kobe. The following conclusions are drawn:

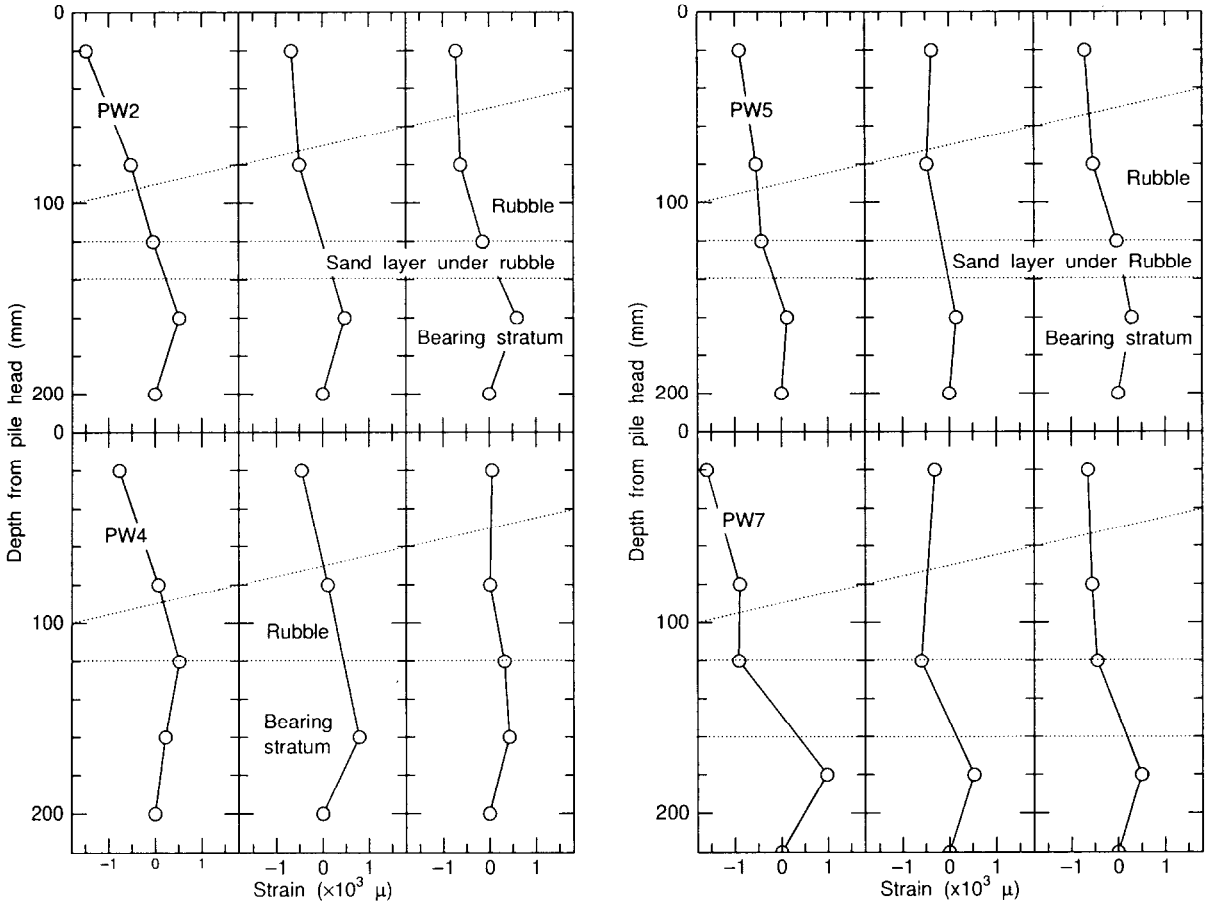

Figure 2.33: Distributions of permanent strain of pile in PW2, 4, 5 & 7.

- Liquefaction of the foundation soil and the backfill behind the caisson during the earthquake caused a large seaward lateral movement of the rubble mound. As a result, a large horizontal displacement gap was formed between the rubble mound and the bearing stratum. This displacement gap caused very large bending moments at the pile tops and in the bearing stratum just below the sand layer. These large bending moment locations agree with the locations where large pile deformations were observed at the Kobe site. Centrifuge model tests can reasonably predict the failure mode of the piled wharf observed in the Kobe Earthquake.

- During the shaking, the wharf gradually moved seawards, and no substantial displacement took place after the shaking as no flow liquefaction occurred. This result suggests that not only the deterioration of the soil strength due to liquefaction but also the continuous cyclic force had a substantial effect on the accumulation of the movement of the wharf.

- The approach bridge connecting the deck of the wharf and the caissons accelerates the seaward movement of the wharf during an earthquake, as the landward movement of the deck is prevented by the caisson through the bridge.

- Variation of thickness of the sand layer under the rubble mound caused a change of deformation mode of the ground and structures. The test without the sand layer beneath the rubble showed no displacement gap between the rubble mound and the bearing stratum, resulting in only a small permanent displacement of the deck, while the thicker liquefiable sand layer did not necessarily cause the large deformation of the soils and structures.

Chapter 3

Lateral resistance of piles in liquefied soil

3.1 Piles in lateral spreading soil due to earthquake

As described in the previous chapter, development of large strains in a liquefied soil layer can induce high bending moments in piles that extend through it. Hence, around an interface between liquefied and non-liquefied soils, a significant curvature will be demanded on a pile due to the difference in soil stiffness. In other words the lateral resistance of the pile drastically changes along the pile length.

In non-liquefied soils, the lateral resistance of a pile may be evaluated by solid mechanics based on concepts of effective stress, though several difficulties arise for partially saturated soils and crusts that constitute soil layers above the ground water table. On the other hand, pile resistance in the liquefying soil drastically changes with the accumulation of excess pore water pressure during an earthquake. Some researchers have put forward a hypothesis that the liquefied soil behaves as a liquid. For instance, Hamada *et al.* (1992) and Satoh *et al.* (1998) conducted shaking table tests in 1g and 50g respectively on the dynamic behavior of a single pile in sloping liquefied sand. They showed that the bending strain of the pile first increased and then dropped to almost zero during the shakings as shown in Fig. 3.1. Though displacement and velocity of the ground are not shown in this figure, the variation of the ground velocity was similar to that of a bending moment of the pile.

This fact supports the hypothesis that the liquefied soil behaves as a liquid, and the loading rate affects the lateral resistance of the pile in the liquefied soil. Supposing that the liquefied sand is a kind of incompressible fluid, determination of the viscosity of the fluid is necessary to estimate the lateral resistance of the pile in the liquefied soil, as an object's drag force in the incompressible fluid is characterized by the viscosity when the size of the object and the velocity of the fluid are given. In order to determine the viscosity of the liquefying soil, many experimental researches were conducted in the 1990s (e.g. Miyajima & Kitaura, 1994; Towhata *et al.*, 1999). However, this idea that the behavior of the liquefied soil can be illustrated by that of an incompressible fluid is not seen to be suitable for the recent performance-based design of pile foundations, as it is very difficult to determine the velocity of the ground during the whole period of the shaking. Without information on the variation of the ground velocity, permanent deformation of the pile foundation cannot be predicted.

In practical seismic design codes for the piled structures, it is prescribed that the displacements of the pile foundation during earthquakes must be assessed by a framed structure analysis subjected to soil movement through soil–structure interaction springs (Railway Technical Research Institute, 1997; Metropolitan expressway public corporation, 1998; The High Pressure Gas Safety Institute of

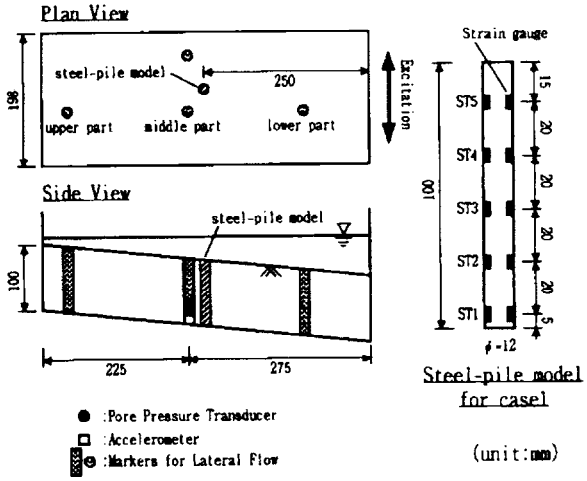

(a) Model setup for centrifuge test.

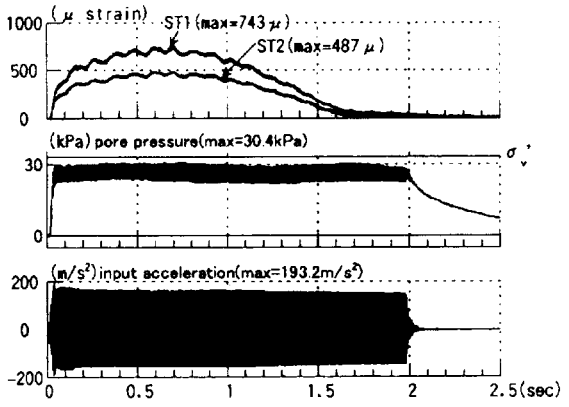

(b) Time histories of bending strain, excess pore water pressure and input motion.

Figure 3.1: Dynamic behavior of single pile in sloping liquefied sand (Satoh *et al.*, 1998).

Japan, 2000). These earthquake resistant design codes in Japan have been summarized by the Japan Society of Civil Engineers (2000). In these codes, a degradation parameter of the lateral resistance in liquefiable soils, which is a reduction factor of the lateral resistance of the pile in the liquefied soil in relation to that in the non-liquefied soil, is in the range of 1/1000 and 1/100. These reduction factors have been determined by back-analyses to fit responses of piles damaged in earthquakes without consideration of the behavior of the soil surrounding the pile. These determinations may be based on an assumption that the degradation parameter of the lateral resistance of the pile is proportional to an effective confining stress of the subsoil, and the volume of soil resisting the pile movement is quite limited adjacent to the pile. Dobry *et al.* (1997) showed relationships between the degradation parameter for *p–y* curves, c_u, and the excess pore water pressure ratio, r_u, obtained by centrifuge model tests. They concluded that the value of lateral forces decreased as the pore pressure ratio increased, as shown in Fig. 3.2. However, in the liquefying soil, the behavior of soil surrounding the pile is still unknown and the lateral resistance mobilization mechanism is also not clarified. Hence, direct measurement of the lateral pile resistance in the liquefied soil and observation of the soil surrounding the pile are attempted here.

3.2 Measurement of lateral resistance of piles in liquefied soil

Information derived from the previous section's shaking table tests is seen to be of value in demonstrating the actual behavior of piles and soils during earthquakes. However, the actual behavior of piles is complicated and affected by several factors. Investigating effects of each factor from the complicated behavior observed in the shaking table tests is not a straightforward process. In order to avoid this complication, i.e. to directly measure the lateral resistance in the liquefied soil, and to easily observe the soil surrounding the pile, the pile was modeled as a buried cylinder that corresponded to a sectional model of the pile at a certain depth in subsoil (Fig.3.3). In order to create a realistic stress condition in the model ground, the model was prepared in a sealed container, and an over burden

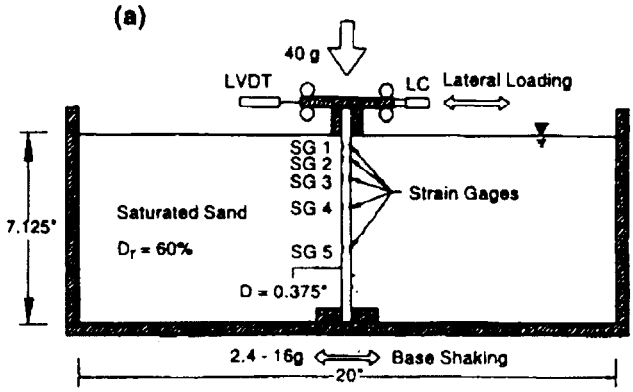

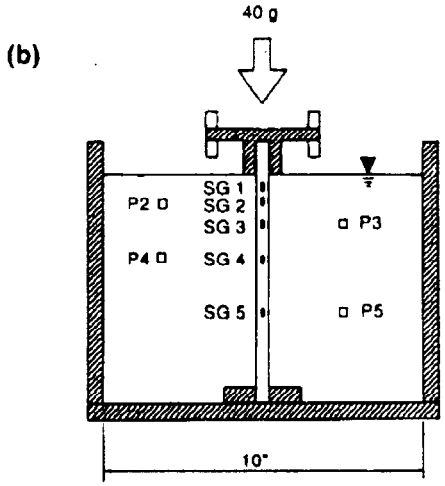

(a) Side view and (b) front view of model setup for centrifuge test.

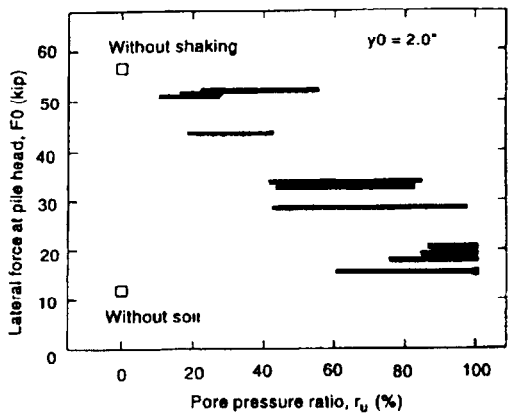

(c) Lateral force at pile head versus pore pressure ratios for 2-inch pile head lateral displacement.

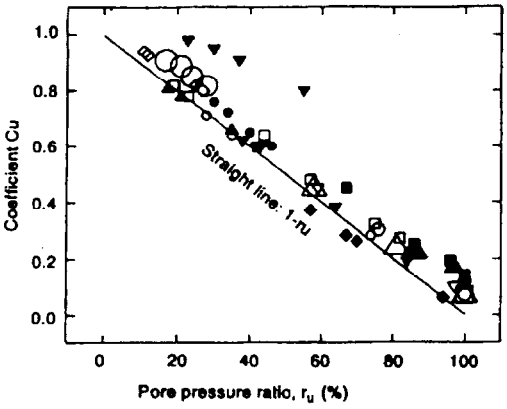

(d) Relationship between degradation parameter and excess pore water pressure ratio.

Figure 3.2: Measurement of lateral resistance of pile in liquefied sand (Dobry *et al.*, 1997).

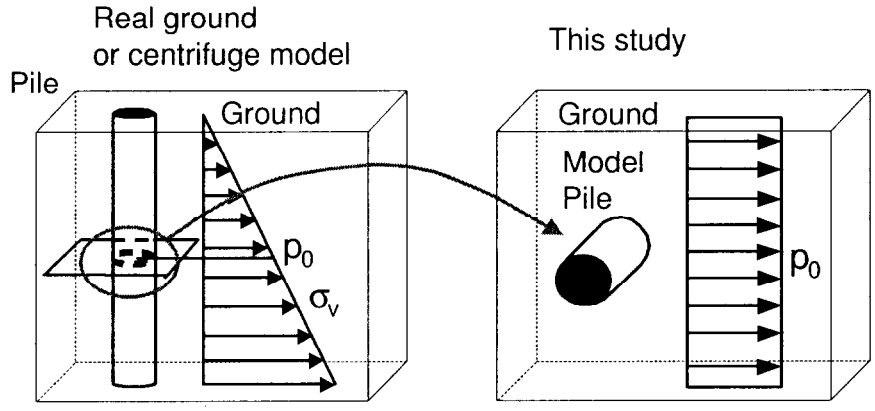

Figure 3.3: Modeling of pile in this study.

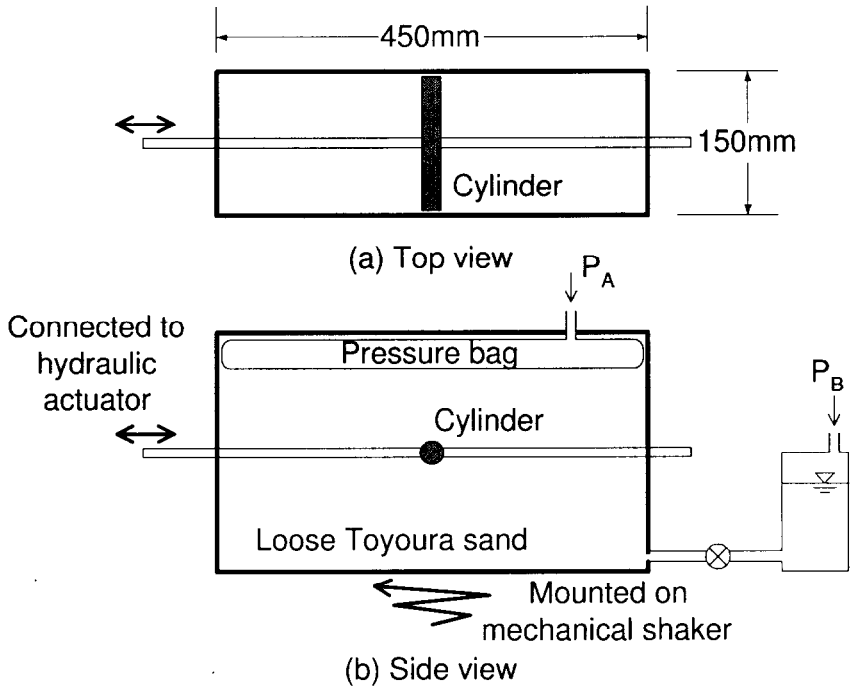

Figure 3.4: Schematic drawing of model container.

pressure was applied to the ground surface by a rubber pressure bag.

This chapter focuses on observing the deformation of the liquefied soil surrounding the pile when the large relative displacement between the pile and the soil is induced. The loading rate effect on the lateral resistance of the pile in the liquefied sand is also investigated.

3.3 Test procedures and conditions

The model container used in this study is schematically illustrated in Fig.3.4. Figure 3.5 shows an overview of the model container mounted on a shaking table. An aluminum model container was used with inner sizes of 450mm in width, 150mm in breadth, and 250mm in height. The front face of the box was a transparent window to observe the deformation of the model ground. A pressure bag made of rubber was attached underneath the top lid of the container to apply an over burden pressure, P_A, on the surface of the soil. A fluid tank was connected to the bottom of the box to supply and drain out fluid and to apply a back pressure, P_B, to the pore fluid of the soil.

Figure 3.6 shows an aluminum-made cylinder equipped with pore and earth pressure transducers. The surface of the cylinder was made smooth by the fabricator. Rubber sheets were put on both ends of the cylinder for lubrication and to prevent sand particles from getting into the gap between the cylinder and the side walls of the container. Two rods were connected to the center of the cylinder. Two load cells were inserted into the respective rods near the cylinder to avoid the influence of friction in measuring the net lateral force on the cylinder. The cylinder was actuated back and forth through the rod by an electro-hydraulic actuator. The actuator was mounted on the side wall of the model container.

Toyoura sand, uniformly graded sub-angular quarts sand (D_{50}=0.19mm,) was used for the model

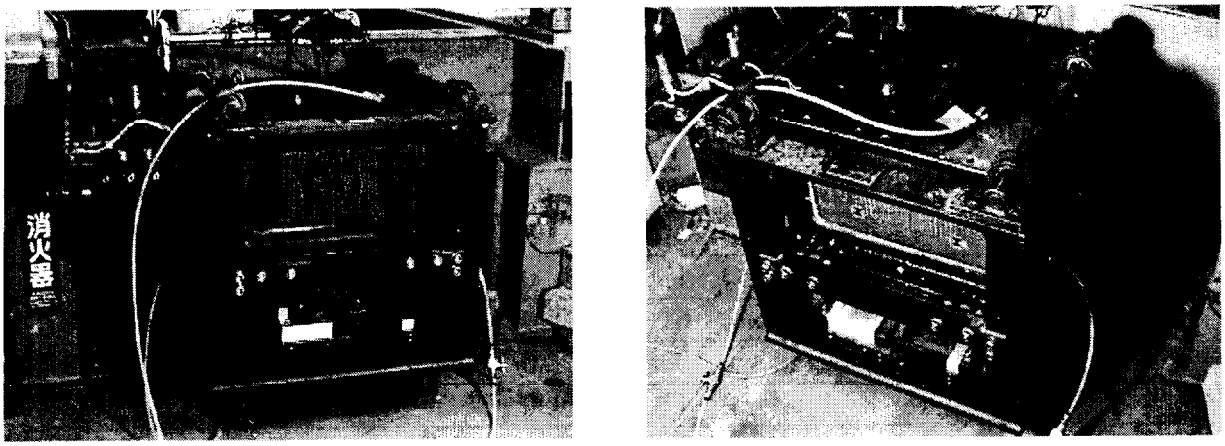

(a) Side view. (b) Bird's eye view.

Figure 3.5: Outer view of model container mounted on shaking table.

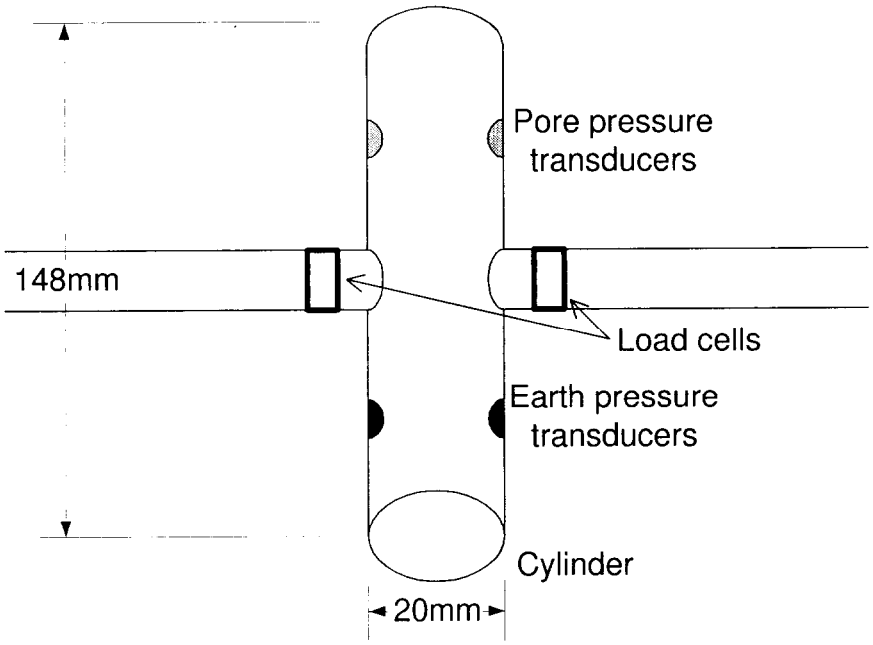

Figure 3.6: Schematic drawing of cylinder.

ground. The ground was prepared by air pluviation to achieve a relative density of 30–40%. It was saturated up to the ground surface with de-aired water or methylcellulose solution under a negative pressure of 98kPa in a large tank by applying a vacuum. The viscosity of the methyl-cellulose-base solution was 50 times higher than that of fresh water. Japanese noodles *somen* were placed between the model ground and the transparent window as markers to observe deformation of the ground. After the saturation, the top lid of the box was attached and the over burden pressure was applied to the soil under the drained condition.

Table 3.1: Test conditions for lateral loading tests of cylinder in liquefied soil.

Case	Pore fluid material	Back pressure P_B (kPa)	Cylinder loading rate V (mm/s)	Container shaking
SW1Q	water	49	1 (monotonic)	×
SW10Q	water	49	10 (monotonic)	×
SW1	water	0	1 (monotonic)	○
SW10	water	0	10 (monotonic)	○
SW100	water	0	100 (cyclic)	○
SM1	methyl. cel. sol.	0	1 (cyclic)	○
SM10	methyl. cel. sol.	0	10 (cyclic)	○
SM100	methyl. cel. sol.	0	100 (cyclic)	○

Having prepared the model, the model container was set on the mechanical shaker (Takemura *et al.* 1989) and the electro-hydraulic actuator was attached to the container. In the tests, the horizontal shaking of the container started two seconds prior to the pile loading. This duration was enough to liquefy the model ground. A horizontal shaking was applied to the container by sinusoidal waves with a frequency of 50Hz and a maximum acceleration of approximately 5g. A period of shaking was 10 seconds.

During the tests, measurements were taken of the acceleration of the container, the horizontal load and displacement of the cylinder, and the earth pressures and pore fluid pressures around the cylinder. Movement of the cylinder and the ground was recorded by a digital video camera.

Table 3.1 shows the test conditions in this study. Effects of the shaking of the ground and the loading rate of the cylinder on the lateral resistance of the cylinder were investigated. In all the cases, the applied over burden pressure was P_A=49kPa. The loading rate of the cylinder, V, was varied from 1mm/s to 100mm/s. In the cyclic loading tests, symmetrical triangular waves were applied in order to achieve a constant loading rate.

In Cases SW1Q and SW10Q, the back pressure P_B of 49kPa was applied to the soil to induce an artificial soil liquefaction without vibration of the ground. Except in these cases, the horizontal sinusoidal motions were applied to the container to generate the excess pore fluid pressure in the ground. Though the application of back pressure P_B=49kPa in SW1Q and SW10Q does not cause the real soil liquefaction, it enable us to create the low effective stress condition subjected to the same stress history as the cases with ground vibration.

At the beginning, de-aired water was used as the pore fluid. However, considering the partial drainage around the cylinder, the migration velocity of the water was relatively large, as the diameter of the cylinder was very small compared with the actual pile. In order to resolve this problem, in the latter half of the series of the tests, scaling laws of the centrifuge modeling were adopted, i.e. a higher viscosity fluid was used as the pore fluid to avoid conflict with the scaling laws for the time of dynamic events and seepage (cf. Appendix B). With this similitude rule, measured lateral resistances of the cylinder correspond to the lateral resistance of the 1m-diameter pile at a depth of 5m, and the loading rate of 1mm/s corresponds to the situation of the pile in a very slow flow of liquefied soil,

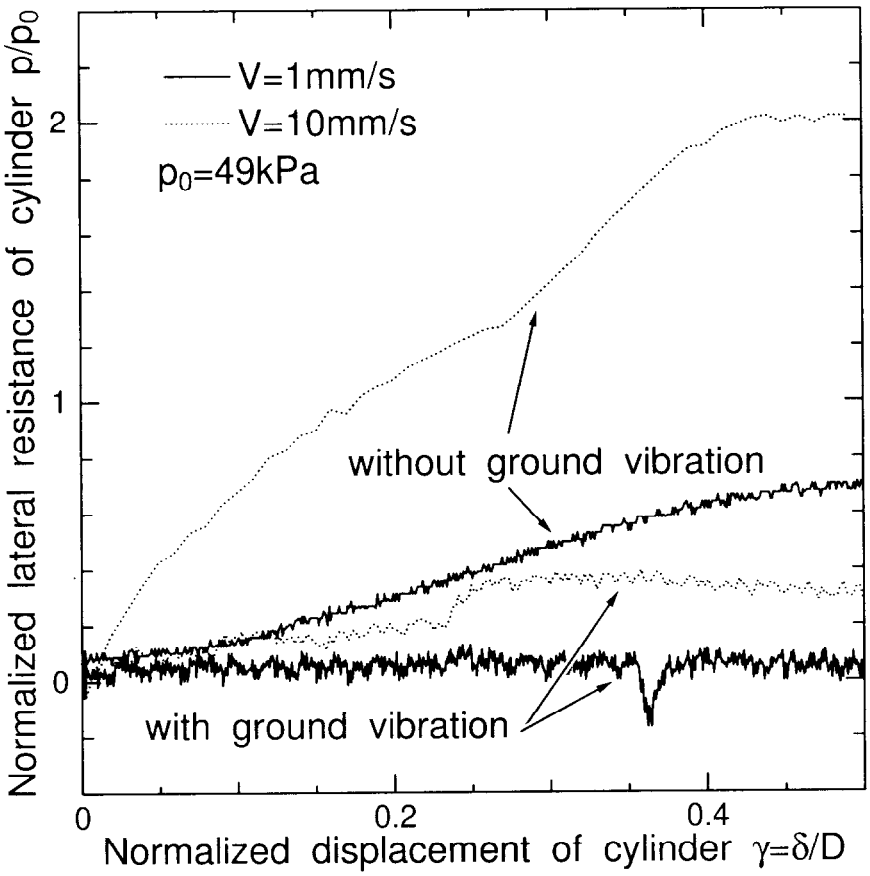

Figure 3.7: Lateral resistances against lateral displacement of cylinder in SW1Q, SW10Q, SW1 & SW10.

while that of 100mm/s corresponds to the vibration of the pile during an earthquake.

3.4 Test results and discussions

3.4.1 Deformation of soil surrounding the pile

Lateral resistances of the cylinder against displacement in cases SW1Q, SW10Q, SW1 and SW10 are plotted in Fig.3.7. The lateral resistance is the lateral force acting on the cylinder divided by a projected area of the cylinder on a vertical plane. In the figure, lateral resistance, p, and displacement of the cylinder, δ, are normalized by an initial over burden pressure, $p_0 = P_A$, and the diameter of the cylinder, D, respectively. Herein the normalized displacement, δ/D, is called the reference strain, γ. Irrespective of the method inducing liquefaction, the larger loading rate makes the lateral resistance larger.

Regarding the difference in the method used to induce liquefaction, the lateral resistances for the cases without vibration of the ground are remarkably larger than those for the cases with vibration. Observed deformation of the soil surrounding the cylinder just after loading are shown in Fig.3.8. The black lines are the noodle markers placed vertically in the soil before the tests. Without shaking, the large amount of soil in front of the cylinder moved forward resulting in a heaving of the ground

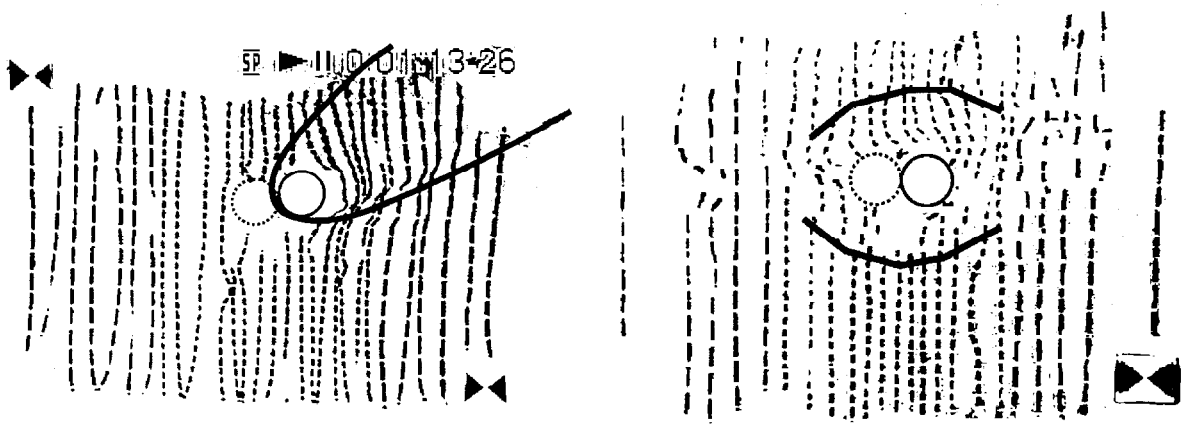

(a) Without ground vibration (SW10Q) (b) With ground vibration (SW10)

Figure 3.8: Deformations of surrounding soil just after loading.

surface of the front side. On the other hand, when shaking was applied, deformation of the soil was quite limited adjacent to the cylinder.

The difference in the soil area influenced may directly affect the lateral resistance of the cylinder as shown in Fig.3.7. The vibration of the ground may cause instability in the contacts of the soil particles and reduce the resistance of the surrounding soil against the movement of the cylinder.

3.4.2 Loading rate effects on lateral resistance

Figure 3.9 shows the first loops of relationships between the lateral resistance and displacement of the cylinder in cases SM1, SM10, and SM100. In these cases, the loading rate was varied from 1mm/s to 100mm/s, and the cylinder first moved toward the actuator-side, i.e. the leftward displacement is taken as negative. The initial resistance was negligibly small in all the cases. The larger lateral resistance is mobilized as the loading rate becomes higher. The lateral resistance was mobilized only after the certain amount of displacement was imposed depending on the loading rate.

The point that a gradient of the loop starts to increase is here defined as a resistance transformation point. The normalized displacement at the point is referred to as the reference strain of the resistance transformation point, γ_L, as shown in Fig.3.10. This reference strain was originally introduced by Yasuda *et al.* (1998) as the point that the shear strength of soil starts to recover in a post liquefaction stress–strain relation.

Reference strains of the resistance transformation point in the first loading are plotted against loading rates in Fig.3.11. In the case of the smallest loading rate, as no obvious recovery of the shear strength was observed in the range of the pile displacement imposed in this study, the reference strain must be larger than the value shown in the figure. The smaller loading rate makes the reference strain of the resistance transformation point larger. This tendency may be associated with not only the dilatancy characteristics of sand but also pore fluid migration around the cylinder.

Figure 3.12 shows time histories of the lateral resistance, displacement of the cylinder, and excess pore fluid pressure around the cylinder in cases SM1 and SM10. It should be noted that the base motion continued only until the end of the first half of the loading cycle in the 1mm/s loading rate case, as the period of the container shaking was 10 seconds. Excess pore fluid pressure of the soil

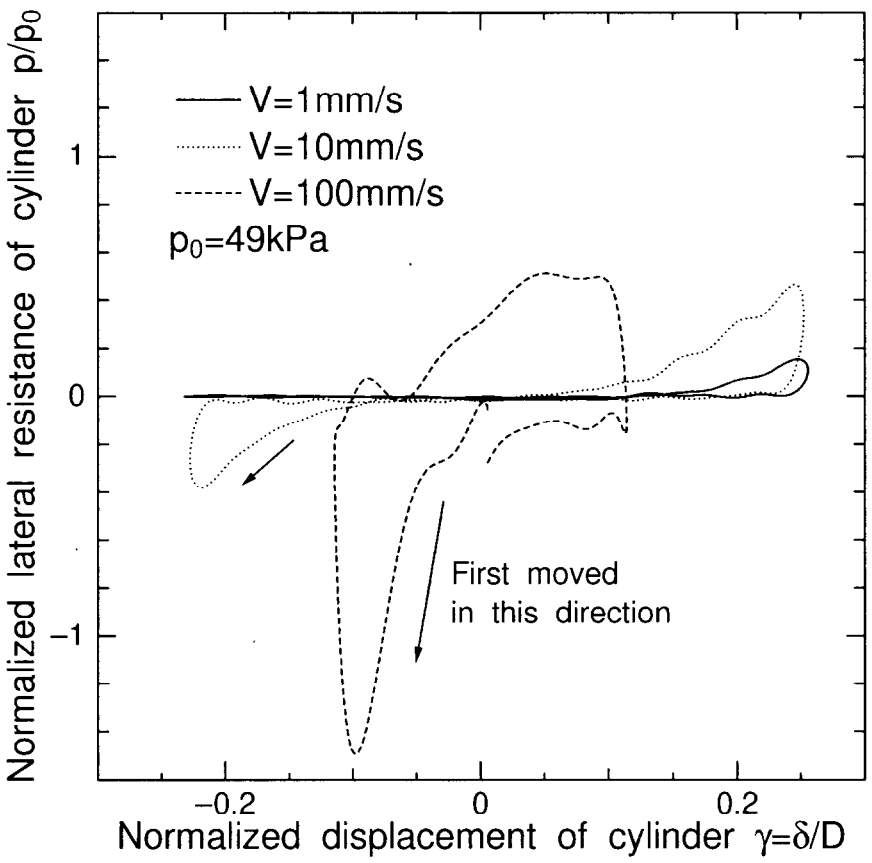

Figure 3.9: Lateral resistances against lateral displacement of cylinder in SM1, SM10 & SM100.

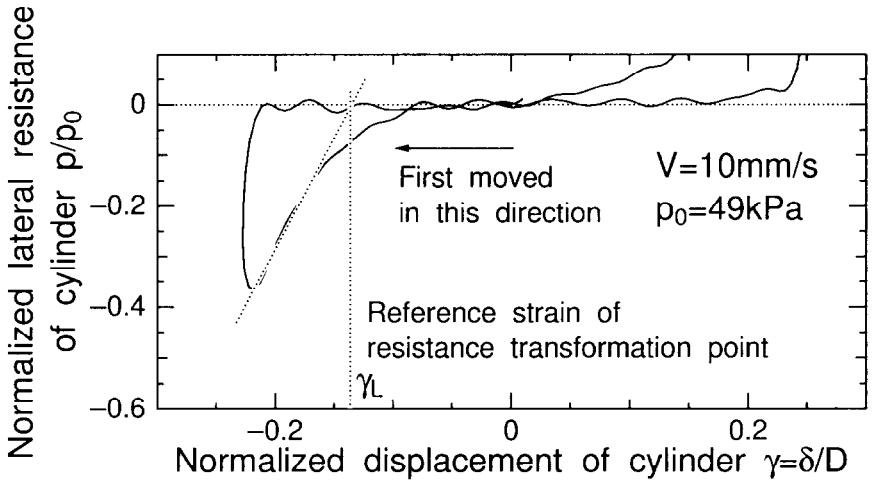

Figure 3.10: Definition of reference strain of resistance transformation point γ_L.

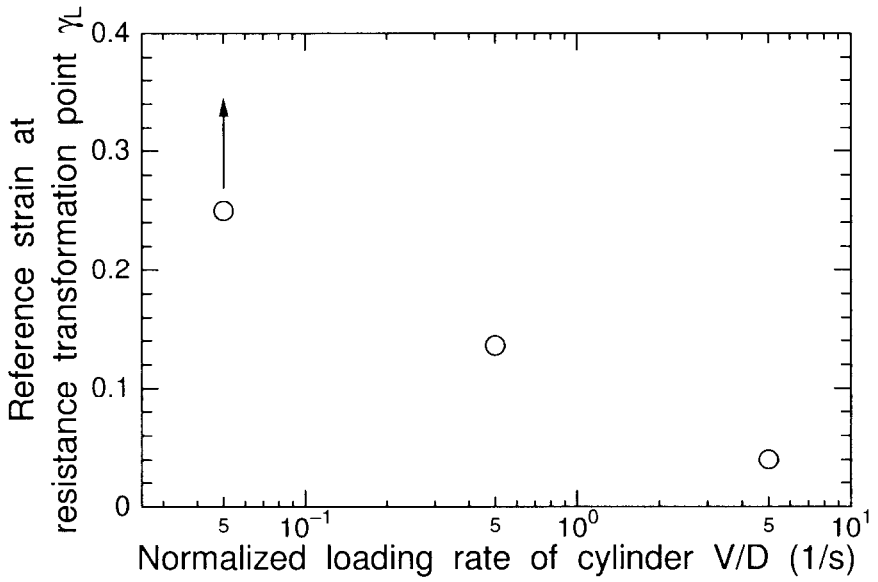

Figure 3.11: Reference strains of resistance transformation point against loading rate in SM1, SM10 & SM100 in first loading.

surrounding the cylinder was measured by the pressure transducers attached to the cylinder in Fig. 3.6. If we look at a first quarter cycle of the last half of the first loading cycle, in both the cases, the pore pressure on the side of the movement direction (the dotted line) once slightly increased by the sand contraction, then it showed rapid decrease due to the sand dilation and a suction force on the back side of the cylinder, while the pressure on the back side (the solid line) monotonically decreased due to the suction force. As a result, the pore pressure decreased on both sides when the maximum displacement of the cylinder was imposed, though the pressure on the side of the direction of movement was larger than that on the other side in both the cases.

Comparing the pore pressure responses in SM1 (V=1mm/s) to those in SM10 (V=10mm/s), the decrease in the pore pressure was smaller, and the displacement of the cylinder when the excess pore fluid pressure started to decrease was larger for the smaller loading rate, as the suction force on the back side of the cylinder will be small when the hydraulic conductivity of the sand is sufficiently larger than the cylinder loading rate. This difference in pore pressure responses would directly affect the cylinder displacement required for the lateral resistance mobilization, i.e., the reference strain of resistance transformation point shown in Fig. 3.11.

Lateral resistances of the cylinder at $\gamma=\delta/D=0.1$, 0.2, and 0.4 in the first loading are plotted against the cylinder loading rate normalized by the soil hydraulic conductivity in Fig. 3.13. The lateral resistance at $\delta/D=0.1$ becomes remarkablely larger when $V/k=10^4$. The threshold V/k value for the lateral resistance at $\delta/D=0.1$ exists between 10^3 and 10^4 for the 1m-diameter pile in the medium loose Toyoura sand. This threshold V/k for the lateral resistance varies with δ/D, as the cylinder displacement required for the lateral resistance mobilization depends on V/k. Let us assume piles in a lateral spreading soil that moves 1m in 10 seconds earthquake period, i.e V=0.1m/s. If the hydraulic conductivity of the liquefied soil is 10^{-5}m/s, V/k becomes 10^4, and the large earth pressure acts on

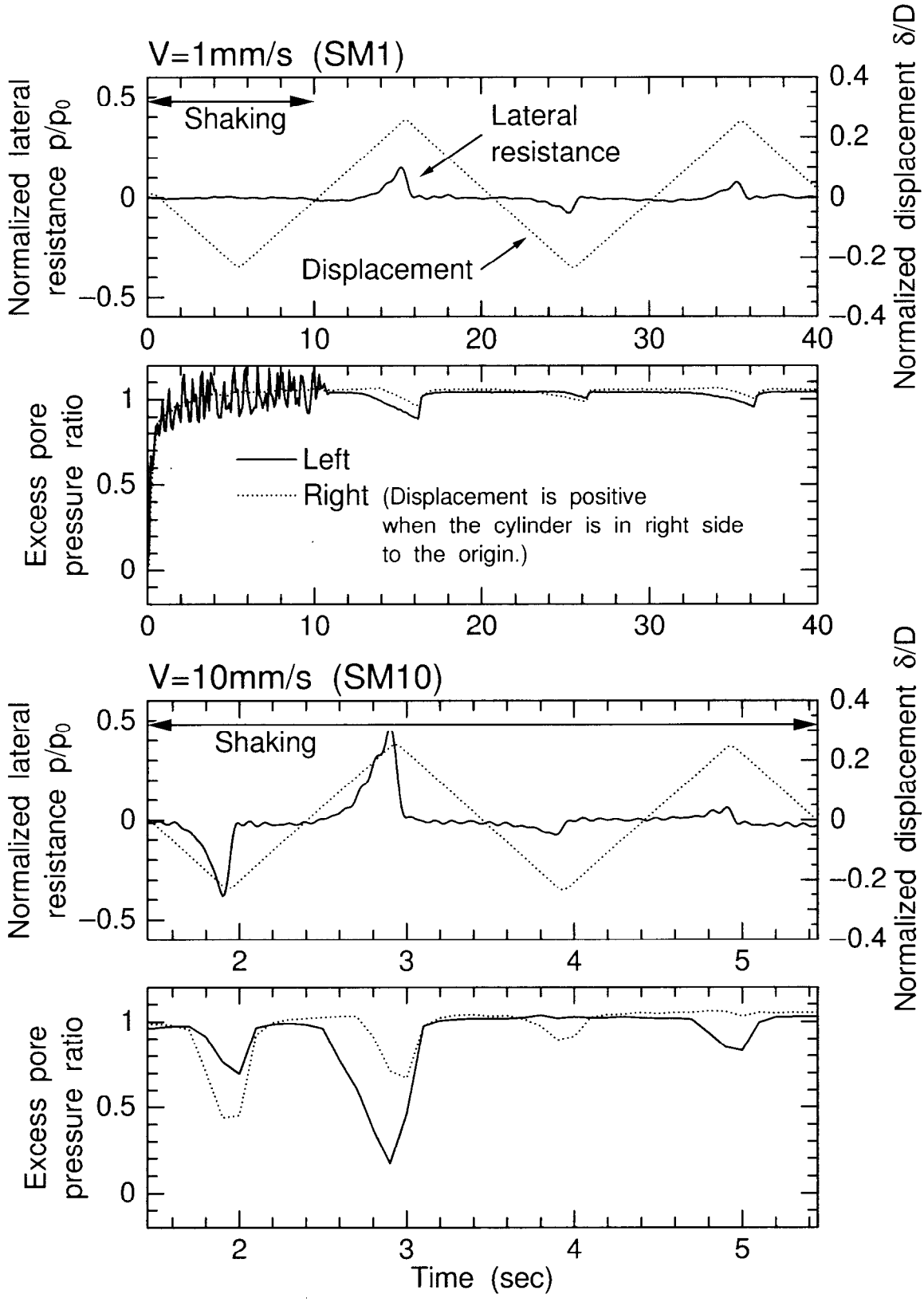

Figure 3.12: Time histories of lateral resistance and displacement of cylinder and excess pore pressure around cylinder in SM1 & SM10.

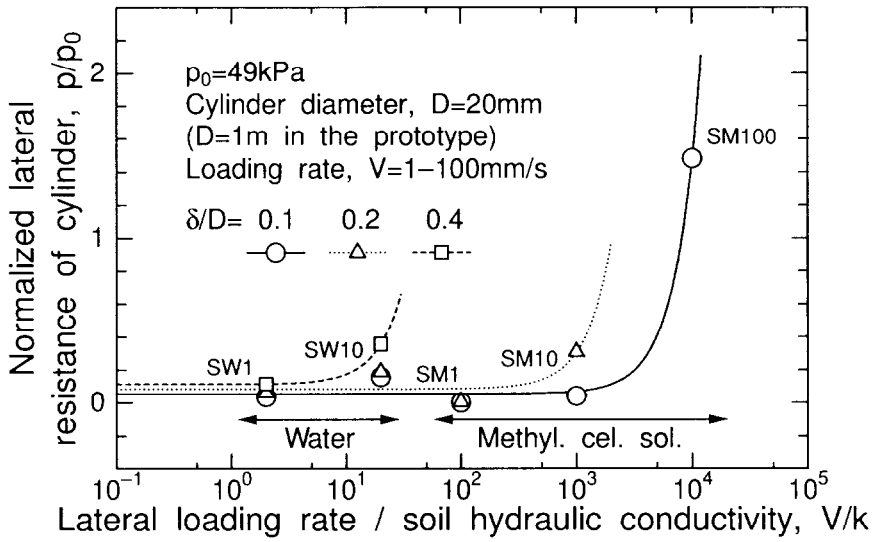

Figure 3.13: Relationships between lateral resistance of cylinder at δ/D=0.1, 0.2 & 0.4 in first loading and cylinder loading rate over soil hydraulic conductivity.

the piles, while the pressure becomes smaller with $k \leq 10^{-4}$m/s.

All indications in this section support that the pore fluid migration rate, i.e. the hydraulic conductivity of the soil with respect to the loading rate, is the crucial factor for mobilization of the lateral resistance of a buried structure in liquefied soil. Thus, soil–water coupled analysis is essentially needed for the evaluation of the lateral resistance of piles in liquefying soils.

3.4.3 For proposal of soil–pile relations in practical design

In this chapter, the lateral resistance of a pile in liquefied soil was mainly examined in term of the relative velocity between the liquefied soil and the pile with respect to the hydraulic conductivity of the soil. For the practical design, a proposal of soil–pile relations in form of soil–pile interaction springs is desirable, as framed structure analyses subjected to the soil movements through soil–pile interaction springs are used for the structure assessment. However, in order to describe the interaction between liquefied soil and piles, several uncertain factors still remain, e.g., (1) the roughness of the pile surface, and (2) the density of the soil.

The pile surface roughness has an influence on the pile lateral resistance even without soil liquefaction. One of the typical examples are shown in Figs. 6.4 & 6.5. These are two-dimensional numerical analysis results on laterally loaded smooth and rough discs in von Mises material, and show obvious different behaviors of the smooth and rough piles. These differences come to the front when the pile is in the frictional material like sand, as the pile surface governs the dilatancy characteristics of sand adjacent to the pile.

The density of the soil, especially the initial void ratio of the soil, much affects the dilatancy characteristics of sand. Ishihara (1993) exhibited undrained triaxial compression test results on Toyoura sand prepared by moist-placement method at relative densities of 12–64%. Stress path shows the change from contractive to dilative behavior when it passes the state of phase transformation for the medium loose to medium dense sand. On the other hand, samples looser than e_0=0.93 never show the

dilative behavior, and exhibit zero residual strength. These differences directly affect (1) the reference strain of the resistance transformation point, and (2) the recovery of the shear strength in Figs. 3.9 & 3.11.

3.5 Summary

Lateral loading tests on the buried cylinder were conducted to study the lateral resistance of a pile in liquefied soil, focusing on observation of the deformation of the liquefied soil surrounding the pile when a large relative displacement between the pile and soil is induced. Lateral resistance of the pile in the liquefying soil is directly measured by the newly developed testing apparatus. The new pile loading system has the capability of applying horizontal cyclic vibrations to the pile during the shaking and allowing the observation of the liquefying sand deformation. The loading rate effect on the lateral resistance of the pile in the liquefied soil was also investigated. The following conclusions were obtained in this study:

- The deformation of soil surrounding the cylinder could be successfully observed by video camera through the transparent window of the box. Without ground vibration, the large amount of soil in front of cylinder moved forward, while the deformation of the soil was quite limited in the vicinity of the cylinder when the shaking was applied. The difference in the deformation mode of the soil directly affected the lateral resistance of the cylinder.

- A larger lateral resistance is mobilized as the loading rate becomes higher. Furthermore, when the loading rate is higher, the cylinder displacement required for the lateral resistance mobilization becomes smaller. These tendencies are associated with not only the dilatancy characteristics of sand but also pore fluid migration around the cylinder. All indications in this study support that the hydraulic conductivity of the soil in relation to the loading rate is the important factor for the mobilization of the lateral resistance of piles in liquefied soils. Thus, the soil–water coupled analysis is essentially needed for the evaluation of the lateral resistance of buried structures in liquefying soil.

Chapter 4

Soil–pile interaction in large soil deformation

4.1 Modeling of piles in large soil deformations

As mentioned in Section 2.5.3, the bending moment responses of piles vary according to relative ground displacement distributions of the piles. In order to evaluate seismic performance of the pile foundation, estimation of the ground displacement profile must be a crucial factor, as the ground displacement distribution during an earthquake depends on the soil profile, i.e. the geological formations and properties of the soils.

Several approaches have been developed for a dynamic response analysis and for a pseudo-static analysis of the pile foundations. One of the methods is a framed structure analysis subjected to the soil movement through soil–pile interaction springs. In this method, the ground displacement profile must be estimated in advance, and then responses of the structure are calculated. The lateral soil movement can be estimated by empirical correlations, similar case histories, finite element analysis results, and so on. The soil–pile interaction is modeled using non-linear p–y springs. Three-dimensional effects in soil–pile interaction are usually involved in the p–y relations though the spring itself is a one-dimensional element. The most complex but accurate method is a three-dimensional finite element analysis that is capable of soil–structure coupled analysis, though there are still difficulties in modeling the soil–structure interface.

In physical modeling, in order to examine the seismic performance of the piles, a shaking table is usually used to simulate the ground motion during an earthquake. However, the observed behavior of the piles is complicated and affected by several factors such as, (1) inertial effect from the superstructure, (2) dynamic response of the soils, and (3) the lateral movement of the soils. Some attempts had been made to avoid the complications in interpreting the pile behavior in the shaking table tests by the following researchers: Horikoshi *et al.* (1998) carried out centrifuge model tests on a pile behind a quay wall subjected to liquefaction-induced lateral spreading of soil. In their tests, in order to control and to simplify the movement of the quay wall, the wall was modeled by a rigid block on a rigid plate. With shaking, the model quay wall slid seaward with almost the same velocity in all the cases. Satoh *et al.* (1998) developed a model quay wall whose movement could be controlled by air cylinders during an shaking. In these two researches, the behavior of the piles subjected to 'given' lateral spreading of soils could be examined as the movements of the quay wall could be given as the boundary conditions.

In order to isolate the effect of the lateral movement of soils on the pile behavior, Tsuchiya *et*

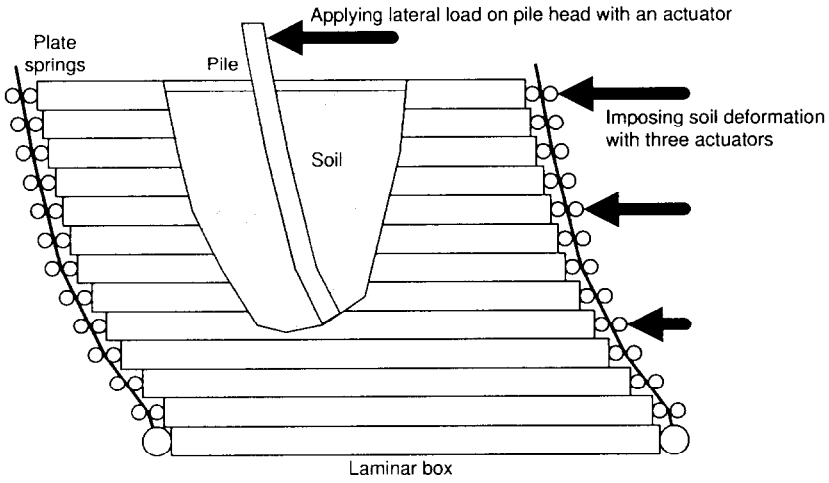

Figure 4.1: Schematic diagram of active type shear box.

al. (1997, 2001) made a new large shear pit that consisted of a huge shear box and actuators. With the actuators mounted beside the shear box, deformation of the shear box could be controlled and any ground displacement could be entered as input data without any inertial effects. Using the same concept, the author and associates developed a new active type shear box in a centrifuge which makes it possible to simulate the large ground deformations generated by an earthquake.

This chapter focuses on the development of the sophisticated computer controlled active type shear box, which is capable of delivering displacement-controlled deformations to the soil in the shear box and a lateral force on the top of the pile foundation independently (Takahashi *et al.*, 2001). Details of the shear box are described, and centrifuge model test results on soil–pile interaction in large soil movements are presented.

4.2 Development of active type shear box in a centrifuge

4.2.1 Preliminary considerations on shear box

As many researchers have pointed out, soil–pile interaction during an earthquake is a highly complicated phenomenon. Experimental study in this chapter focuses on the failure or deformation of piles due to the lateral movement of soil. Therefore, inertial effects of the soil and piles are neglected, and quasi-static conditions are assumed. A schematic diagram of the active type shear box is shown in Fig. 4.1. It consists of the following two main parts: a laminar box and four actuators. The shear box was designed for the Tokyo Tech Mark III centrifuge (Takemura *et al.*, 1999, cf. Appendix A).

Due to the limitation of swinging platform space ($0.9 \times 0.9 \times 0.9$m) for the centrifuge, only three actuators can be mounted for applying forces to the laminar box. The loading rods of the three actuators are connected to the three laminae at different levels, and the lateral force is transmitted to the other laminae through linked vertical thin plate springs. Ideally, in simulating earthquake ground motion, the laminar box and the soil in it should strain uniformly, and uniform stress conditions should be imposed at any level in the horizontal direction as shown in Fig. 4.2(a). However, the soil stress conditions in the active type shear box are different from ideal conditions. As shown in Fig. 4.2(b), if

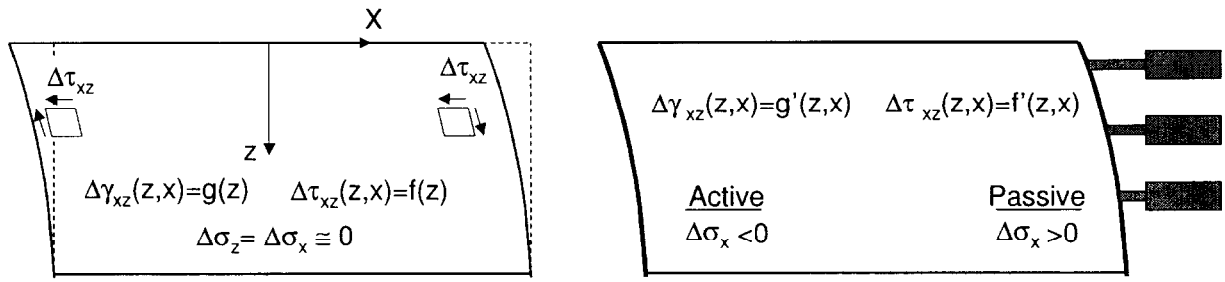

(a) Ideal deformation of level ground due to earthquake.

(b) Deformation of ground in active type shear box.

Figure 4.2: Variations of stress and strain in ideal and model ground.

the soil is subjected to a leftward horizontal displacement at the right boundary, the horizontal normal stress σ_x in the portion near the right end wall would increase, being the passive condition, while σ_x in the portion near the left end wall would decrease, being the active condition. The variation of σ_x causes variation of the mean stress as well as variation of the volumetric strain and shear stress in the horizontal direction.

Although horizontal displacements at the end boundaries can be changed by the three actuators, the displacement profile at the boundaries depends not only on the displacements at the three loading points but also on the deflection of the plate springs. The deflection is determined by the flexural rigidity of the plates and the reaction from the soil to the boundaries. In this section, effects of the geometry of the shear box, the rigidity of the plate springs on the deformation, and the stresses of the soil in the box are investigated.

Geometry of shear box

In order to investigate the effect of the geometry of the shear box on the deformation and stress condition of the soil in it, simple two dimensional finite element analyses were carried out under the plane strain condition. In the analyses, the soil was modeled as elastic perfectly plastic employing the extended von Mises yield criteria with the non-associated flow rule. The height of the soil in the shear box H was fixed at 200mm, and the width W was varied from 200 to 800mm, with the aspect ratio W/H ranging from 1 to 4 in the analyses. The typical FE meshes and the boundary conditions for the analysis are shown in Fig. 4.3. Triangularly-shaped horizontal displacements were monotonically imposed at both the side boundaries with a maximum value of 15mm at the top as shown in Fig. 4.3. Assuming a roughness of the inside surface of the end walls, vertical displacements of the nodes at both the ends were fixed. It was assumed that the shear boxes were strained under 50 gravities (50g). With the constitutive law used, i.e. the elastic perfectly plastic model, analyzed results will be similar at any assumed centrifugal acceleration. As dense Toyoura sand was used in preliminary tests on the performance of the shear box, material properties close to those of dense Toyoura sand (Nakamura *et al.*, 1999) were used in the analyses. A dilation angle of the sand is conventionally assumed to be one-third of the frictional angle. Material parameters used in the analyses are summarized in Table 4.1. The shear modulus was assumed to increase proportionally with depth. Profiles of the vertical stress and the shear modulus of the soil are shown in Fig. 4.4.

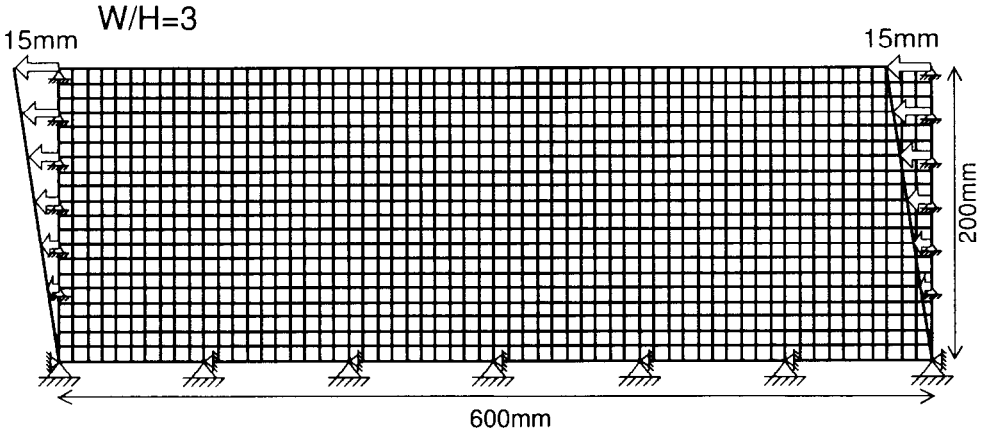

Figure 4.3: Typical FE mesh and boundary conditions for analysis.

Table 4.1: Material parameters used in analysis of active type shear box.

Shear modulus at p'=98kPa	175MPa
Poisson's ratio, ν	0.33
Frictional angle, ϕ	40 deg.
Dilation angle, ψ	13.3 deg. (One third of frictional angle)
Coefficient of earth pressure at rest, K_0	0.5
Unit weight at 50g, γ_{50}	770 kN/m^3

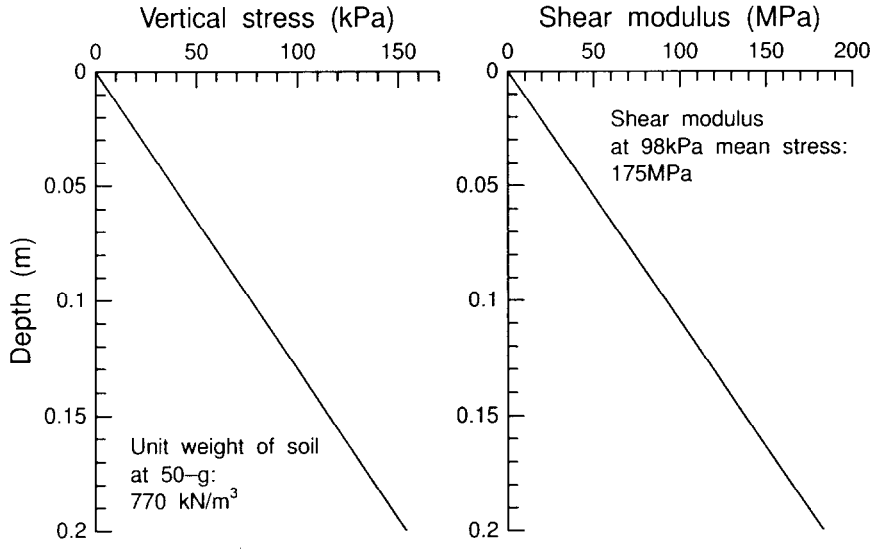

Figure 4.4: Profiles of vertical stress and shear modulus of soil.

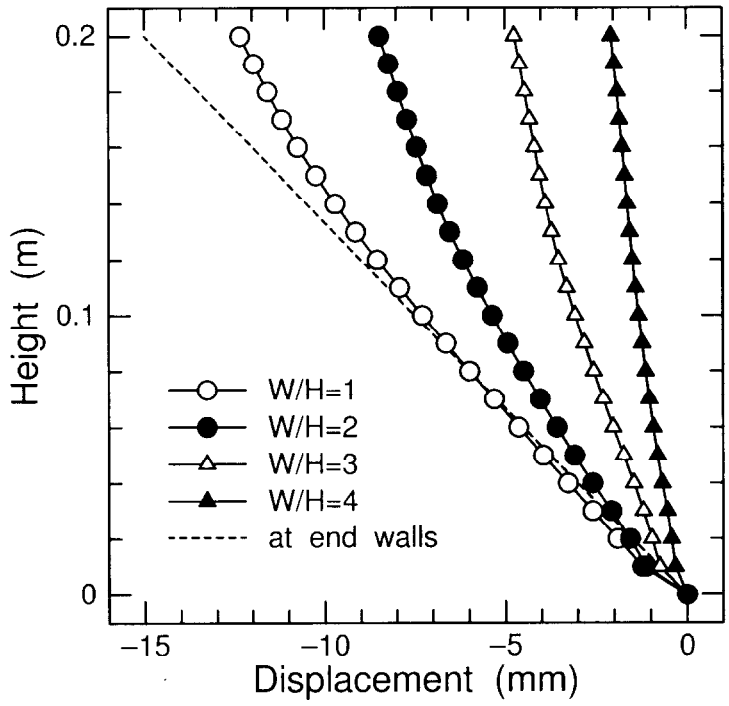

Figure 4.5: Calculated lateral displacement distributions of soil at center of box at final stage of calculation.

Calculated lateral displacement distributions of the soil in the central portion of the box at the final stage of the calculation are shown in Fig. 4.5. The input displacement at the boundary is also plotted as a broken line in the figure. Displacement at the center decreases with increasing W/H ratio. The displacement at the center is almost the same as the input boundary displacement in the case of 200mm–width (W/H=1), while for the cases where W/H=3 & 4, only 30% & 15% of the input displacement were obtained, respectively. From the viewpoint of controlling the deformation of soil, the narrower box is considered suitable for the tests.

Contours of the horizontal normal stress σ_x and shear stress τ_{xz} at the maximum input displacement (15mm at the top) are shown in Fig. 4.6 & 4.7, respectively. If the soil behaved as level ground during an earthquake, the contour lines should be horizontal in both σ_x and τ_{xz}. In the case of the smallest width (W/H=1), the contour lines slanted throughout the whole area. Since the change of the vertical stresses due to the end-wall friction may not be negligible (Whitman & Lambe, 1986) as shown in this case, it is not a good idea to use the aspect ratio W/H=1 for the tests. However, in the cases of larger width, the contour lines tended to the horizontal around the center of the box, while they slanted near the end walls. As the model structures, e.g. piles, are normally placed at the center of the box, it can be said that the use of a wider shear box is better from the viewpoint of the stress condition of the soil. From the above discussions about deformation control and the stress condition of the soil, it could be said that the box with the aspect ratio of 2 to 3 is the best to use for the tests with dense sand and for the situation where strains are not introduced by inertia but by boundary displacement. Since results of the analyses are heavily affected by the constitutive model and parameters

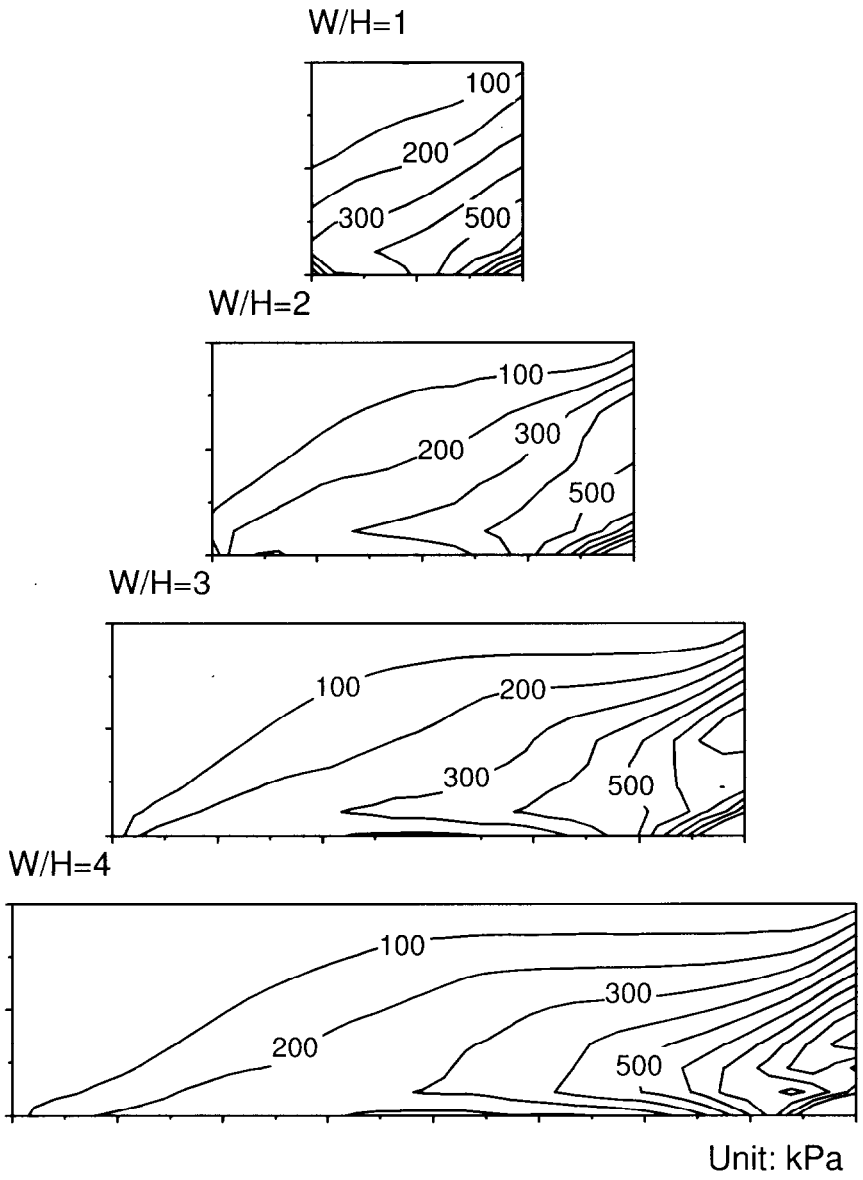

Figure 4.6: Contours of horizontal normal stress σ_x at end of calculation.

of the soil, this aspect ratio may not be applicable for high compressible soil like loose sand. It can be expected that the narrower box is better in the tests with loose sand.

Stiffness of plate springs

In the previous subsection, only the simple shear mode was examined. However, considering real soil deformation due to actual earthquakes, a capability of applying several types of deformation mode to the soil is desirable. For this requirement, the use of plate springs to transmit the force applied by the actuators to the other connected laminae is one of the crucial factors.

Material properties of the spring steel used for the plate springs are shown in Table 4.2. Details of the plate spring connection are shown in Fig. 4.8. The two sets of plate springs were attached at

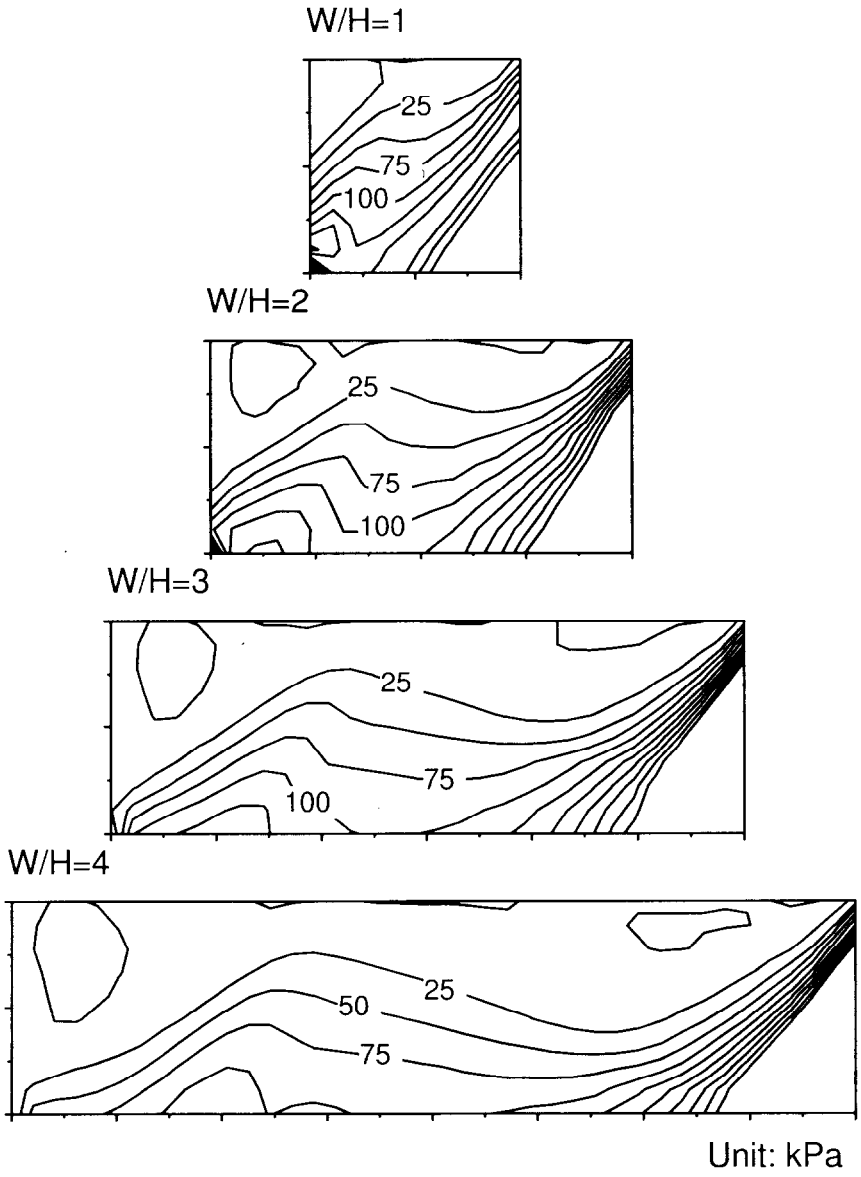

Figure 4.7: Contours of shear stress τ_{xz} at end of calculation.

Table 4.2: Material properties of spring steel of shear box.

Name	SUP3, hardened
Young's modulus	206GPa
Poisson's ratio	0.24
Yield strength	More than 835MPa

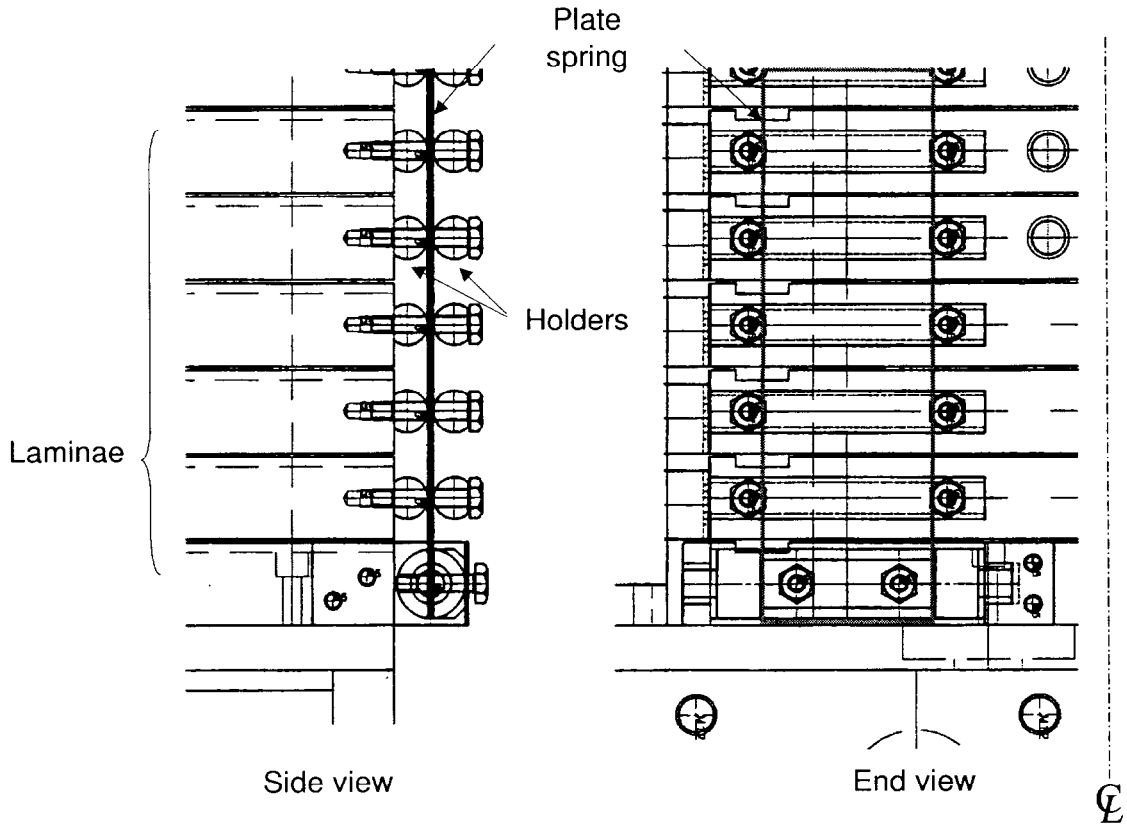

Figure 4.8: Detail of plate spring connection.

Table 4.3: Analysis parameters for plate spring.

Case	Thickness of a steel sheet, t (mm)	Number of layered steel sheets, n	Flexural rigidity of plate spring ($N.m^2$)	Maximum input displacement (mm)
P1	0.3	6	0.14	35.5
P2	0.6	3	0.56	17.8

each end of the shear box. Each set of plate springs consists of several thin steel sheets. Each set was fixed at the base of the shear box in a hinged condition and held by two cylindrical holders fixed at each lamina end as shown in the figure. FE analyses were conducted to examine possible maximum displacements of the laminae within the elastic limit of the plate spring. Plate springs with a size of 50mm in width and 300mm in height were assumed in the analyses. The parameters used in the analyses are listed in Table 4.3. Neglecting the reaction from the soil in the box, the most severe condition was assumed, and displacements of this mode were imposed to the beam at three different levels corresponding to those of the actuators. The typical FE meshes and the boundary conditions for the analyses are shown in Fig. 4.9. The most severe input displacement assumed is shown in Fig.

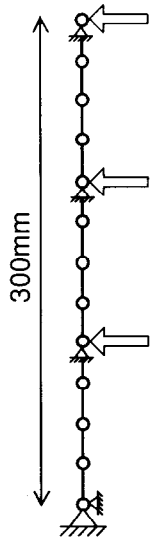

Figure 4.9: Typical FE mesh and boundary conditions for analysis of plate spring.

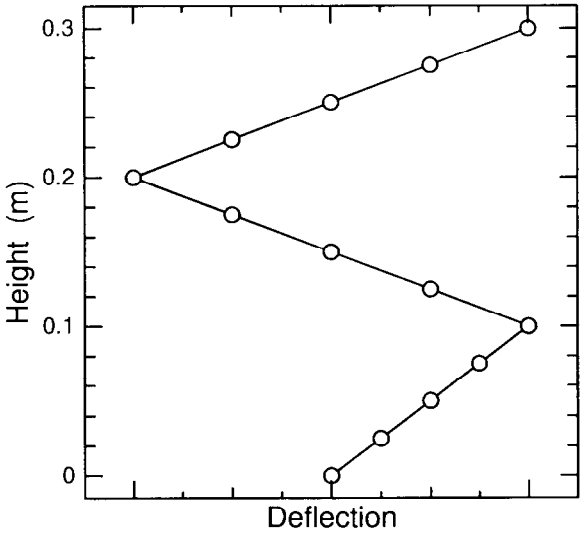

Figure 4.10: Typical input displacement for analysis of plate spring.

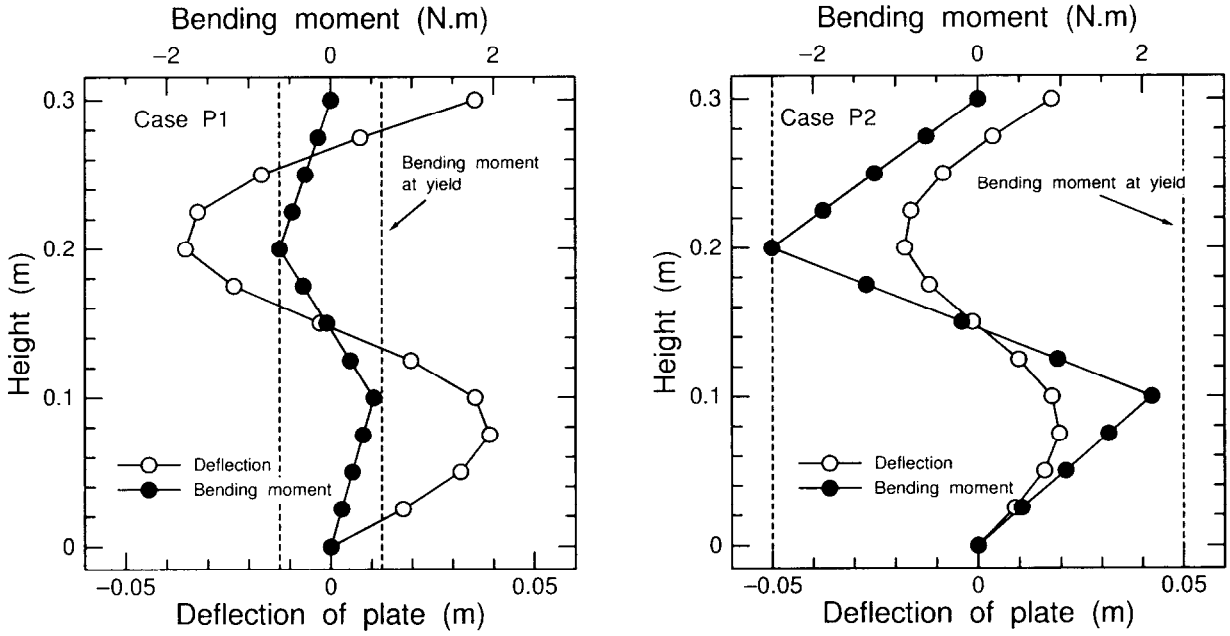

Figure 4.11: Calculated displacement and bending moment distributions of plates.

4.10.

Calculated deflection and bending moment distributions of the plate are shown in Fig. 4.11. Bending moments at yielding are also shown as broken lines. As shown in Fig. 4.11, the maximum deflection of the plate springs with thinner and more steel sheets within the elastic limit is larger than that with thicker and fewer sheets. On the other hand, when the beam is subjected to lateral

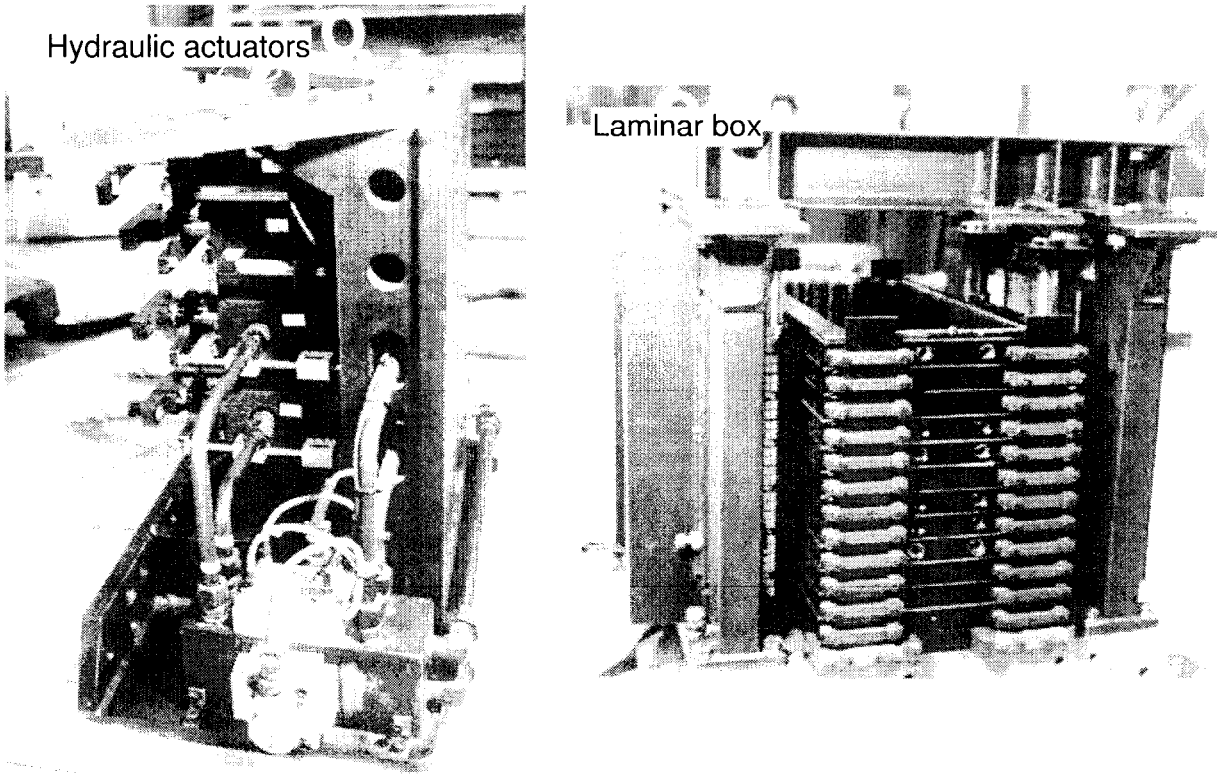

Figure 4.12: Side view of actuators and shear box.

distributed load like earth pressures, the deflection of the beam between the points of loading by the actuators becomes larger for the former springs than the latter. In order to satisfy the non-yielding and less deflection conditions with the same total thickness of the plate springs, both the flexibility and the rigidity are required for the plate springs. It is very difficult to find the optimum combination of the thickness of the spring sheet and the number of layered sheets for the spring plates. However, considering the fact that the tests will be done under 50g or 100g and 20 millimeters in displacement is large enough in terms of pile displacement, the analyzed condition with the high rigidity seems to be a better condition.

4.2.2 System description

The active type shear box was designed to fit the 0.9×0.9m swinging platform of the Mark III Centrifuge at Tokyo Tech. The side view of the active type shear box and the box mounted on the centrifuge are shown in Fig. 4.12 and 4.13, respectively. The shear box was designed to be operational under 100g. The shear box can be disassembled into two parts: the laminar box and the actuators.

The laminar box was made of duralumin (aluminum 2017) with an inner size of 450mm in width, 200mm in breadth, and 325mm in height. If the soil below two-thirds of the model depth is a bearing stratum of a pile foundation, the aspect ratio of the shear zone will be 2.3 (=450mm/200mm), which falls within the suggested range of 2 to 3 specified in the previous section. The box consists of thirteen-stacked 24mm-thick alumite coated duralumin laminae. The outer size of each lamina is W512 $\times$ B202 $\times$ H24mm and the inner size is W452 $\times$ B202 $\times$ H24mm. The laminae are supported by

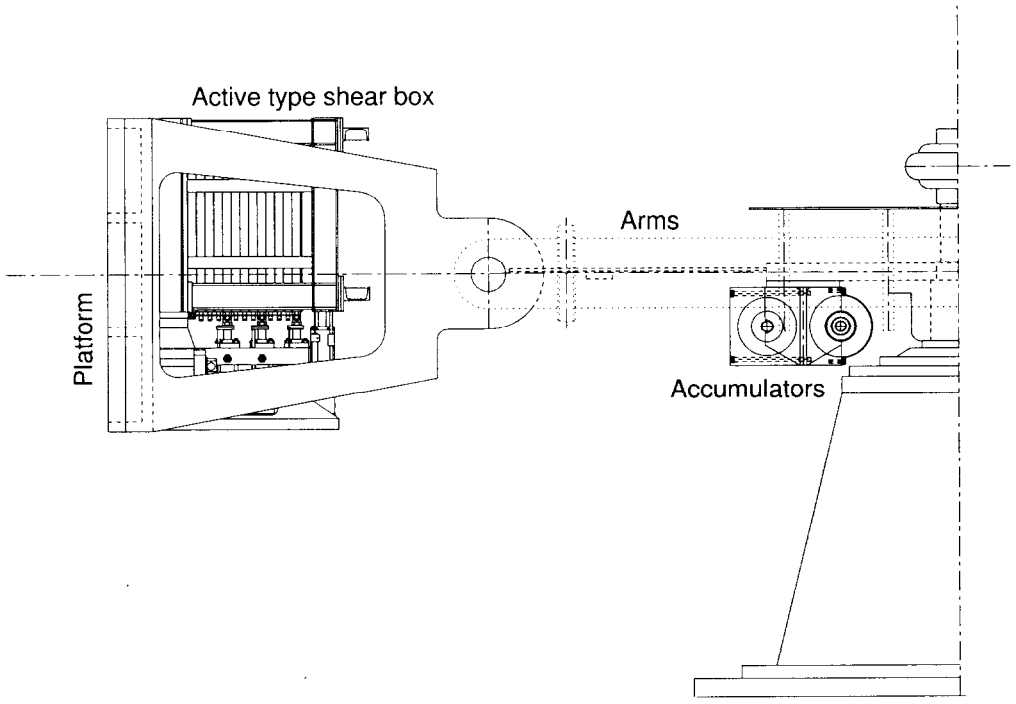

Figure 4.13: Schematic side view of active shear box mounted on the Tokyo Tech Mark III Centrifuge.

roller bearings, which are mounted in grooves on each lamina. To prevent movement perpendicular to the loading direction, four external columns with rollers are placed just outside of the box as shown in Fig. 4.12. A rectangular shape rubber sleeve is placed in the box to inhibit soil particles from getting into gaps between the laminae. Thin aluminum shear sheets roughened by glued Toyoura sand lie just inside both end walls and are fixed to the base of the box. These sheets are for developing shear stresses on the vertical contact surface with the soil. The three actuators are connected with the three laminae directly, and lateral forces are transmitted to the other laminae through four linked sets of thin plate springs. Each thin plate spring consists of three-layers of 0.6mm–thick or six-layers of 0.3mm–thick spring steel sheets. Details of the plate spring connection to the laminae are shown in Fig. 4.8.

Four Servo-Technos Model L9714 linear hydraulic actuators are attached to steel racks as shown in Fig. 4.12. The actuator at the top is used for simulating lateral force acting on the pile head. The bottom three actuators have a stroke of +20mm; the top one has a stroke of ±40mm. All actuators have piston areas of 1260 mm^2 and 880 mm^2 and force capacities of 25.8kN and 18.0kN at 20.5MPa oil pressure when moving outward and inward, respectively. The servo-valve used for each actuator is MOOG J076-101. The peak velocity of the actuator is 133mm/sec. A servo control box is mounted on the centrifuge. A PC in the control room of the centrifuge communicates with the on-board PC installed in the control box through slip rings of the centrifuge. Signals from the on-board PC are fed to the servo valve to give the actuating piston displacements. A closed loop feedback system is built by using the signals collected by linear variable differential transformers (LVDTs) attached on the actuators. The actuator for the pile head loading can also be controlled by a load cell attached

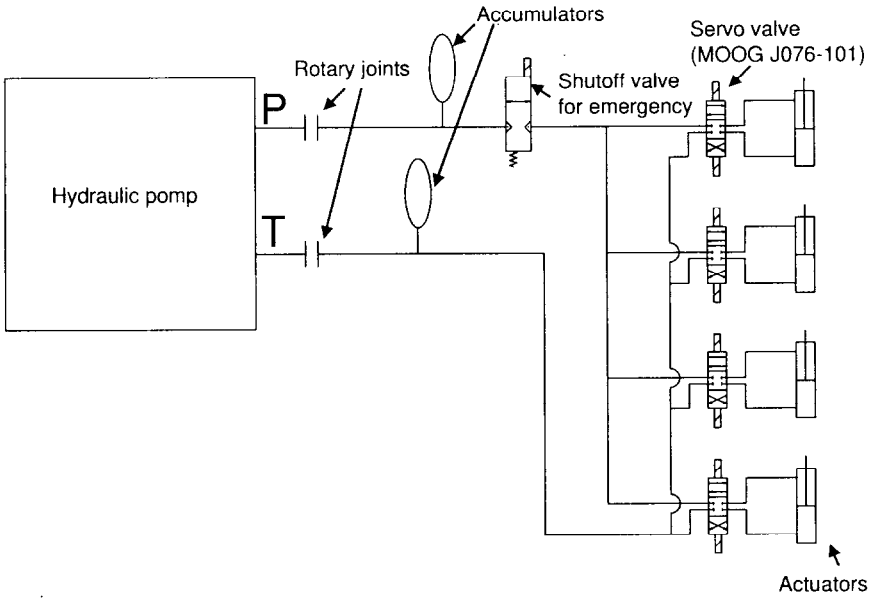

Figure 4.14: Schematic drawing of hydraulic circuit.

Table 4.4: Specifications of active type shear box.

Maximum operational centrifugal acceleration		100g
Actuator	Number	3 for laminar box and 1 for pile head
	Stroke	±20mm for laminar box and ±40mm for pile head
	Force capacity at 20.5MPa oil pressure	25.8kN for outward and 18.0kN for inward
	Peak velocity	133mm/sec
Laminar box	Number of stacks	13
	Inner size	W450 × B200 × H325mm
	Flexural rigidity of plate spring, EI	0.14 N.m^2, 0.56 N.m^2

on the rod of the actuator. A schematic drawing of the hydraulic circuit is shown in Fig. 4.14. Pressurized oil is supplied by a hydraulic pump placed on the laboratory floor. A rotary joint with a maximum pressure of 20.5MPa mounted on the centrifuge is used for charging and discharging oil to the centrifuge during a spinning of the centrifuge. Two four-liter hydraulic accumulators are mounted on the centrifuge to satisfy the required flow rate of the pressurized oil. The four actuators can be manipulated at a frequency of 1Hz with the double amplitude of horizontal displacement of 20mm. Specifications of the active type shear box are summarized in Table 4.4.

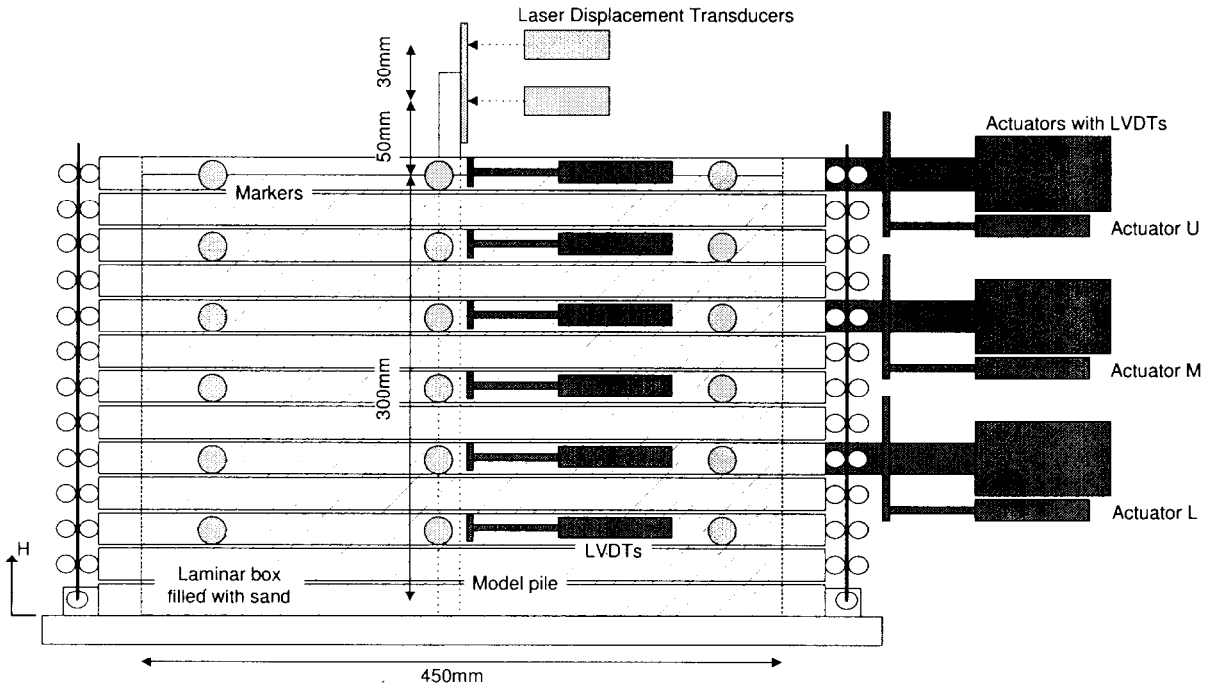

Figure 4.15: Instrumentation in centrifuge tests.

4.2.3 Performance of the active type shear box

A series of centrifuge tests was carried out to examine characteristics of the empty shear box and to observe the deformation of the soil in the shear box and the pile behavior when subjected to large soil deformation. Figure 4.15 illustrates the instrumentation used in the tests. Horizontal displacements of six laminae in the stacks were measured by LVDTs at the mid-portion of the box. Displacements of the actuator rods were also measured using LVDTs. In the cases for the box filled with soil, aluminum markers were placed in the soil during preparation. Positions of the makers were scaled before and after the tests to measure the deformation of the soil. In the tests with model pile foundation, strain gauges were attached inside of the pile at ten different levels. Deflections and angles of the pile head were also measured by two laser displacement transducers.

As a first series of preliminary tests, proof tests on the empty shear box were carried out at 1g and 25g to make a comparison between the input displacements by the actuators and the measured displacements of the laminae using the LVDTs. Since the reliability of the control box on the centrifuge in high centrifugal acceleration was low at the time of preliminary tests, the centrifugal acceleration was set at 25g, although the shear box was designed to be operational under 100g. Test conditions are listed in Table 4.5. Two types of shear deformation mode were assumed as shown in Fig. 4.16(a). The distributions of shear modulus corresponding to these two modes are shown in Fig. 4.16(b). One is a first natural vibration mode for level ground with its shear velocity or shear modulus uniform throughout the depth. The other is another first mode for level ground with a shear velocity that increases with depth. The former mode is referred as 'Type A' and the latter is referred to as 'Type B,' following the foundation design codes for railway structures in Japan (Railway Technical Research

Table 4.5: Test conditions for empty active type shear box.

Case	Centrifugal acceleration (g)	Maximum displacement amplitude of actuators (mm)		
		Actuator L	Actuator M	Actuator U
EA1	1	7.5	13.0	15.0
EA2	25	7.5	13.0	15.0
EB1	1	3.7	8.6	15.0
EB2	25	3.7	8.6	15.0

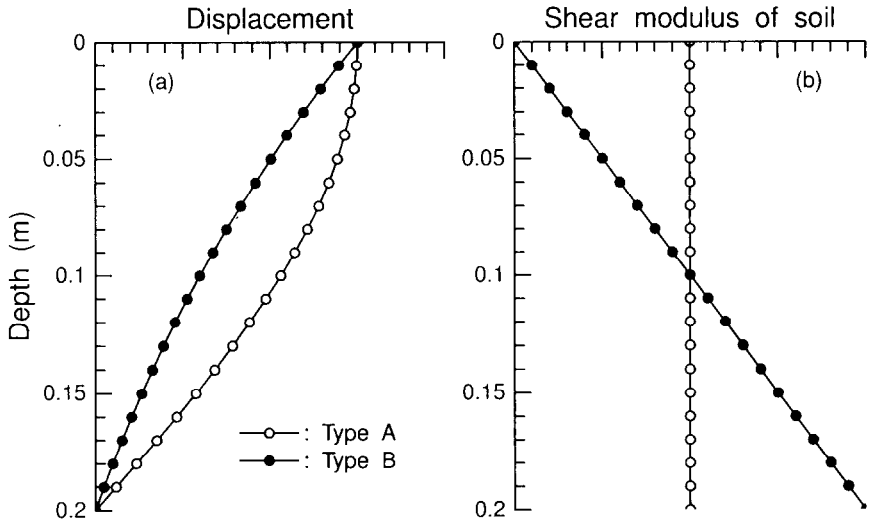

Figure 4.16: Two types of shear deformation mode.

Institute, 1997). In EA1 & EA2, Type A mode was used while Type B mode was used in the other cases. In the test series, the thickness of the spring sheet used for the plate springs was 0.6mm. For each spring plate, 3-layered sheets were used. Sinusoidal waves with a period of 30 seconds were applied to the laminae. Figure 4.17 shows the typical time histories of the actuator rod displacement. Observed horizontal displacement distributions of the laminae when the displacement of the top lamina reached 5, 10 and 15mm are shown in Fig. 4.18. In all the cases, measured displacement of the laminae closely approximates the input motion regardless of the centrifugal acceleration. This implies that frictions between laminae did not significantly affect the performance of the shear box.

A separate series of tests for the shear box filled with dense sand was performed at 25g. Toyoura sand with a relative density of 80% was used for the model ground. The mean grain size of Toyoura sand is 0.2mm, and the coefficient of uniformity is approximately 1.6. Table 4.6 shows the test conditions of this series. The shear deformation mode of the soil in FA1 & FA2 is Type A and that in FB1 & FB2 is Type B. In FA2 & FB2, the soil below two-thirds of the model depth was assumed to be a bearing stratum, and the input displacement was applied only to the upper two-thirds

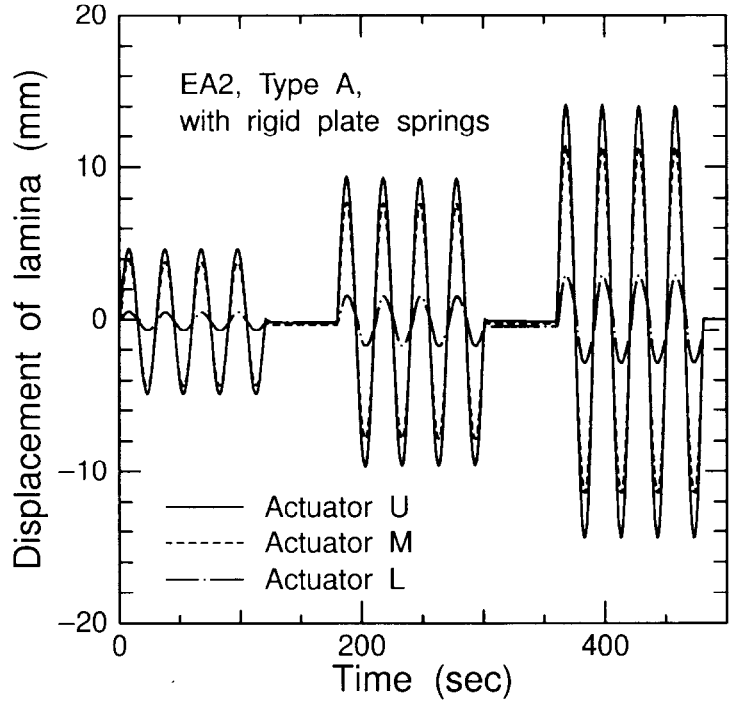

Figure 4.17: Typical time histories of actuator rod displacement.

Table 4.6: Test conditions for active type shear box filled with dense sand.

Case	Centrifugal acceleration (g)	Maximum displacement amplitude of actuators (mm)		
		Actuator L	Actuator M	Actuator U
FA1-F*, R*	25	8.8	15.2	17.5
FA2-F, R	25	0.0	10.6	15.0
FB1-F	25	4.6	9.8	17.5
FB2-F, R	25	0.0	6.0	15.0

∗ F: t=0.3mm, n=6, R: t=0.6mm, n=3 for plate spring

of the model. During earthquake, the soil may move and affect the response of the pile even at the depth corresponding to the lowest one-third of the box. In the application of the box to the soil–pile interaction problem, the pile foundation was not assumed a friction pile but an end-bearing pile in this study, as will be described in detail in a subsequent section. Though the end-bearing pile can be modeled by fixing the pile tip to the base of the box, this is not a realistic boundary condition for the pile. For that reason, the lowest one-third of the soil was assumed to be the bearing stratum. In this series, two types of plate springs were used. One consisted of three-layers of 0.6mm–thick spring steel sheets, and the other consisted of six-layers of 0.3mm–thick sheets. In FB1, the spring plates with three-layers of 0.6mm–thick steel sheets were used. The former plate spring had four times the

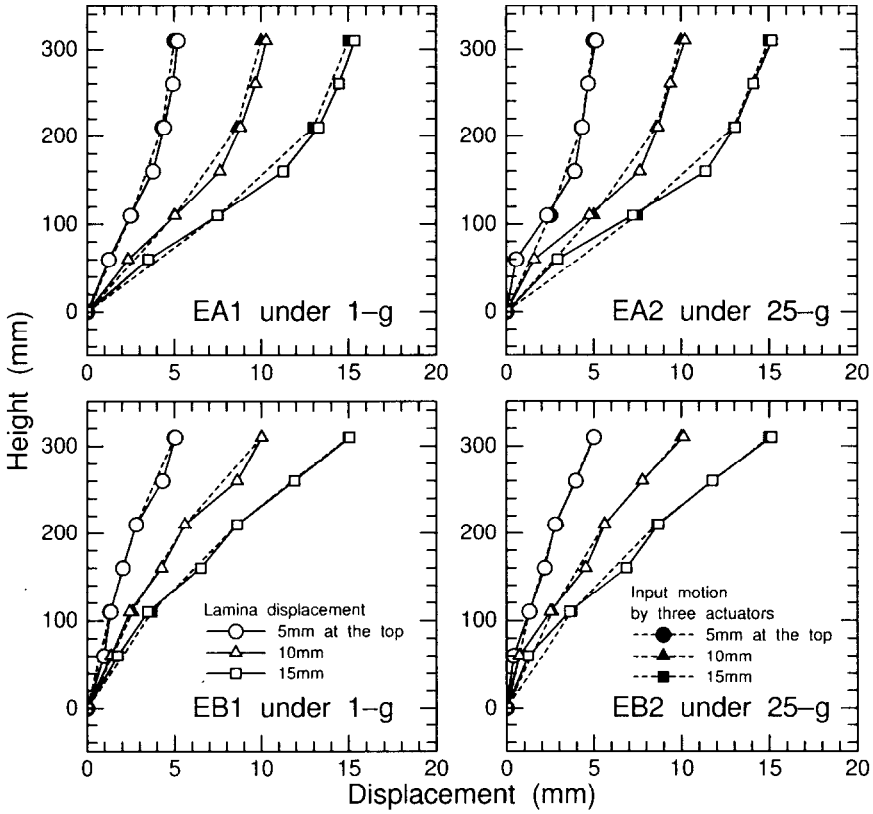

Figure 4.18: Observed horizontal displacement distributions of laminae for empty box.

flexural rigidity of the latter. A single quarter cycle of a sinusoidal wave was applied to the laminae in 120 seconds.

Figure 4.19 shows the distributions of the horizontal displacement of the laminae measured by LVDTs at the center of the box when the displacement of the top lamina reached 1/3, 2/3 and 1 of the maximum input displacements. The displacements of the laminae to which the actuators were directly connected showed good agreement with the target displacements (input motions by the three actuators) which are shown by broken lines. The non-direct-connected laminae, on the other hand, did not attain the target displacements, resulting in many kinks in the distributions. Figure 4.20 shows the displacement distributions of the laminae normalized by the target value. The difference between the measured displacements and the input values is smaller for the plate springs with higher flexural rigidity than for those with smaller rigidity. As shown in Fig. 4.19, the difference between the target and observed displacements does not proportionally increase with the target displacements. Particularly for FB1 and FB2, the difference developed mainly in the first 5mm displacement at the top lamina, and there was little increase of the difference in the rest of the shearing process. As a result, the smaller target displacement is the smaller normalized displacement.

Distributions of the horizontal ground displacements measured with the targets placed at the center of the model ground are compared with those of the laminae and the target values at the end of shearing. These comparisons are shown in Fig. 4.21. In this figure, only the displacements for the cases with large flexural rigidity plate springs (t=0.6mm, n=3) are illustrated. Observed distributions

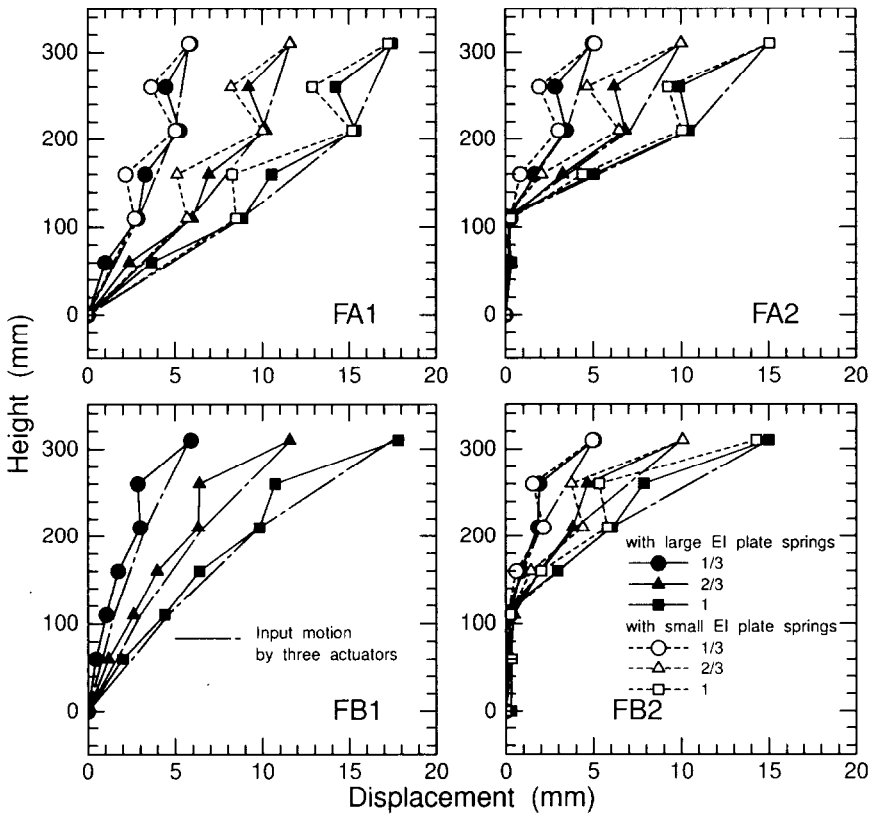

Figure 4.19: Observed horizontal displacement distributions of laminae for shear box filled with dense sand.

of the ground displacement at the center of the model were similar to the input values in all the cases, and the distribution of the ground displacement is smoother than that of the laminae. Figure 4.22 shows the ground displacement distributions normalized by the target values at the end of the shearing. Although in FB1 and FB2, there is a large fluctuation in the lower portion where the displacements of the laminae are small, the ground displacement becomes almost 70–80% of the input value in all the cases. The ratio of the ground displacement to the input displacement from the side end is close to the FE analysis results for the cases with similar aspect ratios. As stress conditions in the ground are complex and different from those that occur during earthquakes as discussed in the previous section, these should be taken into account and examined by numerical analyses in the interpretations of the test results obtained from this apparatus.

4.3 Centrifuge tests on soil–pile interaction

Centrifuge tests on a passive single pile were carried out under 25-g to examine the capability of this apparatus and to investigate the behavior of the pile subjected to large soil movement, specifically the soil–structure interaction during an earthquake. Experimental researches on a passive pile, especially on an arching effect and a pile group effect, have been previously conducted by several researchers (Wang & Yen, 1974; Matsui *et al.*, 1982; Chen *et al.*, 1997). In this test series, the behavior of piles subjected to two types of large soil deformations was observed. The effect of the rigidity of the plate

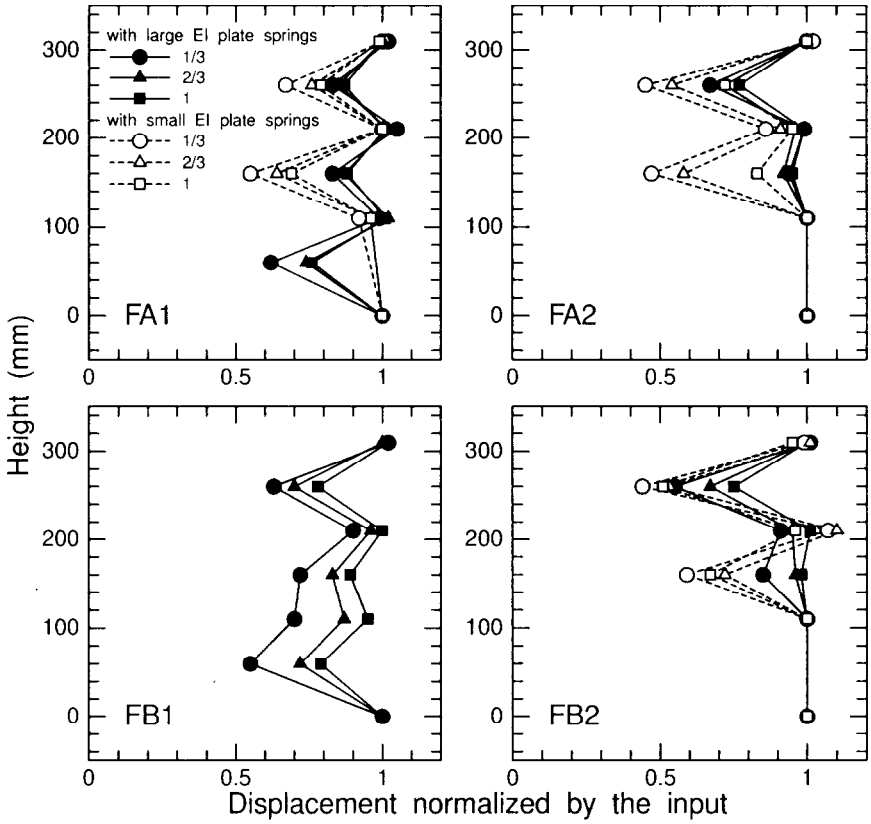

Figure 4.20: Normalized horizontal displacement distributions of laminae for shear box filled with dense sand.

Table 4.7: Material properties of model pipe pile in active type shear box test.

Young's modulus, E	206GPa
Thickness of pile, t	0.50mm
Cross-sectional area, A	2.28×10^{-5} m^2
Centroidal moment of inertia, I	5.99×10^{-10} m^4

springs on the deformation of the pile was examined, since they may govern the deformation of soil in the box. In the tests, the stainless steel model pipe pile, the properties of which are listed in Table 4.7, was placed in the box-center as shown in Fig. 4.15. The diameter of the pile was 75 times as large as the mean diameter of the Toyoura sand and was large enough to conduct the pile loading tests (Garnier & Konig, 1998). The surface of the model pipe pile was smooth. The pile tip was installed into the bearing stratum, which is the lowest one-third of the soil. Imposed soil deformation modes on the box were Type A and Type B, which were the same modes as in FA2 and FB2 in the previous section. Test conditions of this test series are shown in Table 4.8. In PA1 and PB1, only one cycle sinusoidal motion was applied to the laminae in 480 seconds. In PA1C and PA2C, 120-second cycle

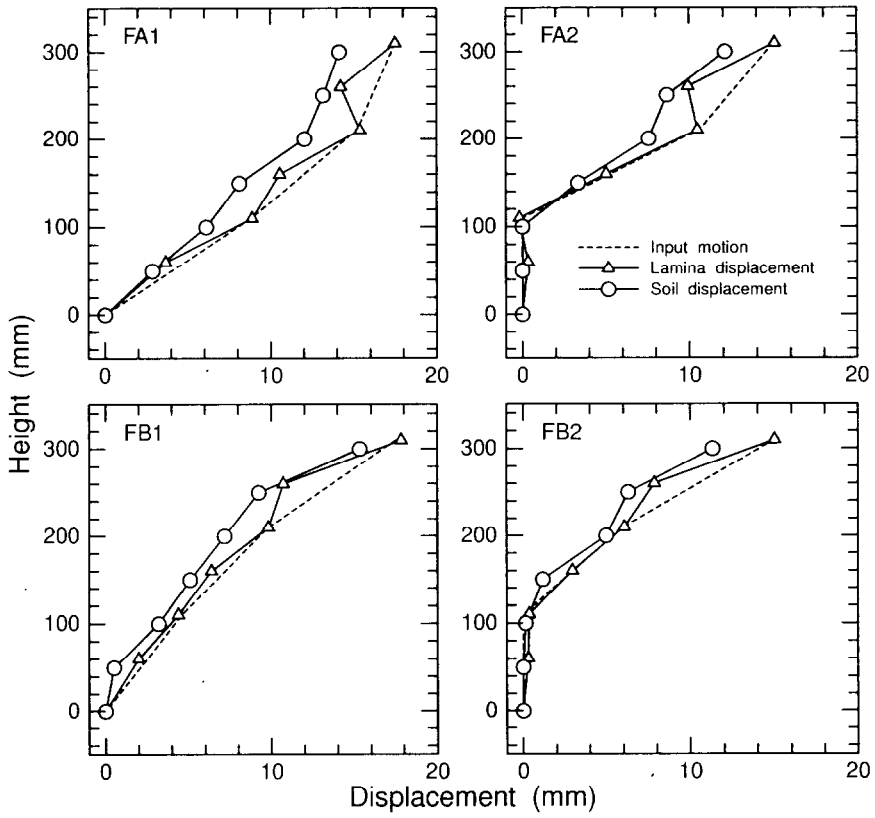

Figure 4.21: Observed horizontal displacement distributions of soil, shear box and input value.

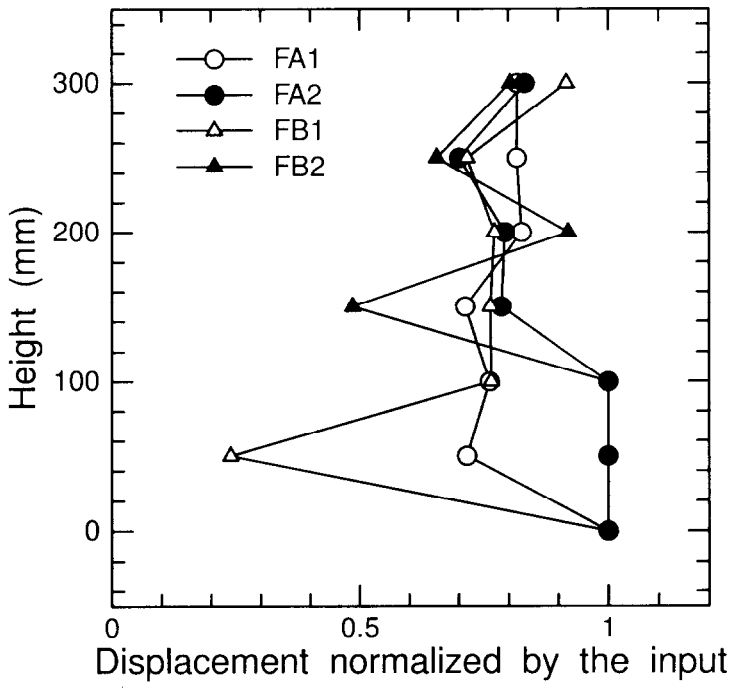

Figure 4.22: Normalized horizontal displacement distributions of soil, shear box and input value.

Table 4.8: Test conditions for single passive pile test.

Case	Thickness of a steel sheet (mm)	Number of layered steel sheets	Maximum displacement amplitude of actuators (mm)		
			Actuator L	Actuator M	Actuator U
PA1	0.3	6	0.0	9.3	14.0
PA1C	0.3	6	0.0	2.0 6.1 10.6	3.2 9.4 15.0
PA2C	0.6	3	0.0	2.0 6.1 10.6	3.2 9.4 15.0
PB1	0.3	6	0.0	5.8	13.2

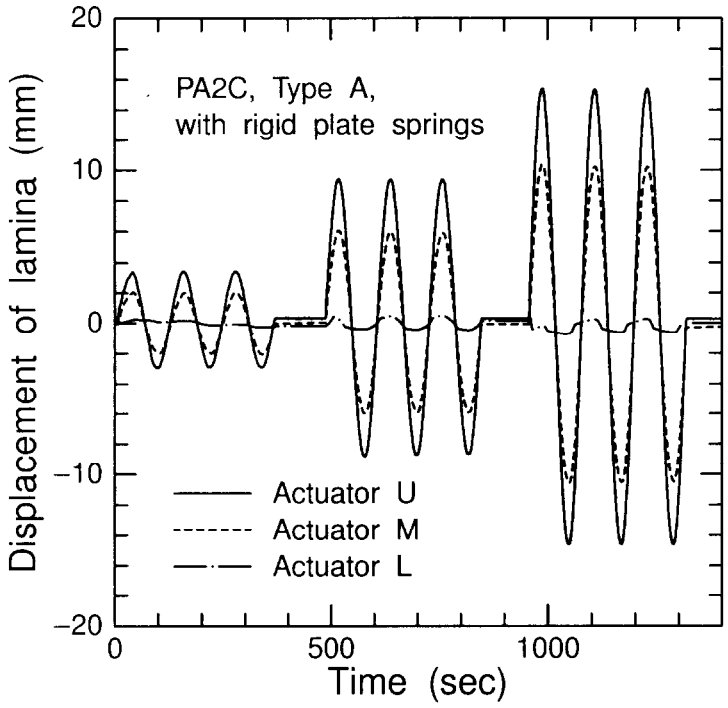

Figure 4.23: Typical time histories of actuator rod displacement in PA2C.

sinusoidal motions were applied to the laminae, where the peak values of the applied waves were increased after applying three cycles, up to 15mm at the top lamina. Figure 4.23 shows typical time histories of the input displacements by the actuators in PA2C.

Relationships between observed displacements at the pile head and the input displacements of the lamina at the ground surface for all the cases are shown in Fig. 4.24. It should be noted that the displacements of the pile at the pile head shown in the figure were measured at the target 50mm above the surface of the ground as shown in Fig. 4.15. In all the cases, the relationship shows non-

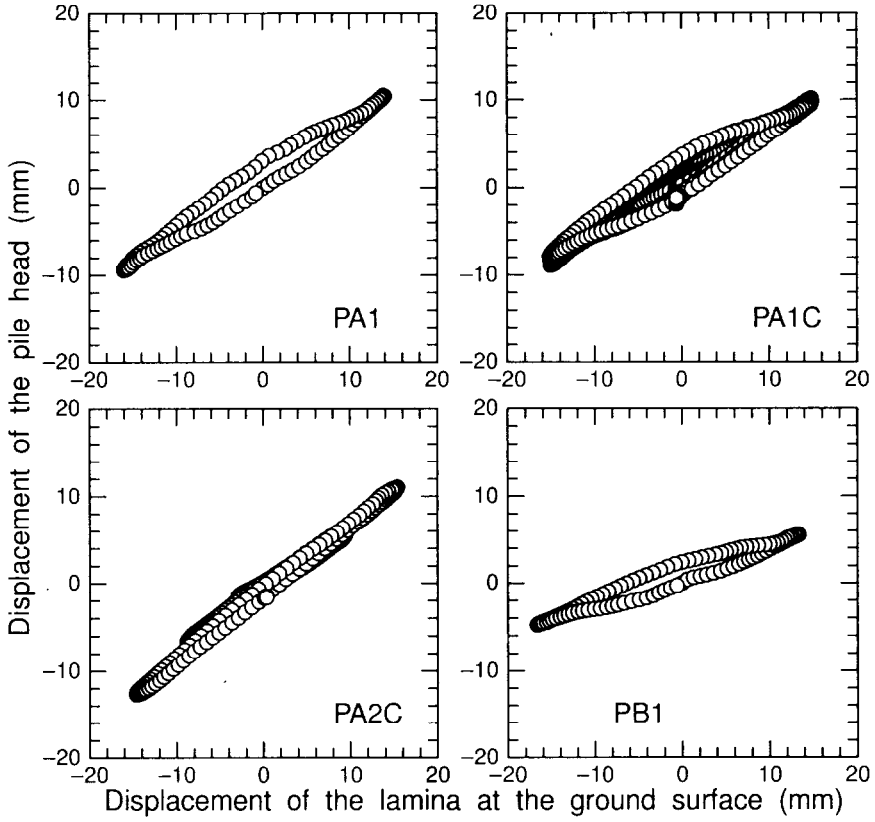

Figure 4.24: Relationship between observed displacement at pile head and input displacement of lamina at ground surface.

linearity, especially in the cases with flexible plate springs (PA1, PA1C and PB1). Though the piles showed yielding when the top lamina displacement reached approximately one diameter as shown in Fig. 4.25, parts of these non-linear relations are attributed to the non-linear response of the soil. Figure 4.25 shows observed bending strain distributions of the pile when the displacement of the top lamina reached 3, 9 and 13mm for the first time in the sequences of the box shearing. The flexibility of the plate springs is expected to affect the deformation of the soil in the box. However, according to the observed bending strain distributions of the pile in PA1 and PA2 which have different flexural rigidities of the plate springs, the effect of the flexural rigidity of the springs on the soil deformation appears to be insignificant at the center of the shear box.

In all the cases, the maximum bending strain can be seen at the depth of 200mm (the height of 100mm) which corresponds to the interface between the less deformed bearing stratum and the strained soil. These results agree with those obtained by Poulos *et al.* (1995) in their small model tests. In their tests, only the triangular displacement distribution could be applied to the soil. Regarding the difference in the input deformation mode, the maximum displacement in PB1 at the pile head is smaller than that of PA1 as shown in Fig. 4.24. These two cases also differ in the bending strain distributions of the pile as shown in Fig. 4.25. As shown in Fig. 4.21, the ground displacement at the center is not so sensitive to the boundary conditions, and the difference with the deformation

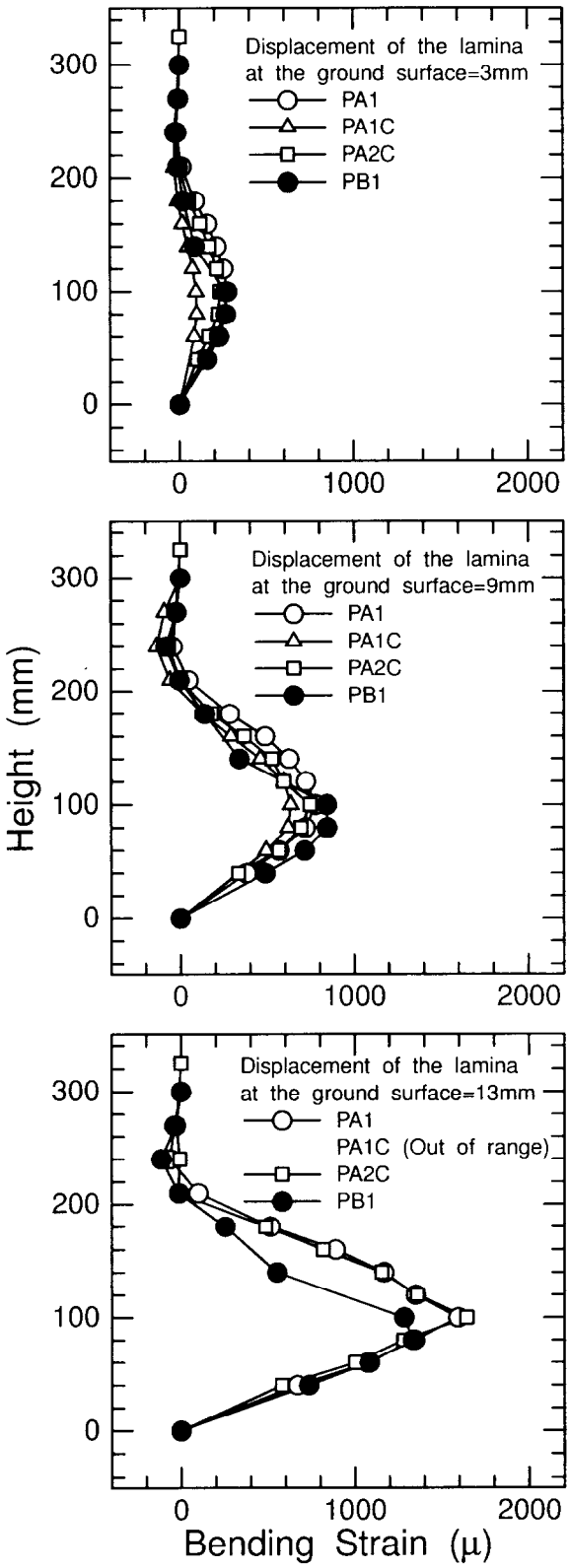

Figure 4.25: Observed bending strain distributions of pile when displacement of top lamina reaches 3, 9, and 13mm.

mode of the soil at the center cannot be clearly seen in the ground displacement in the comparison between FA2 and FB2. However, there is an obvious difference in the response of the pile as shown in Fig. 4.24 and Fig. 4.25. This shows that the response of the pile is very sensitive to the ground displacement or the type of ground motion.

Although further improvement of the apparatus is needed in order to interpret the test results properly, especially for the measurement of the actual ground displacement, it can be concluded that this apparatus could be a valuable tool for studying soil–structure interactions during earthquakes.

4.4 Interpretation of test results and further applications

The observed distributions of the ground displacement at the center of the model were similar to the input motions, becoming almost 70–80% of the input value as shown in the previous section. This fact indicates that the active type shear box has adequate capability in the modeling of the intended strain fields in the soil. However, the soil deformation was mainly caused by lateral normal stresses rather than shear stresses, according to the numerical analyses in the previous section. Hence, the stress condition generated by the shear box is different from the free-field stress situation in earthquakes. Given such a limitation, the obtained test results for earthquake problems cannot be directly applied to practical problems. However, one of the aims of this application in the soil–pile interaction problems during earthquakes is to observe the response of the pile in the different types of soil movements. The test results discussed in the previous section showed that the response of the pile was very sensitive to the mode of ground movement. Therefore, this system can provide useful data for verification of the numerical analyses. It should be noted that the stress conditions in the soil and the soil displacements, e.g. vertical and normal stresses in the soil and the displacement of the soil around the targeted structure, must be measured in the tests for verification. In the Japanese seismic design code for railway structures (Railway Technical Research Institute, 1997), it is prescribed that the displacements of pile foundations during earthquakes must be assessed by the framed structure analyses subjected to soil movements through soil–pile interaction springs. The active type shear box tests also have the capability to fulfill this requirement of the seismic design code.

Although only soil–pile interactions during earthquakes were analyzed in this chapter, the active type shear box can also be used for problems in which the modes of horizontal ground movement play an important role. For instance, assuming that an end wall of the laminar box is a flexible retaining wall and the soil in the box is a surrounding ground at an excavation site, various modes of the wall deflection can be simulated with the mounted actuators. This kind of test makes it possible to investigate the effect of the wall deflection mode on the earth pressure and the deformation and settlement of the ground at the retained side.

4.5 Summary

In this chapter, the newly developed active type shear box in the centrifuge is introduced for the purpose of investigating the behavior of structures subjected to large soil movement. The effects of the configuration of the shear box were investigated with simple finite element analyses. Details of the system were described. Performance of the apparatus and soil–pile interactions in large soil movements were discussed. The following conclusions are derived:

- Considering both deformation control and the stress conditions of the soil, the laminar box with the aspect ratio of 2 to 3 is better to use for the tests with dense sand, based on the simple two

dimensional finite element analysis results.

- Tests on the empty shear box were carried out at 1g and 25g, and it was confirmed that friction between laminae was not significant on the performance of the shear box.
- The displacements of the laminae to which the actuators were directly connected showed quite good agreement with the target displacements, though the non-direct-connected laminae did not attain the target displacements, resulting in many kinks in the distributions in the tests for the shear box filled with dense Toyoura sand. However, the observed distributions of the ground displacement at the center of the model were similar to the input motions. The ground displacements at the center of the model became almost 70–80% of the input values, and they were smoother than those of the laminae.
- Plate springs were attached to the ends of the laminar box to transmit applied lateral displacements from the actuators to all the laminae. The effect of flexural rigidity of the plate springs on the pile deformation was examined. Results showed that the effect of the rigidity of the springs on the soil and pile deformation was not significant.
- Behavior of piles subjected to two types of large soil deformations was observed. It was found that the pile response is very sensitive to the ground displacement or the type of ground motion.
- The active type shear box could be a valuable tool for studying soil–structure interaction during earthquakes though further improvements of the apparatus and detailed numerical analyses are needed in order to interpret the test results properly.

Chapter 5

Numerical modeling of waterfront structure during earthquake

As described in the previous chapters, soil–structure interaction is very complicated and limited information can be derived from physical model tests. In order to further investigate the interaction, the author has developed a finite element analysis code. In this chapter, the governing equations for dynamic porous solid–pore fluid interaction will be introduced. A constitutive model will be shown that can describe monotonic and cyclic loading behavior of sand, including soil liquefaction behavior.

5.1 Equations governing dynamic porous solid–pore fluid interaction in u–p formulation

The mathematical description of dynamic behavior of saturated porous media by Biot (1956a, 1956b, 1962 etc.) clarified concepts in an interpretation of effective stress and of coupled fluid and solid interaction. In this chapter, re-derived and extended Biot equations by Zienkiewicz *et al.* (Zienkiewicz & Bettess, 1982; Zienkiewicz *et al.*, 1999) will be introduced.

Effective stress

Considering a porous material like soil, the effective stress σ'_{ij} can be defined as

$$\sigma'_{ij} \equiv \sigma_{ij} - p\delta_{ij} \tag{5.1}$$

where σ_{ij} is the total stress and p is the pore water pressure when the soil is fully saturated. In this section, tensile components of stress are taken as positive and pressures are negative in compression.

Strain rate and constitutive equation for elastic media

The relationship between an infinitesimal strain rate $\dot{\varepsilon}_{ij}$ and a velocity gradient $\frac{\partial \dot{u}_i}{\partial x_j}$ is defined as

$$\dot{\varepsilon}_{ij} = \frac{1}{2}\left(\frac{\partial \dot{u}_i}{\partial x_j} + \frac{\partial \dot{u}_j}{\partial x_i}\right). \tag{5.2}$$

The strain rate $\dot{\varepsilon}_{ij}$ is additively decomposed into an elastic strain rate $\dot{\varepsilon}^e_{ij}$ and a plastic strain rate $\dot{\varepsilon}^p_{ij}$ as usual, i.e.

$$\dot{\varepsilon}_{ij} = \dot{\varepsilon}^e_{ij} + \dot{\varepsilon}^p_{ij} \tag{5.3}$$

where the elastic strain rate is given by

$$\dot{\varepsilon}^e_{ij} = {D^e_{ijkl}}^{-1}\dot{\sigma_{kl}}'. \tag{5.4}$$

σ_{ij} is a stress and the fourth-order tensor D^e_{ijkl} is an elastic modulus given in the Hooke's type as

$$D^e_{ijkl} = \left(K - \frac{2}{3}G\right)\delta_{ij}\delta_{kl} + G\left(\delta_{ik}\delta_{jl} + \delta_{il}\delta_{jk}\right) \tag{5.5}$$

where K and G are the bulk modulus and shear modulus, respectively, which are functions of stress and internal state variables in general and δ_{ij} is the Kronecker's delta, i.e. $\delta_{ij} = 1$ for $i = j$ and $\delta_{ij} = 0$ for $i \neq j$.

Momentum balance relation for solid–fluid mixture

The overall equilibrium or the momentum balance relation for the solid-fluid mixture can be written as

$$\frac{\partial \sigma_{ij}}{\partial x_j} - \rho \ddot{u}_i - \underline{\rho_f \ddot{w}_i} + \rho b_i = 0 \tag{5.6}$$

where u_i is a displacement of the solid matrix, ρ_f is the density of the fluid, b_i is the body force per unit mass, and $\dot{w}_i$ is the average (Darcy) velocity of percolating water. The density of the total composite ρ is defined as

$$\rho \equiv n\rho_f + (1-n)\rho_s \tag{5.7}$$

where ρ_s is the density of the solid particles and n is the porosity. The underlined term of equation (5.6), i.e. the fluid acceleration relative to the solid, is apparently small and can be omitted (Zienkiewicz *et al.*, 1999). By neglecting this term, the momentum balance relation becomes

$$\frac{\partial \sigma_{ij}}{\partial x_j} - \rho \ddot{u}_i + \rho b_i = 0. \tag{5.8}$$

Flow conservation equation

The flow divergence $\frac{\partial w_i}{\partial x_i}$ is balanced by the augmented storage in the pores of a unit volume of soil in time dt. If the compression of the soil particles is neglected, the flow conservation equation can be derived as

$$\frac{\partial \dot{w}_i}{\partial x_i} + \dot{\varepsilon}_{ii} - \frac{n\dot{p}}{K_f} = 0 \tag{5.9}$$

where $\dot{\varepsilon}_{ii}$ is the increased volume due to a change in strain, and K_f is the bulk modulus of fluid.

Momentum balance of fluid and Darcy's seepage law

If the same unit control volume as that assumed in equation (5.6) is used, the momentum balance of the fluid can be written as

$$\frac{\partial p}{\partial x_i} - R_i - \rho_f \left(\ddot{u}_i + \frac{\ddot{w}_i}{\underline{n}}\right) + \rho_f b_i = 0 \tag{5.10}$$

where R_i is the viscous drag force. As mentioned in the previous subsection, underlined terms of equation (5.10) can be neglected and the equation becomes

$$\frac{\partial p}{\partial x_i} - R_i - \rho_f \ddot{u}_i + \rho_f b_i = 0 \tag{5.11}$$

The drag force R_i can be written as

$$\frac{k}{\rho_f g} R_i = \dot{w}_i \tag{5.12}$$

where k is the hydraulic conductivity and g is the gravitational acceleration at which the hydraulic conductivity is measured. Substituting equations (5.12) and (5.9) into (5.11), the equation for fluid is obtained:

$$\frac{k}{\rho_f g}\frac{\partial}{\partial x_i}\left(\frac{\partial p}{\partial x_i} - \underline{\rho_f \ddot{u}_i} + \rho_f b_i\right) + \dot{\varepsilon}_{ii} - \frac{n\dot{p}}{K_f} = 0. \tag{5.13}$$

The underlined contribution of the solid acceleration can be omitted according to an investigation of the significance of the term (Chan, 1988). The flow conservation equation coupled with the momentum balance of the fluid can be written as

$$\frac{k}{\rho_f g}\frac{\partial}{\partial x_i}\left(\frac{\partial p}{\partial x_i} + \rho_f b_i\right) + \dot{\varepsilon}_{ii} - \frac{n\dot{p}}{K_f} = 0. \tag{5.14}$$

Boundary conditions

Equations (5.8) and (5.14) together with the constitutive relations specified in Section 5.3 define the behavior of the porous solid and the pore water pressure. The unknown variables in the system are the displacement of the solid matrix u_i, the pore water pressure p, and the velocity of fluid flow $\dot{w}_i$. Imposing boundary conditions on these variables completes the problem. Concrete calculation procedures are described in Appendices C & D.

For the total momentum balance, the boundary Γ is divided in two parts. One is the boundary Γ_t on which the values of the total traction t_i are specified, and the other is the boundary Γ_u on which the displacements u_i are given.

$$\begin{aligned} \Gamma &= \Gamma_t \cup \Gamma_u \\ t_i &= \bar{t}_i \quad \text{on} \quad \Gamma = \Gamma_t \\ u_i &= \bar{u}_i \quad \text{on} \quad \Gamma = \Gamma_u \end{aligned} \tag{5.15}$$

For the fluid phase, the boundary Γ is also divided in two parts. One is the boundary Γ_w on which the velocities of fluid flow $\dot{w}_i$ are specified, and the other is the boundary Γ_p on which the pore water pressure p is given.

$$\begin{aligned} \Gamma &= \Gamma_w \cup \Gamma_p \\ \dot{w}_i &= \bar{\dot{w}}_i \quad \text{on} \quad \Gamma = \Gamma_w \\ p &= \bar{p} \quad \text{on} \quad \Gamma = \Gamma_p \end{aligned} \tag{5.16}$$

5.2 Constitutive models for soils under cyclic loading

Many constitutive models that can describe soil behavior under cyclic loading, including liquefying soil behavior, have been proposed by many researchers. Comparisons of the constitutive models have been conducted using site investigation results on damaged structures due to earthquakes and centrifuge studies. The technical committees on soil liquefaction problems of the Japan Geotechnical Society conducted verifications of the numerical analyses through centrifuge model test prediction (1990) and prediction of the permanent displacement of a building damaged in the 1964 Ni'igata Earthquake (1993). In the VELACS Project (*VE*rifications of *L*iquefaction *A*nalysis using *C*entrifuge *S*tudies Project) 23 predictors conducted numerical analyses using their codes on nine different centrifuge models concerning liquefaction problems. In these projects, the predictions were made with

a variety of numerical analysis codes, i.e. constitutive models. Dafalias (1994) reviewed the constitutive models used in the VELACS Project and classified the models into three: empirical models, micro-mechanical and/or multi-mechanism models, and elastoplastic models. This study applies the model to three-dimensional problems, and it was decided to use the elastoplastic model in the numerical analyses.

In order to simulate the soil behavior under cyclic loading, a sequence of loading, unloading, and reloading must be considered. Constitutive models proposed by Oka *et al.* (1999) and Nishi & Kanatani (1990) introduce non-linear kinematic and isotropic hardening that govern the yield surface behavior in stress-ratio space with the non-associated flow rule to simulate the soil response under cyclic loading. These models essentially follow classical plasticity development, i.e. the plastic strain increment is normal to the plastic potential. On the other hand, in subloading (bounding) surface models or nested surfaces models, the current stress point is on a surface other than the yield surface, and a plastic yielding occurs even if the current is inside the yield surface, according to relations between the current stress point and a conjugate stress point on the yield surface, etc. (e.g. Dafalias & Herrmann, 1982; Hashiguchi *et al.*, 1996; Hashiguchi & Chen, 1998; Mroz & Norris, 1982; Prévost, 1985). These constitutive models differently have limitations, e.g., (1) the models proposed by Oka *et al.* (1999) and Nishi & Kanatani (1990) are not applicable to the prediction of cyclic isotropic or anisotropic consolidation behaviors as they obey the non-associated flow rule with a conical yield surface, and they require complex judgments for the stress ratio parameter determination, and (2) bounding surface or multi-surface models proposed by Dafalias & Herrmann (1982), Mroz & Norris (1982) and Prévost (1985) show differently unrealistic strain accumulation behaviors during cyclic loadings.

In this study, an extended subloading surface model proposed by Hashiguchi *et al.* (Hashiguchi *et al.*, 1996; Hashiguchi & Chen, 1998) is adopted in the numerical analyses on centrifuge model studies, since (1) the loading criterion is simple, and (2) the model has the capability to describe realistic strain accumulation behavior during a cyclic loading though many material parameters are needed. Detail of the model is described in the following sections.

5.3 Extended subloading surface model with rotational hardening employing ellipsoid type yield surface

In this section, the signs for stress, stress rate, and strain rate are positive for tension, and all the *stresses* and the *stress parameters* stand for the *effective stresses* even though the prime sign ($'$) is eliminated.

5.3.1 Description of the constitutive model

Normal yield surface

Let a normal yield surface which passes through the origin of stress space and obeys isotropic and rotational hardening be described as

$$f(\hat{p},\hat{\chi}) = F(H) \tag{5.17}$$

where, letting the stress on the normal yield surface be denoted as $\hat{\sigma}$,

$$\hat{\sigma}_m \equiv \frac{1}{3}\hat{\sigma}_{ii}, \quad \hat{p} \equiv -\hat{\sigma}_m, \quad \hat{\sigma}^*_{ij} \equiv \hat{\sigma}_{ij} + \hat{p}\delta_{ij} \tag{5.18}$$

$$\hat{\eta}_{ij} \equiv \hat{Q}_{ij} - \beta_{ij} \quad \hat{Q}_{ij} \equiv \frac{\hat{\sigma}^*_{ij}}{\hat{p}} \tag{5.19}$$

$$\hat{\chi} \equiv \frac{\sqrt{\hat{\eta}_{ij}\hat{\eta}_{ij}}}{\hat{m}}. \tag{5.20}$$

$\hat{m}$ is a function of the material constant ϕ, i.e.,

$$\begin{aligned} \hat{m} &= f_m(\phi) \\ &= \frac{2\sqrt{6}\sin\phi}{3-\sin\phi}. \end{aligned} \tag{5.21}$$

An anisotropy of a critical state in stress space is neglected. H is an isotropic hardening variable. The central axis of the normal yield surface is described as

$$\sigma^*_{ij}/p = \beta_{ij} \tag{5.22}$$

where

$$\sigma_m \equiv \frac{1}{3}\sigma_{ii}, \quad p \equiv -\sigma_m, \quad \sigma^*_{ij} \equiv \sigma_{ij} + p\delta_{ij}. \tag{5.23}$$

Equation (5.17) for the normal yield surface includes only β_{ij} as a variable to describe the anisotropy. Let β_{ij} be called a *rotational hardening variable*. The equation $\sqrt{\hat{\eta}_{ij}\hat{\eta}_{ij}} = \hat{m}$ describes a conical surface whose tip exists at the origin and whose central axis coincides with the central axis $\sigma^*_{ij}/p = \beta_{ij}$ of the normal yield surface.

The isotropic hardening/softening function $F(H)$ for clays is usually given by a function of plastic volumetric strain $\varepsilon^p_v (= \int \dot{\varepsilon}^p_v dt = \int \dot{\varepsilon}^p_{ii} dt)$. On the other hand, the isotropic hardening/softening for sands is also induced by a plastic shear deformation. Then, assume that the plastic shear deformation causes a softening and a hardening for the stress state inside and outside, respectively, of the surface, called the *shear boundary surface*, forming a conical surface whose tip exists in the origin and whose central axis coincides with a hydrostatic axis in the principal stress, similar to a rotational limit surface. And let this surface be described as

$$\frac{\sqrt{\sigma^*_{ij}\sigma^*_{ij}}}{p} = m_d \tag{5.24}$$

$$\hat{m} = f_m(\phi_d) = \frac{2\sqrt{6}\sin\phi_d}{3-\sin\phi_d} \tag{5.25}$$

where σ_{ij} represents the current stress and ϕ_d is a material constant such that the looser the sand, the larger is ϕ_d. Then, let the isotropic hardening/softening function be given as

$$F = F_0 \exp\left(\frac{H}{\lambda - \kappa}\right) \tag{5.26}$$

where λ and κ are material constants describing the slope of a normal consolidation curve and a swelling curve, respectively, in the $(\ln p, v)$ space, and F_0 is the initial value of F. The evolutional rule for the isotropic hardening/softening parameter H is given by

$$\dot{H} = -\dot{\varepsilon}^p_v + \dot{\varepsilon}^p_s \tag{5.27}$$

where

$$-\dot{\varepsilon}_v^p = -\dot{\varepsilon}_{ii}^p, \quad \dot{\varepsilon}_s^p \equiv \mu\sqrt{\dot{\varepsilon}_{ij}^{p*}\dot{\varepsilon}_{ij}^{p*}}\left(\frac{\sqrt{\sigma_{ij}^*\sigma_{ij}^*}}{p} - m_d\right) \tag{5.28}$$

and μ is a material constant.

It is assumed that the normal yield surface keeps a similarity to itself. Then, f is a homogeneous function of $\hat{\sigma}_{ij}$, satisfying Euler's theorem for a homogeneous function. Therefore, by selecting the function f to be homogeneous degree one, the following expression holds, while $\hat{\chi}$ is a dimensionless variable:

$$\begin{aligned} f(\hat{p},\hat{\chi}) &= \hat{p}g(\hat{\chi}) \\ &= \hat{p}(1+\hat{\chi}^2). \end{aligned} \tag{5.29}$$

In the case of $\beta_{ij} = 0$ is a half-ellipsoid whose long axis is parallel to the hydrostatic axis in the stress space. The parameter $\hat{\eta}_{ij}$ was introduced by Sekiguchi and Ohta (1977) in order to describe the rotation of the yield surface concisely. For the formulation of the evolutional equation of the rotational hardening variable β_{ij}, assume as follows:

1. The yield surface rotates around the origin of the stress space.

2. There exists a limit in the range of the rotation of the normal yield surface, and let the surface describing the limit be called the *limit surface for rotational hardening*. Let this surface be given by the following conical surface whose tip exists at the origin and whose central axis coincides with the hydrostatic axis in the principal stress space.

$$\frac{\sqrt{\sigma_{ij}^*\sigma_{ij}^*}}{p} = \hat{m}_b \tag{5.30}$$

   where $\hat{m}_b$ is given by the function f_m for $\hat{m}$ of equation (5.21), the material constant ϕ being replaced by the material constant ϕ_b, i.e.,

$$\begin{aligned} \hat{m}_b &= f_m(\phi_b) \\ &= \frac{2\sqrt{6}\sin\phi_b}{3-\sin\phi_b}. \end{aligned} \tag{5.31}$$

3. The central axis of yield surface rotates so as to approach the conjugate line on the rotational limit surface. The conjugate line is given by the equation $\sigma_{ij}^*/p = \hat{m}_b\hat{\eta}_{ij}/\sqrt{\hat{\eta}_{kl}\hat{\eta}_{kl}}$.

4. For monotonic-proportional loading with $\hat{Q}_{ij} = const.$, i.e. the so-called anisotropic consolidation, the central axis of yield surface approaches the loading path so as to satisfy $\sqrt{\hat{\eta}_{ij}\hat{\eta}_{ij}} = 0$.

5. The rotational rate of the normal yield surface is proportional to the magnitude of plastic deviator stretching, while it is independent of the plastic volumetric stretching which would not be related to anisotropy.

Then, let the evolutional rule of β_{ij} be assumed to be

$$\dot{\beta}_{ij} = b_r \sqrt{\dot{\varepsilon}^{p*}_{kl} \dot{\varepsilon}^{p*}_{kl}} \sqrt{\hat{\eta}_{kl} \hat{\eta}_{kl}} \, \hat{\eta}_{ijb} \tag{5.32}$$

where b_r is a material constant and

$$\dot{\varepsilon}^p_v \equiv \dot{\varepsilon}^p_{ii}, \quad \dot{\varepsilon}^{p*}_{ij} \equiv \dot{\varepsilon}^p_{ij} - \frac{1}{3}\dot{\varepsilon}^p_v \delta_{ij} \tag{5.33}$$

$$\hat{\eta}_{ijb} \equiv \hat{m}_b \hat{t}_{ij} - \beta_{ij} \tag{5.34}$$

$$\hat{t}_{ij} \equiv \frac{\hat{\eta}_{ij}}{\sqrt{\hat{\eta}_{kl} \hat{\eta}_{kl}}}. \tag{5.35}$$

Subloading surface

A subloading surface is given by the similarity to the normal yield surface (5.17) as

$$f(\overline{p}, \overline{\chi}) = RF(H) \tag{5.36}$$

where

$$\overline{\sigma}_{ij} \equiv \sigma_{ij} - \overline{\alpha}_{ij} \tag{5.37}$$

$$\overline{p} \equiv -\frac{1}{3}\overline{\sigma}_{ii}, \quad \overline{\sigma}^*_{ij} \equiv \overline{\sigma}_{ij} + \overline{p}\delta_{ij} \tag{5.38}$$

$$\overline{\eta}_{ij} \equiv \overline{Q}_{ij} - \beta_{ij}, \quad \overline{Q}_{ij} \equiv \frac{\overline{\sigma}^*_{ij}}{\overline{p}} \tag{5.39}$$

$$\overline{\chi} \equiv \frac{\sqrt{\overline{\eta}_{ij} \overline{\eta}_{ij}}}{\overline{m}}. \tag{5.40}$$

$\overline{m}$ is a function f_m of the material constant ϕ, i.e.,

$$\begin{aligned} \overline{m} &= f_m(\phi) \\ &= \frac{2\sqrt{6}\sin\phi}{3 - \sin\phi}. \end{aligned} \tag{5.41}$$

σ_{ij} stands for the current stress which always exists on the subloading surface. $\overline{\alpha}_{ij}$ on the subloading surface is the conjugate point of the null stress on the normal yield surface. Figure 5.1 illustrates the normal yield and subloading surfaces in $p-q$ space. In the figure, β_a is the axial component of β and $q \equiv \sigma_a - \sigma_r$, where σ_a and σ_r are the axial and a radial stresses, respectively, in the axisymmetric stress state, i.e. in the $p-q$ space. $R(0 \leq R \leq 1)$ is the ratio of the size of the subloading surface to that of the normal yield surface, while $R = 0$ and 1 correspond to the purely elastic and the normal yield state, respectively. The similarity of the normal yield and the subloading surface leads to relations

$$\overline{\sigma}_{ij} = R\hat{\sigma}_{ij}, \quad \overline{s}_{ij} = Rs_{ij} \tag{5.42}$$

$$\overline{Q}_{ij} = \hat{Q}_{ij}, \quad \overline{\eta}_{ij} = \hat{\eta}_{ij}, \quad \overline{m} = \hat{m}, \quad \overline{m}_b = \hat{m}_b, \quad \overline{\chi}_{ij} = \hat{\chi}_{ij} \tag{5.43}$$

where

$$\overline{s}_{ij} \equiv s_{ij} - \overline{\alpha}_{ij}. \tag{5.44}$$

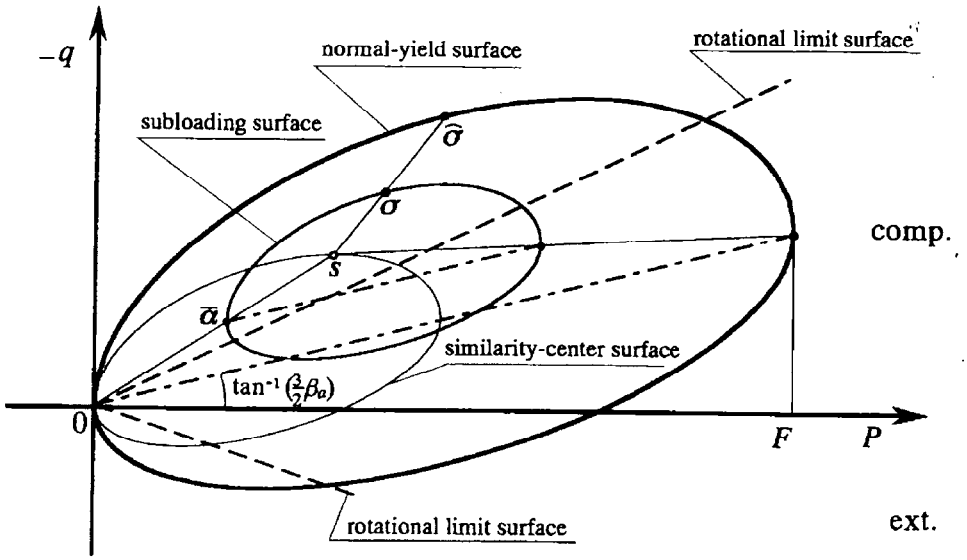

Figure 5.1: Normal yield and subloading surfaces with rotational hardening in $p-q$ space (after Hashiguchi & Chen, 1998).

Let $\hat{\sigma}_{ij}$ be regarded as the conjugate stress on the normal yield surface for the current stress on the subloading surface. s_{ij} is a *center of similarity* of the normal yield and the subloading surfaces. The following expression similar to the equation (5.29) holds:

$$\begin{aligned} f(\overline{p},\overline{\chi}) &= \overline{p}g(\overline{\chi}) \\ &= \overline{p}(1+\overline{\chi}^2). \end{aligned} \tag{5.45}$$

The variable R is calculated from equation (5.36) with the substitution of

$$\overline{\sigma}_{ij} = \sigma_{ij} - (1-R)s_{ij} \tag{5.46}$$

obtained from equations (5.37), (5.42) and (5.44), and then $\overline{\alpha}_{ij}$ is calculated by the equation $\overline{\alpha}_{ij} = (1-R)s_{ij}$.

The evolutional rule of rotational hardening for the general state where the current stress exists on the normal yield surface or in its interior is given from equations (5.32)–(5.35) and (5.43) as

$$\dot{\beta}_{ij} = b_r\sqrt{\dot{\varepsilon}^{p*}_{kl}\dot{\varepsilon}^{p*}_{kl}}\sqrt{\overline{\eta}_{kl}\overline{\eta}_{kl}}\,\overline{\eta}_{ijb} \tag{5.47}$$

where

$$\overline{\eta}_{ijb} \equiv \overline{m}_b\bar{t}_{ij} - \beta_{ij} \tag{5.48}$$

$$\bar{t}_{ij} \equiv \frac{\overline{\eta}_{ij}}{\sqrt{\overline{\eta}_{kl}\overline{\eta}_{kl}}} \tag{5.49}$$

$$\begin{aligned} \overline{m}_b &= f_m(\phi_b) \\ &= \frac{2\sqrt{6}\sin\phi_b}{3-\sin\phi_b}. \end{aligned} \tag{5.50}$$

Evolutional rule of similarity-center

Let the evolutional rule of the similarity-center s_{ij} of the normal yield and the subloading surfaces be formulated below. The surface which passes through the similarity-center s_{ij} and is similar to the normal yield surface with respect to the origin of stress space, called a *similarity-center surface* is described as

$$f(p_s, \chi_s) = R_s F(H) \tag{5.51}$$

where $R_s (0 \leq R_s \leq 1)$ is the ratio of the size of the similarity-center surface to that of the normal yield surface. The following expression which is similar to equations (5.29) and (5.45) holds:

$$\begin{aligned} f(p_s, \chi_s) &= p_s g(\chi_s) \\ &= p_s (1 + \chi_s^2). \end{aligned} \tag{5.52}$$

where

$$p_s \equiv -\frac{1}{3} s_{ii}, \quad s_{ij}^* \equiv s_{ij} + p_s \delta_{ij} \tag{5.53}$$

$$\eta_{ijs} \equiv Q_{ijs} - \beta_{ij}, \quad Q_{ijs} \equiv \frac{s_{ij}^*}{p_s} \tag{5.54}$$

$$\chi_s \equiv \frac{\sqrt{\eta_{ijs} \eta_{ijs}}}{m_s}. \tag{5.55}$$

m_s is a function f_m of the material constant ϕ, i.e.

$$\begin{aligned} m_s &= f_m(\phi) \\ &= \frac{2\sqrt{6} \sin\phi}{3 - \sin\phi}. \end{aligned} \tag{5.56}$$

The following inequality must hold since the similarity-center has to exist inside the normal yield surface, i.e. the similarity-surface cannot become larger than the normal yield surface:

$$f(p_s, \chi_s) \leq F(H) \tag{5.57}$$

Equation (5.57) leads in the differential form to

$$\frac{\partial f(p_s, \chi_s)}{\partial s_{ij}} \left\{ \dot{s}_{ij} + \frac{1}{F} \left(\frac{\partial f(p_s, \chi_s)}{\partial \beta_{kl}} \dot{\beta}_{kl} - \dot{F} \right) s_{ij} \right\} \leq 0 \quad \text{for} \quad f(p_s, \chi_s) = F(H) \quad \text{i.e.} \quad R_s = 1. \tag{5.58}$$

Equations (5.57) and (5.58) are called an *enclosing condition of the similarity-center.*

In the state $R_s = 1$ in which the similarity-center exists on the normal yield surface the vector $\sigma - s$ makes an obtuse angle with the vector $\partial f(p_s, \chi_s)/\partial \beta$ which is outward normal to the similarity-center surface coinciding with the normal yield surface, while σ exists inside the normal yield surface. Then, let the following equation be assumed, which satisfies inequality (5.58):

$$\dot{s}_{ij} + \frac{1}{F} \left(\dot{F} - \frac{\partial f(p_s, \chi_s)}{\partial \beta_{kl}} \dot{\beta}_{kl} \right) s_{ij} = c \sqrt{\dot{\varepsilon}_{kl}^p \dot{\varepsilon}_{kl}^p} \, \tilde{\sigma}_{ij} \tag{5.59}$$

from which the evolutional rule of the similarity-center is obtained as follows:

$$\dot{s}_{ij} = c \sqrt{\dot{\varepsilon}_{kl}^p \dot{\varepsilon}_{kl}^p} \, \tilde{\sigma}_{ij} + \frac{1}{F} \left(\frac{\partial f(p_s, \chi_s)}{\partial \beta_{kl}} \dot{\beta}_{kl} - \dot{F} \right) s_{ij} \tag{5.60}$$

where c is a material constant and

$$\tilde{\sigma}_{ij} \equiv \sigma_{ij} - s_{ij}. \tag{5.61}$$

Consistency condition for subloading surface

Differentiation of equation (5.36) leads to

$$\frac{\partial f(\overline{p},\overline{\chi})}{\partial \overline{\sigma}_{ij}}\dot{\overline{\sigma}}_{ij}+\frac{\partial f(\overline{p},\overline{\chi})}{\partial \beta_{ij}}\dot{\beta}_{ij}=R\dot{F}+\dot{R}F \tag{5.62}$$

where $\dot{\overline{\sigma}}_{ij}$ is given from equation (5.46) as

$$\dot{\overline{\sigma}}_{ij}=\dot{\sigma}_{ij}-(1-R)\dot{s}_{ij}+\dot{R}s_{ij}. \tag{5.63}$$

Equation (5.62) includes $\dot{R}$ in addition to the stress rate $\dot{\sigma}_{ij}$ and the rates of internal state variables $\dot{F},\dot{\beta}_{ij},\dot{s}_{ij}$ which are related to the plastic stretching $\dot{\varepsilon}^p_{ij}$. Therefore, the relation of $\dot{R}$ to $\dot{\varepsilon}^p_{ij}$ has to be formulated in order to use equation (5.62) as a consistency condition.

Then, assume that the stress and the subloading surface approaches the normal yield surface, i.e. that the ratio R of the size of the subloading surface to that of the normal yield surface increases monotonically, satisfying the following relation in the plastic loading process:

$$\left.\begin{array}{rl} R=0: & \dot{R}=+\infty \\ 0<R<1: & \dot{R}>0 \\ R=1: & \dot{R}=0 \\ R>1: & \dot{R}<0 \end{array}\right\} \quad \text{for} \quad \dot{\varepsilon}^p\neq\mathbf{O}. \tag{5.64}$$

Then, the evolutional rule of R in the plastic loading process is given as

$$\dot{R}=U\sqrt{\dot{\varepsilon}^p_{ij}\dot{\varepsilon}^p_{ij}} \quad \text{for} \quad \dot{\varepsilon}^p\neq\mathbf{O} \tag{5.65}$$

where U is a monotonically decreasing function of R satisfying

$$\begin{array}{rl} R=0: & U=+\infty \\ 0<R<1: & U>0 \\ R=1: & U=0 \\ R>1: & U<0. \end{array} \tag{5.66}$$

The function U is defined as follow:

$$U=u_1\left(\frac{1}{R^{m_1}}-1\right) \tag{5.67}$$

where u_1 and m_1 are material constants. Substituting equation (5.65) into equation (5.62), the following extended consistency condition for the subloading surface is obtained:

$$\frac{\partial f(\overline{p},\overline{\chi})}{\partial \overline{\sigma}_{ij}}\dot{\overline{\sigma}}_{ij}+\frac{\partial f(\overline{p},\overline{\chi})}{\partial \beta_{ij}}\dot{\beta}_{ij}=R\dot{F}+U\sqrt{\dot{\varepsilon}^p_{kl}\dot{\varepsilon}^p_{kl}}F. \tag{5.68}$$

The associated flow rule is adopted:

$$\dot{\varepsilon}^p_{ij}=\lambda\overline{N}_{ij} \quad (\lambda>0) \tag{5.69}$$

where λ is a positive proportionality factor, and the second-order tensor $\overline{N}_{ij}$ is the normalized outward normal of the subloading surface, i.e.

$$\overline{N}_{ij}\equiv\frac{\frac{\partial f(\overline{p},\overline{\chi})}{\partial \sigma_{ij}}}{\sqrt{\frac{\partial f(\overline{p},\overline{\chi})}{\partial \sigma_{kl}}\frac{\partial f(\overline{p},\overline{\chi})}{\partial \sigma_{kl}}}}. \tag{5.70}$$

Table 5.1: Material parameters for constitutive model.

Param.	Characterized by / Affection to	
λ, κ	Isotropic normal consolidation and swelling curves.	Material constants
G or ν	Shear modulus.	
μ, ϕ_d	Undrained stress path and phase transformation line.	
ϕ	Shape of subloading surface.	
u_1, m_1	Approaching rate to normal yield state.	
c	Width of hysteresis loop.	
b_r, ϕ_b	Rate and range of the evolution of anisotropic hardening.	
F_0	Over consolidation ratio.	Initial values
β_{ij0}	Stress path of anisotropic consolidation.	
s_{ij0}	Shape of hysteresis loop.	

Substituting equations (5.47), (5.63) and (5.69) into the extended consistency condition (5.68) for the subloading surface and further substituting the result into equations (5.3) and (5.4), the positive proportionality factor λ is obtained as

$$\lambda = \frac{\overline{N}_{ij}\dot{\sigma}_{ij}}{D_p} = \frac{\overline{N}_{ij}D^e_{ijkl}\dot{\varepsilon}_{kl}}{D_p + \overline{N}_{ij}D^e_{ijkl}\overline{N}_{kl}} \tag{5.71}$$

where

$$D_p \equiv \overline{N}_{ij}\overline{a}_{ij} + \overline{N}_{ij}\overline{\sigma}_{ij}\left(\frac{F'}{F}h - \frac{1}{RF}\frac{\partial f(\overline{p},\overline{\chi})}{\partial \beta_{kl}}b_{kl} + \frac{U}{R}\right) \tag{5.72}$$

$$\overline{a}_{ij} \equiv \frac{\dot{\overline{\alpha}}_{ij}}{\lambda} = (1-R)z_{ij} - Us_{ij} \tag{5.73}$$

$$F' \equiv \frac{dF}{dH} = \frac{F}{\lambda - \kappa}, \quad h \equiv \frac{\dot{H}}{\lambda} \quad (\dot{F} = F'\lambda h) \tag{5.74}$$

$$b_{ij} \equiv \frac{\dot{\beta}_{ij}}{\lambda} = b_r\sqrt{\overline{N}^*_{kl}\overline{N}^*_{kl}}\sqrt{\overline{\eta}_{kl}\overline{\eta}_{kl}}\,\overline{\eta}_{ijb} \tag{5.75}$$

$$z \equiv \frac{\dot{s}_{ij}}{\lambda} = c\tilde{\sigma}_{ij} + \frac{1}{F}\left(F'h - \frac{\partial f(p_s,\chi_s)}{\partial \beta_{kl}}b_{kl}\right)s_{ij} \tag{5.76}$$

$$\overline{N}^*_{ij} \equiv \overline{N}_{ij} - \frac{1}{3}\overline{N}_{kk}\delta_{ij}. \tag{5.77}$$

The loading criterion is given by

$$\left.\begin{array}{ll} \dot{\varepsilon}^p \neq \mathbf{O}: & \overline{N}_{ij}D^e_{ijkl}\dot{\varepsilon}_{kl} > 0 \\ \dot{\varepsilon}^p = \mathbf{O}: & \overline{N}_{ij}D^e_{ijkl}\dot{\varepsilon}_{kl} \leq 0 \end{array}\right\}. \tag{5.78}$$

5.3.2 Sensitivity of material parameters on soil behavior

The material parameters used in this constitutive model are listed in Table 5.1. Hashiguchi & Chen (1998) showed simulation results of (1) element tests on monotonic and cyclic drained tests presented

Table 5.2: Reference parameters for medium dense Toyoura sand.

G_s	e_0	κ	λ	ν	ϕ	ϕ_d	μ
2.65*	0.79*	0.0013*	0.0072*	0.33*	40°	25°*	0.9
ϕ_b	b_r	u_1	m_1	c	β_{ij0}	$F_0/(-\sigma_{m0})$	s_{ij0}
30°	1.0×10^2	4.0	1.0*	30.0	$\frac{\sigma_{ij0}-\sigma_{m0}\delta_{ij}}{(-\sigma_{m0})}$*	1.2	$0.2\,\sigma_{ij0}$

The values marked with a asterisk were fixed throughout the parametric study.

at the International workshop on constitutive equations for granular non-cohesive soils in 1987 (Saada & Bianchini (eds), 1989), (2) well known monotonic undrained tests by Castro (Castro, 1969), and (3) cyclic undrained test (Ishihara *et al.*, 1975) on sands. According to the simulation results, the model is seen to perform well. However, there are many parameters that must be specified to simulate a particular soil behavior.

The parameters of λ, κ can be determined from the isotropic normal consolidation and swelling curves. G or ν may be determined from the shear modulus obtained by some element tests. ϕ_d can be determined by a phase transformation line in the undrained tests. β_{ij0} can be determined by a stress path of anisotropic consolidation, i.e. the coefficient of earth pressure at rest. F_0/p_0 corresponds to an overconsolidation ratio, where $p_0 \equiv -\sigma_{m0}$.

The parameters shown in the preceding paragraph can be determined by the element tests, and the users of this model can understand their physical meanings. However, in the determination of the other parameters, i.e. μ, ϕ, u_1, m_1, b_r, ϕ_b, c and s_{ij0}, the users have to fit these parameters into the element tests by trial and error.

In this section, the sensitivity of these parameters on undrained soil behavior under cyclic loading is examined by a parametric study. Table 5.2 shows the reference parameters for the calculations. The shear modulus, G was determined by $G \equiv \frac{3(1-2\nu)}{2(1+\nu)} \frac{\nu(-\sigma_m)}{\kappa}$ in this study. These material properties were chosen to approximate those of the medium dense Toyoura sand, and the asterisked values were fixed throughout the parametric study.

The slope of the normal consolidation line, λ, in the table may cause the reader to feel that λ is smaller than that of the ordinary sand but it is nevertheless correct. Figure 5.2 shows typical isotropic consolidation test results on Toyoura sand together with the test result by Miura (1975). The stress level in the consolidation tests by Miura is very high, though very clear yielding of the sand can be seen. It was reported that crushing of grains was observed on the normal consolidation line obtained by Miura. Grain crushing is impossible within the targeted stress level in this study. Hence, in determining the slope of the normal consolidation line, the consolidation test result by the author was chosen, as the stress level of the consolidation was almost the same as that in the actual liquefiable layer.

Soil behavior in cyclic loading

The typical stress path and the stress–strain relationship of undrained cyclic triaxial tests for isotropically consolidated sand, both in the laboratory (Towhata, 1981) and in the numerical analysis, are

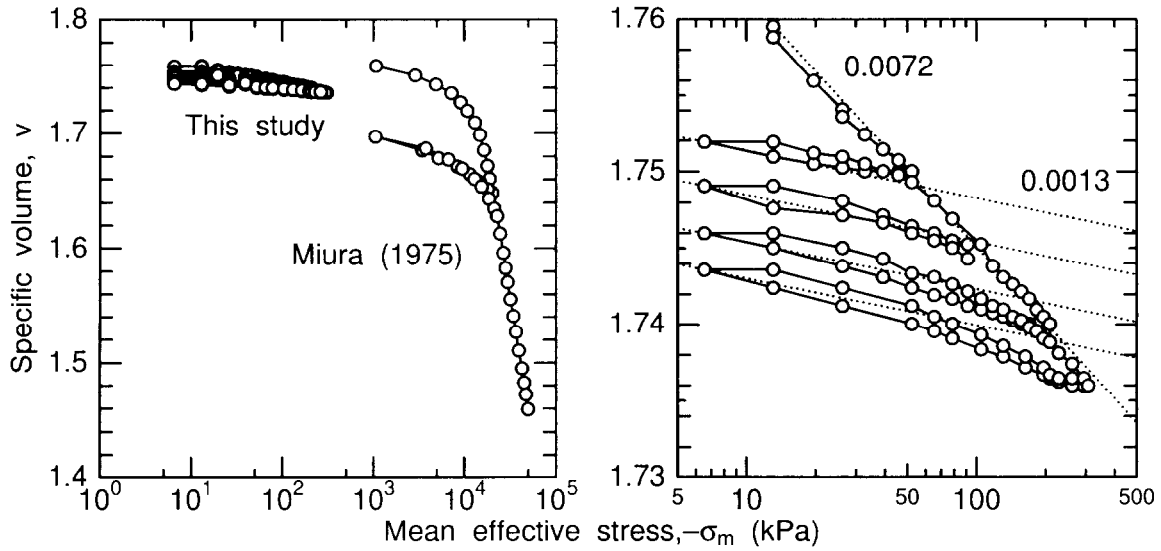

Figure 5.2: Typical isotropic consolidation test results on Toyoura sand together with test result by Miura (1975) in v–$\ln(-\sigma_m)$ space.

shown in Fig. 5.3 and 5.4, respectively. The soil parameters used in the analysis were the same as those listed in Table 5.2. When the stress path shows a cyclic mobility, the stress–strain relations in the laboratory show a continuous increase of the axial strain, especially in the extension side. No convergence in the stress–strain relations can be seen, and the calculated stress–strain relation becomes closed loops. The material parameters for the (relative) stress ratios, $\overline{m}$, $\overline{m}_b$, m_s and m_d, are constant for simplicity in this study, though these parameters are functions of the loading direction in the original model, i.e. anisotropy in the shape of the yield surface and the rotation limit are considered in the original model, but they are eliminated in this study. With the original model, as these parameters will be smaller on the extension side than on the compression side, i.e. the slopes of the failure line and the phase transformation line on the extension side become small, the accumulation of the axial strain on the extension side will be accelerated. Some differences can be seen in the stress–strain relations between the calculated and the laboratory test results, although the calculated stress paths are similar to those in the laboratory.

In order to examine the undrained behavior of the sand in the numerical analyses, simulations of the cyclic triaxial tests were conducted. In the calculations, it was assumed that the sample was isotropically or anisotropically consolidated under a mean confining pressure of 98kPa, and then a cyclic axial stress was applied to the sample. Calculated stress paths and stress–strain relations together with movements of the similarity center and the vertex of the normal yield surface are illustrated in Figs. 5.5 and 5.7, where $p \equiv -\sigma_m$ and $\varepsilon_q \equiv -2(\varepsilon_a - \varepsilon_r)/3$. Variation of the internal variables F, R, and β_q are also shown in Figs. 5.6 and 5.8, together with the stress ratio, q/p, where β_q is the axial component of β.

In all the cases, the isotropic hardening/softening function, F, gradually increases, while the ratio of the size of the subloading surface to that of the normal yield surface, R, decreases before the stress path crosses the shear boundary surface that corresponds to the phase transformation line. However, once the stress path crosses the shear boundary surface, F decreases suddenly and β and R show large

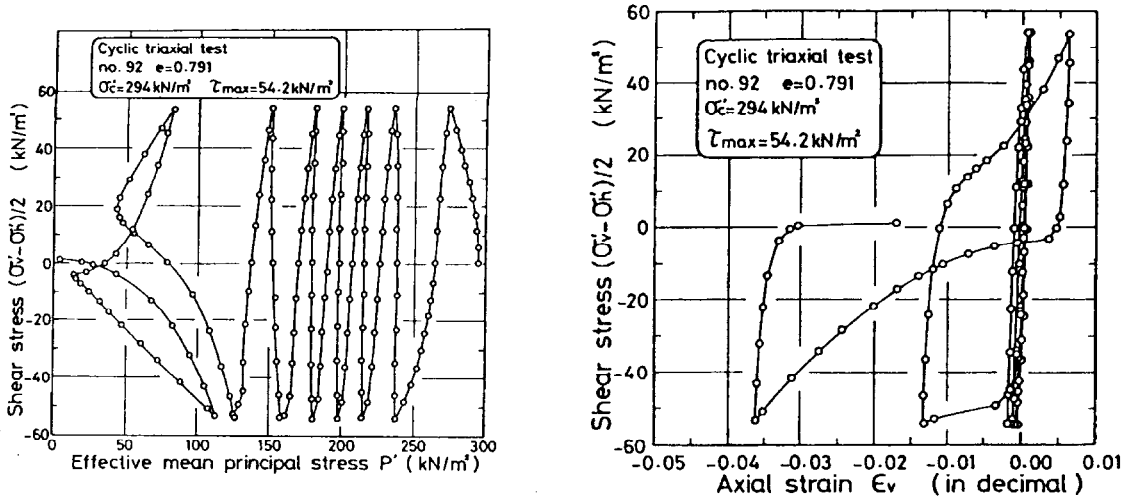

Figure 5.3: Typical stress path and stress–strain relation in undrained cyclic triaxial test for isotropically consolidated sand in laboratory (Towhata, 1981).

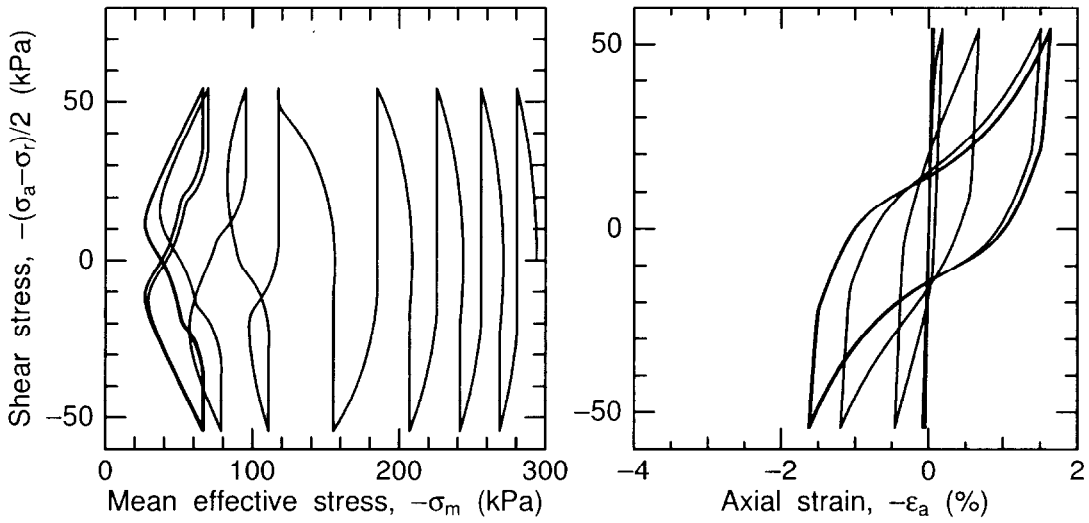

Figure 5.4: Typical stress path and stress–strain relation in undrained cyclic triaxial test for isotropically consolidated sand in calculation.

fluctuations. In other words, once the stress path crosses the phase transformation line, the cyclic mobility occurs along with the rotation hardening and the expansion/contraction of the subloading surface. Turning to the stress–strain relation, though the calculated stress–strain relations become closed loops for the isotropically consolidated sample, the residual shear strain is accumulated with cycle loading for the anisotropic consolidation, when the cyclic mobility occurs.

Sensitivity of material parameters

The user of the constitutive model has to determine the material parameters to fit the element tests by trial and error when he/she wants to solve a particular initial/boundary value problem. In this subsection, the sensitivity of each parameter on the soil behavior was examined one by one. In the

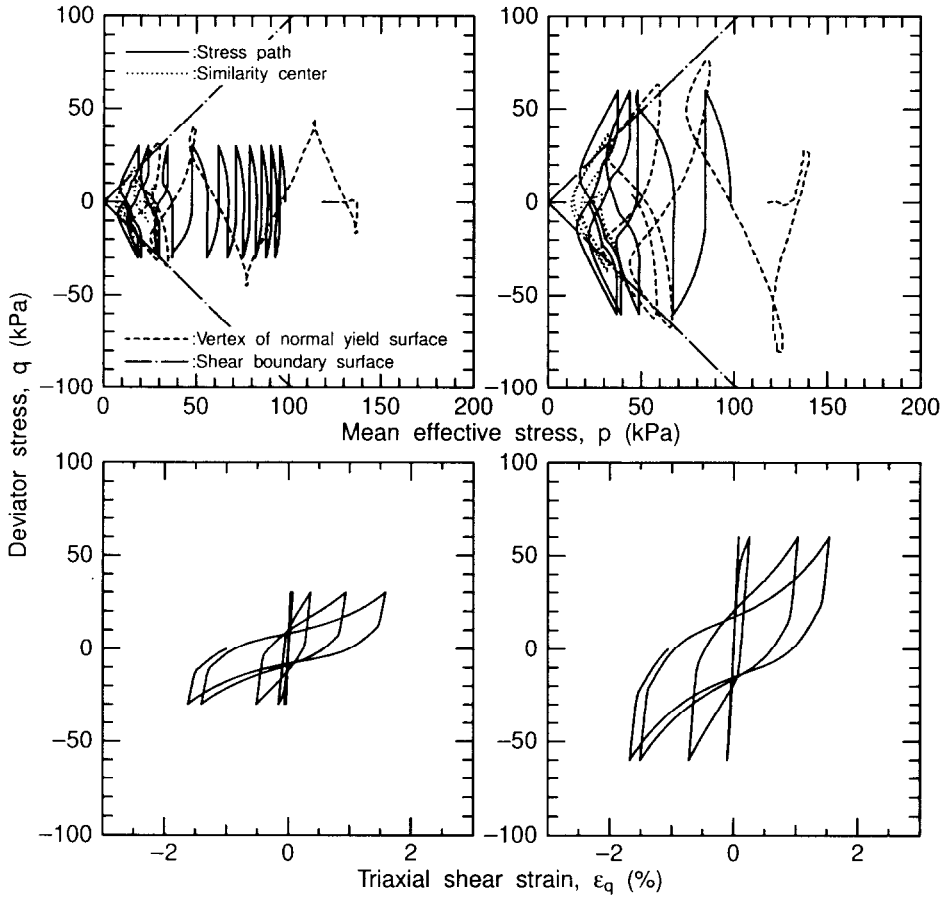

Figure 5.5: Typical stress paths and stress–strain relations in undrained cyclic triaxial test for isotropically consolidated sample together with movements of similarity center and vertex of normal yield surface.

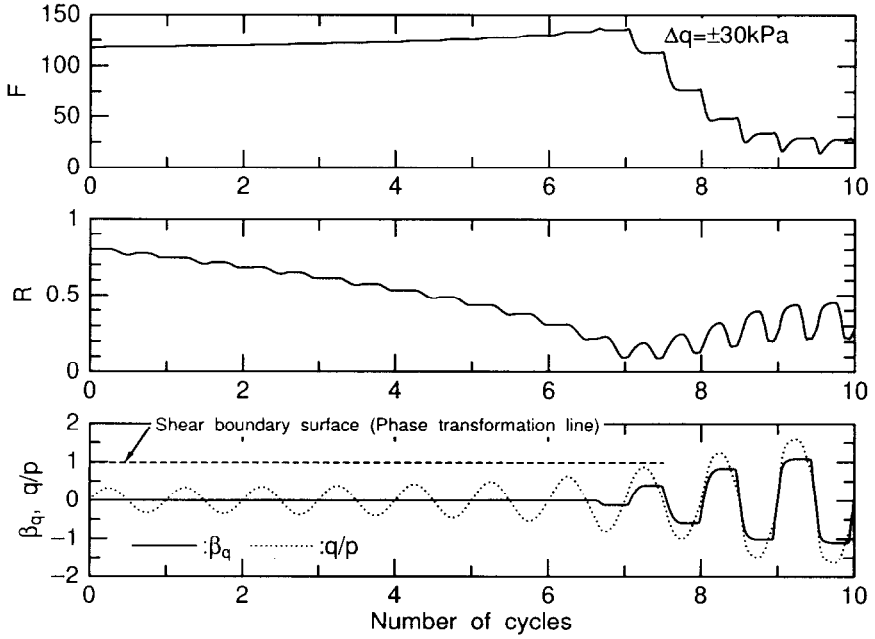

Figure 5.6: Variations of internal variable; F, R and β_q together with stress ratio, q/p for isotropically consolidated sample.

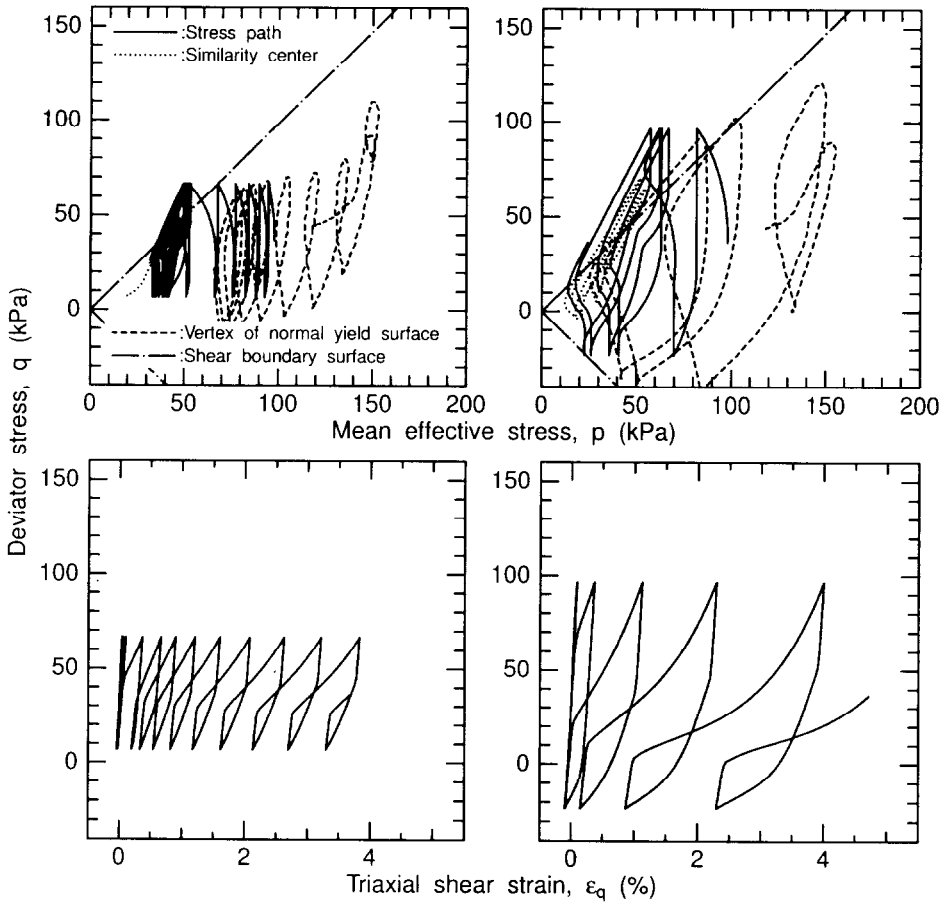

Figure 5.7: Typical stress paths and stress–strain relations in undrained cyclic triaxial test for anisotropically consolidated (K_0=0.7) sample together with movements of similarity center and vertex of normal yield surface.

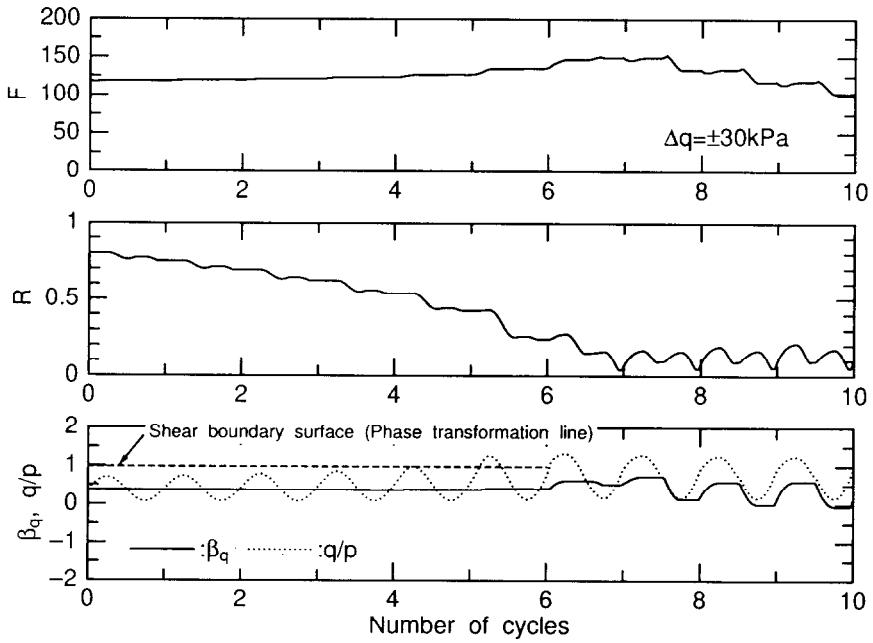

Figure 5.8: Variations of internal variable; F, R and β_q together with stress ratio, q/p for anisotropically consolidated (K_0=0.7) sample.

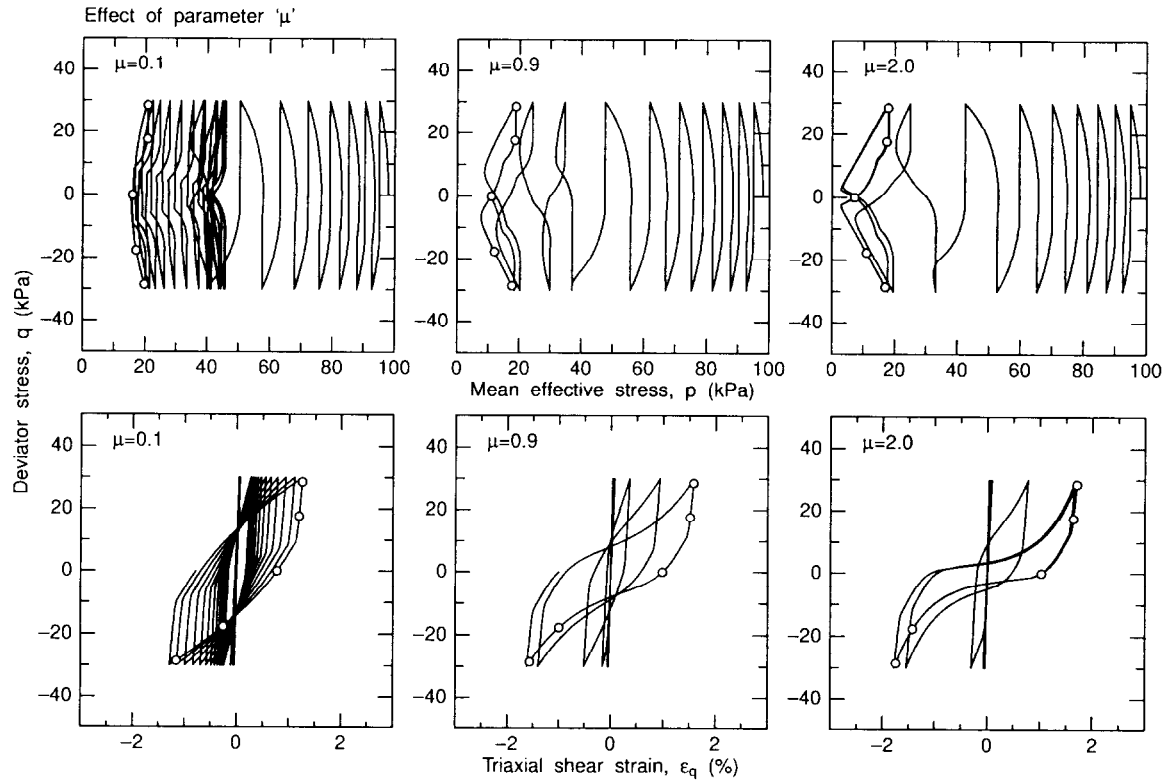

(a) Stress paths and stress–strain relations.

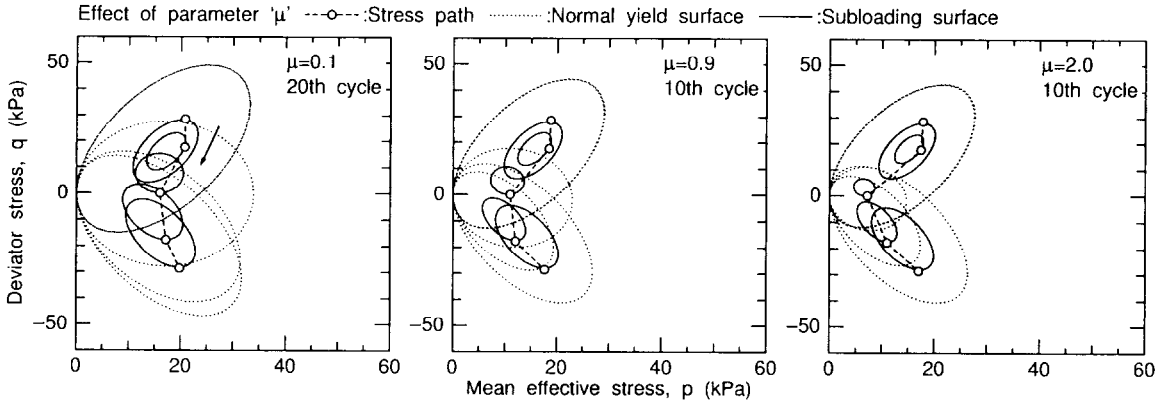

(b) Stress paths and movements of normal yield surface and subloading surface.

Figure 5.9: 'μ' variation effect on behavior of isotropically consolidated soil in undrained cyclic triaxial test.

calculations, it was assumed that the sample is isotropically/anisotropically consolidated under a mean confining pressure of 98kPa, and then a cyclic axial stress of Δq=±30kPa was applied to the sample under the undrained condition.

(1) Isotropic hardening/softening; μ (Fig. 5.9)

The parameter μ is the weighting factor for the contribution of the plastic shear strain to the isotropic hardening/softening of the soil. As the isotropic hardening/softening of clay is induced by the de-

crease/increase of plastic volumetric strain, the parameter μ is always naught in the constitutive models for clay, e.g. Cam-clay model and Sekiguchi-Ohta model.

In the case of larger μ, i.e. when the isotropic hardening/softening largely depends on the plastic shear strain, the stress–strain relation shows rapid hardening and softening, and the stress path approaches the origin of the stress space when the cyclic mobility occurs. As a result, the larger μ makes the stress–strain relation sharper and the hysteretic damping smaller. However, an arbitrary positive value does not apply to μ: the soil does not reach failure, and the deviator stress increases without limit when the value of the parameter μ is not lower than one, though no calculated result is shown here.

(2) Ratio of size of the subloading surface to that of the normal yield surface; u_1 (Fig. 5.10) and movement of similarity center of the normal yield surface and the subloading surface; c (Fig. 5.11)

The parameters u_1 and c basically affect the shape of the stress–strain relation of the soil once the stress path crosses the phase transformation line. As a smaller u_1 makes smaller the time derivative of the ratio of the size of the subloading surface to that of the normal yield surface, $\dot{R}$, the subloading surface becomes smaller, and it makes the closer approach of the stress path to the origin of the stress space easier when the cyclic mobility occurs.

A larger c makes the velocity of the similarity center of the surfaces, $\dot{\mathbf{s}}$, larger. With the larger c, the movement of the similarity center becomes relatively faster than the hardening and the rotation of the normal yield surface. As a result, the subloading surface becomes smaller, and it makes the closer approach of the stress path to the origin of the stress space easier, in a fashion similar to the smaller u_1.

The stress–strain relation comes to show rapid hardening/softening and smaller hysteretic damping when the parameter u_1 becomes larger or when the parameter c becomes smaller. As shown in the figures, remarkable differences in the parameter variation effects on the soil behavior cannot be seen between these two parameters for isotropically consolidated sand.

Figures 5.12 and 5.13 show the stress paths and the stress-strain relations for anisotropically consolidated sand (K_0=0.7). The accumulative rate of the residual shear strain was heavily influenced by variation of the parameter u_1, while clear differences cannot be seen in the stress-strain relations for the parameter c.

(3) Rotational hardening; b_r & ϕ_b (Figs. 5.14 & 5.15)

The parameters b_r and ϕ_b also affect the behavior of the subloading surface and the normal yield surface once the stress path crosses the phase transformation line. The stress–strain relation comes to show rapid hardening/softening and the smaller hysteretic damping when the parameters b_r and ϕ_b become smaller. For the anisotropically consolidated sand, the accumulative rate of the residual shear strain increases as b_r and ϕ_b decrease, as shown in Figs. 5.16 and 5.17. These parameter variation effects are similar to that of the parameter u_1.

(4) Shape of the normal yield surface and the subloading surface; ϕ (Fig. 5.18)

With smaller ϕ, the development of the excess pore water pressure becomes faster before the cyclic mobility, and the stress path comes closer to the origin of the stress space during the cyclic mobility. In other words, the larger ϕ makes the liquefaction resistance larger.

The critical state surface cannot be explicitly determined, as the normal yield surface will rotate.

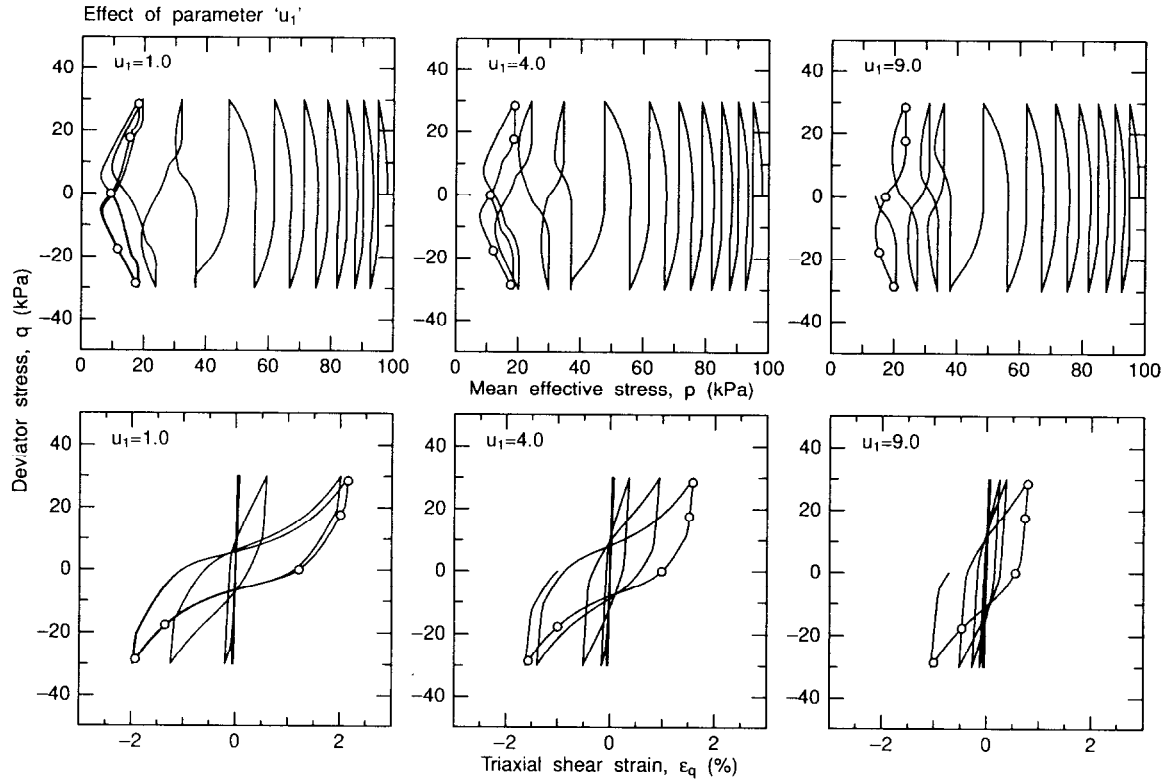

(a) Stress paths and stress–strain relations.

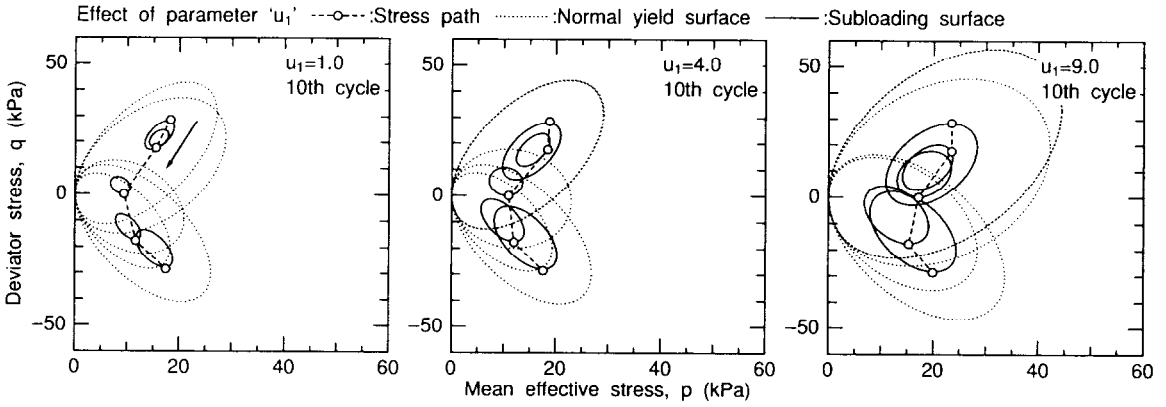

(b) Stress paths and movements of normal yield surface and subloading surface.

Figure 5.10: 'u_1' variation effect on behavior of isotropically consolidated soil in undrained cyclic triaxial test.

Since the critical state surface is a function of ϕ, the parameter ϕ should be carefully determined when the failure of the soil plays an important role in the structure performance evaluation.

(5) Initial location of the similarity center; s_0 (Fig. 5.19)

The stress paths and the stress–strain relations at the beginning of the cyclic loadings and during the cyclic mobility are essentially the same, irrespective of the initial location of the similarity center. However, immediately after the start of the normal yield surface rotation, the stress path rapidly ap-

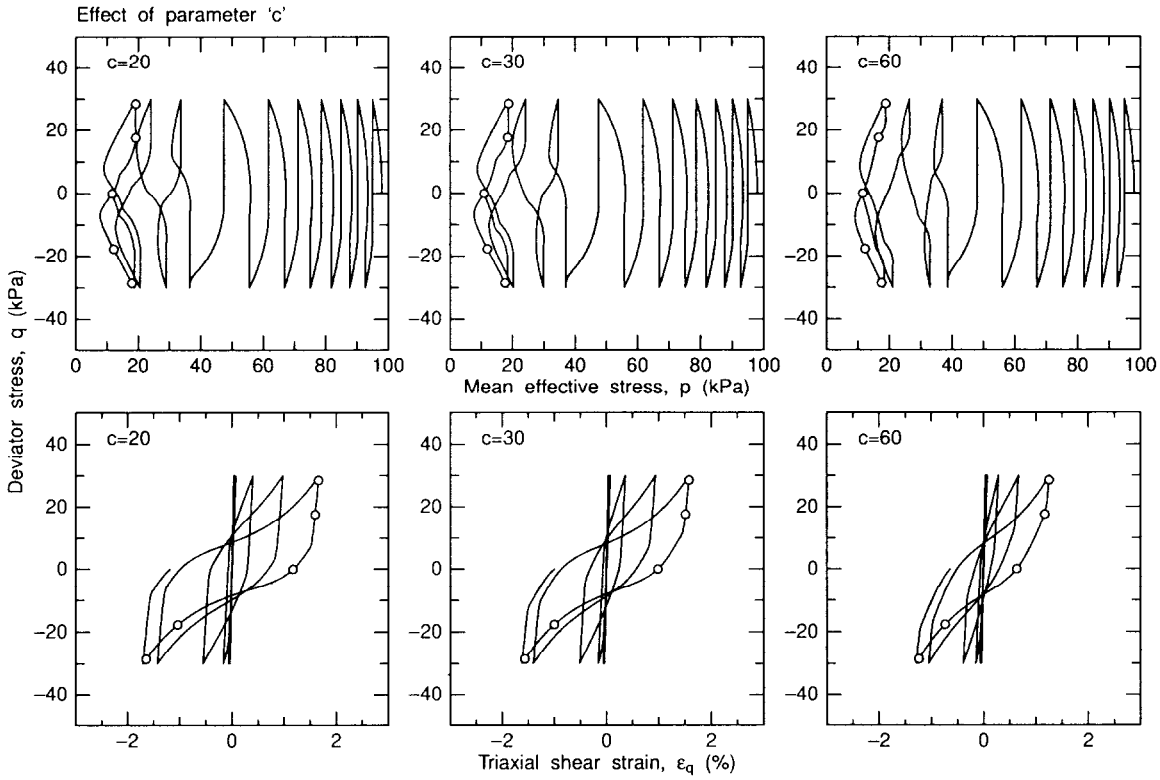

(a) Stress paths and stress–strain relations.

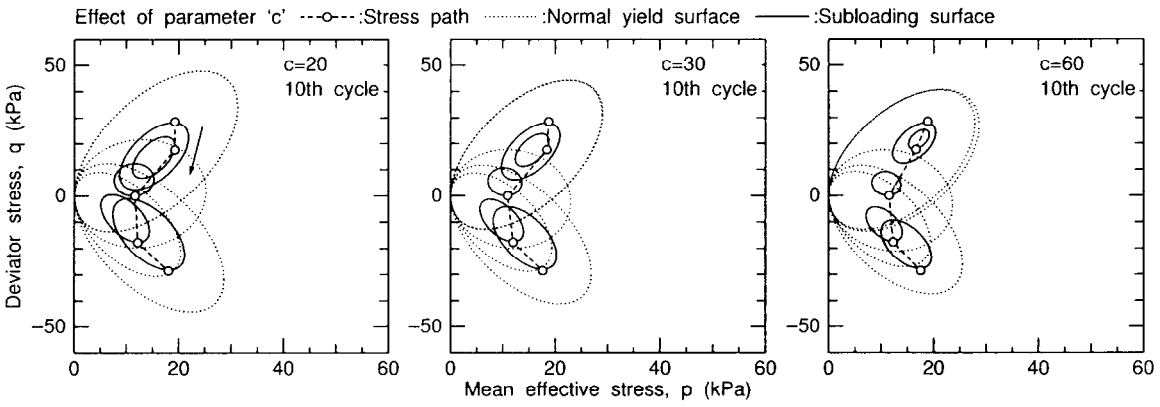

(b) Stress paths and movements of normal yield surface and subloading surface.

Figure 5.11: 'c' variation effect on behavior of isotropically consolidated soil in undrained cyclic triaxial test.

proaches the origin of the stress space in the case of the larger s_{ij0}/σ_{ij0}, while it gradually approaches the origin in the case of the smaller s_{ij0}/σ_{ij0}. As this parameter only affects development of the excess pore water pressure before the cyclic mobility, the initial location of the similarity center will be an appropriate parameter for fitting the liquefaction resistance to the laboratory test results.

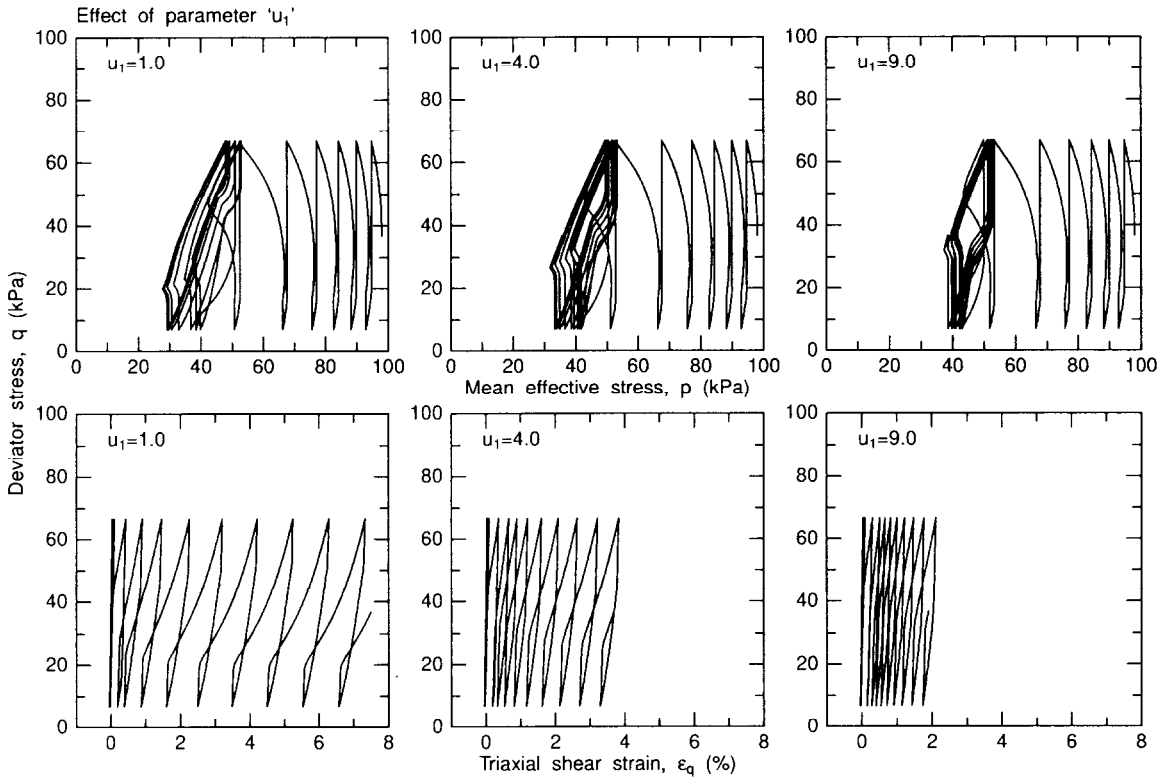

Figure 5.12: 'u_1' variation effect on behavior of anisotropically consolidated soil in undrained cyclic triaxial test (K_0=0.7).

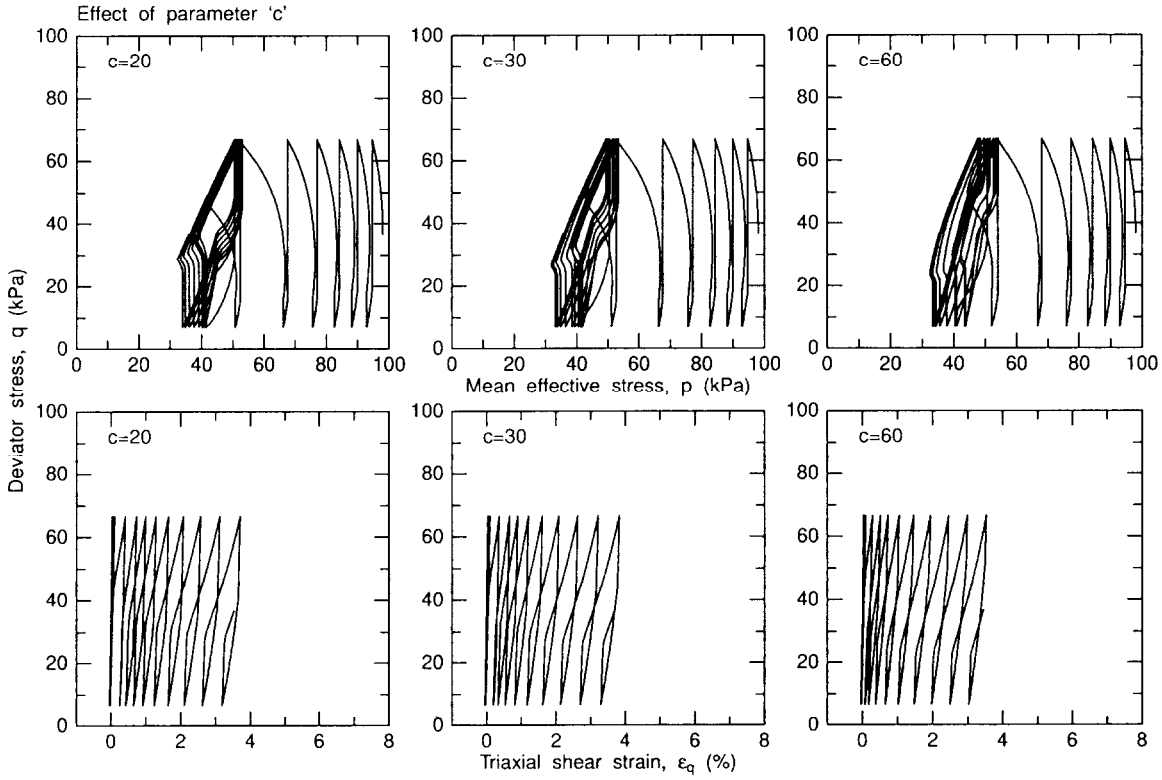

Figure 5.13: 'c' variation effect on behavior of anisotropically consolidated soil in undrained cyclic triaxial test (K_0=0.7).

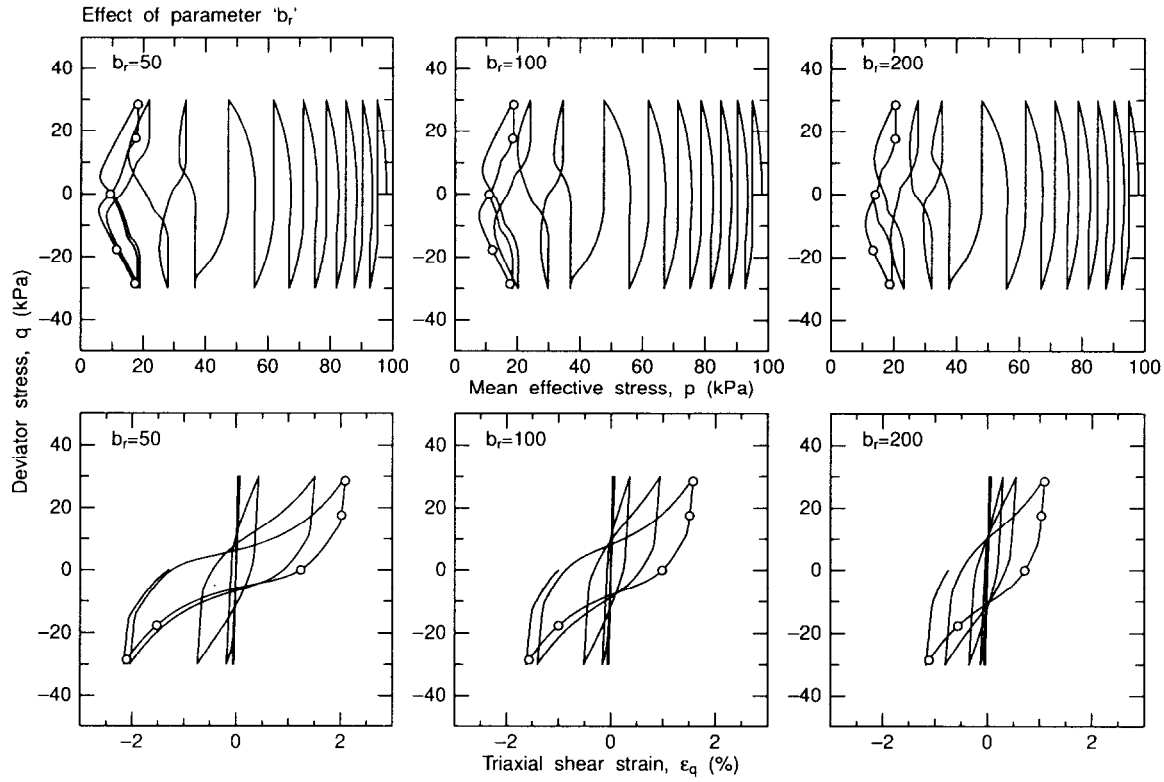

(a) Stress paths and stress–strain relations.

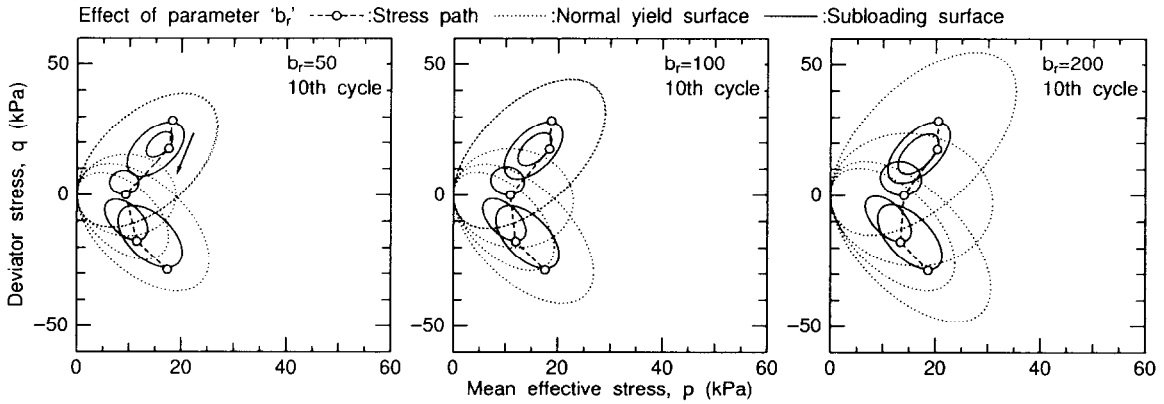

(b) Stress paths and movements of normal yield surface and subloading surface.

Figure 5.14: 'b_r' variation effect on behavior of isotropically consolidated soil in undrained cyclic triaxial test.

(6) Overconsolidation ratio; F_0 (Fig. 5.20)

At the beginning of the cyclic loadings, the parameter F increases, and the ratio of the size of the subloading surface to that of the normal yield surface, R, decreases with the cyclic loading as observed in the other cases. However, immediately after the start of the normal yield surface rotation, the stress path ceases to move toward the origin of the stress space. After certain duration, the stress path begins to approach the origin again. The overconsolidation ratio, $F_0/(-\sigma_{m0})$, influences the period of this

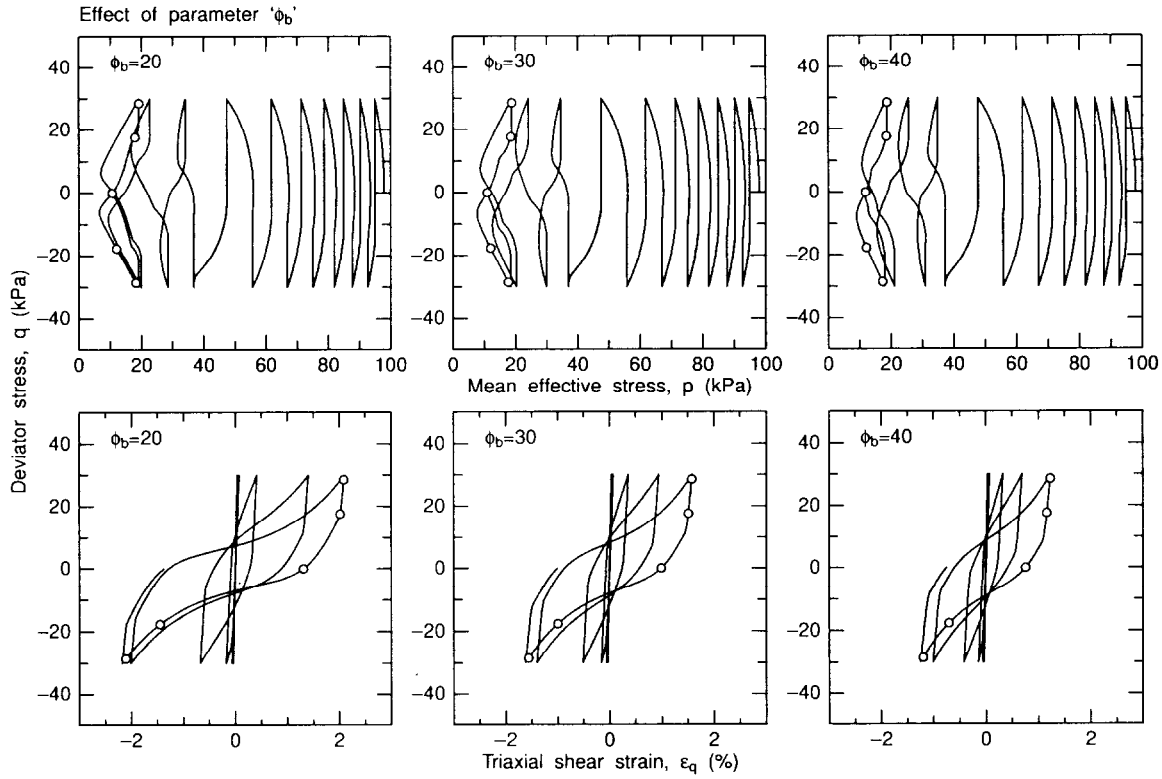

(a) Stress paths and stress–strain relations.

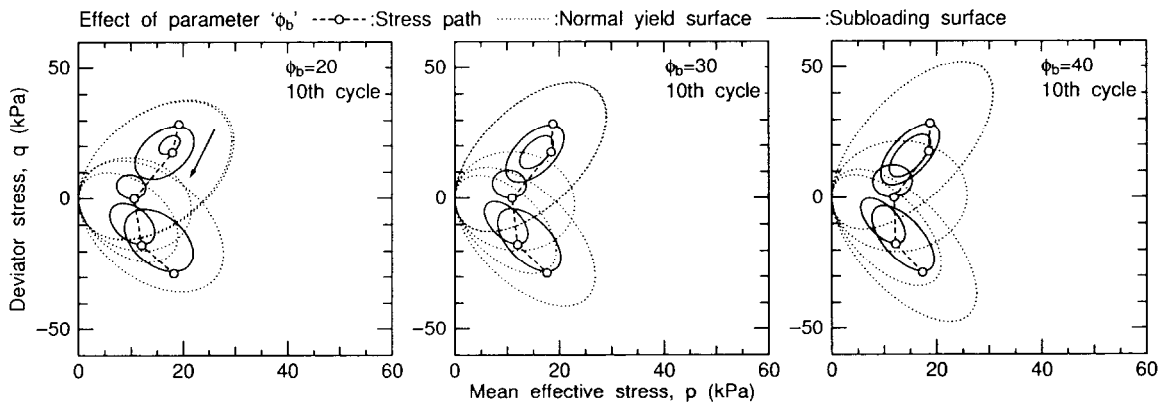

(b) Stress paths and movements of normal yield surface and subloading surface.

Figure 5.15: 'ϕ_b' variation effect on behavior of isotropically consolidated soil in undrained cyclic triaxial test.

delay as shown in the figure. Figure 5.21 shows the variation of the internal variables F, R, and β_q together with the stress ratio q/p. The period of this delay, e.g. about four cycles (6 to 12 cycle) for $F_0/(-\sigma_{m0})$=4, becomes larger as the overconsolidation ratio increases.

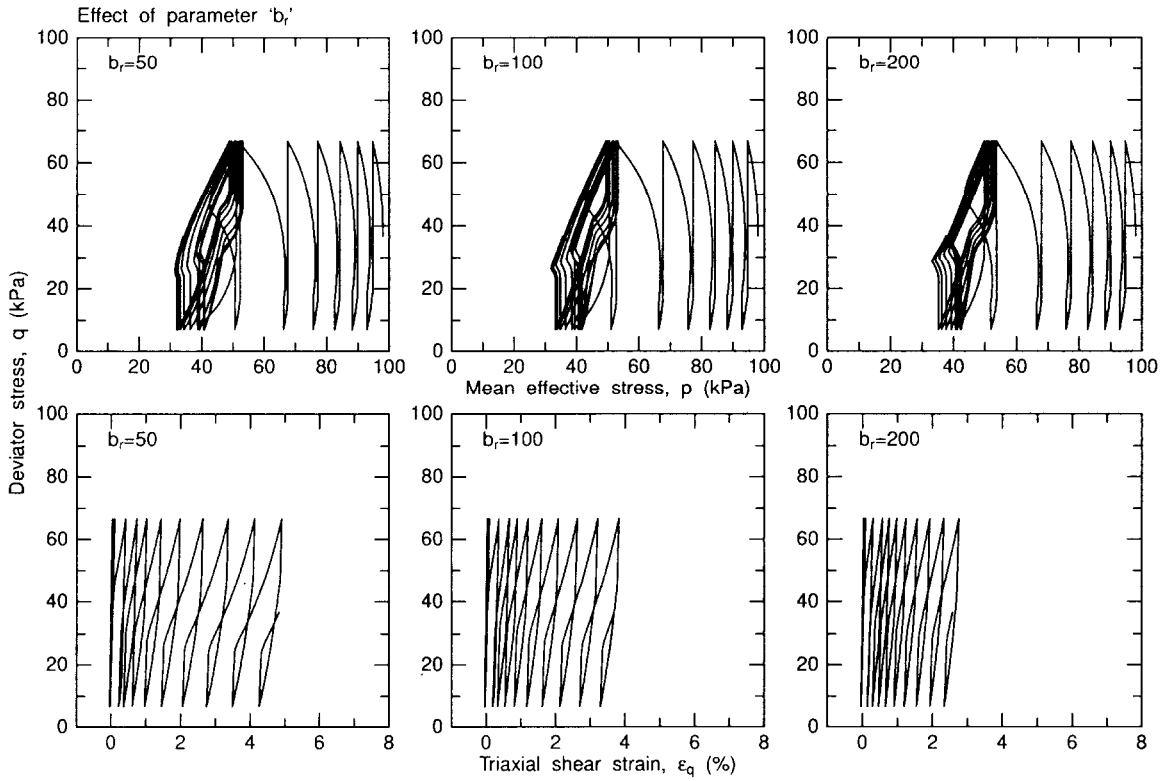

Figure 5.16: 'b_r' variation effect on behavior of anisotropically consolidated soil in undrained cyclic triaxial test (K_0=0.7).

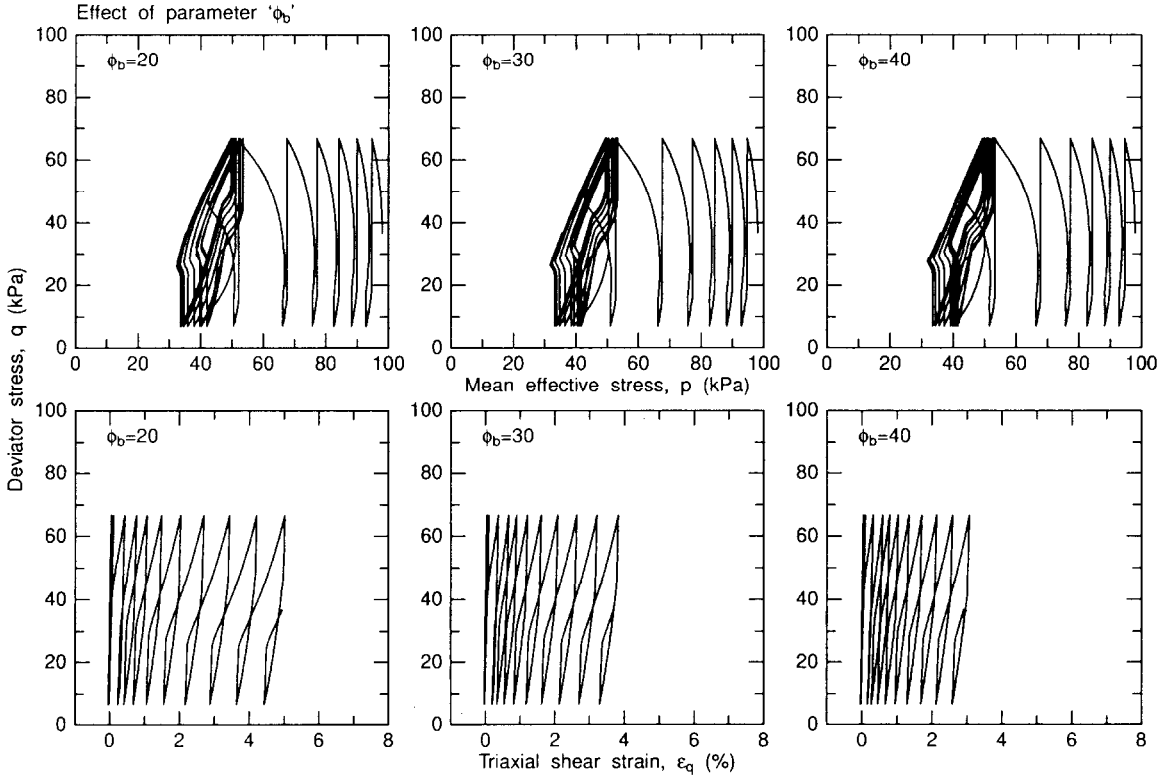

Figure 5.17: 'ϕ_b' variation effect on behavior of anisotropically consolidated soil in undrained cyclic triaxial test (K_0=0.7).

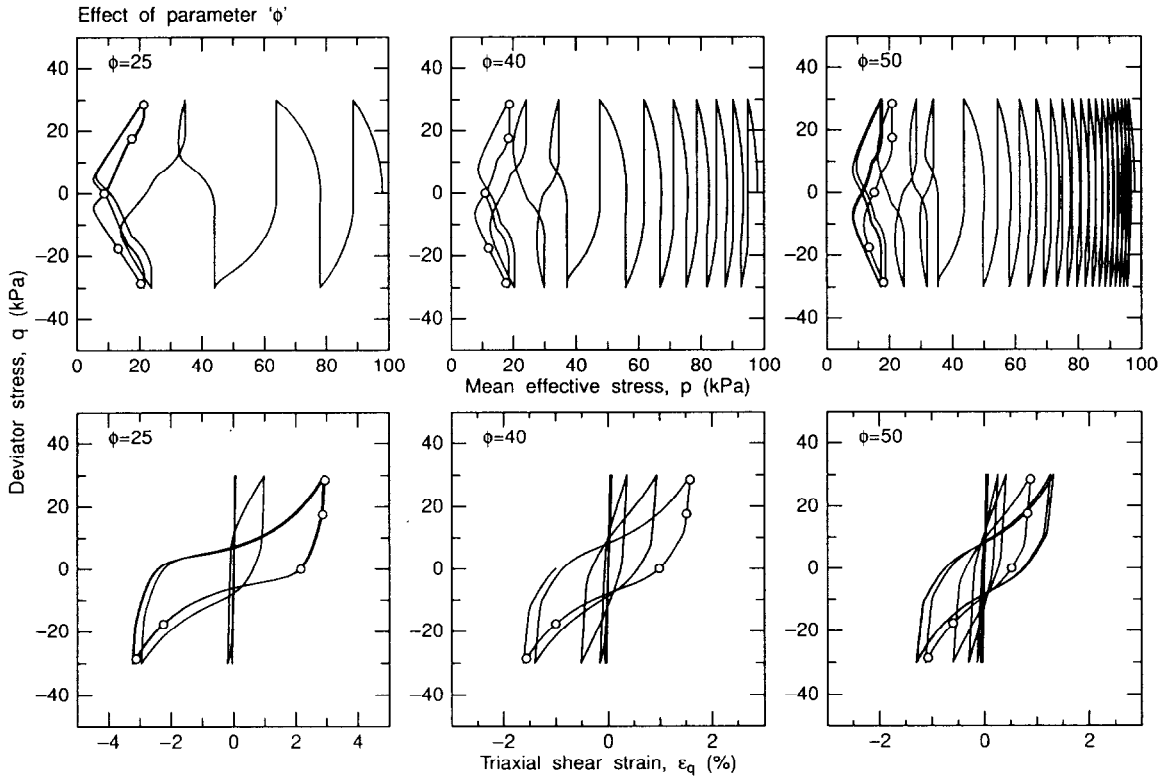

(a) Stress paths and stress–strain relations.

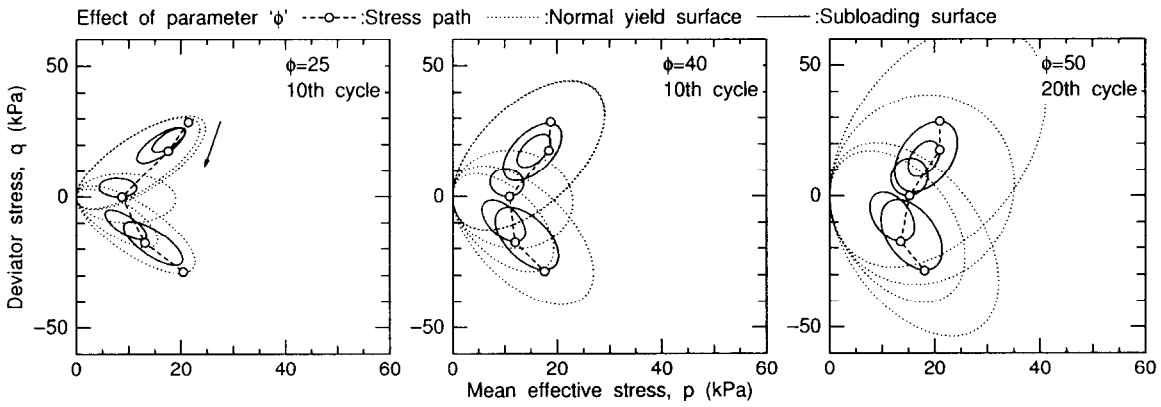

(b) Stress paths and movements of normal yield surface and subloading surface.

Figure 5.18: 'ϕ' variation effect on behavior of isotropically consolidated soil in undrained cyclic triaxial test.

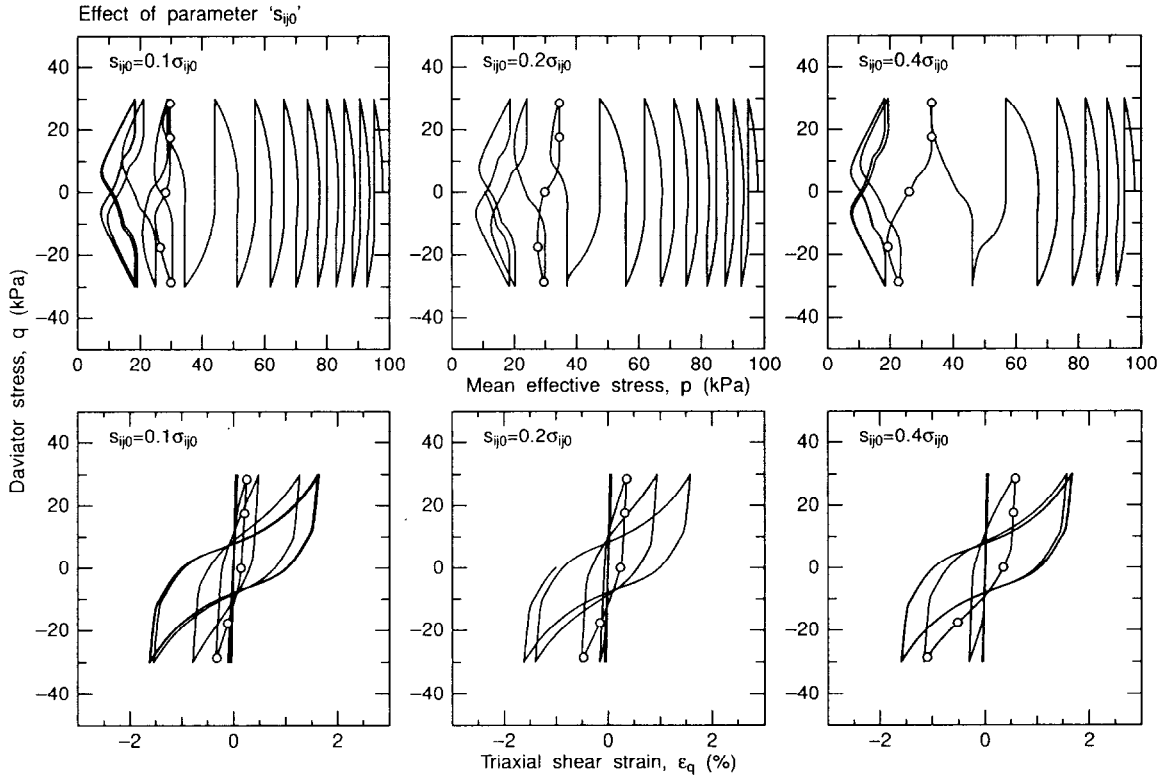

(a) Stress paths and stress–strain relations.

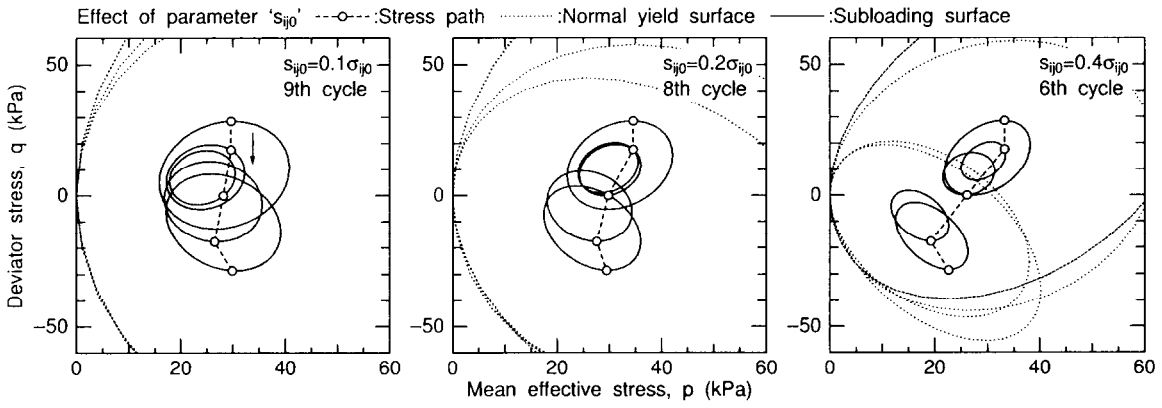

(b) Stress paths and movements of normal yield surface and subloading surface.

Figure 5.19: 's_0' variation effect on behavior of isotropically consolidated soil in undrained cyclic triaxial test.

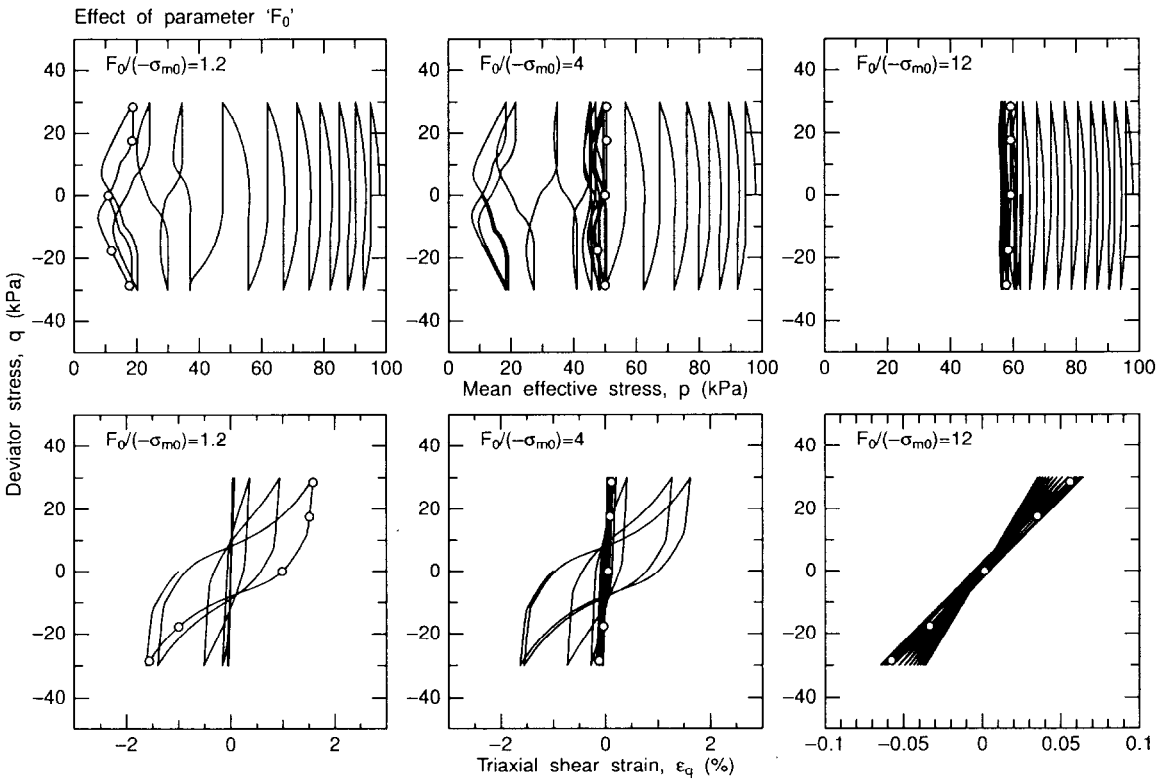

(a) Stress paths and stress–strain relations.

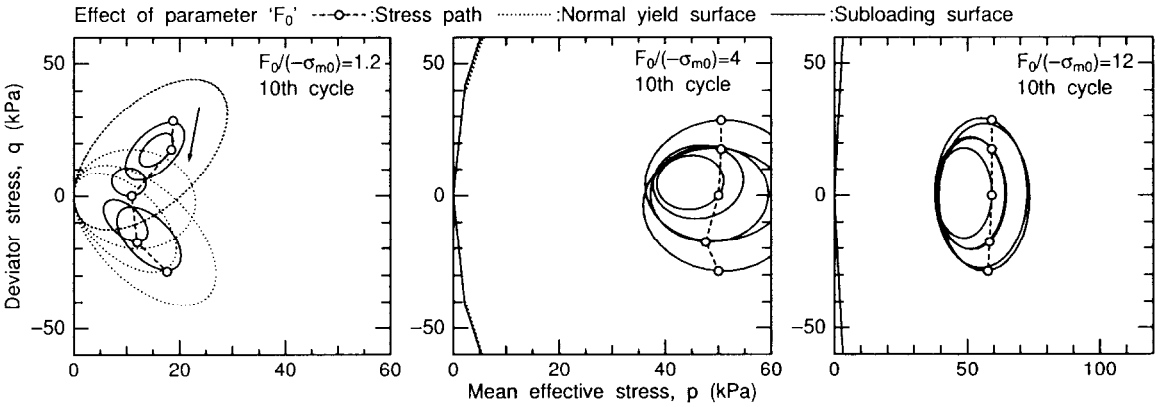

(b) Stress paths and movements of normal yield surface and subloading surface.

Figure 5.20: 'F_0' variation effect on behavior of isotropically consolidated soil in undrained cyclic triaxial test.

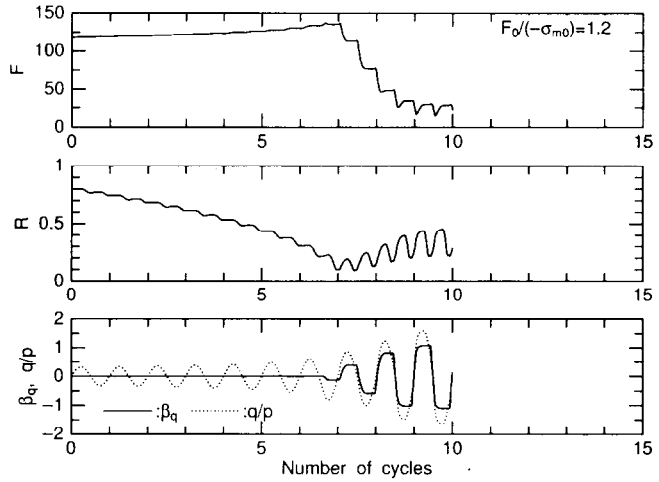

(a) $F_0/(-\sigma_{m0})$=1.2

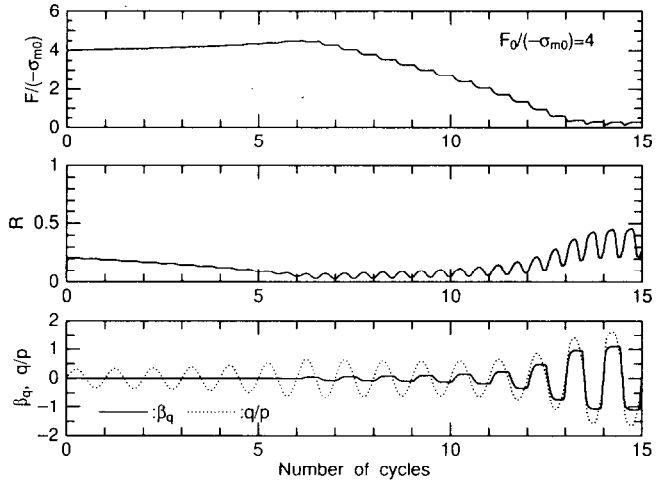

(b) $F_0/(-\sigma_{m0})$=4

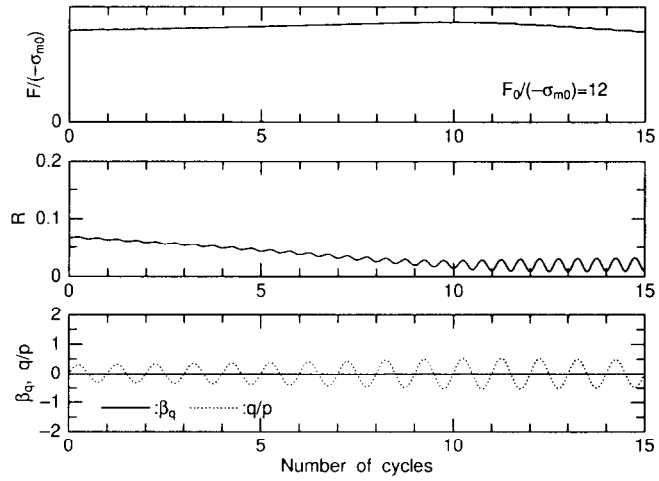

(c) $F_0/(-\sigma_{m0})$=12

Figure 5.21: 'F_0' variation effect on variations of internal variable; F, R and β_q.

5.4 Simulation of waterfront structure during earthquake by 2D FE analysis

A finite element analysis code has been newly developed based on the equations governing the dynamic porous solid–pore fluid interaction in u–p formulation incorporating the constitutive model proposed by Hashiguchi et al (1996, 1998), described in the previous sections. In order to examine the applicability of the numerical analysis code to liquefaction problems, a simulation of the centrifuge model test on the caisson type quay wall subjected to backfill liquefaction was conducted (Kuwano *et al.*, 1999, Takahashi, 2001).

5.4.1 Outline of physical and numerical model test

Centrifuge model test

The centrifuge used in the tests was the Tokyo Tech Mark II Centrifuge (Takemura *et al.* 1989, cf. Appendix A). An aluminum model container with inner sizes of 450mm in width 150mm in breadth, and 250mm in height was used. Rubber sheets were placed at both sides of the container to absorb stress waves from the side boundaries.

The model setup used in this study is shown in Fig. 5.22. The model caisson was 80mm in height, 150mm in depth, and 50mm in width and was put on a level ground of 80mm in height and 430mm in width. Toyoura sand, uniformly graded sub-angular quartz sand (D_{50}=0.19mm), was used for the model ground. The ground was prepared by air pluviation to achieve a relative density of 60%. The density of the model caisson was 2.1Mg/m^3. The model caisson had rough surfaces and earth pressure cells as shown in Fig. 5.23. Backfill sand was then placed behind the quay wall. The model did not include foundation rubble or stone backfill. Thin white Japanese noodles *somen*, on which black dots

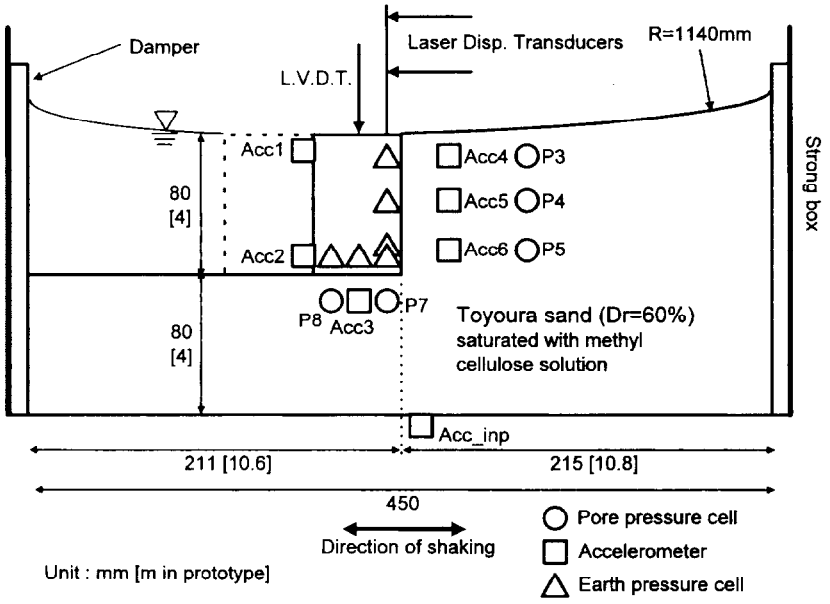

Figure 5.22: Model setup for centrifuge test.

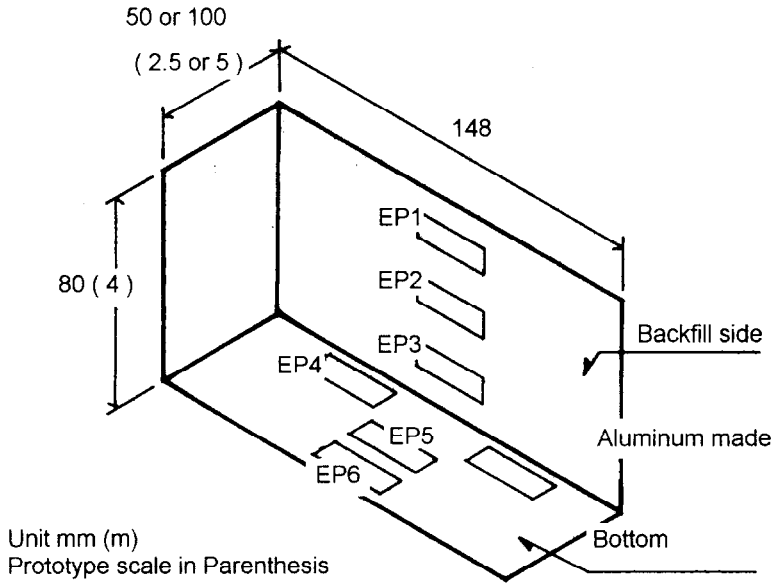

Figure 5.23: Detail of model caisson.

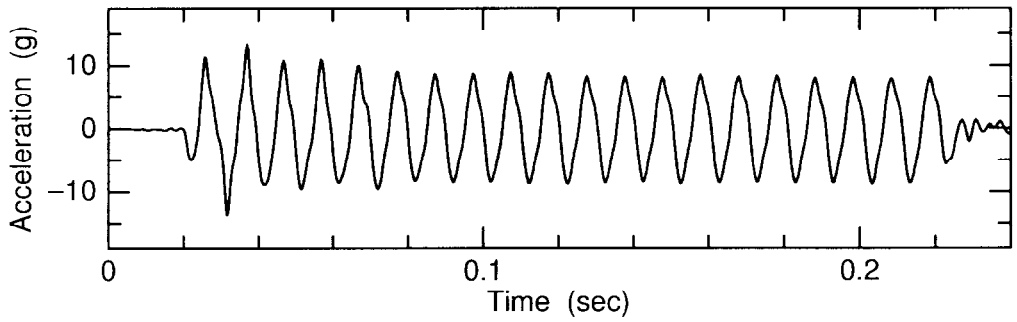

Figure 5.24: Input acceleration time history.

were marked, were placed between the ground and the front window to observe ground deformations. The model ground was saturated up to the ground surface with a methyl-cellulose-base solution with a viscosity of 50 cSt, 50 times higher than that of water. This solution was used as pore fluid to avoid conflict in scaling laws with the time on dynamic events and seepage (cf. Appendix B).

After the ground was saturated, the model was put in a centrifugal acceleration field of 50g. Shaking table tests were then performed. Twenty sinusoidal waves with amplitude 8.5g (165gal in the prototype) were applied to the bottom of the model. The input frequency was 100Hz, 2Hz in the prototype scale. The input acceleration record is shown in Figure 5.24. Earth pressures on the caisson as well as accelerations, displacements of the caisson, and pore pressures in the ground were monitored during the shaking. Permanent deformation of the ground was measured as the displacements of the

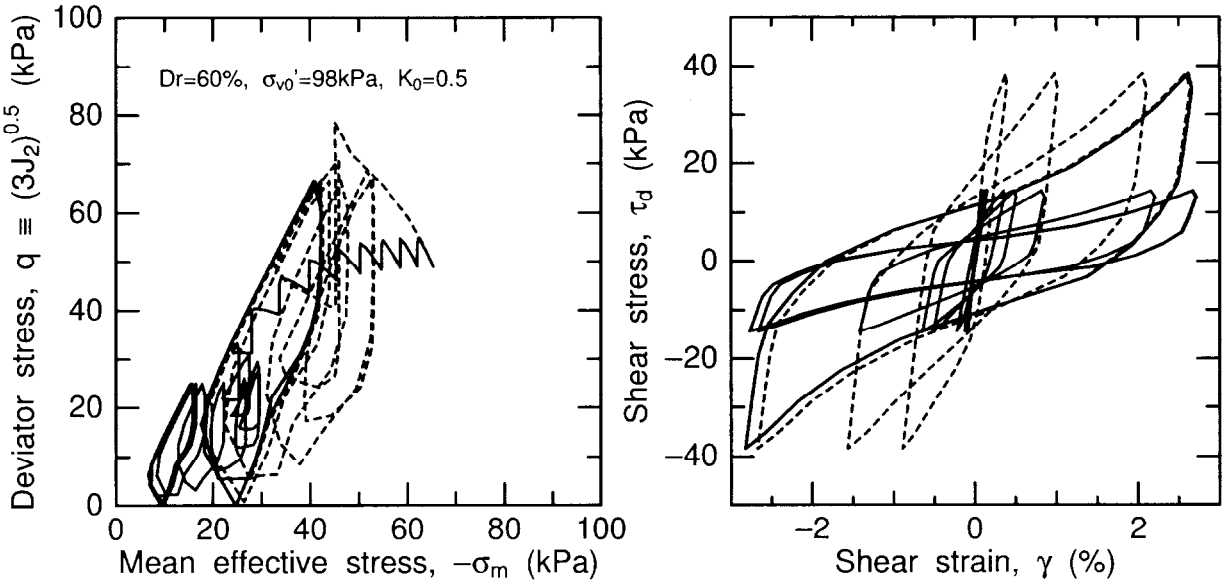

Figure 5.25: Calculated cyclic simple shear test results on Toyoura sand.

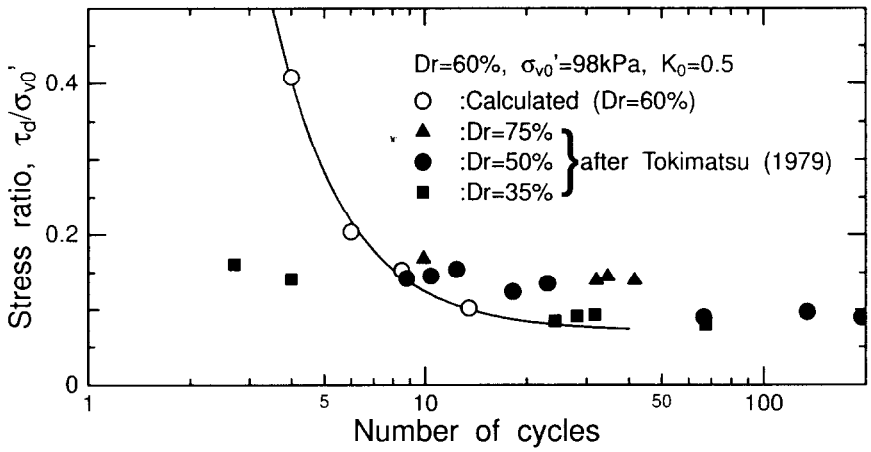

Figure 5.26: Liquefaction resistance curve for Toyoura sand.

markers after the shaking.

Numerical analysis

In order to numerically simulate the centrifuge model test, two dimensional finite element analyses were conducted under the plane strain condition. Geomaterial parameters used in the analysis are the same as the parameters used in the parametric study in the previous subsection. These material parameters are listed in Table 5.2. The hydraulic conductivity of the sand was 1.0×10^{-5}m/sec when the methylcellulose solution was used as pore fluid. Typical calculated cyclic simple shear test results and the liquefaction resistance curve are illustated in Figs. 5.25 and 5.26 respectively, where $q \equiv \sqrt{3J_2} = \sqrt{\frac{3}{2}(\sigma_{ij} - \delta_{ij}\sigma_{kk}/3)(\sigma_{ji} - \delta_{ji}\sigma_{kk}/3)}$. The liquefaction resistance curve is a relation between the ratio of the cyclic shear stress to the initial confining stress and the number of loading

cycles required to cause shear strain of 5% in the double amplitude in general. The liquefaction resistances plotted as filled marks in Fig. 5.26 were obtained by a ring torsion apparatus (Tokimatsu, 1979). Though the calculated liquefaction resistances at the smaller number of loading cycles are larger than those of the laboratory test results, the calculated curve is generally close to that obtained in the laboratory.

The size of an element was 10×10mm. Fluid flow velocities were set to zero at all the boundaries except at the surface of the ground. In order to take into account the fact that the horizontal movement of the soil was not allowed at the side boundaries in the centrifuge test, the horizontal displacements of the nodes at the side boundaries are fixed. In general, as the waves should appropriately be permitted to transmit from/to the analysis domain to/from the outside of the analysis domain in-situ, appropriate boundary conditions other than the fixed condition should be considered.

The applied earthquake motion was similar to the wave utilized in the centrifuge test. In order to obtain the numerical solution, the differential equations are integrated in time. The integration scheme used in time was Newmark's β method (cf. Appendix C), and the time step for the integration was Δt=0.00004sec. System damping was represented by Rayleigh damping, and the damping ratio was 1% in a first mode of free vibration of the system. The first vibration frequency of the system was 0.0066sec, 0.33sec in the prototype scale.

Before the dynamic response analysis, a static analysis was conducted to estimate the initial stress condition of the ground. Ideally, in-situ, the sedimentation process of the soil, the construction procedure, and previous earthquake records at the site should be taken into account in the static analysis to obtain the stress condition of the ground before earthquake. However, in the centrifuge model tests, it is very difficult to build the structures in-flight by the same manner as in actual construction. Therefore the structure and the ground surrounding the structure are first made on a laboratory floor under 1g field, and then centrifugation is applied to the model. In this study, a simple two-step loading of gravity was adopted in the static analysis to estimate the stress condition before the earthquake: In the first step, a stress analysis was conducted with the assumption that a deformation modulus of each soil is uniform irrespective of the confining pressure. Then, in the second step, the stress analysis was carried out with the stress-dependent deformation modulus using the stress condition obtained in the first step. In all the numerical analyses on the centrifuge model tests shown in this dissertation, the static analyses were conducted prior to the dynamic response analyses in this manner.

5.4.2 Numerical analysis result and discussions

Dynamic responses of the caisson and the ground

Figure 5.27 shows time histories of the acceleration of the caisson top, the pore water pressures in the backfill, and the earth pressures acting on the caisson in both the numerical analysis and the centrifuge model test. Solid lines represent the responses in the numerical analyses, and dotted lines represent the responses in the centrifuge model tests. The calculated acceleration record of the caisson measured at the top agrees with that in the centrifuge test not in amplitude but in phase, while the calculated pore and earth pressures are similar to those in the physical test. Even in the calculated pressures, an inconsistency is found in the earth pressure at the caisson top, i.e. the earth pressure at the top decreased with shaking in the calculation, while it gradually increased in the physical test.

This difference may be caused by a limitation in the numerical analysis. In the analysis, the caisson and the adjacent soil were perfectly connected, i.e. they shared the nodes at the interface,

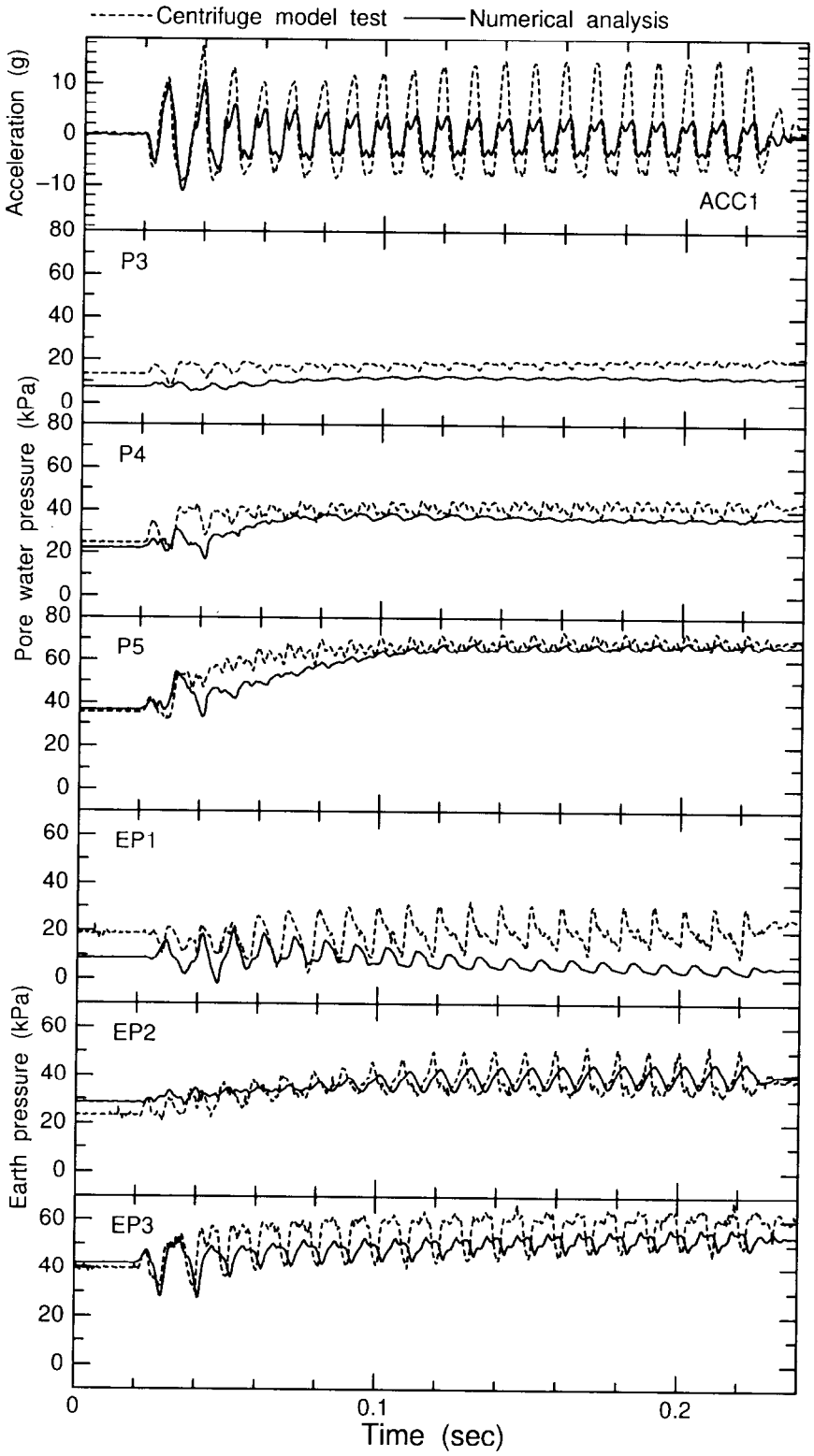

Figure 5.27: Variations of acceleration, pore water pressure and earth pressure for both numerical analysis and centrifuge model test.

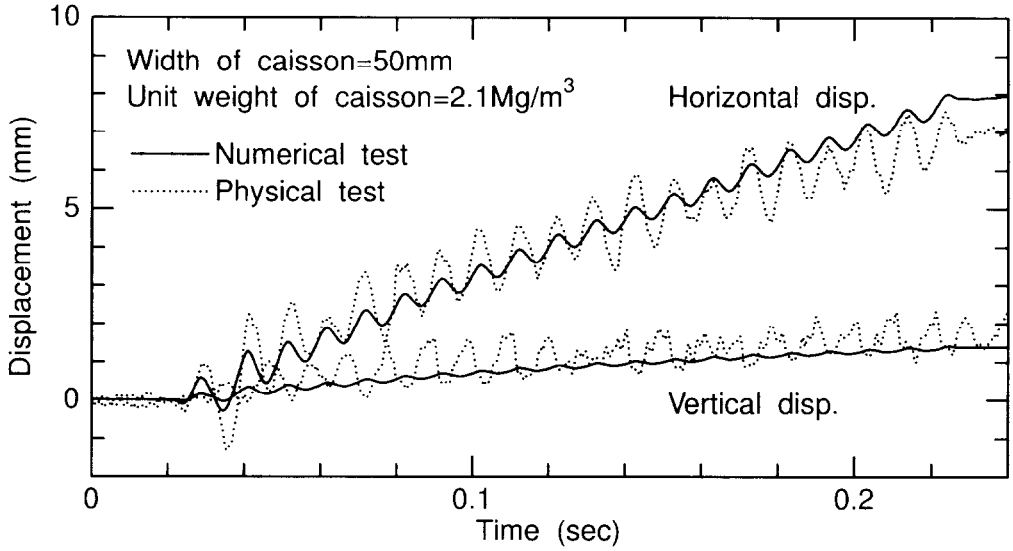

Figure 5.28: Time histories of displacement of caisson at the top.

thus a separation of the caisson and the adjacent soil was not allowed, while it was allowed in the physical model test. As the adjacent soil had to follow the movement of the caisson at all times in the numerical analysis, the soil element was dragged by the caisson when the caisson moved seawards, showing the negative earth pressure at the shallower portion. Although several joint elements have been proposed to simulate the separation between the elements, e.g. Goodman & Taylor (1968), Toki *et al.* (1982), Ohnishi & Ohtsu (1982) & Yoshida (1993), and though some of them in consideration of the fluid flow between the elements (Ohnishi & Ohtsu, 1982; Yoshida, 1993), there is no joint element which considers the fluid flow in both the interface direction and the direction perpendicular to the interface. Thus no joint element was adopted in the interface between the structure and the soil in this study.

Permanent displacements of the caisson and the ground

Time histories of the horizontal and vertical displacements of the caisson at the top for the numerical analysis and the centrifuge model test are shown in Fig. 5.28. The displacements increased almost linearly with time in both the horizontal and the vertical directions. Calculated results were very close to the centrifuge test results, though the calculated amplitudes of the displacement oscillations were smaller than those in the model tests. This tendency is consistent with the acceleration response of the caisson.

Figure 5.29 shows the permanent deformations of the model ground for the numerical analysis and the centrifuge model test. The ground deformation in the physical tests was obtained by measuring the displacements of the noodle targets placed between the ground and the front window by comparing photographs taken before and after the shaking. Deformation patterns were seen to be essentially the same in both the physical and the numerical model tests.

Permanent horizontal and vertical displacements of the ground surface are illustrated in Fig. 5.30. The displacements for the centrifuge test were obtained from the displacements of the noodle targets at shallow depth. Some inconsistencies can be found between the numerical and the physical model

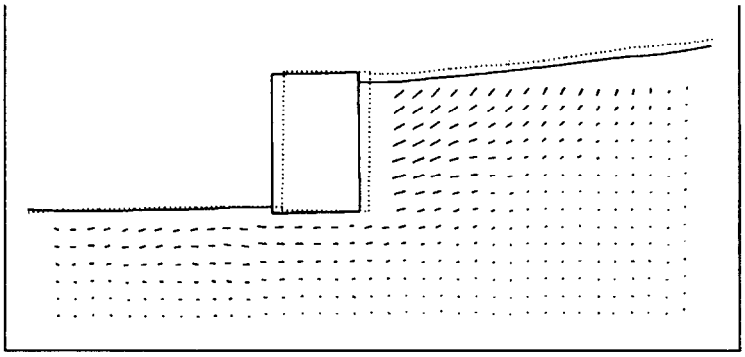

(a) Physical model test

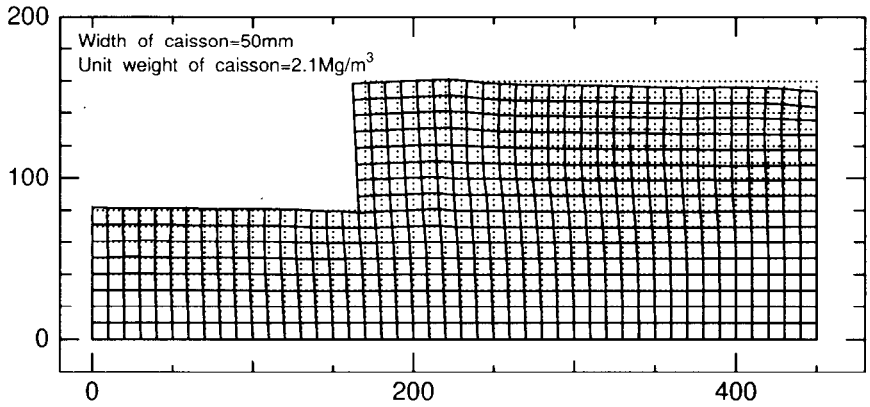

(b) Numerical model test

Figure 5.29: Permanent deformations of model ground.

tests: In the physical test the lateral displacement decreased with distance from the wall and became almost zero at a distance of 160mm, while in the numerical analysis the lateral deformation of the ground came to the side boundary. In the vertical direction, the settlement was almost constant in the physical test, while it was small near the caisson in the numerical analysis. These differences may be caused by the modeling limitation of the interface between the caisson and the adjacent soil as mentioned above and the boundary conditions at both the ends.

Applicability to liquefaction problem

In this section, two-dimensional analysis was conducted on the caisson type quay wall subjected to backfill liquefaction. The liquefaction observed in the targeted physical model test is categorized as 'no flow liquefaction.' Though some limitation and inconsistency are recognized in the comparison between the numerical analysis and the centrifuge model test, it can be concluded that the present procedure has fundamental applicability in the analysis of no flow liquefaction problems.

5.5 Summary

This chapter introduced the governing equations for dynamic porous solid–pore fluid interaction and the constitutive model proposed by Hashiguchi *et al.* (1996, 1998) which can describe the monotonic

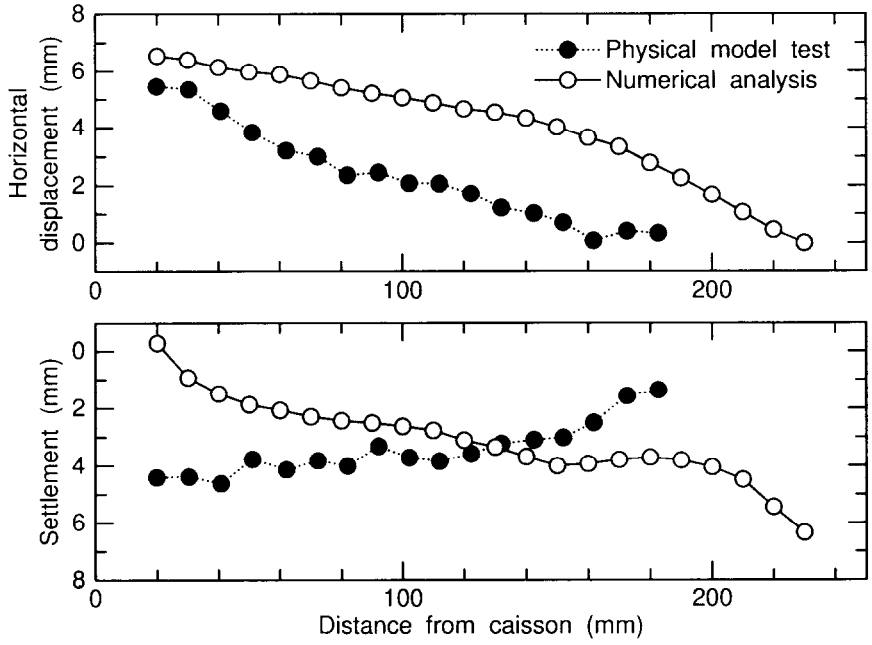

Figure 5.30: Permanent displacements of ground surface.

and cyclic loading behavior of sand including soil liquefaction behavior. The sensitivity of each parameter of the constitutive model on the soil behavior was examined one by one in order to understand how the variation of the parameters affects the soil behavior.

A new finite element analysis code has been developed based on the equations governing the dynamic porous solid–pore fluid interaction in u–p formulation incorporating the constitutive model proposed by Hashiguchi *et al.* (1996, 1998). In order to examine the applicability of the analysis code to the liquefaction problems, a simulation of the centrifuge model test on a caisson type quay wall subjected to backfill liquefaction was conducted. It was found that the present program has fundamental applicability in the analysis of no flow liquefaction problems, though some limitations and inconsistencies are recognized in comparing the numerical analysis and the centrifuge model test.

Chapter 6

Evaluation of soil–pile interaction in large soil movement

6.1 Numerical modeling of soil–pile interaction in 3D FE analysis

Several approaches have been developed for evaluating soil–pile interactions during earthquakes. These approaches yield procedures ranging from simple to complicated. One of the simple methods is the framed structure analysis subjected to soil movements through soil–pile interaction springs. In this method, the soil–pile interaction is modeled using non-linear *p–y* springs. Three-dimensional effects of soil–pile interactions are usually involved in the *p–y* relations. On the other hand, the most complicated but accurate method is the three-dimensional finite element analysis that is capable of soil–structure coupled analysis, though there are still difficulties in modeling the pile and soil–structure interface.

Confining the modeling of the three-dimensional finite element analysis on the restriction that the soils were modeled by solid elements, four types of the pile modeling method can be listed as shown in Table 6.1. The easiest method models the pile foundation with solid elements (e.g. Kimura *et al.*, 1991; Wakai *et al.*, 1997). Since the accurate stress of a section of the pile can only be obtained at the integration points of the solid element, the solid element of the pile must be finely divided into elements when the evaluation of the bending of the pile is a main concern of the analysis. On the other hand, when the pile is modeled by beam elements, the bending of the pile can be simulated in the ordinary course of events. However, the diameter of the pile cannot be considered, as the beam element does not have physical diameter. In the analysis of building foundations, since the diameters of the pile are relatively smaller than those of the massive infrastructure facilities, some analyses have succeeded only with beam elements for the pile (e.g. Fukutake *et al.*, 1993; Fujii *et al.*, 1998).

Still, proper measures are needed to overcome these problems. Zhang *et al.* (2000) have proposed to use a hybrid element that consists of both beam and solid elements for the pile modeling as shown in Fig. 6.1(a). The beam element bears most of the force acting on the pile, while the neighboring solid elements bear less and exist as measures of the diameter effects. A flexural rigidity, EI, and an axial stiffness, EA, of the pile can be decomposed as follows;

$$EI = E'I_{beam} + E'I_{solid} \tag{6.1}$$

Table 6.1: Pile modeling methods for three-dimensional finite element analyis.

Pile	Advantage	Limitation	Advocates
Solid elements	Easy implementation	Low accuracy in pile bending	Many researchers e.g. Kimura *et al.* (1991), Wakai *et al.* (1997)
Beam elements	Easy implementation	No size effect of pile	Many researchers e.g. Fukutake *et al.* (1993), Fujii *et al.* (1998)
Solid elements + Beam elements	Pile size effect can be considered.	Difficulties in implementation of non-linear behavior	e.g. Zhang *et al.* (2000)
Shell elements	Most accurate for steel pipe pile	Huge number of freedoms	Very few or Nobody

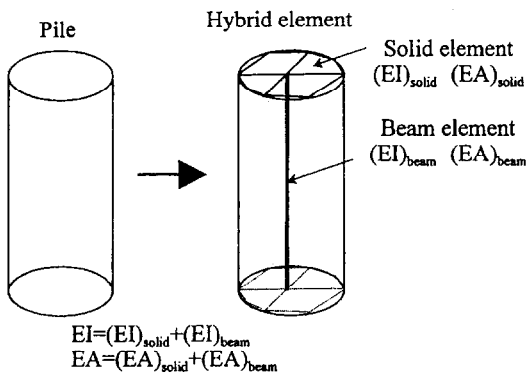

(a) Schematic view of hybrid element.

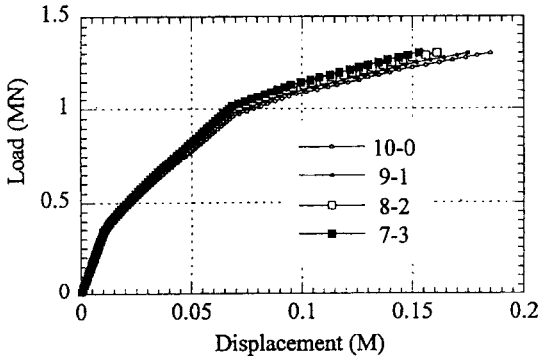

(b) Load–displacement relations for I_{beam} : I_{solid}=10:0, 9:1, 8:2 & 7:3.

Figure 6.1: Hybrid element that consists of beam and solid elements for pile modeling and load–displacement relations for cantilever (after Zhang *et al.*, 2000).

$$EA = E'A_{beam} + E'A_{solid} \tag{6.2}$$

where E is the Young's modulus, I is the moment of inertia and A is the area of the pile section. EI and EA are given and I_{solid} and A_{solid} depend on the section of the pile, i.e. $I_{solid} = I$ and $A_{solid} = A$, when the uniform pile section is assumed. Thus, E' and A_{beam} can be written as

$$E' = \frac{1}{I_{beam}/I_{solid} + 1} E \tag{6.3}$$

$$A_{beam} = \frac{I_{beam}}{I_{solid}} A. \tag{6.4}$$

Figure 6.1(b) illustrates the relationships between load and displacement for a cantilever modeled by their hybrid elements subjected to a lateral load at the top. According to the relations shown in

the figure, the modeling method is seen to perform well in the air, and Zhang *et al.* concluded that $I_{beam}/I_{solid}=9$ is better for the analysis. However, if $I_{beam}/I_{solid}=9$, the solid element surrounding the beam element becomes relatively soft, and it may affect the behavior of the soil surrounding the pile since the pile is generally embedded into the ground and the earth pressure acts on the pile. Moreover, there are several difficulties in the implementation of the non-linear models for the beam element to the hybrid element, as the behavior of the solid elements part must be associated with that of the beam element part.

The most complicated method models the pile foundation with shell elements. This method has the possibility of accurately modeling the steel pipe pile including the local buckling. However, since the number of the freedoms in the analysis becomes huge, this method has seldom or never been applied to the non-linear FE analysis for the liquefaction problem.

The methods listed here each have advantages and limitations. In the next section, simple but sufficient methods will be presented for modeling piles subjected to large soil movement.

6.2 Modeling of pile and soil–pile interface

In simulating pile behavior, the volumetric effects of the pile on the soil–pile interaction must be considered. In this study, for ease of implementation of the non-linear behavior of the pile, the beam element was used for the pile. Considering the diameter of the pile, empty space is inserted between the solids and the beam elements for the pile. The nodes of the beam element for the pile and the solid elements for the adjacent soil are connected as follows:

For a pile whose surface is assumed to be rough, e.g. a cast in place pile, the nodes of the adjacent soil elements and those of the pile are tied to each other at each depth, i.e. the displacement of the nodes of the soil surrounding the pile is the same as that of the pile at each depth, as shown in Figs. 6.2(a) and 6.3(a). As a result, the nodes of the soil adjacent to the pile at the soil–pile interface perfectly attain the movement of the pile and the pile behaves as a rough pile. For the sake of convenience, let us refer to the pile modeled by this method as the pile *without slippage*, as there is no relative displacement between the nodes of the adjacent soil elements and those of the pile.

Meanwhile, for the pile whose surface is assumed to be smooth, e.g. the steel pipe pile, *radial spokes* made of truss elements connecting the beam elements and the solid elements surrounding the beam are introduced to model the soil–pile connection as shown in Fig. 6.2(b). Since an axial strain of the truss element implemented in ordinary FE analysis codes, including the code used in this study, is an infinitesimal strain, i.e. it is defined as the ratio of an elongation to an original length in the original truss direction, an axial force does not change when the distance between the nodes of the truss element does not vary in the original truss direction. Using this characteristic of the truss element, only nodal forces in the original truss direction are transmitted through the truss element, i.e., the node of the solid element at the soil–pile interface can freely move to perpendicular directions to the original truss axis as shown in Fig. 6.3(b). As a result, the node of the soil element at the soil–pile interface can slip on the tangential plane to the pile surface when the axial stiffness of the truss element is large enough, and the pile behaves as a perfectly smooth pile. For the sake of convenience, let us refer to the pile modeled by this method as the pile *with slippage*, as the nodes of the adjacent soil elements can freely move in the directions other than the axial direction of the truss elements connecting the pile and the soil.

In order to verify the performance of the connections between the pile and the soil adjacent to

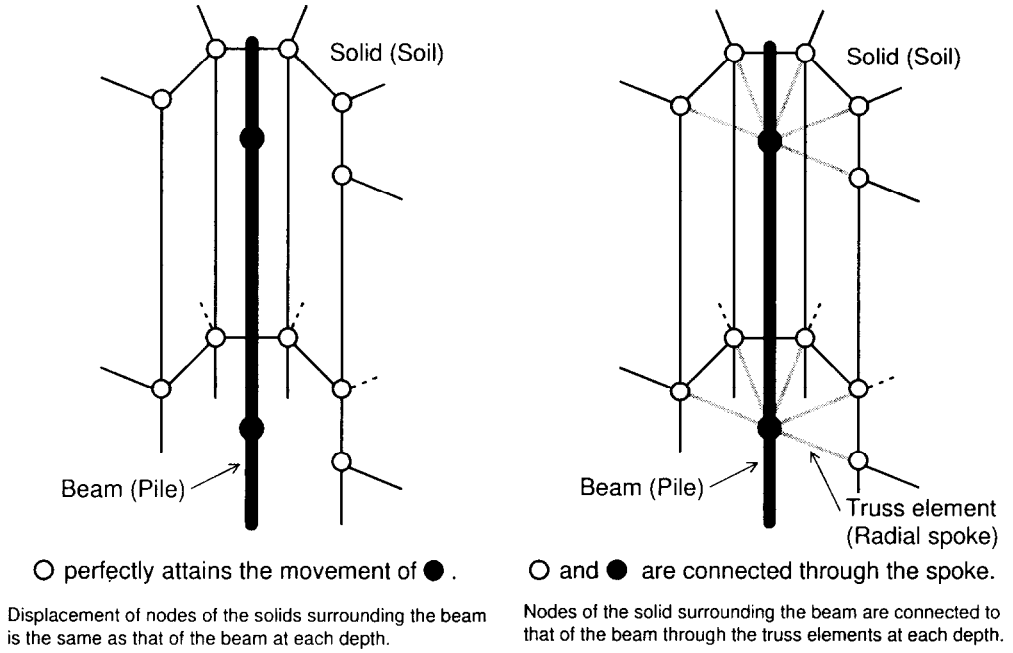

Pile without slippage — Pile with slippage

(a) For rough pile. (b) For smooth pile.

Figure 6.2: Connections between beam elements for pile and solid elements for soil surrounding pile.

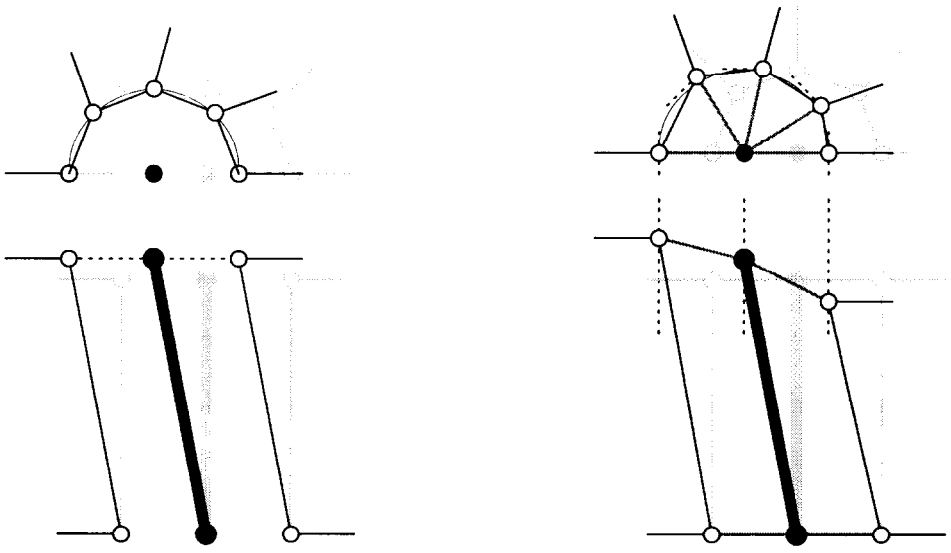

Pile without slippage — Pile with slippage

(a) For rough pile. (b) For smooth pile.

Figure 6.3: Conceptual diagrams of displacements of nodes of solid elements for soil adjacent to beam element for pile.

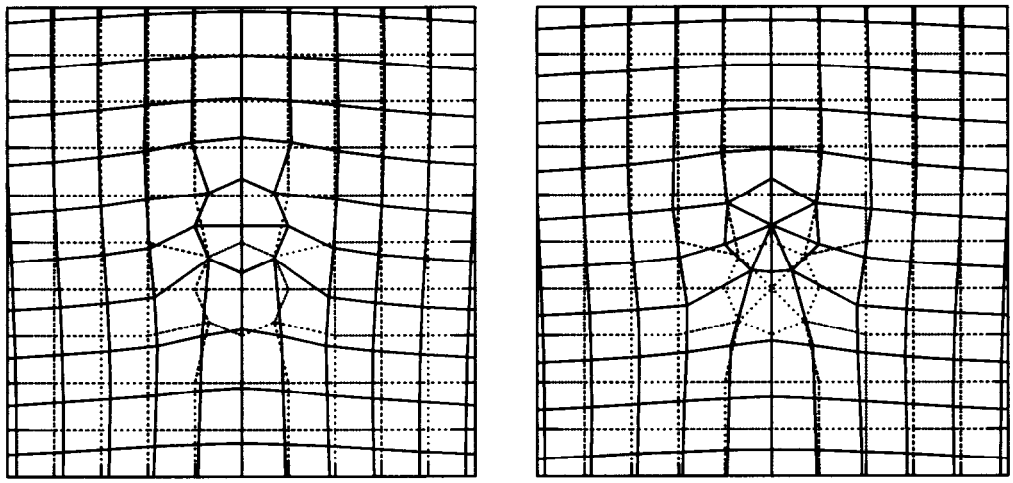

(a) Without slippage (u/D=0.135) (b) With slippage (u/D=0.135)

Figure 6.4: Deformations of solid surrounding disc, where displacement scale is magnified by a factor of five.

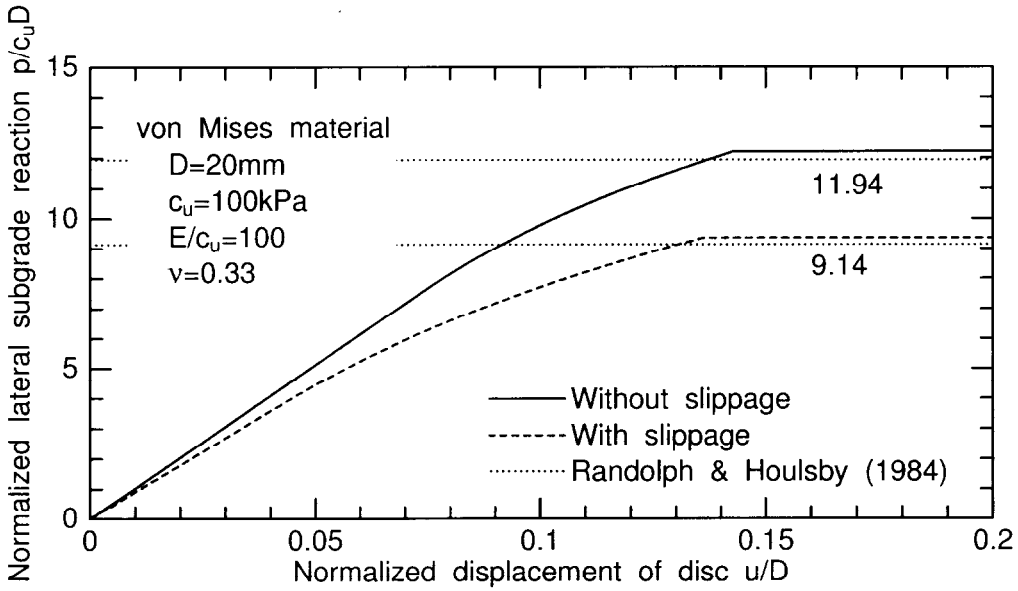

Figure 6.5: Normalized load–displacement relations of disc in von Mises material.

the pile, two-dimensional analyses on a laterally loaded disc were conducted. The pile section was modeled as a disc. It was assumed that the disc with a radius of R=20mm was placed in a soil mass whose shape is a square 30R on a side. The size of the element was 10 × 10mm. The displacement in the loading direction was fixed on a side of the square perpendicular to the loading direction. The displacement in the direction perpendicular to the loading was also fixed on the center line through the center of the disc and perpendicular to the fixed side. The soil was assumed to be von Mises material with a Young's modulus of $100c_u$ (where c_u=100kPa) and a Poisson's ratio of 0.33. The node at the center of the disc was assumed to have the same displacement as the nodes of the soil located at the

interface between the soil and the disc for a disc without slippage, i.e. a rough disc. For the case of the smooth disc, the node was assumed to be connected to the nodes of the soil located at the interface between the soil and the disc through the truss elements, simulating the disc with slippage.

The axial stiffness of the truss element for the smooth ring that corresponds to the pipe pile in the three-dimensional analysis was calculated as follows:
Radial displacement of the ring, u, stressed elastically can be written as

$$u = Ar + \frac{B}{r}. \tag{6.5}$$

The elastic equations in cylindrical coordinates under the plain strain condition are

$$E\varepsilon_r = E\frac{\partial u}{\partial r} = \sigma_r - \nu(\sigma_\theta + \sigma_z), \tag{6.6}$$

$$E\varepsilon_\theta = E\frac{u}{r} = \sigma_\theta - \nu(\sigma_z + \sigma_r), \tag{6.7}$$

$$E\varepsilon_z = \sigma_z - \nu(\sigma_r + \sigma_\theta) = 0. \tag{6.8}$$

Solving these equations under the condition that the ring is subjected to a pressure of $(-p)$ at the outer surface, i.e. $\sigma_r = p$ on $r = r_1$ (outer surface) and $\sigma_r = 0$ on $r = r_0$ (inner surface):

$$u = \frac{(1+\nu)p}{E\left(1-\frac{r_0^2}{r_1^2}\right)}\left\{(1-2\nu)r + \frac{r_0^2}{r}\right\}, \tag{6.9}$$

$$\left.\frac{dp}{du}\right|_{r=r_1} = \frac{E\left(1-\frac{r_0^2}{r_1^2}\right)}{(1+\nu)\left\{(1-2\nu)r_1 + \frac{r_0^2}{r_1}\right\}}. \tag{6.10}$$

From equation (6.10) and the share of surface area of the pile that each truss element has to sustain, the axial stiffness of the truss element will be determined. In the following three-dimensional FE analyses on pile behavior in this chapter, equation (6.10) will be used for the determination of the axial stiffness of the spokes for simplicity, though the axial strain of the pipe piles are not naught.

Figure 6.4 illustrates the deformations of the soil around the disc at a normalized displacement of u/D=0.135, where u is displacement and D is the diameter of the disc. In the case allowing the slippage between disc and soil, the deformation of the adjacent soil is relatively limited around the disc, and the soil moves to the back of the disc. Normalized load–displacement relations of the disc in the soil are shown together with exact solutions based on the plastic theory by Randolph & Houlsby (1984) in Fig. 6.5. Though the ultimate resistances of the disc by the numerical analyses were overestimated compared to those of the analytical solutions, it can be concluded that the present modeling methods for the soil–pile interface function well.

6.3 Verification of pile and soil–pile interface modeling through simulations of *active* and *passive* pile model tests

In order to verify the performance of the connections between the pile and the soil adjacent the pile, three-dimensional analyses on *active* and *passive* pile model tests were conducted. The laterally

Table 6.2: Material parameters for constitutive model.

G_s	e_0	κ	λ	ν	ϕ	ϕ_d	μ
2.65	0.664/0.682*	0.0013	0.0072	0.33	30°	25°	0.6
ϕ_b	b_r	u_1	m_1	c	β_{ij0}	$F_0/(-\sigma'_{m0})$	s_{ij0}
30°	1.0×10^2	4.0	1.0	30.0	$\frac{\sigma'_{ij0}-\sigma'_{m0}\delta_{ij}}{(-\sigma'_{m0})}$	1.2	$0.2\ \sigma_{ij0}$

$*$ 0.664 for *active pile* (Dr=85%) and 0.682 for *passive pile* (Dr=80%).

Table 6.3: Material properties of model pipe pile for active and passive pile tests.

	Active pile	Passive pile
Young's modulus, E (GPa)	206	
Diameter of pile, D (mm)	10	15
Thickness of pile, t (mm)	0.50	
Cross-sectional area, A (mm^2)	1.49×10^{-5}	2.28×10^{-5}
Centroidal moment of inertia, I (mm^4)	1.69×10^{-10}	5.99×10^{-10}

loaded pile at the pile head actively affects the movement of the adjacent soil, while the pile in the large soil movement passively follows that of the soil. The former and the latter pile are called the *active pile* and the *passive pile*, respectively. Targeted centrifuge model tests were carried out by Koda (2000) and the author and associates (2001). An outline of the tests will be briefly described here.

Model ground and piles

Toyoura sand, uniformly graded sub-angular quartz sand (D_{50}=0.19mm), was used for the model ground. The ground was prepared by air pluviation to achieve a relative density of 85% and 80% for the active and the passive pile tests, respectively. Material parameters for the sand are summarized in Table 6.2. In the determination of the material parameters, G_s, κ, λ, ν, ϕ_d, ϕ_b, b_r, u_1, m_1, c, β_{ij0}, $F_0/(-\sigma'_{m0})$, and s_{ij0}/σ_{ij0} were set to the values for the medium dense sand utilized in the previous chapter, and ϕ and μ were varied to fit the element test results as shown in Fig. 6.6, though the stress–dilatancy relation was not similar to that of the element tests. As anisotropy in the shape of the yield surface and the rotation limit are eliminated in this study, the parameters were set to fit the triaxial compression tests.

The stainless steel-made model pipe pile, the properties of which are listed in Table 4.7, was used in the tests. The surface of the model pipe pile was smooth. An index for the roughness of the material surface, R_{max} is in the range of 0.3–1.5μm in 2.5mm, which is defined as the relative height between the highest peak and the lowest trough along the profile over a specified gauge length (Koda, 2000). Uesgi (1987) introduced a normalized roughness, $R_n = R_{max}/D_{50}$, as the index for the interface roughness, where D_{50} is the mean diameter of the soil particle. He measured the friction between the sand and the several construction materials by direct shear tests. Assuming that a pile

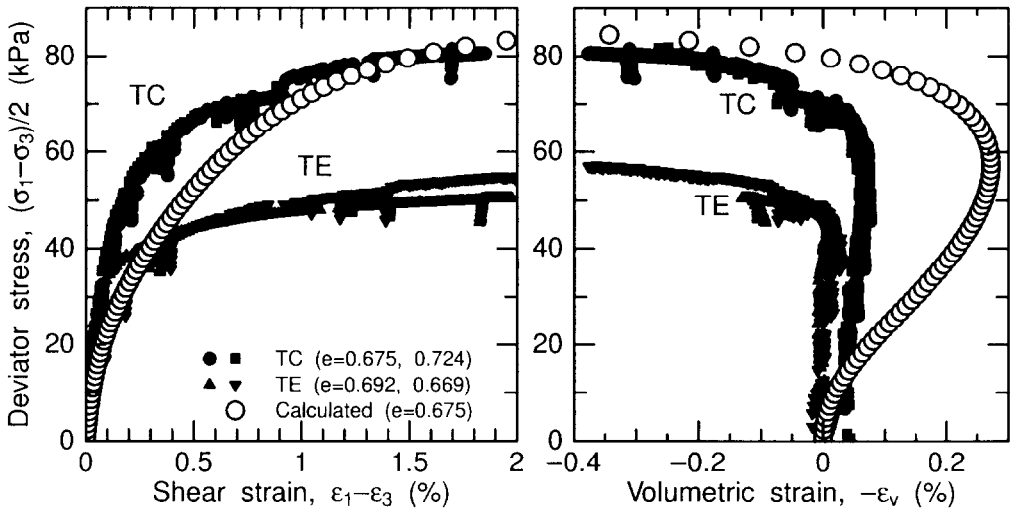

Figure 6.6: Triaxial compression (TC) and extension (TE) tests and numerical analysis results on Toyoura sand on condition that effective confining stress, p'=98kPa, was kept constant.

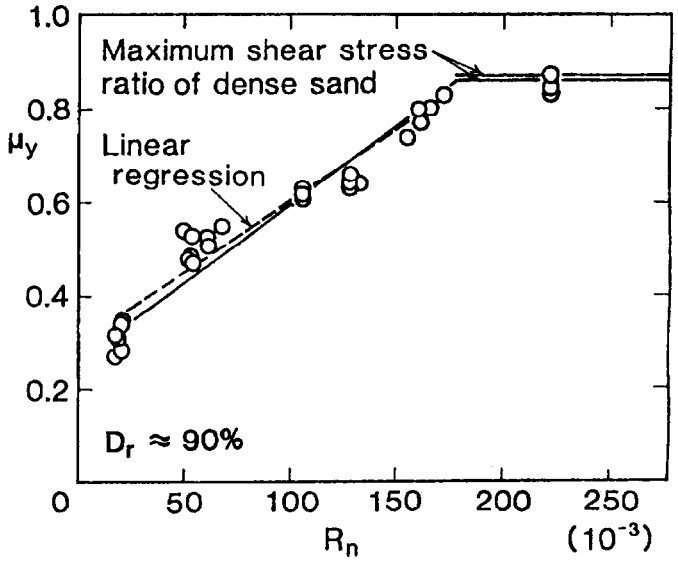

Figure 6.7: Coefficient of maximum friction, μ_y in relation to normalized roughness (after Uesugi, 1987, retouched).

with $R_{max}=1.5\times10^{-3}$mm is installed in a Toyoura sand layer whose D_{50}=0.19mm, then $R_n=8\times10^{-3}$. Figure 6.7 shows the coefficient of the maximum friction, μ_y, in relation to the normalized roughness. Though the normalized roughness of the pile used in this study is out of range of their test results, it can be said that the model pipe pile used was smooth but not naught.

Strain gauges were instrumented inside of the pile to measure the bending strain of piles. The

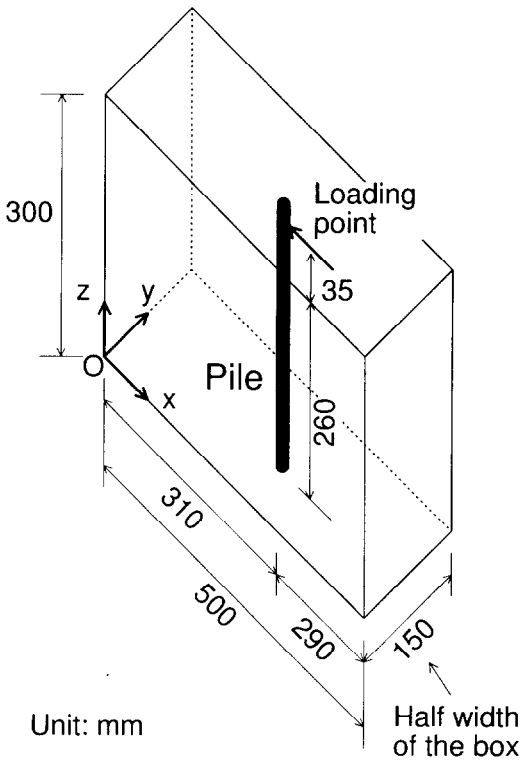

Figure 6.8: Dimension of analytical domain for *active pile*.

relationship between the bending strain, ε_b, and the bending moment, M, can be written as

$$M = EI\left(-\frac{1}{\rho}\right) = EI\frac{\varepsilon_b}{r_i} \tag{6.11}$$

where ρ is the radius of beam curvature, EI is the flexural rigidity and r_i is the inner radius of the pipe pile. This bending strain is the longitudinal normal strain of the beam at the distance of r_i from the neutral axis of the beam section.

6.3.1 Physical and numerical model tests on active pile

Test conditions

The targeted centrifuge model test on the pile subjected to lateral load on the pile top was conducted by Koda (2000). Test codes of the centrifuge tests were H8550105F and H0050105 (cyclic loading) in his dissertation. A strong box with inner sizes of 500mm in width, 300mm in breadth, and 360mm in height was used. Dry Toyoura sand with a relative density of 85% was used for the model ground. The model pipe pile used in the test had 300mm in total length. The embedment depth in the model ground was 260mm. Lateral load was applied to the pile head 35mm above the ground surface by an electric motor jack at the rate of 1mm/min at 50g. Applied load was measured using a load cell. Strain gauges were attached inside the pile at eleven different levels. Deflections and inclination of the pile head were also measured by two laser displacement transducers.

The location of the pile in the model ground is schematically illustrated in Fig. 6.8. In the numerical analyses, in order to examine the differences in the response of the pile and the ground,

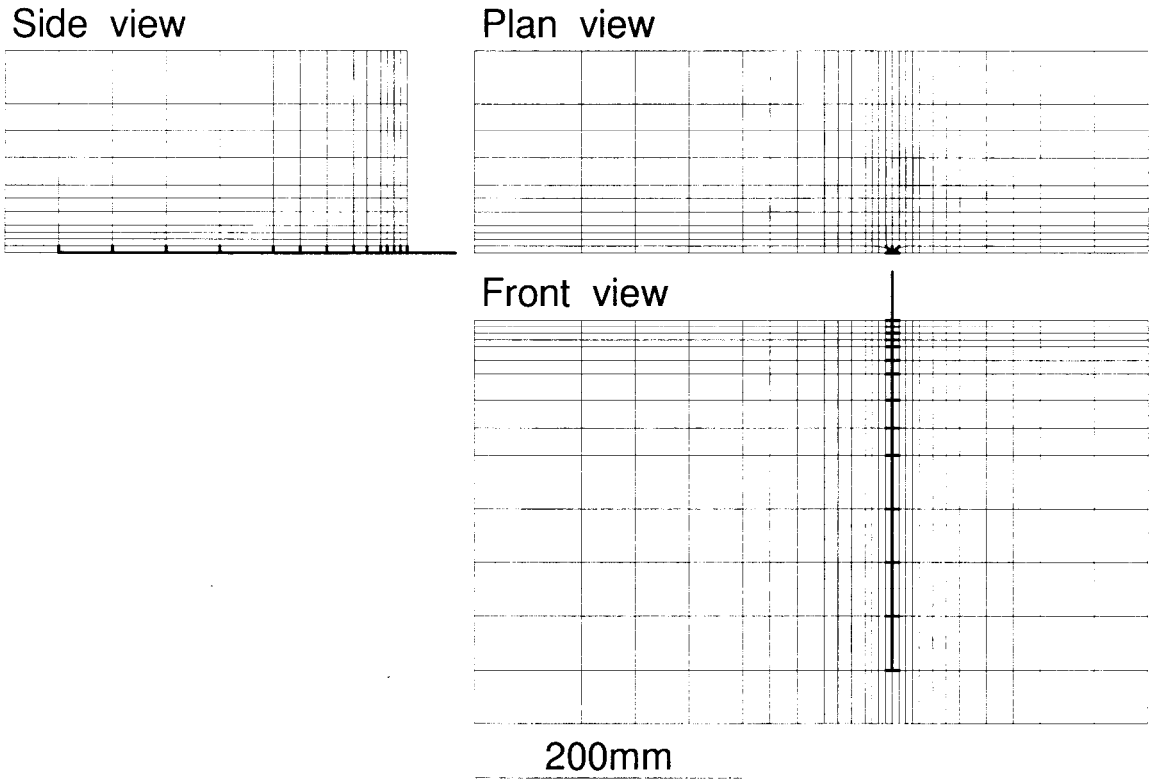

Number of solid elements: 3978, Number of nodes: 4861

Figure 6.9: Finite element mesh for *active pile* with slippage between pile and soil.

the two types of connection method between the pile and the soil which are described above were adopted. The finite element mesh for the active pile with slippage between the pile and soil is shown in Fig. 6.9. Thick lines in the figure represent the beam and the truss elements.

In the numerical analyses, only half of the ground was modeled, taking advantage of symmetry. The planes x=0 and x=500mm were allowed to move freely in the y– and z–directions but not in the x–direction. Identically, the planes y=0 and y=150mm were allowed to move freely in the x– and z–directions but not in the y–direction. At the bottom plane z=0, all movements were restrained. In this study, a simple two-step loading of gravity, 50g, was adopted in the static analysis to estimate the initial stress condition as described in the previous chapter. Then, lateral displacement was given to the pile top with the increment of 0.1% of the pile diameter.

Test results and discussion

Figure 6.10 shows the calculated lateral load–displacement relations together with the physical model test results. Displacement in this subsection is taken as positive when the node moves leftward. Irrespective of the pile–soil connection methods, the calculated curves show amazingly good agreement with the physical model test results. Comparing the two calculated load–displacement curves, the curve for the pile with slippage is practically on that of the physical tests, while the curve for the pile without slippage draws apart from the physical model test results as the lateral displacement

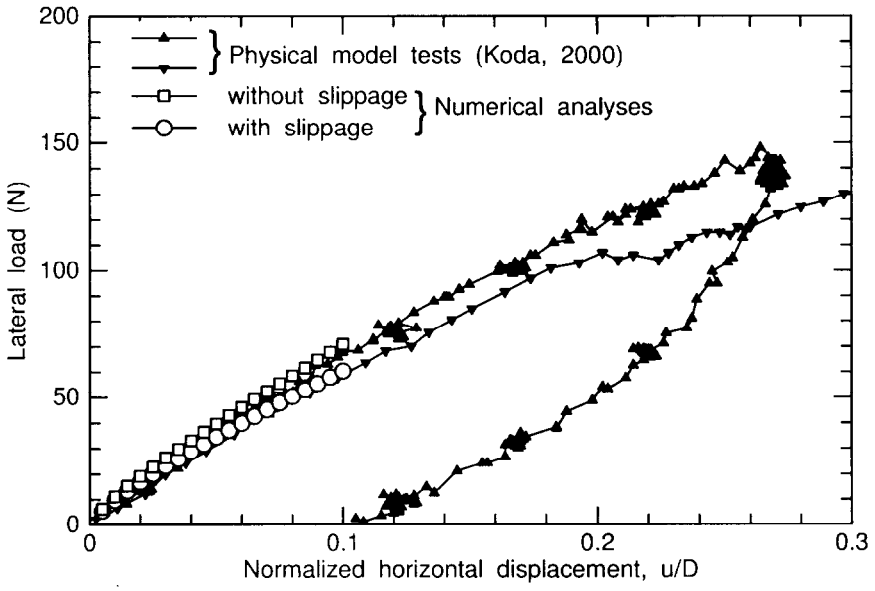

Figure 6.10: Lateral load–displacement relations of laterally loaded pile.

of the pile head increases. Essentially, the physical model test results are within the range of these calculated load–displacement curves. Considering the fact that the surface of the steel pipe pile may not be perfectly smooth, these calculated results are reasonable and acceptable.

Bending strain distributions obtained by the numerical and physical model tests at u/D=0.02, 0.05, and 0.10 are illustrated in Fig. 6.11, where u is the displacement of the pile top and D is the diameter of the pile. The calculated bending strain distributions for the pile with slippage show good agreement with the physical model test results along the pile as shown in Fig. 6.11(a). When the pile is perfectly fixed to the adjacent soil, i.e. the surface of the pile is rough, the maximum bending strain increases and the location of the maximum bending strain shifts slightly upward, compared with the pile with slippage, as shown in Fig. 6.11(b).

Figures 6.12 and 6.13 show contours of the stress ratio, q/p' in Section A & B at u/D=0.02, 0.05, and 0.10 respectively, where $p' \equiv -\sigma_{ii}/3$ and $q \equiv \sqrt{3J_2} = \sqrt{\frac{3}{2}(\sigma_{ij}+\delta_{ij}p')(\sigma_{ji}+\delta_{ji}p')}$. The soil elements blacked out have the larger stress ratio and approaches failure. The soil elements that exceed the shear boundary surface, i.e. the phase transformation line, are the elements whose stress ratio are over q/p'=0.98 as ϕ_d=25°. The gross area of the elements that exceed the shear boundary surface is almost the same in both the cases, though that of the elements approaching the shear boundary surface, i.e. the elements in the range of q/p'=0.8–1.0, is somewhat larger for the pile without slippage.

Contours of the mean effective stress, p' in Section A at u/D=0.02, 0.05, and 0.10 are illustrated in Fig. 6.14. The mean effective stress at the shallower portion near the pile varied with the pile loading. On the front side, p' at the shallower portion gradually increased, while that at the shallower portion in the back and that at the middle depth on the front side decreased with loading. These tendencies were remarkable in the case without slippage, as the soil adjacent to the pile was confined by the friction between the pile and the soil. As a result, the maximum bending strain increases, and the location of the maximum bending strain shifts slightly upward, compared with the pile with slippage

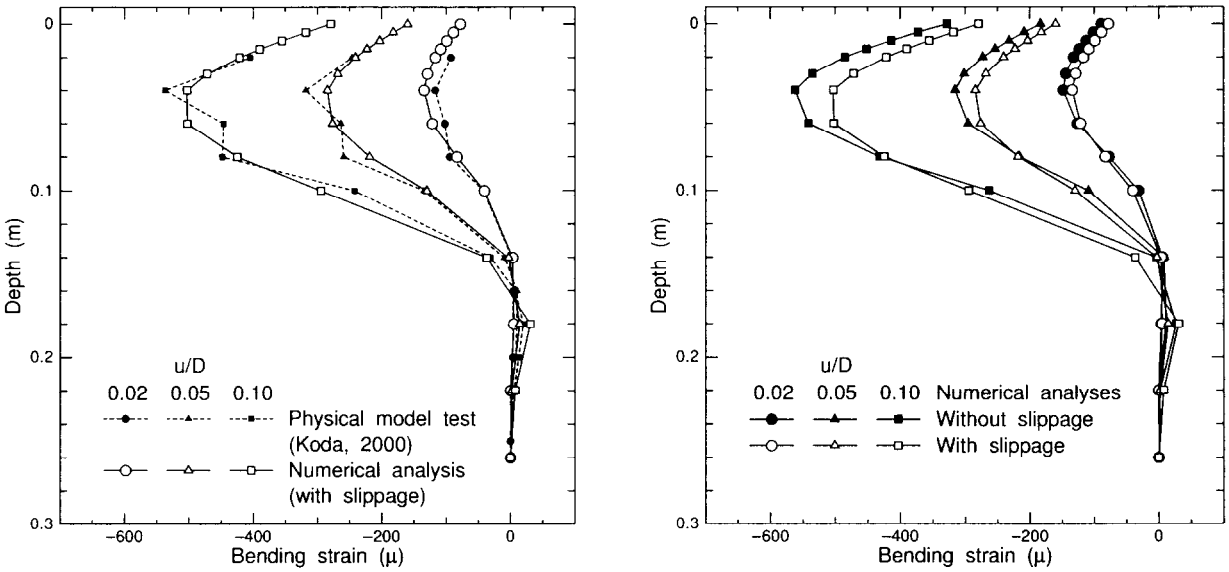

(a) Calculated bending strain of the pile with slippage and the centrifuge test results.

(b) Comparison between the pile with and without slippage.

Figure 6.11: Bending strain distributions of laterally loaded pile.

as shown in Fig. 6.11(b).

Permanent ground surface deformation in the physical model test is illustrated in Fig. 6.15. Figure 6.16 shows the deformations of the ground at u/D=0.02. In the physical model test, the deformation of soil is limited around the pile. In the case allowing slippage between the pile and the soil, the deformation of the adjacent soil is relatively limited around the pile, and the soil moves to the back of the pile. Presence of the apparent slippage can be seen in the deformation of the soil surrounding the pile.

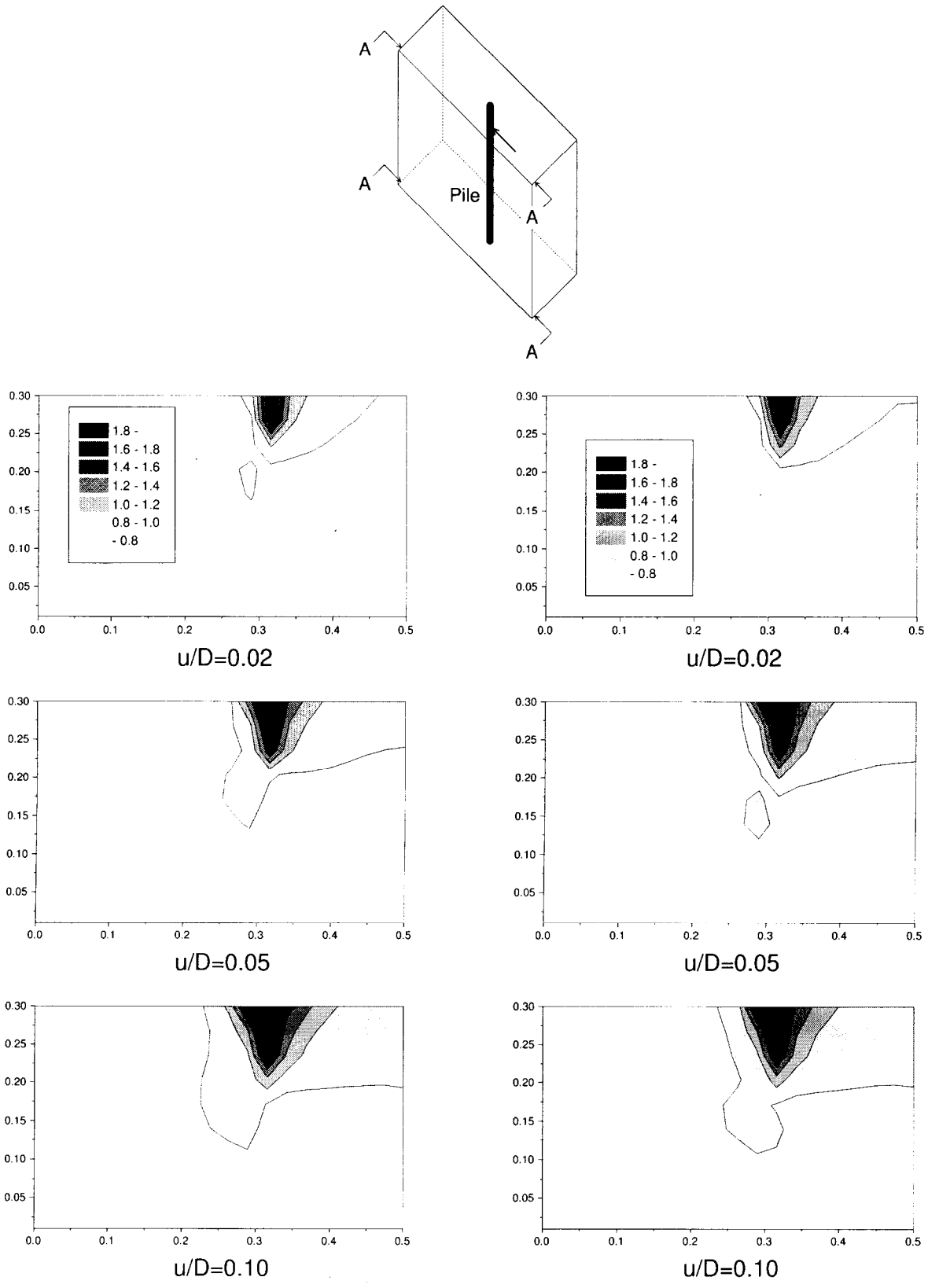

(a) without slippage. (b) with slippage.

Figure 6.12: Contours of stress ratio, q/p', in Section A.

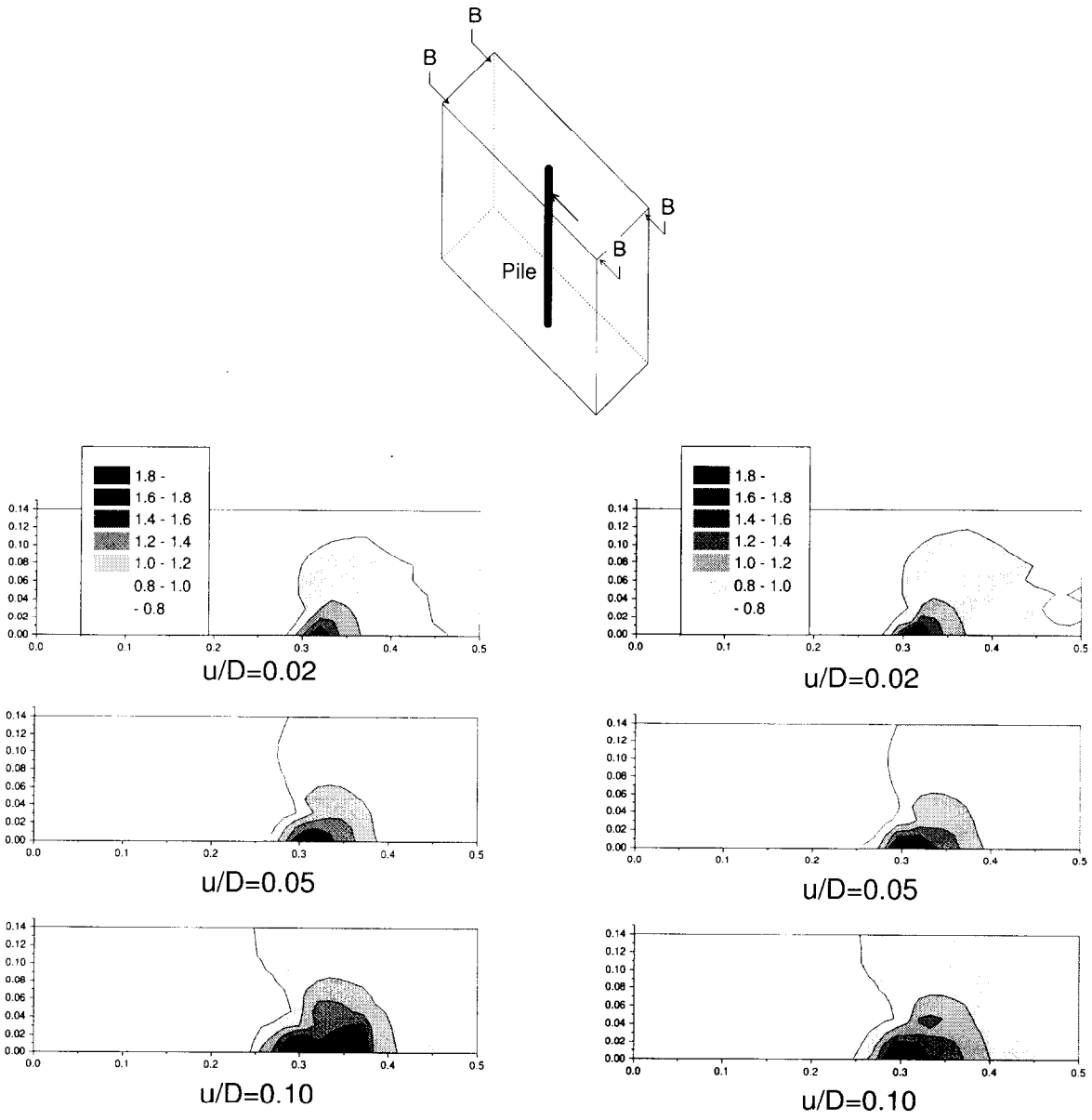

(a) without slippage.

(b) with slippage.

Figure 6.13: Contours of stress ratio, q/p', in Section B.

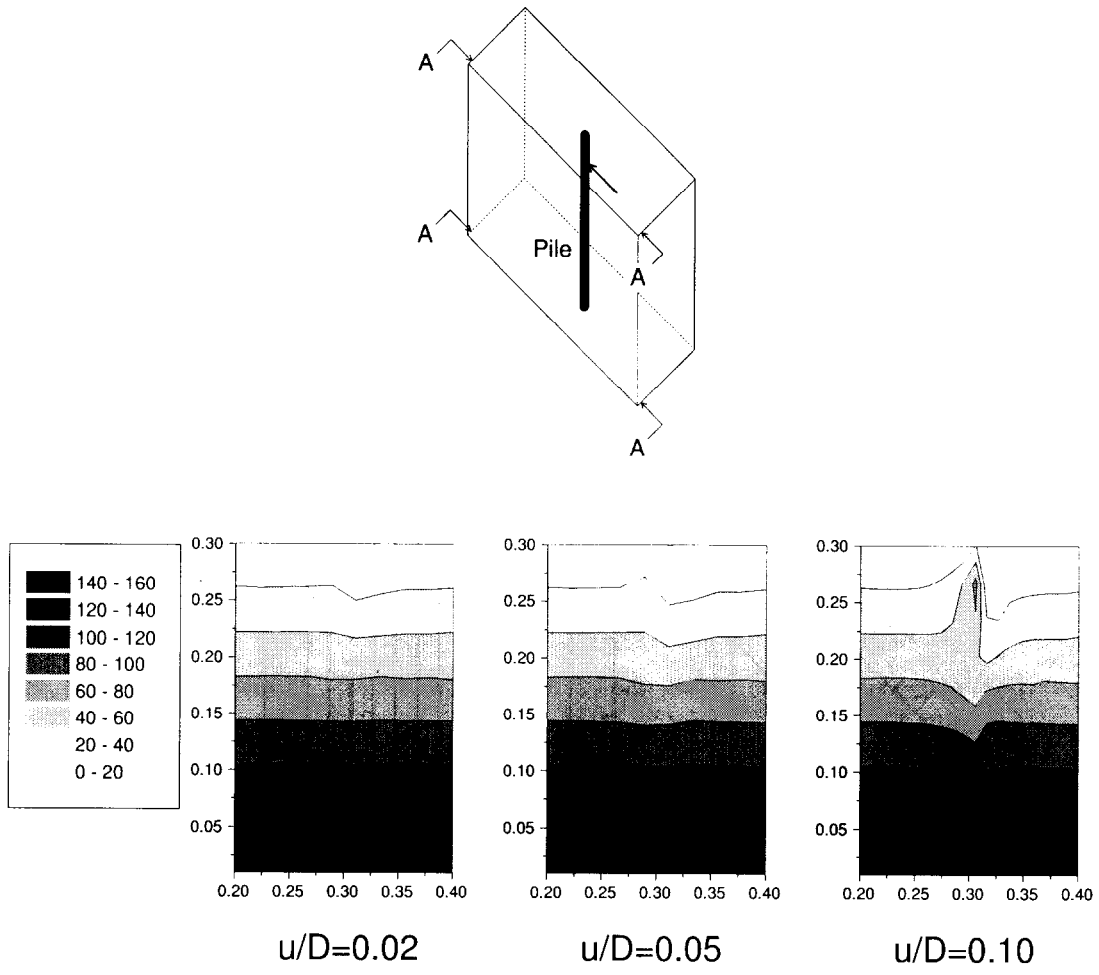

(a) without slippage.

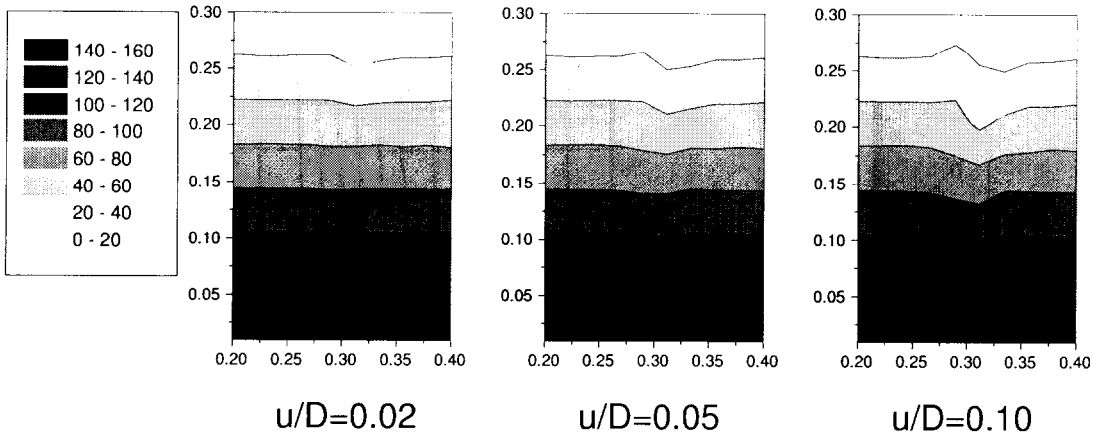

(b) with slippage.

Figure 6.14: Contours of mean stress, p', in Section A (Unit: kPa).

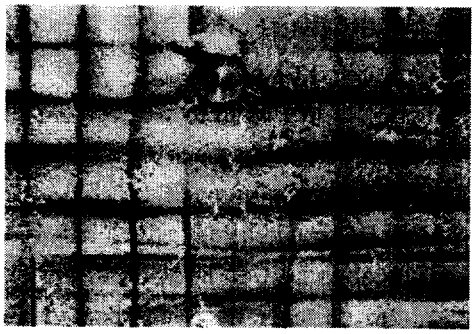

Figure 6.15: Permanent ground surface deformation in physical model test, where loading direction is downward in this photograph (after Koda, 2000).

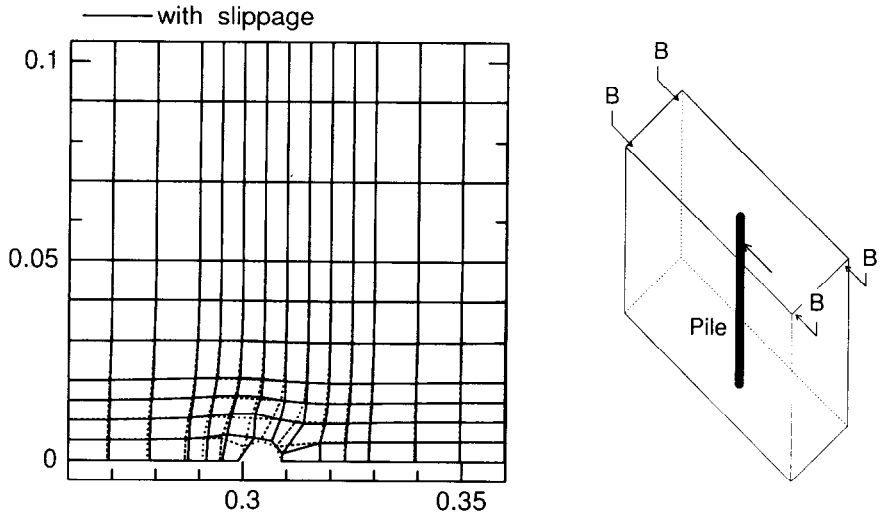

(a) Enlarged plan view in Section B.

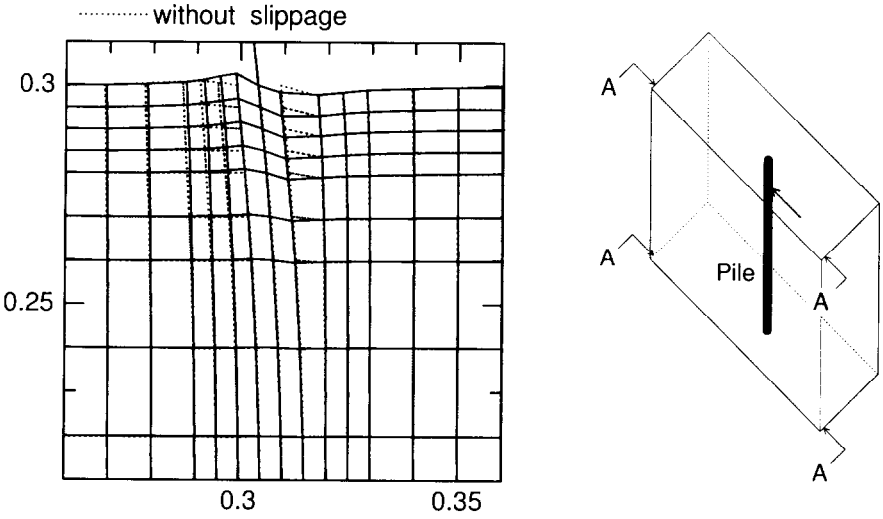

(b) Enlarged side view in Section A.

Figure 6.16: Deformations around pile at u/D=0.1, where displacement scale is magnified by a factor of ten.

6.3.2 Physical and numerical model tests on passive pile

Test conditions

The targeted centrifuge model test on the pile in large soil movement is the test case 'PA1' in Chapter 4. Toyoura sand with relative density of 80% was used for the model ground. The model pipe pile used in the test had 320mm in total length. The embedment depth in the model ground was 300mm. Horizontal displacement was imposed to the laminar box by three hydraulic jacks. Only one cycle sinusoidal motion was applied to the laminae in 480 seconds at 25g. Test conditions of this test are summarized in Table 4.8. The imposed shear deformation mode of the soil was Type A (cf. Fig. 4.16). The soil below two-thirds of the model depth was assumed to be a bearing stratum, and the input displacement was applied only to the upper two-thirds of the model. Horizontal displacements of six laminae in the stacks were measured by LVDTs at the mid-portion of the box. Displacements of the actuator rods were also measured using LVDTs. Strain gauges were attached inside of the pile at ten different levels. Deflections and angles of the pile head were also measured by two laser displacement transducers.

The location of the pile in the model ground is schematically illustrated in Fig. 6.17. In the numerical analysis, since the model pipe pile in the physical model test was smooth and the pile with slippage was seen to perform well in the analyses on the active pile, the pile was modeled as the

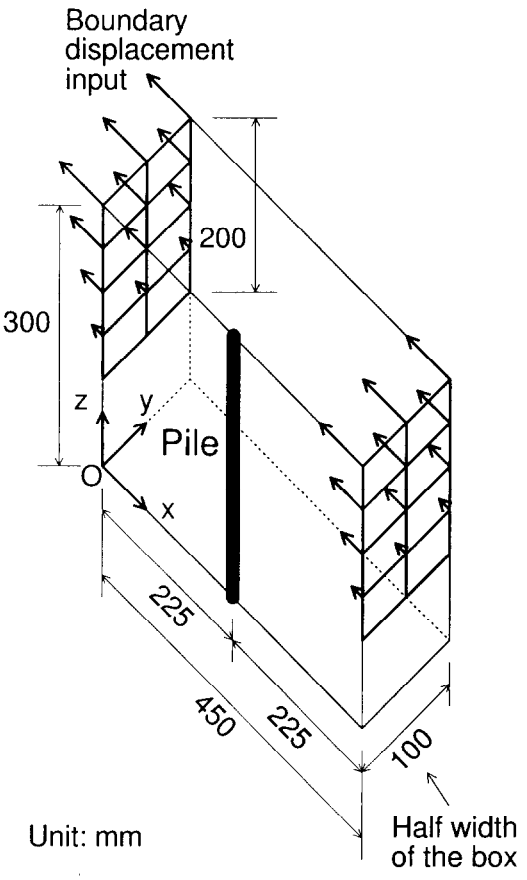

Figure 6.17: Dimension of analytical domain for *passive pile*.

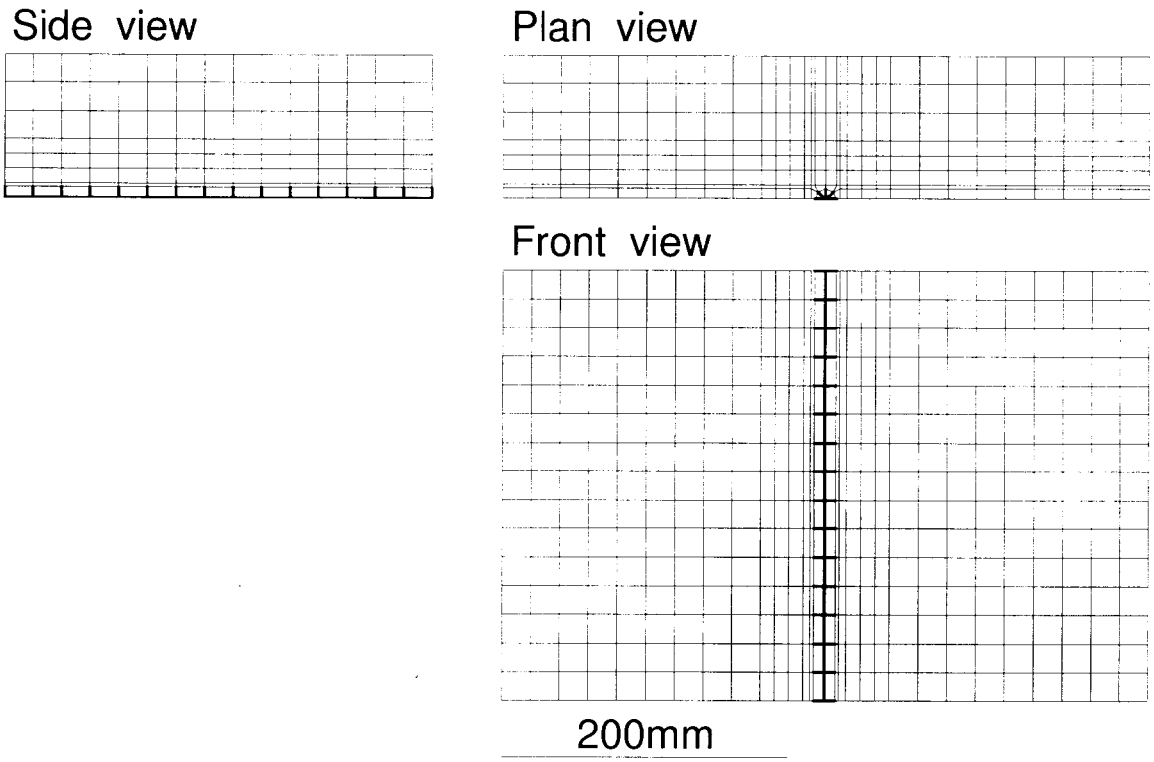

Number of solid elements: 3570, Number of nodes: 4464

Figure 6.18: Finite element mesh for *passive pile*.

smooth pile, i.e. the pile with slippage. The finite element mesh for the passive pile is shown in Fig. 6.18. Thick lines in the figure represent the beam and the truss elements.

In the numerical analysis, only half of the ground was modeled, taking advantage of symmetry. The planes x=0 and x=450mm were allowed to move freely in the y– and z–directions but not in the x–direction. The x–directional input displacement was applied to the upper two-thirds of the model ground at these planes. The planes y=0 and y=100mm were allowed to move freely in the x– and z–directions but not in the y–direction. At the bottom plane z=0, only movement in the z–direction was restrained, according to the physical model test condition. In this calculation, a simple two-step loading of gravity, 25g, was adopted in the static analysis to estimate the initial stress condition, the same way as in the active pile analyses. Lateral displacement was given to the side boundaries with the increment of 1.33% of the pile diameter.

Test result and discussion

Figure 6.20 shows contours of the mean stress, p', in Section A when the normalized displacement of the top lamina, u_L/D, reached 0.2, 0.6, and 0.86, where u_L is the displacement of the top lamina and D is the diameter of the pile. Contours of the stress ratio, q/p' in Section A at u_L/D=0.2, 0.6, and 0.86 are also illustrated in Fig. 6.19. The soil elements blacked out in Fig. 6.20 have the larger stress ratio and approaches failure.

The mean stress increased to several-fold and formed a high confining stress brace between the

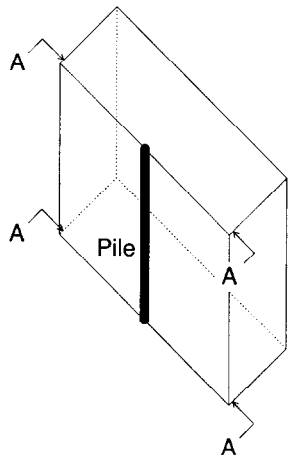

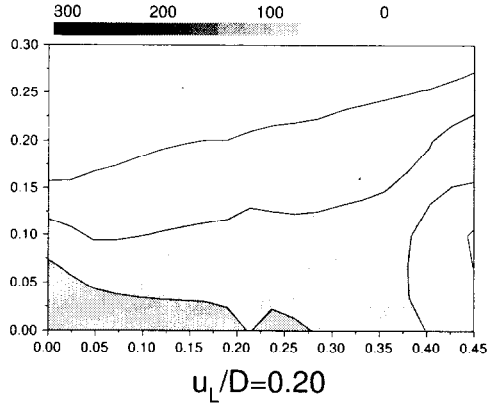

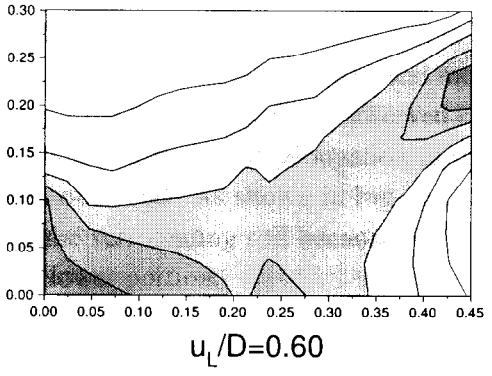

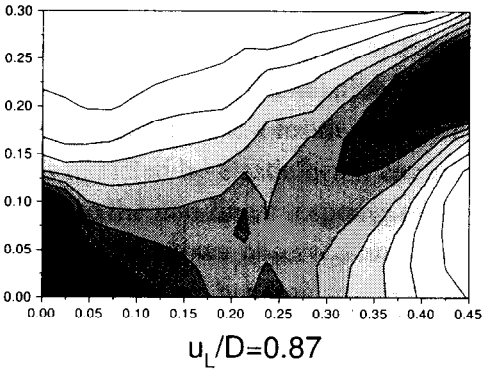

Figure 6.19: Contours of mean stress, p', in Section A (Unit: kPa).

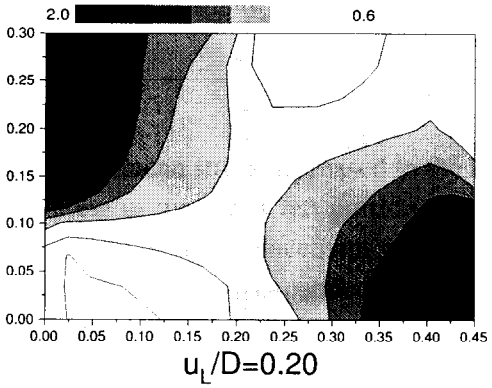

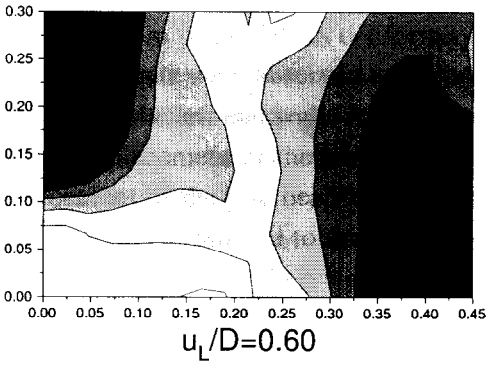

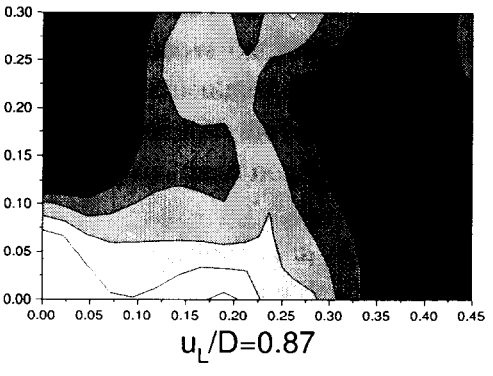

Figure 6.20: Contours of stress ratio, q/p', in Section A.

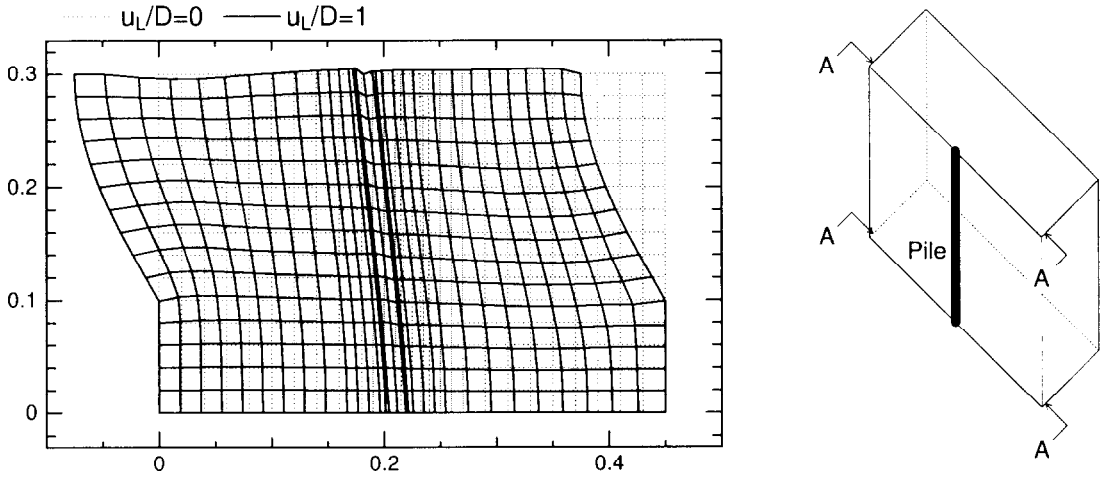

Figure 6.21: Deformations around pile in Section A at $u_L/D=0$ & 1, where displacement scale is magnified by a factor of five.

upper right and the lower left portion with loading. As a result, the mean stress decreased in the lower right portion, and there was no large variation of the mean stress in the upper left portion. In these portions the stress ratio became larger and approached failure early on as displacement was imposed on the box. In the right half of the soil domain, an area with a large stress ratio expanded with loading, and the passive zone was developed in the shallower portion behind the pile.

Figure 6.21 shows the deformations of the ground in Section A at $u_L/D=0$ & 1. Enlarged plan and section views of the ground around the pile at $u_L/D=1$ are also illustrated in Fig. 6.22. As the movement in the y– and z–direction were not restrained at the bottom plane $z=0$ in conformity with the boundary conditions in the physical model test, small displacements were observed at the bottom. The heaving of the surface was observed except at the portion near the left end wall. As the interface elements functioned well, elongation of the pile, i.e. vertical displacement of the nodes of the pile, was not observed. As shown in Fig. 6.22, the lateral displacement of the pile head was larger than that of the surrounding soil because of the larger stiffness of the pile compared to that of the soil in the shallower portion.

The relationship between observed displacement at the pile head and the input displacement of the lamina at the ground surface is shown in Fig. 6.23. Displacement in this subsection is taken as positive when the node moves leftward. It should be noted here that the displacement of the pile at the pile head shown in the figure was measured at the target 50mm above the surface of the ground as shown in Fig. 4.15. The relationship shows non-linearity and the calculated curve is close to that of the physical model test result, though the difference becomes larger with the box shearing. As the pile was modeled by elastic beam elements in the numerical analysis, these non-linear relations are attributed to the non-linear response of the soil.

Figure 6.24 shows observed and calculated bending strain distributions at $u_L/D=0.2$, 0.6, and 0.87. The maximum bending strains in the physical model test can be seen at a depth of 200mm (a height of 100mm) which corresponds to the interface between the less deformed bearing stratum and the sheared soil in the physical model test, while the maximum strains in the numerical analysis are

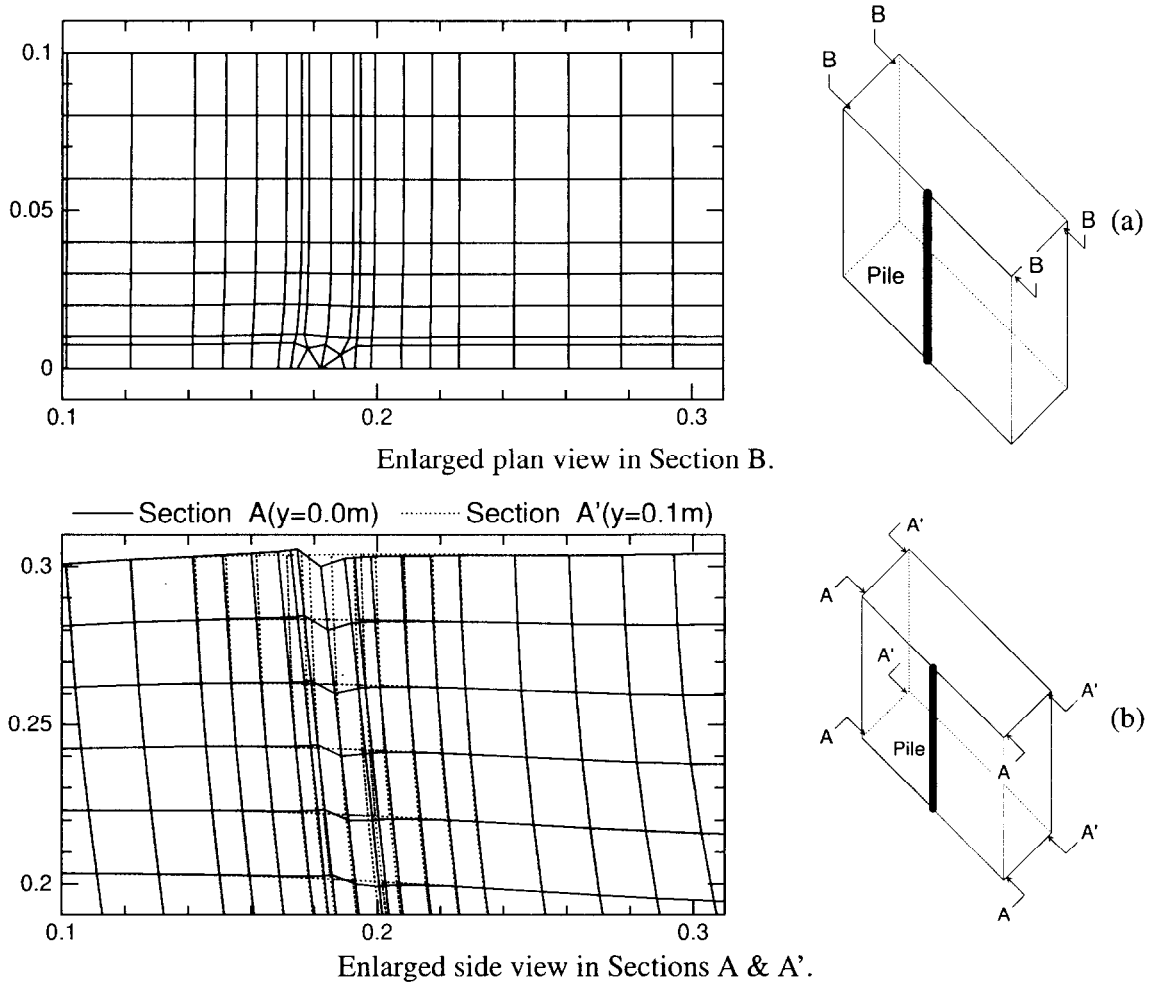

Figure 6.22: Enlarged deformations around pile in Sections A, A' & B at $u_L/D=1$, where displacement scale is magnified by a factor of five.

located slightly below the interface. As seen in the relationship between the displacement at the pile head and the input displacement of the lamina, the difference between the numerical and the physical model test results becomes larger with the progress of the box shearing.

In $u_L/D=0.87$, the maximum bending strain drastically increased in the physical test, as the strain of the model pile exceeded the yield point. This may be one of the reasons that the numerical analysis result departed from the physical model test results. The other reason for this difference may be in the modeling of the interface between the soil and the shear box bottom. Though the case without slippage at the bottom is not presented here, the shape of the bending strain distribution of the pile was quite different from that in the physical model test when the nodes at the bottom perfectly were fixed to the box. This fact and the result of the numerical analysis with the perfectly smooth interface imply that the slippage surely existed on the interface between the soil and the shear box bottom, but the interface was not perfectly smooth. Though some differences were seen between the numerical and the physical tests, overall response of the pile could be well simulated by this numerical analysis.

6.3.3 Summary of active and passive pile model test simulations

Three-dimensional finite element analyses on *active* and *passive* piles were conducted to verify the performance of the connections between the pile and the soil adjacent to the pile. The analysis on the active pile quite agreed with the physical model test result in load–displacement relation and in the bending strain distributions when perfect slippage between the pile and the adjacent soil was considered. Meanwhile, the numerical analysis result on the passive pile was not as excellent compared to the active pile case, though the result was similar to the physical test, and the numerical analysis could capture the overall response of the pile.

The simulation of the passive pile is more difficult than that of the active pile for the following reason: The active pile is directly subjected to the load, while the load acting on the passive pile is generated in consequence to the deformation of the soil surrounding the pile. In other words, the delicate difference in the deformation characteristics of the soil can make the response of the pile quite different. In this context, it can be concluded that the performance of the proposed connection method between pile and soil is validated through these numerical analyses.

6.4 Evaluation of seismic performance of pile-supported wharf by 3D FE analysis

6.4.1 Outline of numerical analysis

The targeted centrifuge-shaking table test on the pile-supported wharf is the test case 'PW2' in Chapter 2. Detailed test conditions of the physical model test are described in Chapter 2. The model setup used in this study is shown in Fig. 6.25 (h_s=20mm). The location of the deck and the caisson in the model ground is schematically illustrated in Fig. 6.26. The members constituting the wharf, i.e., piles, deck, and approach bridge, were modeled by beam elements. In the numerical analysis, as the model

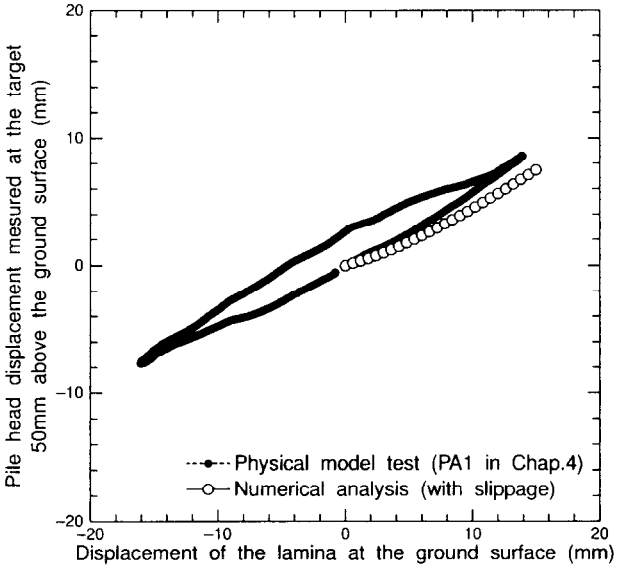

Figure 6.23: Relationship between lamina displacement at ground surface and pile head displacement (PA1 in Chap. 4).

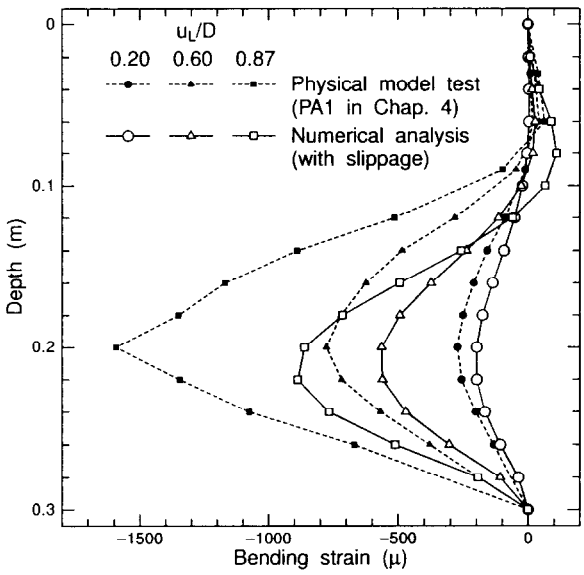

Figure 6.24: Bending strain distributions of pile in active type shear box (PA1 in Chap. 4).

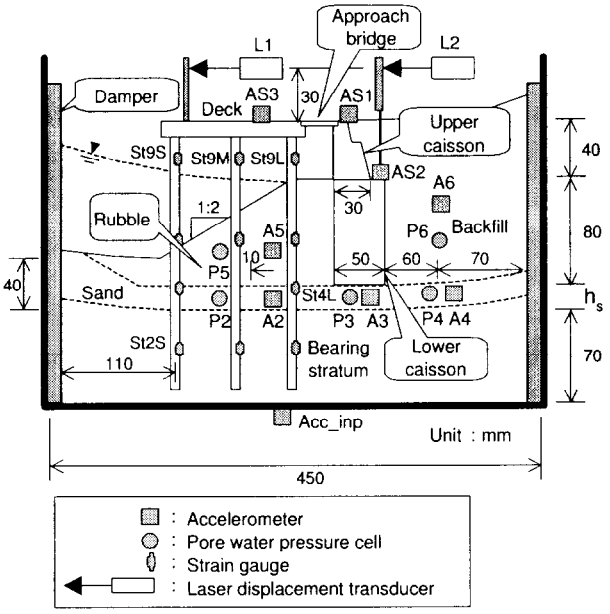

Figure 6.25: Model setup for centrifuge tests, h_S=20mm (the same as Fig. 2.15).

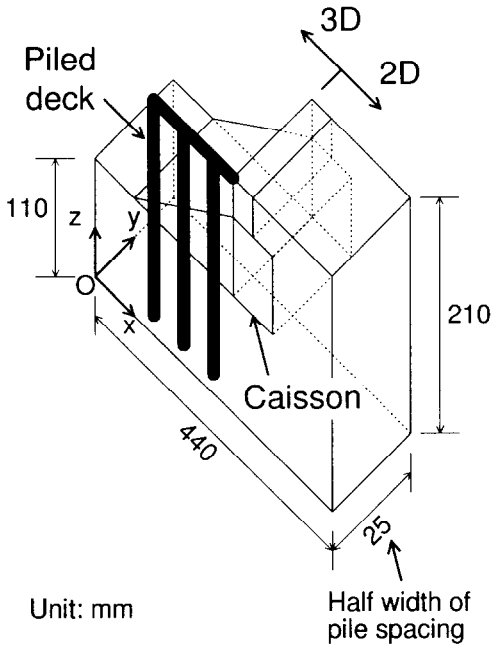

Figure 6.26: Dimension of analytical domain for piled wharf.

pipe pile in the physical model test was smooth and the pile with slippage was seen to perform well in the analyses on the active and the passive piles, the pile was modeled as the smooth pile, i.e. the pile with slippage. Though the approach bridge placed between the deck and the caisson transmitted only the compressive axial load in the physical model test, the bridge was simply connected to the deck and the caisson in a hinged condition in the numerical analysis. The finite element mesh and the soil layers for the piled wharf are shown in Fig. 6.27. The material parameters of the soil layers identified in the figure are listed in Table 6.4. Parameters and characteristics of the sand layer that may play a key role in this analysis are essentially the same as those in the analysis in Chapter 5. Thick lines in the figure represent the beam and the truss elements. In the numerical analysis, only half of the pile spacing was modeled, taking advantage of symmetry. Also in order to reduce the number of freedoms in the numerical analysis, a hybrid analytical domain that consists of two– and three–dimensional analytical domains is assumed. As the soil–pile interaction is a typical three-dimensional problem; the ground near the pile-supported wharf is modeled in three-dimensions. Meanwhile, the gravity type caisson and its backfill are modeled in two-dimensions, as the length of the quay wall is usually long enough to be modeled in 2D. In this particular case, the width of the three-dimensional analytical domain can be easily determined, as the width of the full analytical domain is relatively narrow. However, when a pile foundation behind the quay or in the level ground is main concern, the wider analytical domain is required (cf. subsection 6.4.4). Assuming the pile foundation in the wider analytical domain, we encounter difficulties in determination of the width of the three-dimensional analytical domain, i.e., the wider 3D analytical domain makes the computation time longer, while the insufficient 3D analytical domain width brings poor results for the structure performance evaluation. Three-dimensional analytical domain width determination based on the width of the passive zone be-

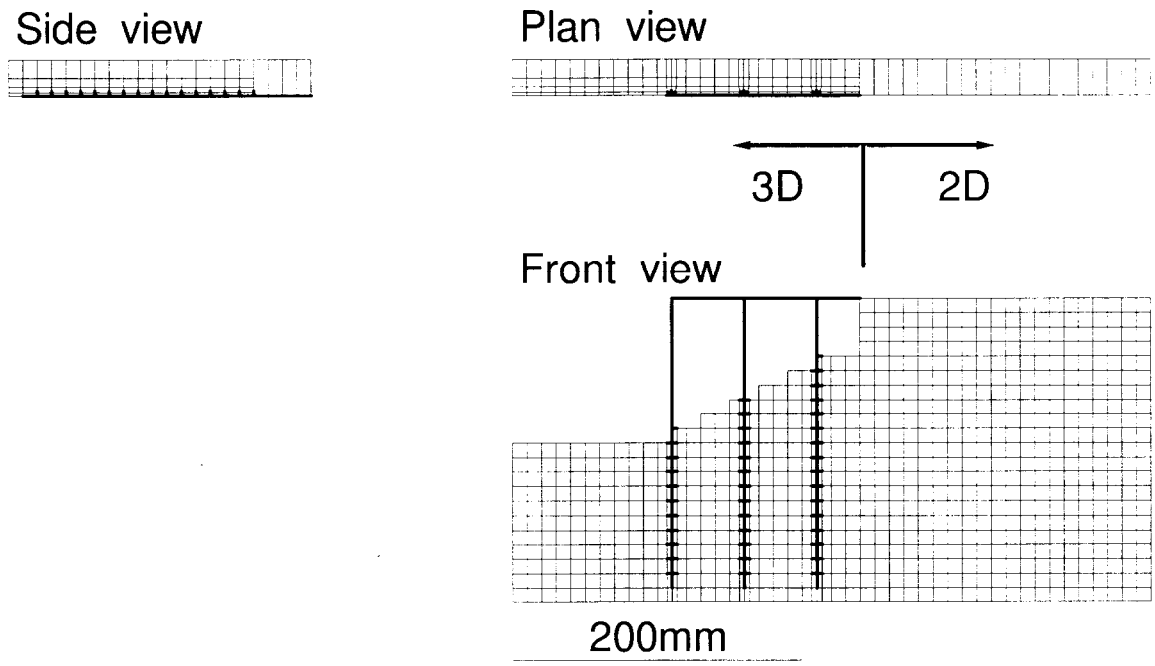

Number of solid elements: 1506 for 3D and 420 for 2D.

(a) Finite element mesh.

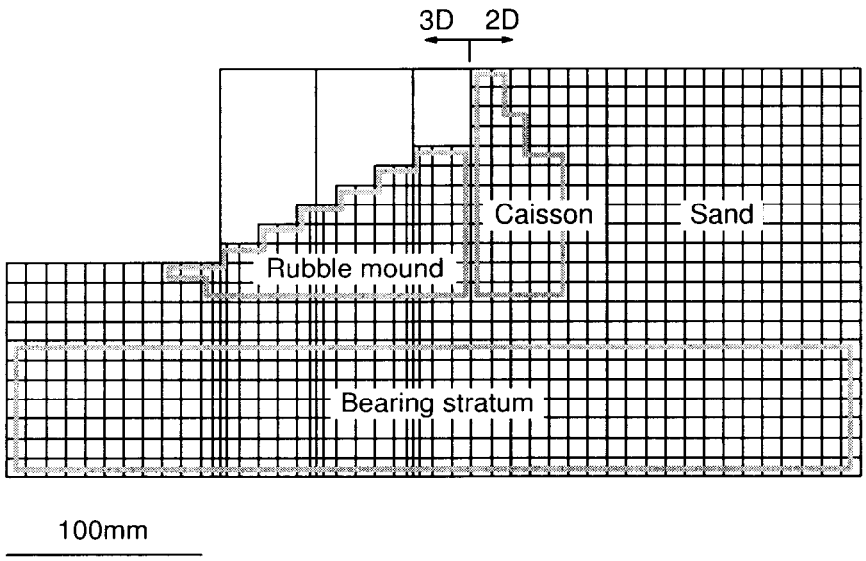

(b) Soil layers.

Figure 6.27: Finite element mesh and soil layers for piled wharf.

Table 6.4: Material parameters for numerical analysis on piled wharf.
(a) Material parameters for soil layers

Parameter	Sand layer	Rubble mound	Bearing stratum
G_s	2.65	2.69	2.64
e_0	0.79	0.81	0.76
κ	0.0013	0.001	0.0005
λ	0.0072	0.01	0.005
ν	0.33	0.33	0.33
ϕ	40°	47°	45°
ϕ_d	25°	25°	25°
μ	0.9	0.9	0.9
ϕ_b	30°	30°	30°
b_r	100	100	100
u_1	4	9	9
m_1	1	1	1
c	30	30	30
β_{ij0}	$\frac{\sigma_{ij0}-\sigma_{m0}\delta_{ij}}{(-\sigma_{m0})}$	$\frac{\sigma_{ij0}-\sigma_{m0}\delta_{ij}}{(-\sigma_{m0})}$	$\frac{\sigma_{ij0}-\sigma_{m0}\delta_{ij}}{(-\sigma_{m0})}$
$F_0/(-\sigma_{m0})$	1.2	2.4	2.4
s_{ij0}	$0.2\ \sigma_{ij0}$	$0.2\ \sigma_{ij0}$	$0.2\ \sigma_{ij0}$
k^* (m/s)	1.0×10^{-5}	1.4×10^{-3}	1.0×10^{-4}

$*$: With the methyl-cellulose-base solution.

(b) Material parameters for wharf members and caisson

Parameter	Pile	Deck	Approach bridge	Caisson
ρ (Mg/m^3)	7.92	7.64	2.71	2.50
E (GPa)	190	70	70	1.0
ν	-	-	-	0.27
I (mm^4)	8.88	764	13.3	-
A (mm^2)	1.51	91.7	40.0	-

hind the piles is one of the choices, while trail and error process is preferably needed to determine the 3D domain width. In order to satisfy consistencies of nodal forces and pore pressure in the interface between two– and three–dimensional analytical domains, the thickness of the solid element in the two–dimensional analytical domain is taken into account.

The planes x=0 and x=440mm were allowed to move freely in the y– and z–directions but not in the x–direction. The planes y=0 and y=25mm were allowed to move freely in the x– and z–directions but not in the y–direction. At the bottom plane z=0, all movements were restrained. Fluid flow velocities were set to zero at all the boundaries except at the surface of the ground.

The applied earthquake motion was similar to the wave obtained in the centrifuge test. In order to obtain the numerical solution, the differential equations are integrated along time. The integration

scheme used was Newmark's β method (cf. Appendix C), and the time step for the integration was Δt=0.0002sec. System damping was represented by Rayleigh damping, and the damping ratio was 1% in the first mode of free vibration of the system. The first vibration frequency of the system was 0.0056sec, 0.28sec in the prototype scale.

6.4.2 Acceleration and excess pore water pressure responses

Time histories of acceleration of the deck, AS3; excess pore water pressure at the rubble mound, P5; the sand layer beneath rubble, P2 & P4; and the backfill, P6, in the numerical and the physical model tests are illustrated in Fig. 6.28. The calculated acceleration record of the deck agrees with that in the centrifuge test. Regarding the excess pore water pressure responses, the numerical analysis results are essentially similar to those in the physical test. In the numerical analysis, pore pressure at the sand layer just beneath the rubble, P2, is smaller than that in the physical test, while that at the sand layer beneath the backfill, P4, shows rapid accumulation of pore pressure compared to the physical test.

Figure 6.29 shows contours of excess pore water pressure ratio in Sections A and A' at t=0.12sec and 0.24sec. The ratio is defined as the excess pore water pressure divided by the effective over burden pressure before an earthquake. The excess pore water pressure ratio beneath the caisson remained small in value, as the over burden pressure was relatively larger. Apart from the excess pore water pressure adjacent to the pile, remarkable differences between Section A and Section A', i.e. three-dimensional effects cannot be seen during or after the earthquake,

6.4.3 Displacements of wharf and ground

Time histories of lateral displacements of the piled deck and the caisson are shown in Fig. 6.30. The lateral displacements shown in these figures are measured at targets 30mm above the surface of the deck as shown in Fig. 6.25. In both the numerical and the physical tests, it is apparent from the figure that the caisson and the piled deck moved together in the early stage of shaking. The displacements of the caisson, however, became larger than those of the piled deck, a result of the relatively large tilting of the caisson. Permanent displacement of the wharf in the numerical analysis is 80% of that in the centrifuge test. The wharf in the centrifuge test shows a drastic increase in displacement in the early stage of shaking, while it gradually increases with time in the numerical analysis.

Figure 6.31 illustrates the deformation of the model ground in Section A at t=0.24sec. Comparing Fig. 6.31 to Fig. 2.22, the deformation pattern was seen to be almost the same in both the physical and the numerical model tests. Enlarged deformations around the wharf in Sections A, A', B & B' are shown in Fig. 6.32. The displacement scale in the figures is magnified by a factor of five. Relatively large lateral displacement gaps between the pile and the surrounding soils in the sea-side and the middle row were observed, while such gaps were small in the land-side row. In all the rows, lateral displacement of the rubble is larger than those of the piles, and the piles behaved as passive piles, while lateral pile displacements are larger than the soil displacement in the bearing stratum, and the piles behaved as active pile. The large seaward displacement of the rubble mound induced a rotational movement as well as the lateral deformation of the wharf. The pile in the sea-side row was penetrated into the bearing stratum, while that in the land-side row was pulled out, as shown in Fig. 6.32.

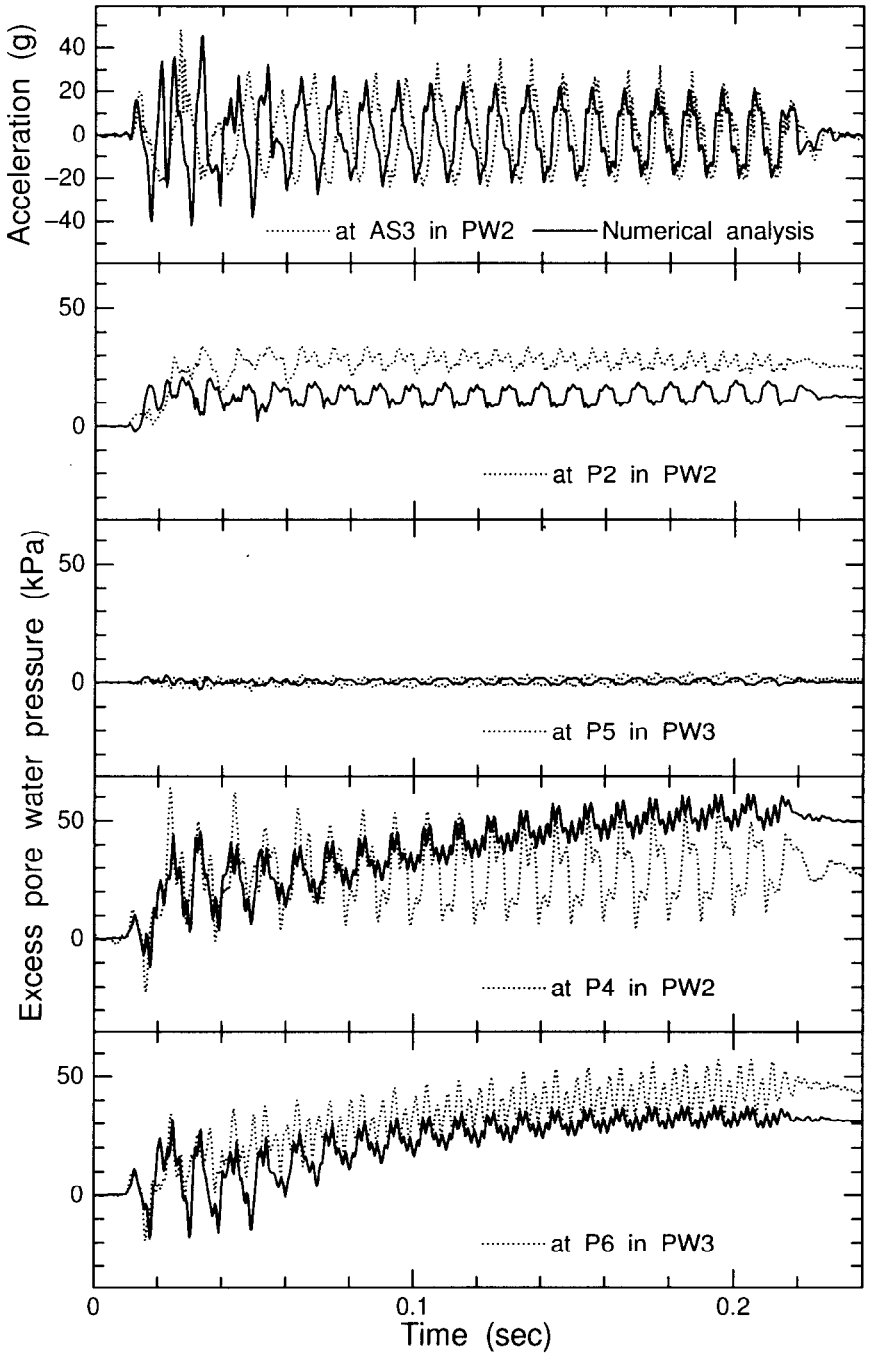

Figure 6.28: Time histories of acceleration at AS3 and excess pore water pressures at P2, P5, P4 & P6.

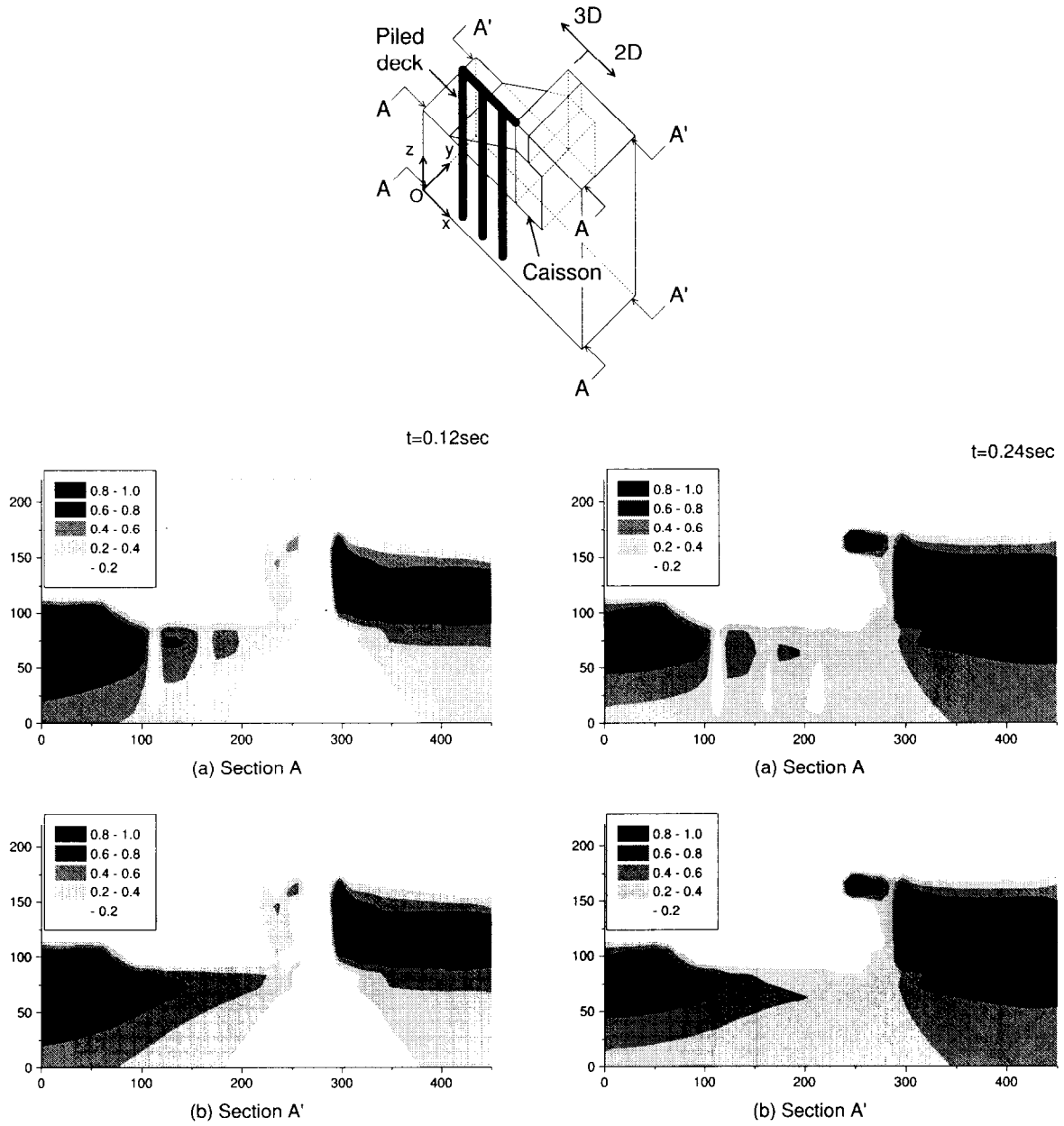

(a) t=0.12sec (during the earthquake). (b) t=0.24sec (after the earthquake).

Figure 6.29: Contours of excess pore water pressure ratio in Sections A & A'.

6.4.4 Model container side walls' effects on permanent deformation of wharf and ground

The permanent deformation of the model ground in Figs. 6.31 & 6.32 exhibits the ground heaving in front of the rubble mound. The side walls of the model container could restrain the deformation of the model ground, and this deformation restriction resulted in the seabed heaving. In order to

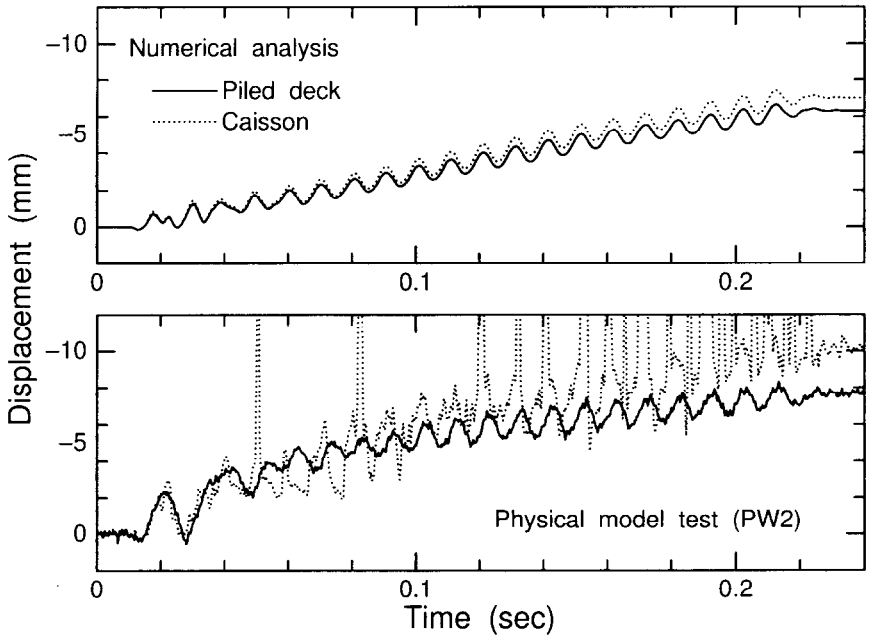

Figure 6.30: Time histories of lateral displacements of piled deck and caisson.

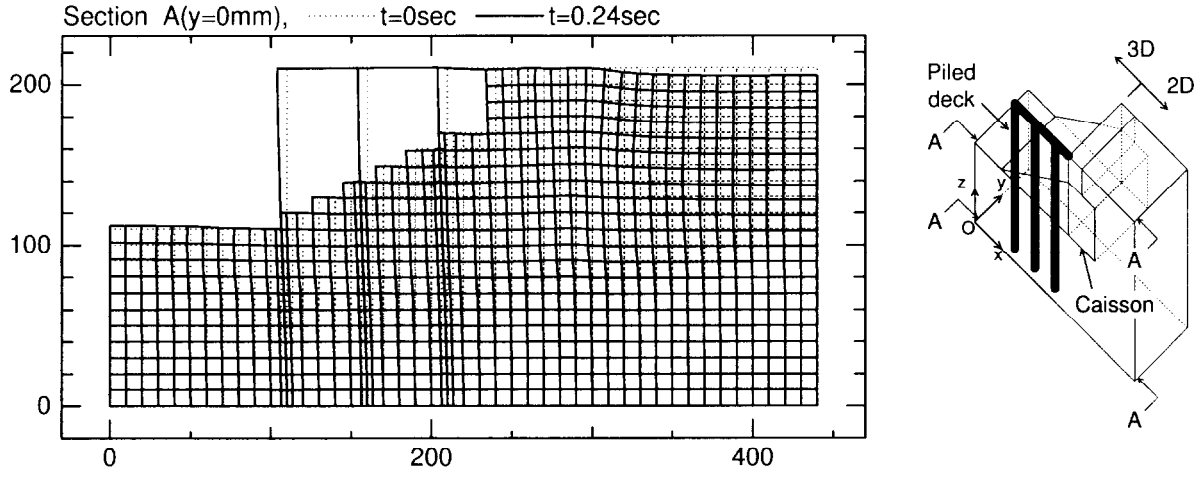

Figure 6.31: Deformation in Section A at t=0 & 0.24sec.

examine the model container side walls' effects on permanent deformation of the quay as well as the model ground, two-dimensional numerical analyses without the piled deck were conducted. In 2D FE analyses, the width of the model container was varied. One is the model whose width (W) is the same as that of the 3D FE analysis (W=440mm), and corresponds to case PW3 in Chapter 2. The other is the model with the double width of the 3D FE analysis (W=880mm).

Figure 6.33 shows the permanent deformations of the model ground for both the cases. The displacement scale in the figure is magnified by a factor of two. The large seabed heaving and backfill settlement were observed in the case of W=440mm, while the heaving and the settlement in the case of W=880mm were smaller than those in W=440mm. The quay wall and the rubble mound showed

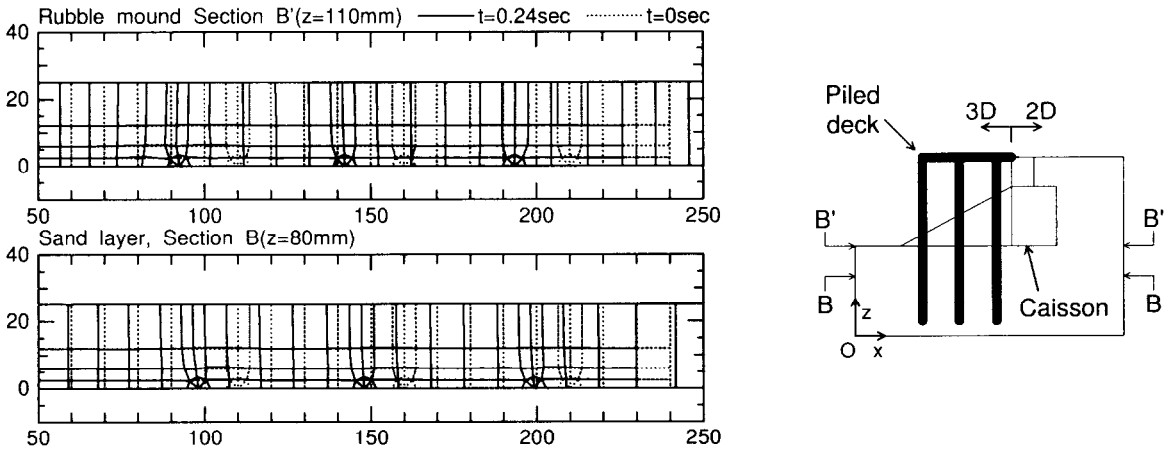

(a) Enlarged plan view in Section B & B'.

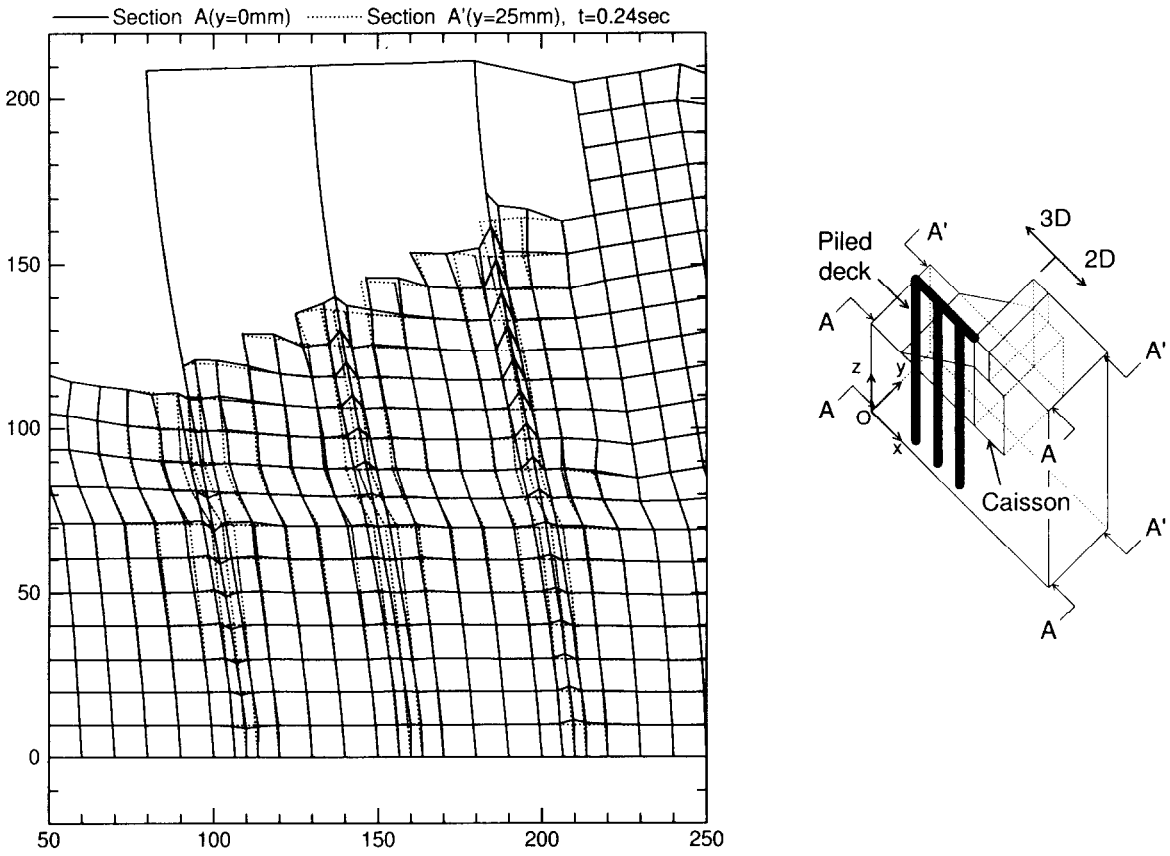

(b) Enlarged side view in Sections A & A'.

Figure 6.32: Enlarged deformations around wharf in Sections A, A', B & B', where displacement scale is magnified by a factor of five.

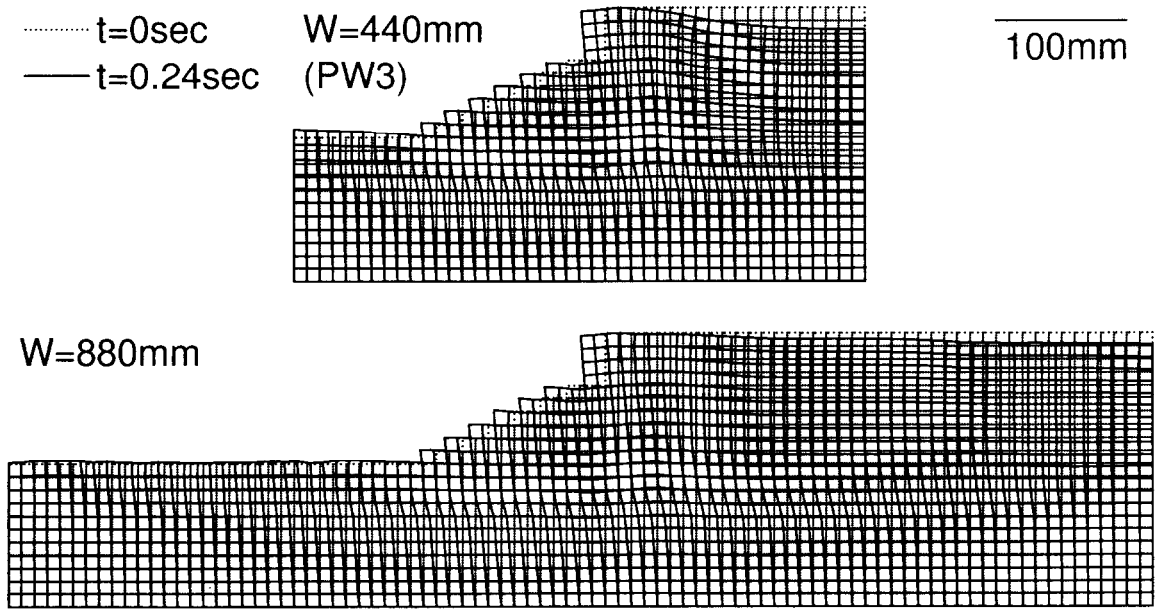

(a) Permanent deformations of model ground at t=0 & 0.24sec.

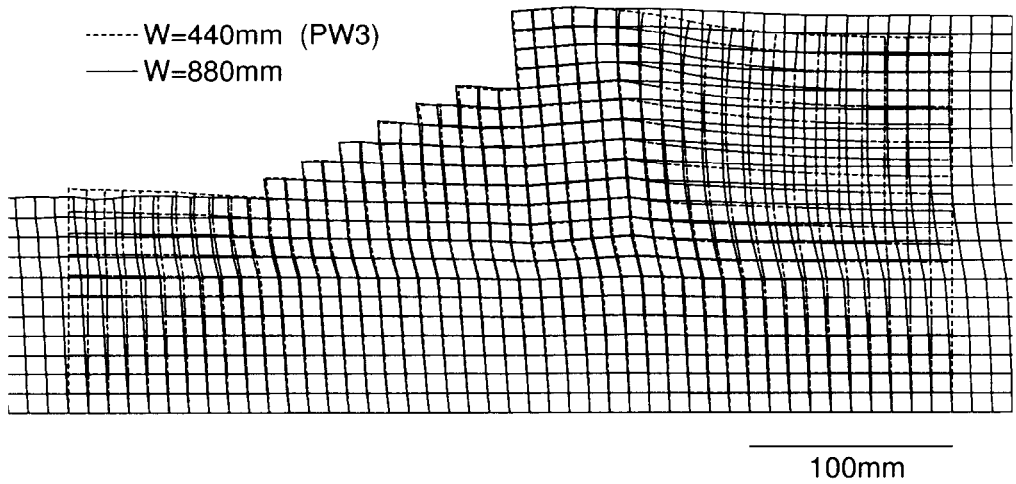

(b) Enlarged permanent deformations of model ground at t=0.24sec.

Figure 6.33: Permanent deformations of model ground in 2D FE analysis, where displacement scale is magnified by a factor of two.

almost the same permanent displacement in both the cases. This fact supports the conclusion that the wharf responses obtained in this study were not much affected by the side walls of the model container, while the distances of the model container side walls from the quay heavily influence the deformation of the ground, since the quay movement is the cause and the deformations of the backfill and the seabed are the consequence. Therefore, determining the width of the analytical domain behind the quay is important and has effects on the piled structure responses when the targeted piled structure is located behind the quay.

6.4.5 Responses of wharf members

Calculated strain distributions of piles along the depth just after shaking are shown in Fig. 6.34 together with the physical model test results. As shown in this figure, very large negative and positive strains appeared at the top of the piles and in the bearing stratum just below the sand layer. Though the bending strain distributions in the numerical analysis are similar to those in the centrifuge test, and the points where the large bending strain was observed agree with the locations where large deformation of piles were observed at the Kobe site as illustrated in Figs. 2.7 and 2.11, there are differences between the numerical and the physical test in the value of the maximum bending strain of the pile. In the physical test, the maximum bending strain appears at top of the pile in the sea-side row, while it appears in the land-side row in the numerical test. This may be caused by the difference in fixity of the pile heads; in the numerical analysis, the pile heads are rigidly fixed to the deck, while the actual fixity condition of the pile heads is uncertain, and the pile heads could not be perfectly fixed to the model deck in the physical test.

Variations of the axial strain and force of the pile tops in both the numerical and physical tests are shown in Fig. 6.35. The axial force shown in the figure is not for the half pile section but for the full section. The variations of the axial strain are essentially small, though small accumulations of the axial strain were observed in the numerical analysis. Comparing the axial and the bending strain variations, the effect of axial force variation on the pile deformation is relatively smaller than that of the bending moment, since the pile supporting mass is smaller than that of any other pile-supported structures. However, the axial force variation may affect the pile tip stability in the bearing stratum, as the penetration and the pulling out of the piles were observed in Fig. 6.32. Discussions on the pile tip stability will be made in the following subsection.

Variation of strains at the top of the piles, St9S & St9L (z=190mm), at the depth of the interface

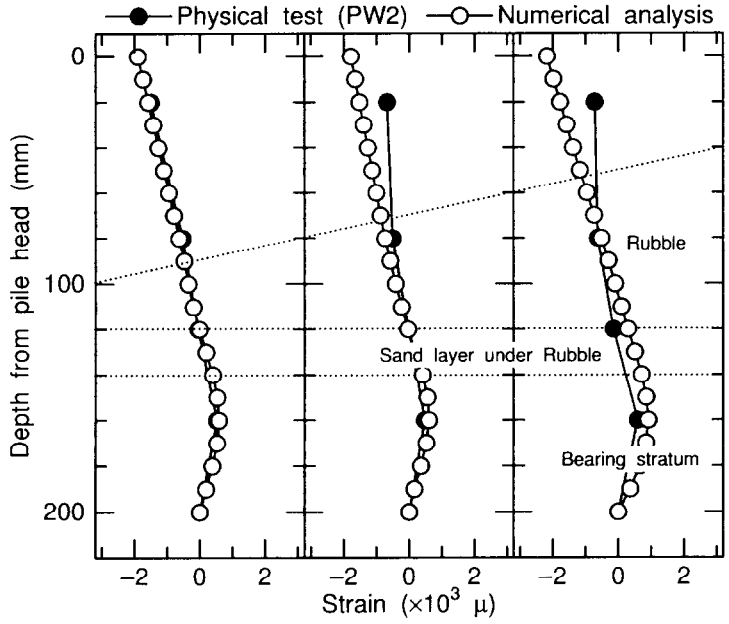

Figure 6.34: Permanent strain distributions of pile at t=0.24sec.

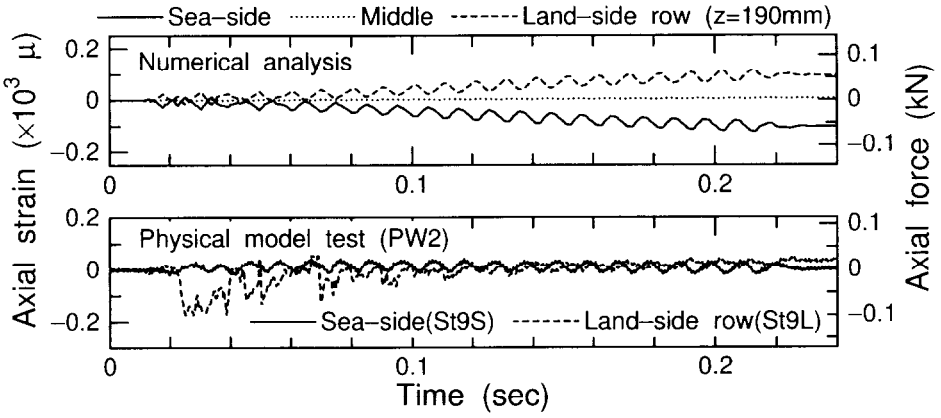

Figure 6.35: Variations of axial strain of pile.

between the sand layer and the rubble, St4S & St4L (z=90mm), and at the lower point of the pile in the bearing stratum just below the sand layer, St2S & St2L (z=50mm), are illustrated in Fig. 6.36 for the sea-side and the land-side rows. In measuring the pile strain in the physical test at z=190mm in the land-side row, a discontinuity was observed around t=0.03sec. (1) This discontinuity, and (2) the large fluctuation of the axial strain in the land-side row in the early stages of shaking in Fig. 6.35, supplies further evidence that the pile head was not perfectly fixed to the model deck as mentioned above.

Even taking this fact into account, the strains observed at the pile top, z=190mm, are larger than those in the ground. Though the amplitude of the pile strain at z=190mm in the numerical analysis is smaller than that in the physical test, variations of the pile strain are reasonably simulated by the numerical analysis. Both the larger amplitude and the larger permanent strain at the top of the piles suggests that the large deformation at the pile top initiated the failure of the wharf before the deformation at the lower portion of the pile around the sand layer under the rubble mound. This conclusion can be derived from both the numerical and the physical test and is consistent with the framed structure analysis result by Minami *et al.* (1997).

6.4.6 Ground responses at pile tips

As mentioned in the previous subsections, the penetration and the pulling out of the pile tips (Fig. 6.32) and the axial force variations of the piles (Fig. 6.35) were observed in the numerical analysis, while they were not remarkable in the physical model test. The pile tip stability in the bearing stratum must be taken into account in order to evaluate the seismic performance of the piled structures, though attentions are mainly paid to the lateral soil–pile interactions in this study. Figure 6.37 shows the variations of the mean effective stress and the stress paths at the pile tip. In the numerical analysis, the pile axial force was directly transferred to the pile tip, as the pile was modeled as the perfectly smooth pile, and no skin resistance could be expected. As a result, the mean effective stress at the pile tip in the sea-side row increased tenfold with large fluctuation and the stress path approached failure due to the piled deck tilting, while no remarkable stress variation was observed in the middle and the land-side rows.

Excessive settlement at the pile tip in the sea-side row and local failure of the soil around the tip

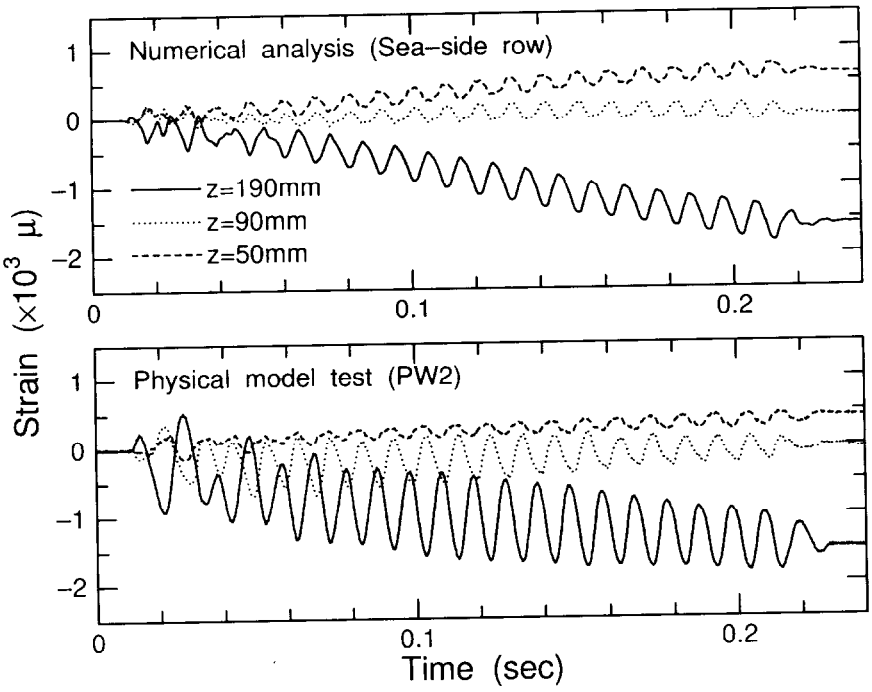

(a) Pile in sea-side row.

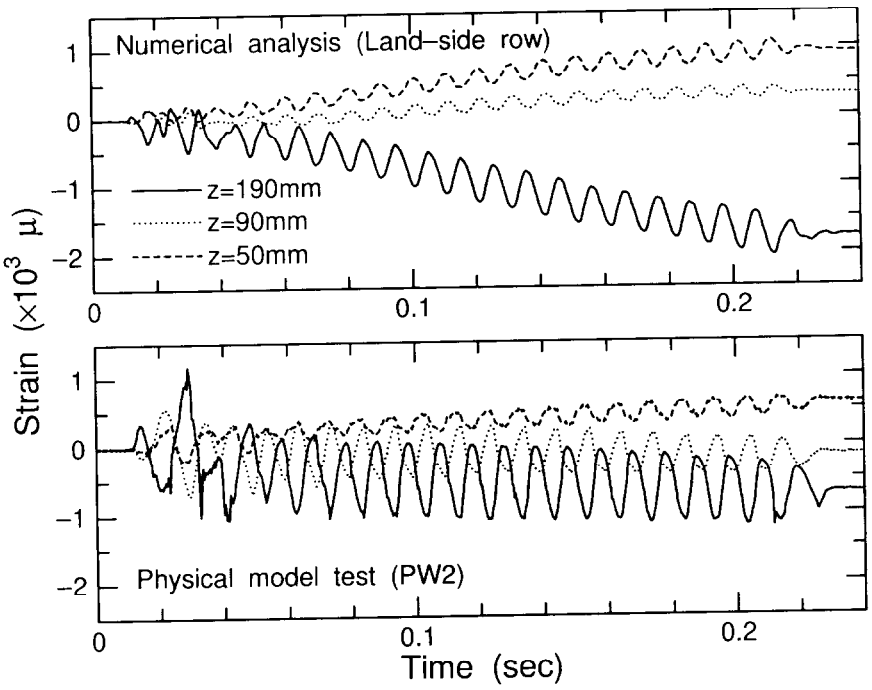

(b) Pile in land-side row.

Figure 6.36: Variations of bending strain of pile.

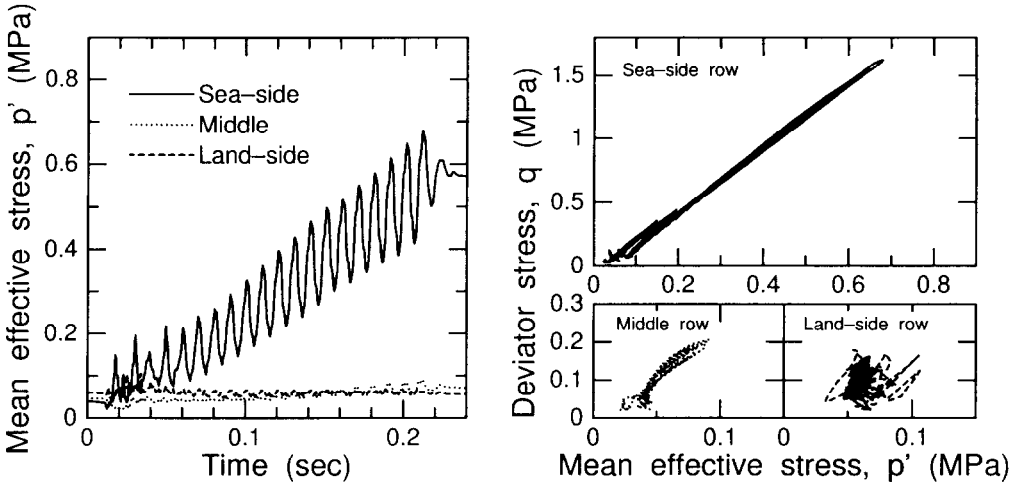

Figure 6.37: Variations of mean effective stress and stress paths at the pile tip.

were not observed, since the thickness of the soil layer beneath the pile tips was small, and the piles were modeled as closed-end piles in both the numerical analysis and the centrifuge model test. Even if the wider and deeper modeling domain is adopted, difficulties still remain in the pile tip modeling, especially in the modeling of the pile penetration. In the finite element analysis, the penetration of the open-end pipe piles cannot be modeled by the proposed pile modeling methods, as the soils are basically modeled as continuum, while they are usually used for the easy pile driving in actual sites. It is impossible to replicate precisely all the details of the prototype in the small-scale centrifuge model tests. All these facts indicate that the appropriate method to analyze the piled structure performance must be chosen on the basis of a proper understanding of the application scope.

6.4.7 *p–y* relations

Several *p–y* relations for laterally loaded piles have been proposed (e.g. Japan Road Association, 1996; Railway Technical Research Institute, 1997; American Petroleum Institute, 1993), where p is the lateral resistance of the soil and y is the relative displacement between the pile and soil. These proposed relations are basically formulated to fit lateral loading test results on piles in the field. In this subsection, *p–y* relations usually used in the simple method, i.e. the framed structure analysis subjected to soil movements through soil–pile interaction springs, were calculated from this finite element analysis result.

Figure 6.38 shows *p–y* relations obtained from the three-dimensional finite element analysis for three different soil layers. The relative displacement y is defined as the difference between the displacement of soil in Section A', u_g, and that of the pile in Section A, u_p, i.e. $y \equiv u_g - u_p$. When the relative displacement, y, is negative, seaward displacement of the soil is larger than that of the pile in this analysis. In the sand layer beneath the rubble, the lateral resistance is relatively smaller than that in the other layers, as large excess pore water pressure was accumulated though it was not perfectly liquefied as shown in Fig. 6.28. In all the layers, the lateral resistance showed an inclination to reach (or had already reached) an ultimate state when the earthquake motion approached the end.

The ultimate (maximum) lateral resistance, p_{max}, is usually characterized by a passive earth pres-

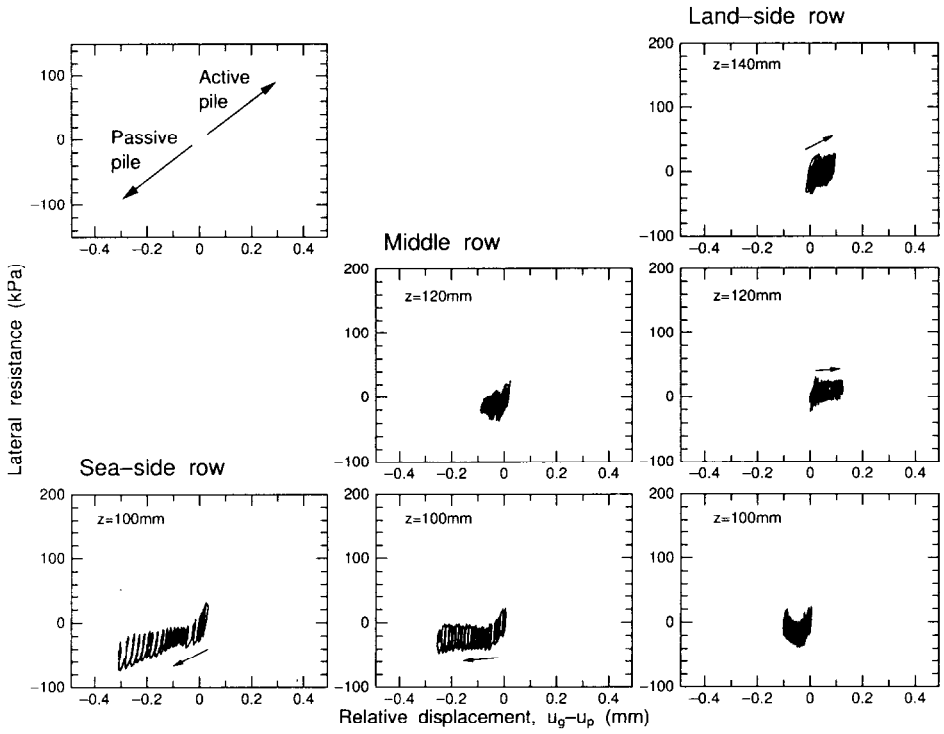

(a) Rubble mound.

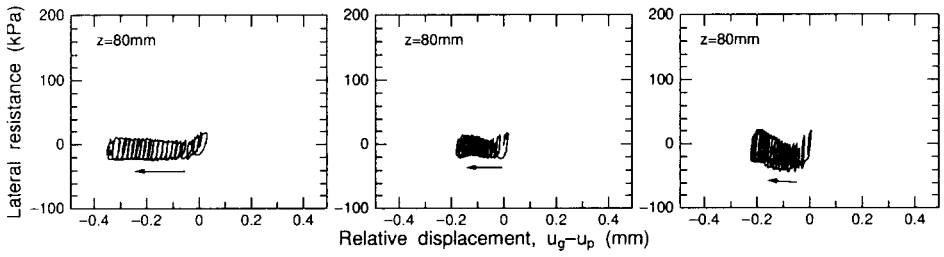

(b) Sand layer.

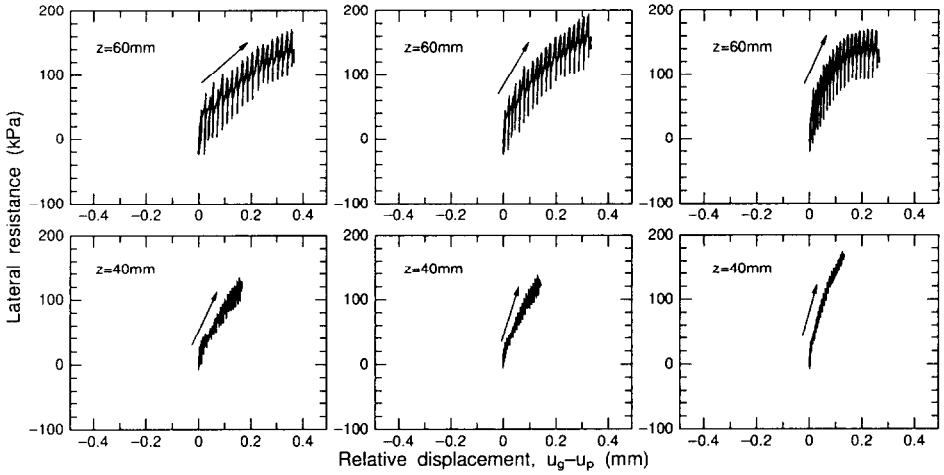

(c) Bearing stratum.

Figure 6.38: Relationships between lateral resistance and relative displacement obtained from FE analysis.

Table 6.5: Passive earth pressure coefficients obtained by the Coulomb theory for soil layers.

Soil layer	Internal friction, ϕ (deg.)	Slope angle, β (deg.)	K_p
Bearing stratum	45	0	5.83
Sand layer	40	0	4.60
Rubble mound	47	-26.6 (-1:2)	2.14
	47	0	6.44
	47	26.6 (1:2)	35.5

sure coefficient, K_p, multiplied by a 3D influence coefficient. For instance, Broms (1965) expressed the ultimate lateral resistance for a pile in sand as

$$p_{max} = 3K_p\sigma'_v \tag{6.12}$$

where σ'_v is the effective over burden pressure. In order to obtain the multiplying coefficient, the lateral resistance is normalized by σ'_v. The passive earth pressure coefficient without wall friction can be expressed by the Coulomb theory as

$$K_p = \frac{\cos^2\phi}{\left\{1-\sqrt{\frac{\sin\phi\sin(\phi+\beta)}{\cos\beta}}\right\}^2} \tag{6.13}$$

where ϕ is the internal frictional angle and β is the slope angle of the ground surface. The passive earth pressure coefficients for soil layers are summarized in Table 6.5. Passive earth pressure coefficient for the bearing stratum and the rubble is around six, when the slope angle of the ground is naught. The relationship between lateral resistance normalized by effective over burden pressure and relative displacement normalized by diameter of the pile is shown in Fig. 6.39 for three different soil layers.

In the bearing stratum, the ultimate normalized resistance is seen to be in the range of $K_p(\simeq 6)$ and $2K_p(\simeq 12)$ or more, where K_p is the passive earth pressure coefficient for level ground, i.e. β=0. The value of the ultimate normalized resistance depends on the depth and the location of the pile in the slope. The upper limit of the range in the bearing stratum, $2K_p$, corresponds to a design value for railway structures (Railway Technical Research Institute, 1997) and is close to the value of $3K_p$ that is a design value for highway bridges (Japan Road Association, 1996) and for port facilities (Japan Port and Harbour Association, 1998). These design values of ultimate lateral resistance seem to be not so far from the numerical analysis results, as is to be expected.

Meanwhile, in the rubble mound the ultimate normalized resistance is in the range of $0.1K_p(\simeq 0.5)$ and $0.6K_p(\simeq 4)$ except at the toe of the mound slope. The ultimate normalized resistance in the rubble mound is remarkably smaller than that in the bearing stratum. Determination of the passive earth pressure coefficient, K_p, and the 3D influence coefficient for the ultimate lateral resistance of the pile is still open to dispute, as the influence of sloping ground on lateral resistance is not yet clear. In the physical modeling, Terashi *et al.* (1991) examined the influence of sloping ground on lateral resistance in dry sand by centrifuge model tests, and the result revealed that the reduction

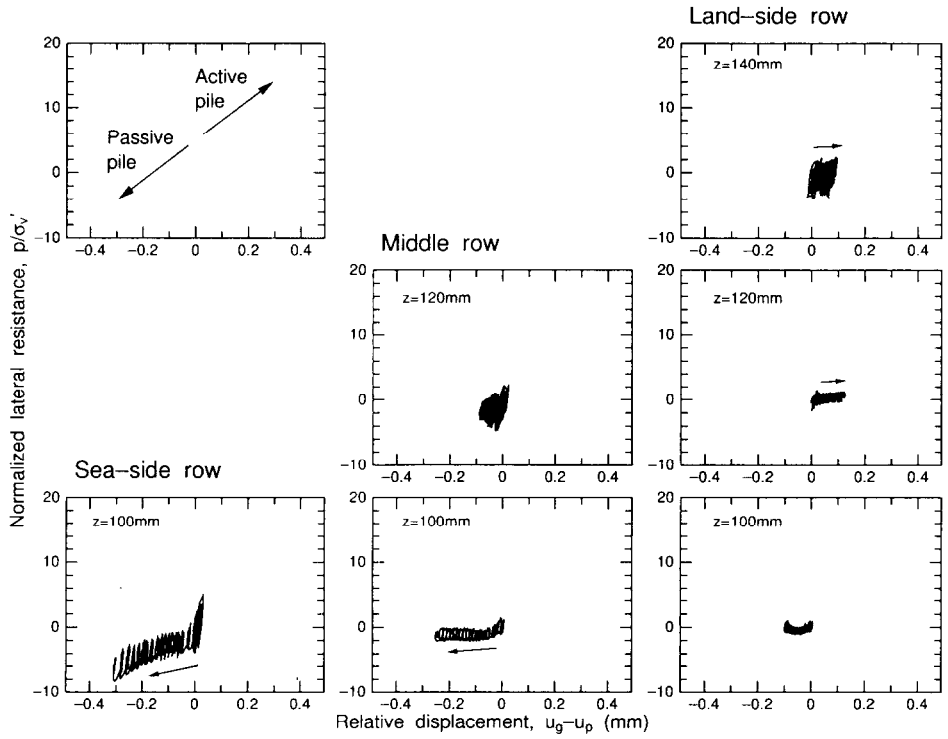

(a) Rubble mound.

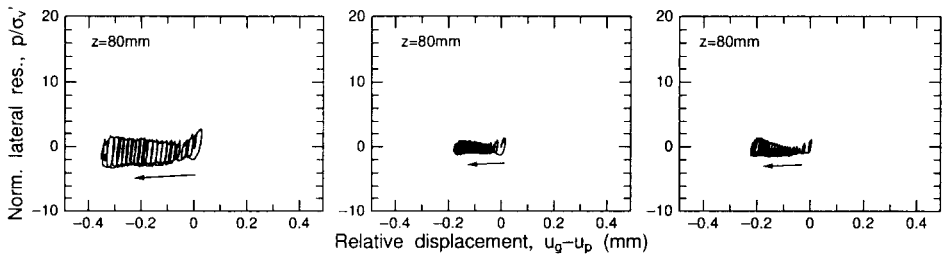

(b) Sand layer.

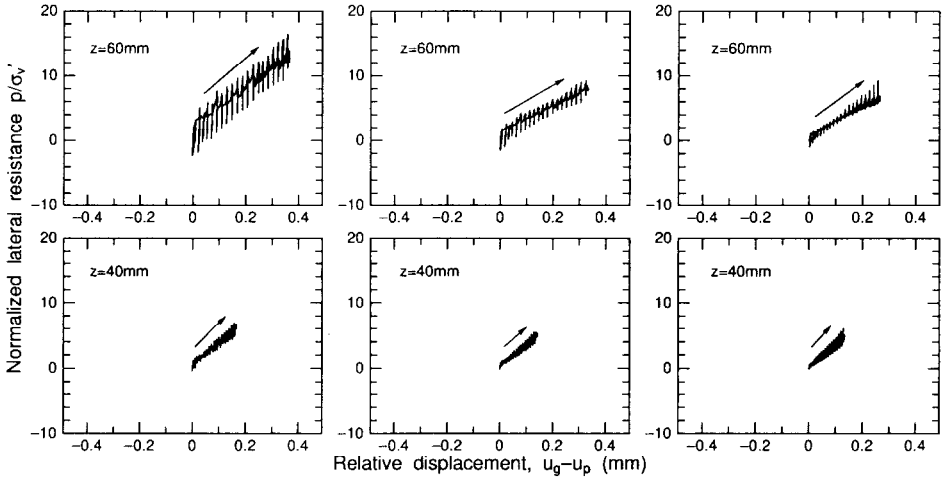

(c) Bearing stratum.

Figure 6.39: Relationships between normalized lateral resistance and relative displacement obtained from FE analysis.

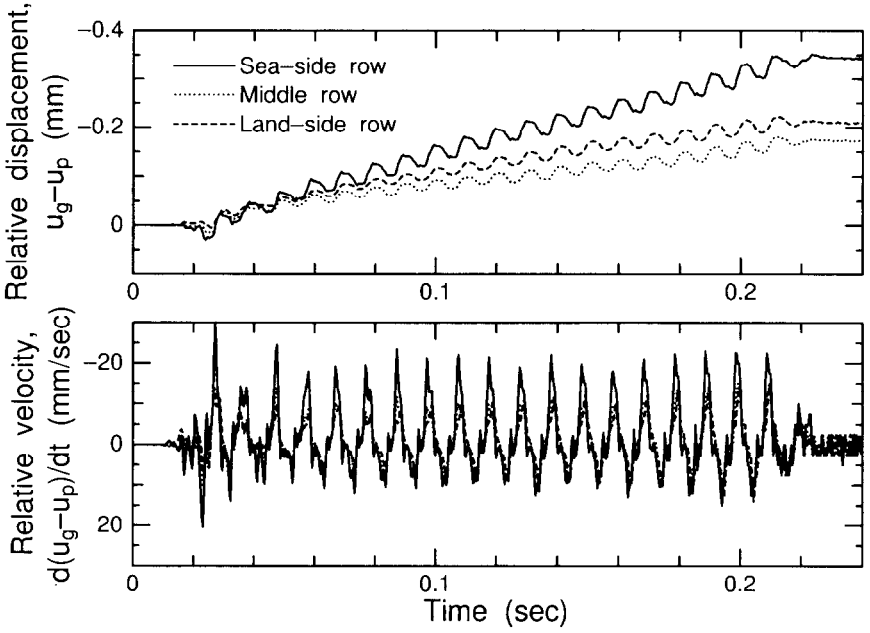

Figure 6.40: Variations of relative displacement and relative velocity in sand layer.

factor of ultimate resistance in sloping ground compared to that in level ground can be formulated by an exponential function, i.e. when a pile is in sloping ground, the resistance in a shallower portion is extensively smaller than that in a deeper portion.

In the design standard for port facilities in Japan, lateral resistance of piles in the upper half of the rubble is neglected, and only that in the lower portion is considered, i.e. the rubble resists the pile movement below a virtual slope surface passing through the mid-height points of the slope. This assumption is on the safe side, only if the lateral resistances of the piled deck against an inertial force of the deck during an earthquake or lateral shiploads are considered. However, as shown in Figs. 6.38 and 6.39, even in the upper half of the rubble mound the piles resist movement of the rubble. According to the numerical analysis result, lateral resistance of piles should be considered even above the virtual surface when the rubble moves seaward due to liquefaction of foundation soils.

For the sake of comparison between the relations obtained from FE analysis for the liquefiable sand layer and that directly measured in the model tests in Chapter 3, relative velocity of the surrounding soil against the pile and the normalized lateral resistance are calculated. Variations of relative displacement and velocity of the surrounding soil against the pile are illustrated in Fig. 6.40. A negative value in relative displacement indicates that the permanent displacement of the soil is larger than that of the pile. Except the pile in the land-side row, the values were positive, the pile being passive pile. In the land-side row, the value was positive in the first half of shaking, while it became negative in the last half, and the pile behaved as an active pile. The maximum velocity of the pile was around 20mm/sec. Figure 6.41 shows relationships between lateral resistance normalized by the initial over burden pressure and relative displacement obtained from FE analysis in the sand layer. As shown in the figure, the maximum normalized resistance is in the range of 0.5 to 1.5 and is consistent with the direct measured resistance in Chapter 3, though relative displacements are smaller than those

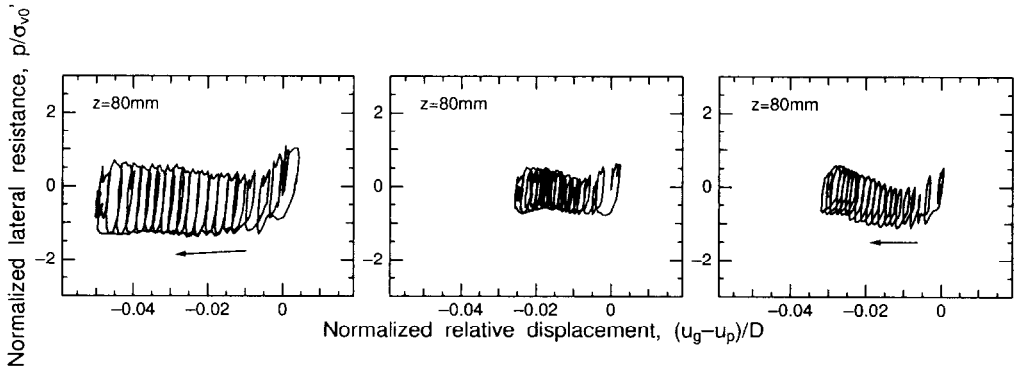

Figure 6.41: Relationships between normalized lateral resistance and relative displacement obtained from FE analysis in sand layer.

in the physical model tests.

According to the lateral resistance–relative displacement relations obtained by the FE analysis, regular *p–y* relations cannot be applicable to a piled structure in sloping ground even though sloping ground effects are taken into account. Three-dimensional finite element analysis can be a productive procedure for the evaluation of soil–pile interaction related problems in geometrically complicated ground.

6.4.8 Summary of simulation of model test on pile-supported wharf

Three-dimensional finite element analysis on a pile-supported wharf was conducted to evaluate soil–pile interaction during an earthquake and to verify the performance of the pile modeling technique. The numerical analysis results were similar to the physical results, and the numerical analysis could capture the overall response of the pile-supported wharf as well as the response of the soils surrounding the wharf. These results reveal that the proposed connection method between pile and soil performs well even for the numerical analysis on the liquefaction problem.

Three-dimensional FE analysis requires a large number of freedoms to model a targeted structure and the surrounding soils. Since reducing the number of freedoms in 3D numerical analysis is desired to obtain a numerical analysis result in a matter of hours or a day, a hybrid analytical domain that consists of two– and three–dimensional analytical domains was introduced: As the soil–pile interaction is a typical three-dimensional problem, the ground near the pile-supported wharf is modeled in three-dimensions, while the gravity type caisson and its backfill is modeled in two-dimensions, as the length of the quay wall is usually long enough to be modeled in 2D. With this hybrid method, the number of nodes can be reduced by 40% from a full 3D analysis in this particular case.

In order to evaluate soil–pile interaction in terms of the *p–y* relation that is usually used in conventional analysis, *p–y* relations were calculated from this finite element analysis result. In the non-liquefiable layers, ultimate normalized resistances of piles obtained by FE analysis in the layer just below the liquefying soil are in the range of those in practical design codes in Japan, while they are apparently smaller in the sloping rubble mound. Determination of the passive earth pressure coefficient, K_p, and the 3D influence coefficient for the ultimate lateral resistance of a pile is still open to dispute. In the liquefiable layer, the maximum normalized resistance is in the range of 0.5 to 1.5 and

though the relative displacement is smaller, it is consistent with the direct measured resistance in the physical model tests.

6.5 Summary

In this chapter, pile modeling methods using three-dimensional finite element analysis are proposed which consider the effect of the pile volume on the soil–pile interaction and the slippage between the pile surface and adjacent soils. In the modeling of the pile, two types of pile surface conditions are considered, i.e. perfectly smooth and rough conditions. The modeling of these two conditions can be achieved only by imposing particular boundary conditions or connecting the pile and soil using truss elements, both of which are implemented in ordinary FE analysis codes for smooth and rough surface piles, respectively. The proposed methods are applied to several centrifuge model tests, and the performance of the pile modeling method is verified. In order to reduce the number of freedoms in the three-dimensional FE analysis, a hybrid analytical domain that consists of two– and three–dimensional analytical domains was introduced. The following conclusions are derived:

- The analysis on the active pile agreed with the physical model test in both load–displacement relation and the bending strain distributions, while the numerical analysis on the passive pile did not agree as closely as the active pile case, though the results were similar to the physical test results and captured the overall response of the pile. These results indicate that the proposed modeling method is applicable to soil–pile interaction problems under static load.

- Behavior of the pile-supported wharf installed into the liquefiable soil and subjected to earthquake motion was also simulated. The numerical analysis result reveals that the proposed connecting method between pile and soils performs well even for liquefaction problems.

- Soil–pile interaction during an earthquake was examined in terms of the p–y relation that is usually used in conventional analysis. In the non-liquefiable layer, ultimate normalized resistance of the pile obtained by the FE analysis in the layer just below the liquefying soil is in the range specified in practical design codes in Japan, while they are apparently smaller in a sloping rubble mound. Determination of the passive earth pressure coefficient, K_p, and the 3D influence coefficient for the ultimate lateral resistance of a pile is still open to dispute. In the liquefiable layer, the maximum normalized resistance is consistent with the direct measured resistance in model tests of Chapter 3, though the relative displacements are smaller than those in the model tests.

- In order to reduce the number of freedoms in the numerical analysis on pile-supported wharf, a hybrid analytical domain that consist of two– and three–dimensional analytical domains was introduced. With this hybrid method, the number of nodes can be reduced by 40% from a full 3D analysis in this particular case.

Chapter 7

Conclusions

In this dissertation, soil–pile interaction in liquefaction-induced lateral spreading of soils has been investigated. Detailed observation of a pile-supported wharf in liquefaction-induced laterally spreading soil has been made through shaking table tests in a centrifuge. Following the shaking table tests, soil–pile interactions in liquefied and non-liquefied soils have been experimentally investigated through pile loading tests with newly developed apparatuses. Based on the result of these physical model tests, pile-modeling methods for large soil movements during earthquakes in three-dimensional finite element analysis have been proposed.

The conclusions obtained from the present study are as follows:

In ***Chapter 2***, centrifuge model tests were carried out to investigate the dynamic behavior of a pile-supported wharf in front of backfilled gravity type caissons, focusing on the failure mechanism of the piles, the effects of liquefaction in the backfill and underlying sand layer on the permanent deformation of the wharf during earthquakes, and the dynamic interaction between the piled deck and caisson through the approach bridge. The targeted piled structure is the pile-supported wharf damaged in the 1995 Hyogo-ken Nambu Earthquake at Takahama, Kobe.

Liquefaction of the foundation soil and the backfill behind the caisson during an earthquake causes large seaward lateral movement of the rubble mound. As a result, a large horizontal displacement gap was formed between the rubble mound and the bearing stratum. This displacement gap caused a very large bending moment at the pile top and in the bearing stratum just below the sand layer. These locations where large bending moments were observed agreed with the locations where large pile deformations were observed at the Kobe site. Centrifuge model tests could have reasonably predicted the failure mode of the piled wharf observed in the Kobe Earthquake.

The test results with and without the approach bridge connecting the deck of the wharf and the caissons revealed that the plate accelerated the seaward movement of the wharf during the earthquake, as the landward movement of the deck was prevented by the caisson through the plate.

Varying the thickness of the sand layer under the rubble mound caused a change of the deformation mode of both ground and structures. The test without the sand layer showed no displacement gap between the rubble mound and the bearing stratum, resulting in small permanent displacement of the wharf, while the thicker liquefiable sand layer does not necessarily cause the large deformation of soils and structures.

Chapter 3 shows lateral loading test results on a buried cylinder which reveal the lateral resistance of the pile in liquefying soil. The tests focus on observing the deformation of the soil surrounding the pile when a large relative displacement between the pile and the soil was induced. The lateral resistance of the pile in the liquefying soil is directly measured by a newly developed testing apparatus. The new pile loading system has the capability of applying horizontal cyclic vibrations to the pile during an earthquake and allowing observation of the deformation of the liquefying sand surrounding the pile.

The deformation of the soil surrounding the cylinder was successfully observed by video camera through the transparent window of the box. Without ground vibration, a large amount of soil in front of the cylinder moved forward, while deformation of the soil was quite limited in the vicinity of the cylinder when ground vibration was applied. The difference in the deformation mode of the soil affected the lateral resistance of the cylinder.

The loading rate effect on the lateral resistance of a pile in liquefied soil was also investigated. Larger lateral resistance is mobilized as the loading rate becomes higher. Furthermore, when the loading rate is higher, the cylinder displacement required for recovery of the shear strength becomes smaller. These tendencies are associated with not only the dilatancy characteristics of sand but also pore fluid migration around the cylinder. All indications in this study support that the hydraulic conductivity of the soil in relation to the loading rate is the important factor for the mobilization of the lateral resistance of piles in liquefied soils. Thus, the soil–water coupled analysis is essentially needed for the evaluation of the lateral resistance of buried structures in liquefying soil.

A active type shear box in a centrifuge is developed to investigate the behavior of structures subjected to large soil movements in ***Chapter 4***. The experimental study in this chapter particularly focuses on failure or deformation of the piles due to lateral movement of the soil. Therefore, inertial effects of soil and piles were neglected, and a quasi-static condition was assumed. With this system, deformation of the shear box can be controlled, and any ground displacement can be entered as input data without inertial effects, though stress conditions of the soil in the box are different from the ideal condition, i.e. ground motion during an earthquake. In order to investigate the effect of the geometry of the shear box on the deformation and stress conditions of the soil in it, simple two dimensional finite element analyses were carried out. The numerical analysis results reveal that a laminar box with the aspect ratio of 2 to 3 is better to use for tests with dense sand, considering both deformation control and stress conditions of the soil.

In advance of the pile-loading test, centrifuge tests on the shear box filled with dense sand were carried out to examine the deformation of the soil in the shear box. Ground displacement at the center of the model became almost 70–80% of the input value, and the curve shape of the ground displacement distribution was smoother than that of the laminae. After the preliminary tests, behavior of the pile subjected to two types of large soil deformations was examined. The test results showed that the response of the pile is very sensitive to the ground displacement and the type of ground motion.

The active type shear box has adequate capability in modeling the intended strain fields in soils. The active type shear box could be a valuable tool for studying soil–structure interaction during an earthquake, though further improvements of the apparatus and detailed numerical analyses are needed in order to interpret the test results properly.

Chapter 5 introduces the governing equations for dynamic porous solid–pore fluid interaction and the constitutive model proposed by Hashiguchi *et al.* (1996, 1998), which can describe the monotonic and cyclic loading behavior of sand, including soil liquefaction behavior. The sensitivity of each parameter of the constitutive model was examined one by one using the finite difference method in order to understand how the variation of the parameters affect soil behavior.

Also in this chapter, a new finite element analysis code is developed based on the equations governing the dynamic porous solid–pore fluid interaction in u–p formulation which incorporate the constitutive model proposed by Hashiguchi *et al.* In order to examine the applicability of the analysis code to liquefaction problems, a numerical simulation was conducted of the centrifuge model test on the caisson type quay wall subjected to backfill liquefaction. The numerical analysis result reveals that the present procedure has fundamental applicability in the analysis of no flow liquefaction problems, though some limitations and inconsistencies are recognized in the comparison between the numerical analysis and the centrifuge model test results.

In ***Chapter 6***, pile modeling methods using three-dimensional finite element analysis are proposed, considering the pile volume effect on the soil–pile interaction and the slippage between the pile surface and the adjacent soils. In modeling a pile, two types of pile surface conditions, i.e. perfectly smooth and rough conditions, are considered. Modeling these two conditions can be achieved only by (1) imposing particular boundary conditions or (2) connecting the pile and soil using truss elements, for piles with smooth and rough surfaces, respectively. The proposed methods are applied to several centrifuge model tests, and the performance of the pile modeling methods are verified.

The analysis on active piles agreed well with the physical model test in both the load–displacement relation and the bending strain distributions, while the numerical analysis on passive pile did not agree as closely as the active pile case, though the results were similar to the physical test results and captured the overall response of the pile. These results indicate that the proposed modeling method is applicable to soil–pile interaction problems under static load.

Behavior of a pile-supported wharf installed into liquefiable soil and subjected to earthquake motion was also simulated. The numerical analysis result reveals that the proposed connecting method between pile and soils performs well even for liquefaction problems. Soil–pile interaction during an earthquake was examined in terms of the p–y relation that is usually used in conventional analysis. In a non-liquefiable layer, ultimate normalized resistance of the pile obtained by FE analysis in the layer just below the liquefying soil is in the range of those in practical design codes in Japan, while they are apparently smaller in a sloping rubble mound. Determination of the passive earth pressure coefficient, K_p, and the 3D influence coefficient is still open to dispute. In a liquefiable layer, the maximum normalized resistance is consistent with the measured resistance in model tests of Chapter 3, though the relative displacements are smaller than those in the model tests.

In order to reduce the number of freedoms in the numerical analysis on pile-supported wharf, a hybrid analytical domain that consist of two– and three–dimensional analytical domains was introduced. With this hybrid method, the number of nodes can be reduced by 40% from a full 3D analysis in this particular case.

Bibliography

Abdoun, A. & Dobry, R. 1998. Seismically induced lateral spreading of two-layer sand deposit and its effect on pile foundations, *Proceedings of the International Conference Centrifuge 98*, Vol.1, 321–328.

American Petroleum Institute. 1993. Recommended practice for planning, designing and constructing fixed offshore platforms, *API RP 2A-WSD, 20th ed.*.

Biot, M.A. 1956a. Theory of propagation of elastic waves in a fluid-saturated porous solid, Part I–Low-frequency range, *Journal of the Acoustical Society of America*, Vol.28, No.2, 168–178.

Biot, M.A. 1956b. Theory of propagation of elastic waves in a fluid-saturated porous solid, Part II–High-frequency range, *Journal of the Acoustical Society of America*, Vol.28, No.2, 179–191.

Biot M.A. 1962. Mechanics of deformation and acoustic propagation in porous media, *Journal of Applied Physics*, Vol.33, No.4, 1482–1498.

Broms, B.B. 1965. Design of laterally loaded piles, *Journal of Soil Mechanics Division, ASCE*, Vol.91, SM3, 79–99.

Castro, G. 1969. Liquefaction of sands, *Ph.D. Thesis, Harvard Soil Mechanics Series*, No.81.

Chen, L.T., Poulos, H.G. & Hull, T.S. 1997. Model tests on pile groups subjected to lateral soil movement, *Soils and Foundations*, Vol. 37, No. 1, 1–12.

Chan, A.H.C. 1988. *A unified finite element solution to static and dynamic geomechanics problems*, PhD Dissertation, University College of Swansea.

Dafalias, Y.F. & Herrmann, L.R. 1982. Bounding surface formulation of soil plasticity, *Soil Mechanics–Transient and cyclic loads*, 253–282, John Wiley & Sons, Chichester.

Dafalias, Y.F. 1994. Overview of constitutive models used in VELACS, *Proceedings of the International Conference on the Verification of Numerical Procedures for the Analysis of Soil Liquefaction Problems*, Vol.2, 1293–1303.

Dobry, R., Taboada, V. & Liu, L. 1997. Centrifuge modeling of liquefaction effects during earthquake, *Proceedings of the 1st International Conference on Earthquake Geotechnical Engineering (IS-Tokyo'95)*, Vol.3, 1291–1324.

Egan, J.A., Hayden, R.F., Scheibel, L., Otus, M. and Serventi, G.M. 1992. Seismic repair at Seventh Street Marine Terminal, *Proceedings of the 1992 ASCE Specialty Conference on Grouting, Soil Improvement and Geosynthetics*, Vol.2, 867–878.

Fujii, S., Isemoto, N., Satou, Y., Kaneko, O., Funahara, H., Arai, T. & Tokimatsu, K. 1998. Investigation and analysis of a pile foundation damaged by liquefaction during the 1995 Hyogoken-Nambu Earthquake, *Soils and Foundations, Special Issue on Geotechnical Aspects of the Jan. 17, 1995 Hyogoken-Nambu Earthquake*, No. 2, 179–192.

Fukutake, K, Ohtsuki, A. & Fujikawa, S. 1993. Three-dimensional liquefaction analysis of shaking table test on soil–structure interaction *Proceedings of the 22th JSCE Earthquake Engineering Symposium*, 595–598 (in Japanese).

Garnier, J. & Konig, D. 1998. Scale effects in piles and nails loading tests in sand, *Proceedings of the International Conference Centrifuge 98*, Vol.1, 205–210.

Goodman, R.E. & Taylor, R.L. 1968. A model for the mechanics of jointed rock, *Journal of the Soil Mechanics Division, ASCE*, Vol.94, SM3, 637–659.

Great Hanshin Earthquake investigation committee of JGS. 1996. *Investigative report on Great Hanshin-Awaji Earthquake*, The Japanese Geotechnical Society.

Hamada, M., Ohtomo, K., Sato, H. & Iwatate, T. 1992. Experimental study of effects of liquefaction-induced ground displacement on in-ground structure, *Proceedings of the 4th Japan-US Workshop on Earthquake Resistant Design of Lifeline Facilities and Countermeasures for Soil Liquefaction*, Technical Report NCEER-92-0019, Vol.1, 481–492.

Hamada, M., Isoyama, R. & Wakamatsu, K. 1996. Liquefaction-Induced Ground Displacement and Its Related Damage to Lifeline Facilities, *Soils and Foundations, Special Issue on Geotechnical Aspects of the Jan. 17 1995 Hyogoken-Nambu Earthquake*, No.1, 81–97.

Hamada, M. & Wakamatsu, K. 1998. Liquefaction-induced ground displacement triggered by quay-wall movement, *Soils and Foundations, Special Issue on Geotechnical Aspects of the Jan. 17 1995 Hyogoken-Nambu Earthquake*, No.2, 85–95.

Hashiguchi, K., Ueno, M. & Chen, Z.P. 1996. Elastoplastic constitutive equation of soils based on the concepts of subloading surface and rotational hardening, *Journal of Geotechnical Engineering, JSCE*, III-36, No.547, 127–144 (in Japanese).

Hashiguchi, K. & Chen, Z.P. 1998. Elastoplastic constitutive equation of soils with the subloading surface and the rotational hardening. *International Journal for Numerical and Analytical Methods in Geomechanics*, Vol.22, 197–277.

High Pressure Gas Safety Institute of Japan. 2000. *Recommended practices for earthquake resistant design of gas pipelines* (in Japanese).

Hiro-oka, A., Okamura, M., Takemura, J. & Kimura, T. 1995. Dynamic behaviors of compacted sands surrounded by liquefied loose sand, *Proceedings of the 1st International Conference on Earthquake Geotechnical Engneering*, Vol. 2, 681–686.

Horikoshi, K., Tateishi, A. & Fujiwara, T. 1998. Centrifuge modeling of a single pile subjected to liquefaction-induced lateral spreading, *Soils and Foundations, Special Issue on Geotechnical Aspects of the Jan. 17 1995 Hyogoken-Nambu Earthquake*, No. 2, 193–208.

Iai, S. 1989. Similitude for shaking table tests on soil–structure–fluid model in 1g gravitational field, *Soils and Foundations*, Vol.29, No.1, 105–118.

Iai, S. & Sugano, T. 1999. Soil–structure interaction studies through shaking table tests, *Proceedings of the 2nd International Conference on Earthquake Gotechnical Engineering*, Vol.3, 927–940.

Inagaki, H., Iai, A., Sugano, T., Yamazaki, H. & Inatomi, T. 1996. Performance of caisson type quay walls at Kobe port, *Soils and Foundations, Special Issue on Geotechnical Aspects of the Jan. 17 1995 Hyogoken-Nambu Earthquake*, No.1, 119–136.

Ishihara, K. 1985. Stability of natural deposits during earthquakes, *Proceedings of the 11th International Conference on Soil Mechanics and Foundation Engineering*, Vol.1, 327–376.

Ishihara, K. 1993. Liquefaction and flow failure during earthquakes, *Géotechnique*, Vol.43, No.3, 351–415.

Ishihara, K., Yasuda, S. & Nagase, H. 1996. Soil characteristics and ground damage, *Soils and Foundations, Special Issue on Geotechnical Aspects of the Jan. 17 1995 Hyogoken-Nambu Earthquake*, No.1, 109–118.

Ishihara, K., Tatsuoka, F. & Yasuda, S. 1975. Undrainded deformation and liquefaction of sand under cyclic stresses, *Soils and Foundations*, Vol.15, 29–44.

Japan Association for Steel Pipe Piles. 1995. *Investigative report on steel pipe piles damaged in the 1995 Hyogo-ken Nambu Earthquake* (in Japanese).

Japan Port and Harbour Association. 1998. *Supplements for design standards for port and harbour structures* (in Japanese).

Japan Road Association. 1996. *Seismic design specifications of highway bridges* (in Japanese).

Japan Society of Civil Engineers. 2000. *Earthquake resistant design codes in Japan*, JSCE, Tokyo.

Kimura, M., Yashima, A. & Shibata, T. 1991. Three-dimensional finite element analysis of laterally loaded piles, *Proceedings of the International Conference on Computer Method and Advance in Geomechanics*, 145–150.

Koda, M. 2000. Study on lateral resistance of single pile subjected to lateral load on pile top, *Dr.Eng. Thesis, Tokyo Institute of Technology.*

Matsui, T., Hong, W.P. & Ito, T. 1982. Earth pressures on piles in a row due to lateral soil movements, *Soils and Foundations*, Vol. 22, No. 2, 71–81.

Matsui, T. & Oda, K. 1996. Foundation damage of structures, *Soils and Foundations, Special Issue on Geotechnical Aspects of the Jan. 17 1995 Hyogoken-Nambu Earthquake*, No.1, 189–200.

McCullough, N.J., Dickenson, S.E. & Schlechter, S.M. 2001a. The seismic performace of piles in waterfront applications, *Proceedings of ASCE Ports 2001 Conference.*

McCullough, N.J., Schlechter, S.M. & Dickenson, S.E. 2001b. Centrifuge modeling of pile-supported wharves for seismic hazards, *Proceedings of Recent Advances in Geotechnical Earthquake Engineering and Soil Dynamics Conference.*

Metropolitan expressway public corporation. 1998. *Design method for foundations subjected to lateral spreading due to liquefaction* (in Japanese).

Minami, K., Takahashi, K., Yokota, H., Sonoyama, T., Kawabata, N. & Sekiguchi, K. 1997. Investigation results and dynamic response analyses on the damaged 'T' wharf in the Kobe port, *Foundation Engineering and Equipment (Kiso-ko)*, Vol.25, No.9, 112–119 (in Japanese).

Miyajima, M. & Kitaura, M. 1994. Experiments on force acting of underground structures in liquefaction-induced ground flow, *Proceedings of the 5th US-Japan Workshop on Earthquake Resistant Design of Lifeline Facilities and Countermeasures against Soil Liquefaction*, 445–455.

Mroz, Z. & Norris, V.A. 1982. Elastoplastic and viscoplastic constitutive models for soils with application to cyclic loading, *Soil Mechanics–Transient and cyclic loads*, 173–217

Miura, N. 1975. Effect of water on the behavior of a quartz-rich sand under high stresses, *Soils and Foundations*, Vol.15, No.4, 1–12.

Nakamura, Y., Kuwano, J. & Hashimoto, S. 1999. Small-strain stiffness and creep of Toyoura sand measured by a hollow cylinder apparatus, *Proceedings of Pre-Failure Deformation of Geomaterials*, Vol. 1, 141–148.

Nishi, K. & Kanatani, M. 1990. Constitutive relations for sand under cyclic loading based on elasto-plasticity theory, *Soils and Foundations*, Vol.30, No.2, 43–59.

Nishizawa, S., Hashimoto, M., Sakata, Y. & Sonoi, K. 1998. Investigation and analysis of a landing pier of steel pipe piles damaged by the 1995 Hyogoken-Nambu Earthquake, *Soils and Foundations, Special Issue on Geotechnical Aspects of the Jan. 17 1995 Hyogoken-Nambu Earthquake*, No.2, 133–146.

Ohnishi, Y. & Ohtsu, H. 1982. Coupled stress flow analysis of discontinuous media by finite elements, *Journal of Japan Society of Civil Engineers*, No.322, 111–120 (in Japanese).

Ohtsu, H., Hatsuyama, Y., Tateishi, A. & Horikoshi, K. 1997. A study on pile foundations damaged by the 1995 Hyogoken Nambu Earthquake, *Proceedings of International Conference on Deformation and progressive failure in geomechanics*, 583–588.

Oka, F., Yashima, Tateishi, A., Taguchi, Y. & Yamashita S. 1999. A cyclic elasto-plastic constitutive model for sand considering a plastic-strain dependence of the shear modulus, *Géotechnique*, Vol.49, No.5, 661–680.

Port and Harbour Research Institute. 1997. Damage to port and port-related facilities by the 1995 Hyogoken-nanbu Earthquake, *Technical note of the Port and Harbour Research Institute, Ministry of Transport, Japan*, No.857 (in Japanese).

Poulos, H.G., Chen, L.T. & Hull, T.S. 1995. Model tests on single piles subjected to lateral soil movement, *Soils and Foundations*, Vol. 35, No. 4, 85–92.

Prévost, J.H. 1985. A simple plasticity theory for frictional cohesionless soils, *Soil Dynamics and Earthquake Engineering*, Vol.4, 9–17.

Railway Technical Research Institute. 1997. Seismic design for foundations, *Foundation design codes for railway structures*, 116–117 (in Japanese).

Randolph, M.F. & Houlsby, G.T. 1984. The limiting pressure on a circular pile loaded laterally in cohesive soil, *Géotechnique*, Vol.34, No.4, 613–623.

Saada, A.S & Bianchini, G. (eds). 1989. *Proceedings of the International Workshop on Constitutive Equations for Granular Non-cohesive Soils*, Balkema.

Sakemi, T., Tanaka, M., Higuchi, Y., Kawasaki, K. & Nagura, K. 1995. Permeability of pore fluids in the centrifuge field, *Proceedings of the 10th Asian Regional Conference on Soil Mechanics and Foundation Engineering*, 481–484.

Satoh, H., Ohbo, N. & Yoshizako, K. 1998. Dynamic test on behavior of pile during lateral ground, *Proceedings of the International Conference Centrifuge 98*, Vol.1, 327–332.

Sekiguchi, H., & Ohta, H. 1977. Induced anisotropy and time dependency in clays. *Proceedings of the Constitutive Equations of Soils, Specialty Session 9, 9th International Conference of Soil Mechanics and Foundation Engneering*, 229–238.

Sugano, T., Oikawa, K., Santo, M. & Nakahara, T. 1998. Shaking table test on the damaged vertical pile-supported wharf during the 1995 Hyogo-ken Nambu Earthquake, *Proceedings of the 33rd Japan National Conference on Geotechnical Engineering*, Vol.1, 947-948 (in Japanese).

Takahashi, K., Minami, K., Yokota, H., Sonoyama, T., Tatsumi, Y. & Noji, M. 1997. Site investigation and static elasto-plastic analyses on the damaged pier in the Kobe port, *Foundation Engineering and Equipment (Kiso-ko)*, Vol.25, No.10, 104–110 (in Japanese).

Takahashi, A., Kawaguchi, Y., Takemura, J. & Kusakabe, O. 1998a. Dynamic stability of piled pier in front of gravity type caisson wall, *Proceedings of the Symposium on Lateral flow and Permanent deformation of soil structures during earthquake*, 363–368 (in Japanese).

Takahashi, A., Takemura, J., Kawaguchi, Y., Kusakabe, O. & Kawabata, N. 1998b. Stability of piled pier subjected to lateral flow of soils during earthquake, *Proceedings of the Centrifuge '98 (IS-Tokyo '98)*, Vol.1, 365–370.

Takahashi, A., Takemura, J., Kawaguchi, Y., Kusakabe, O. & Kimura, T. 1999a. Dynamic behaviour of piled pier located in front of gravity type caisson wall during earthquake, *Proceedings of the 11th Asian regional conference on soil mechanics and geotechnical engineering*, Vol.1, 495–498.

Takahashi, A., Takemura, J. & Kawaguchi, Y. 1999b. Centrifuge model tests on dynamic behavior of piled pier subjected to liquefaction-induced lateral flow during earthquake, *Journal of Geotechnical Engineering, JSCE*, III-49, No.638, 131–142 (in Japanese).

Takahashi, A., Takemura, J., Suzuki, A. & Kusakabe, O. 2001. Development and performance of an active type shear box in a centrifuge, *International Journal of Physical Modelling in Geotechnics*, Vol.1, No.2, 1–18.

Takahashi, A. 2001. Numerical analyses on dynamic interaction between quay wall and liquefied sand, *Proceedings of the 36th Japan National Conferece on Geotechnical Engineering*, Vol.2, 1851–1852, (in Japanese).

Takemura, J., Kimura, T., & Suemasa, N. 1989. Development of Earthquake simulators at Tokyo Institute of Technology, *Technical Report, No. 40, Dept. Civil Engrg. Tokyo Institute of Technology*, 41–60.

Takemura, J., Takahashi, A., Kusakabe, O. & Kimura, T. 1998. Centrifuge model tests on a dynamic stability of piled pier in front of gravity type caisson wall, *Proceedings of the 2nd Japan-UK*

workshop on implications of recent earthquakes on seismic risk, TIT/EERG98-6, 111–120.

Takemura, J., Kondoh, M., Esaki, T., Kouda, M. & Kusakabe, O. 1999. Centrifuge model tests on double propped wall excavation in soft clay, *Soils and Foundations*, Vol. 39, No. 3, 75–87.

Terashi, M., Kitazume, M, Maruyama, M. & Yamamoto, Y. 1991. Lateral resistance of a long pile in or near the slope, *Proceedings of the Centrifuge '91*, 245–234.

Technical council on lifeline earthquake engineering of ASCE. 1998. Chapter 2, Experience from past earthquakes, *Seismic guidelines for ports,* TCLEE Monograph No.12, ASCE.

Toki, K., Miura, F. & Otake, T. 1982. Non-linear seismic response analysis of soil–structuer interaction system by 3-dimentional joint element, *Journal of Japan Society of Civil Engineers*, No.322, 51–61 (in Japanese).

Tokimatsu, K. 1979. Generation and dissipation of pore water pressures in sand deposits during earthquakes, *Dr.Eng. Thesis, Tokyo Institute of Technology.*

Tokimatsu, K. & Asaka, Y. 1998. Effects of liquefaction-induced ground displacements on pile performance in the 1995 Hyogoken-Nambu Earthquake, *Soils and Foundations, Special Issue on Geotechnical Aspects of the Jan.. 17 1995 Hyogoken-Nambu Earthquake*, No. 2, 163–177.

Tokimatsu, K. 1999. Performance of pile foundations in laterally spreading soils, *Proceedings of the 2nd International Conference on Earthquake Gotechnical Engineering*, Vol.3, 957–964.

Towhata, I. 1981. Effect of rotaion of principal stress axes on deformation characteristics of sand, *Dr.Eng. Thesis, The University of Tokyo.*

Towhata, I., Vargas-Mongem W., Orense, R.P. & Yao, M. 1999. Shaking table tests on subgrade reaction of pipe embedded in sandy liquefied subsoil, *Soil Dynamics and Earthquake Engineering*, Vol.18, No.5, 347–361.

Tsuchiya, T., Kikuchi, D., Yamada, T., Kakurai, M. & Yamashita, K. 1997. Lateral loading tests on the model pile in the large scale shearing pit considering deformation of pile top and ground, *Proceedings of the 32nd Japan National Conference on Geotechnical Engineering*, 1545–1548 (in Japanese).

Tsuchiya, T., Kakurai, M., Yamashita, K. & Hamada, J. 2001. Large-scale laminar shear box for lateral pile loading tests with ground displacements, *International Journal of Physical Modelling in Geotechnics*, Vol.1, No.2, 43–53.

Uesugi, M. 1987. Friction between dry sand and construction materials, *Dr.Eng. Thesis, Tokyo Institute of Technology.*

Wakai, A., Ugai, K., Matsuda, T. & Gose, S. 1997. Analyses of lateral displacement of a pile supported abutment constructed in a soft subsoil profile, *Soils and Foundations*, Vol.37, No.4, 65–76.

Wang, W.L. & Yen, B.C. 1974. Soil arching in slopes, *Journal of the Geotechnical Engineering Division, ASCE*, Vol.100, GT1, 61–78.

Whitman, R.V. & Lambe, P.C. 1986. Effect of boundary conditions upon centrifuge experiments using ground motion simulation, *Geotechnical Testing Journal, GTJODJ*, Vol. 9, No. 2, 61–71.

Yasuda, S., Terauchi, T., Morimoto, H., Erken, A. & Yoshida, N. 1998. Post liquefaction behavior of several sands, *Proceedings of the 11th European Conference on Earthquake Engneering*.

Yoshida, N. 1993. Proposal of joint element for liquefaction analysis, *Proceedings of the 22th JSCE Earthquake Engineering Symposium*, Vol.1, 31–34 (in Japanese).

Zhang, F., Kimura, M., Nakai, T. & Hoshikawa, T. 2000. Mechanical behavior of pile foundations subjected to cyclic lateral loading up to the ultimate state, *Soils and Foundations*, Vol.40, No.5, 1–17.

Zienkiewicz, O.C. & Bettess, P. 1982. Soils and other saturated media under transient, dynamic conditions; General formulation and the validaity of various simplifying assumptions, *Soil Mechanics–Transient and cyclic loads*, 1–16, John Wiley & Sons, Chichester.

Zienkiewicz, O.C., Chan, A.H.C., Pastor, M., Schrefler, B.A. & Shiomi, T. 1999. *Computional geomechanics – with special reference to earthquake engineering*, John Wiley & Sons, Chichester.

Appendix A

Geotechnical centrifuges used in this study

Geotechnical centrifuges were used for the physical model tests in this study. Specifications of the centrifuges are described here.

A.1 The Tokyo Tech Mark II Centrifuge

The Tokyo Tech Mark II Centrifuge was used for the model tests in Chapters two, five, and Appendix E. The centrifuge is a beam type centrifuge having a pair of parallel arms that hold platforms on which the model container and a weight for counterbalance are mounted as shown in Fig. A.1. The radius of rotation is 1.38m, which is the distance from the rotating shaft to the platform base. The surface of the

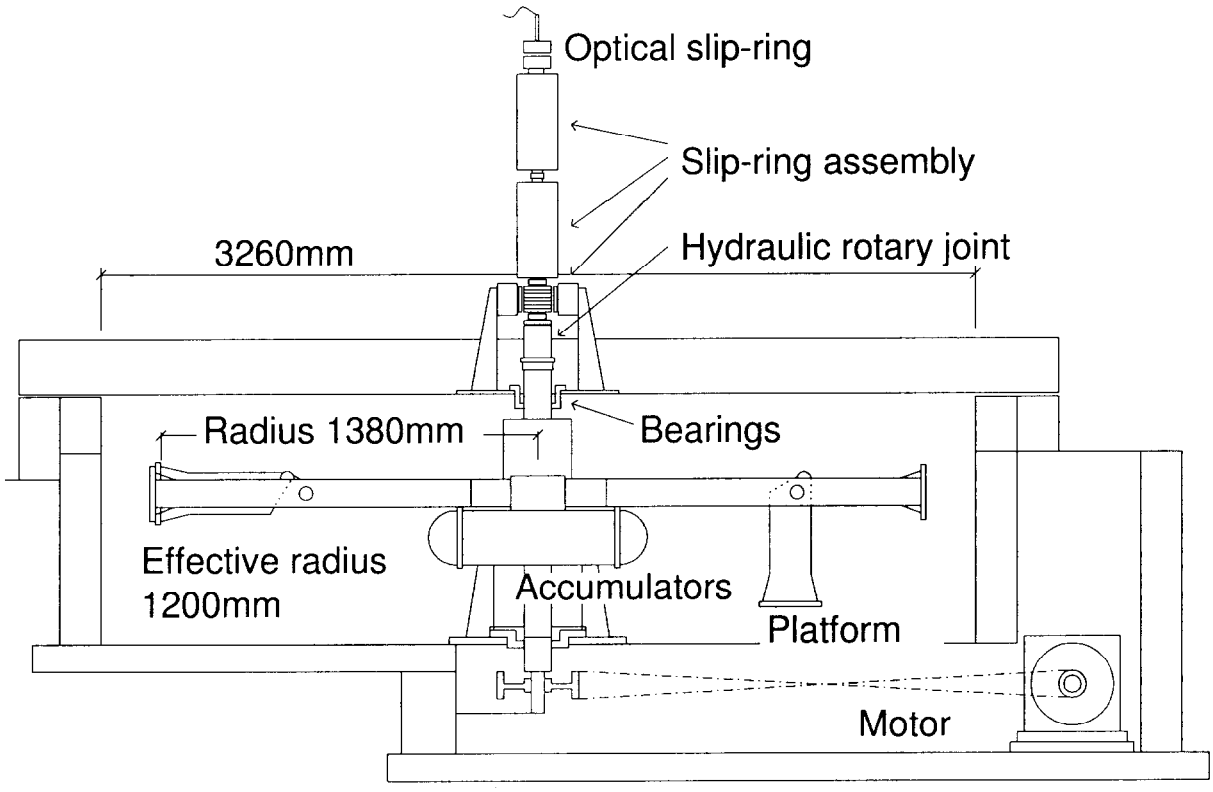

Figure A.1: Section view of the Tokyo Tech Mark II Centrifuge.

Table A.1: Specifications of the Tokyo Tech Mark II Centrifuge.

Radius	Platform radius	1.38m
	Effective radius	1.0–1.2m
Platform dimensions	Width	0.6m
	Depth	0.25m
	Maximum height	0.6m
Capacity	Maximum payload	37.5g.ton
	Maximum number of rotation	330rpm
	Maximum payload at 150g	250kg
Electrical slip rings	For instrumentation	72 channels
	For operation	10 channels
Optical rotary joint	Number of ports	1
Rotary joint	Number of ports for air and water	2
	Working pressure for air and water	1MPa
	Number of ports for oil	2
	Working pressure for oil	14MPa

swinging platform is slightly inclined to the horizontal at rest. As the spinning rate of the centrifuge increases, the platform swings up into the vertical plane at about 8g where it is restrained by a kick bar. As a result, the inclination of resultant acceleration of the centrifugal acceleration, ng, and the Earth's gravity becomes n:1 to the platform surface. This type of swinging platform is also used at the Cambridge University*. Specifications of the centrifuge are summarized in Table A.1.

For data acquisition, two types of signal transmission methods are used. One is classical electrical slip rings. Transducers are connected to the slip rings through a junction box, and signals are transferred to amplifiers on the laboratory floor. The other type is an optical rotary joint. Transducers are connected to signal conditioners on the centrifuge. Analog signals from the transducers are amplified there and then are converted to digital signals by A/D converters. The digital signals are transferred to a PC on the lab. floor through the optical rotary joint.

A hydraulic rotary joint with a maximum pressure of 14MPa mounted on the centrifuge is used for charging and discharging oil to the centrifuge. Two hydraulic accumulators are mounted on the centrifuge to charge and discharge the pressurized oil and to supply it to a shaking table during spinning of the centrifuge. Figure A.2 shows the front view of the hydraulic shaker†. The table of the shaker is actuated by an electro-servo hydraulic actuator. Specifications of the shaker are summarized in Table A.2.

* Phillips, R. 1995. Centrifuge modelling: practical considerations, R.N.Talyor (eds), *Geotechnical Centrifuge Technology*, 34–60, Blackie Academic & Professional, London.

† Takemura, J., Kimura, T., & Suemasa, N. 1989. Development of Earthquake simulators at Tokyo Institute of Technology, *Technical Report, No. 40, Dept. Civil Engrg. Tokyo Institute of Technology*, 41–60.

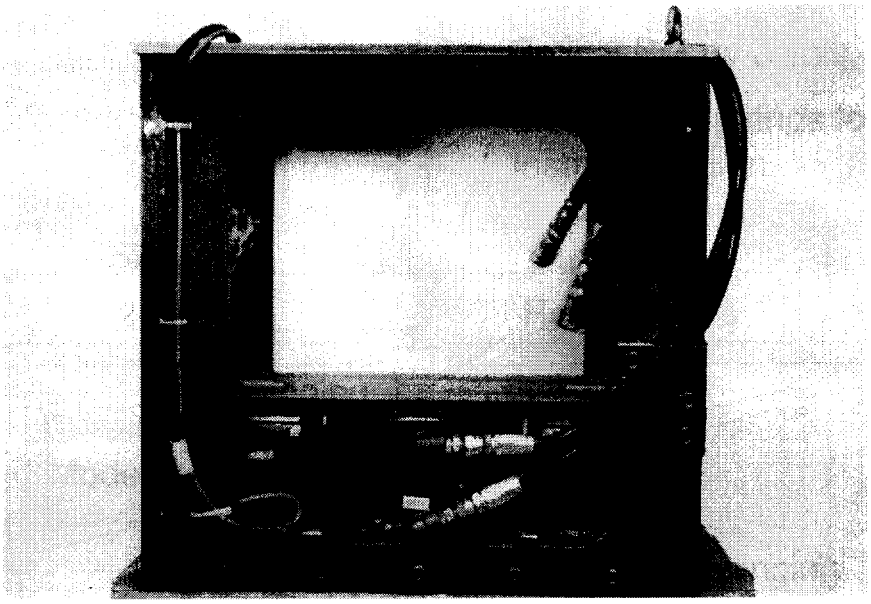

Figure A.2: Front view of hydraulic shaker for the Tokyo Tech Mark II Centrifuge.

Table A.2: Specifications of hydraulic shaker for the Tokyo Tech Mark II Centrifuge.

Max weight of shaking mass	60kg
Amplitude	±3mm
Table size (width × breadth)	510 × 250mm
Frequency	0–200Hz
Max centrifugal acceleration	100g
Max horizontal acceleration	25g at 100Hz
Pressure source	21MPa

A.2 The Tokyo Tech Mark III Centrifuge

The Tokyo Tech Mark III Centrifuge[‡] was used for the model tests in Chapter four. This centrifuge is a beam type centrifuge having a pair of parallel arms that hold platforms on which the model container and a weight for counterbalance are mounted as shown in Fig. A.3. Radius of rotation is 2.45m, which is the distance from the rotating shaft to the platform base. The surface of the swinging platform is always normal to the resultant acceleration of the centrifugal acceleration, ng, and Earth's gravity. Specifications of the centrifuge are summarized in Table A.3.

For data acquisition, two types of signal transmission methods are used. One is classical electrical slip rings. Transducers are connected to the slip rings through a junction box and signals are transferred to amplifiers on the laboratory floor. The other type is an optical rotary joint. Transducers are

[‡] Takemura, J., Kondoh, M., Esaki, T., Kouda, M. & Kusakabe, O. 1999. Centrifuge model tests on double propped wall excavation in soft clay, *Soils and Foundations*, Vol. 39, No. 3, 75–87.

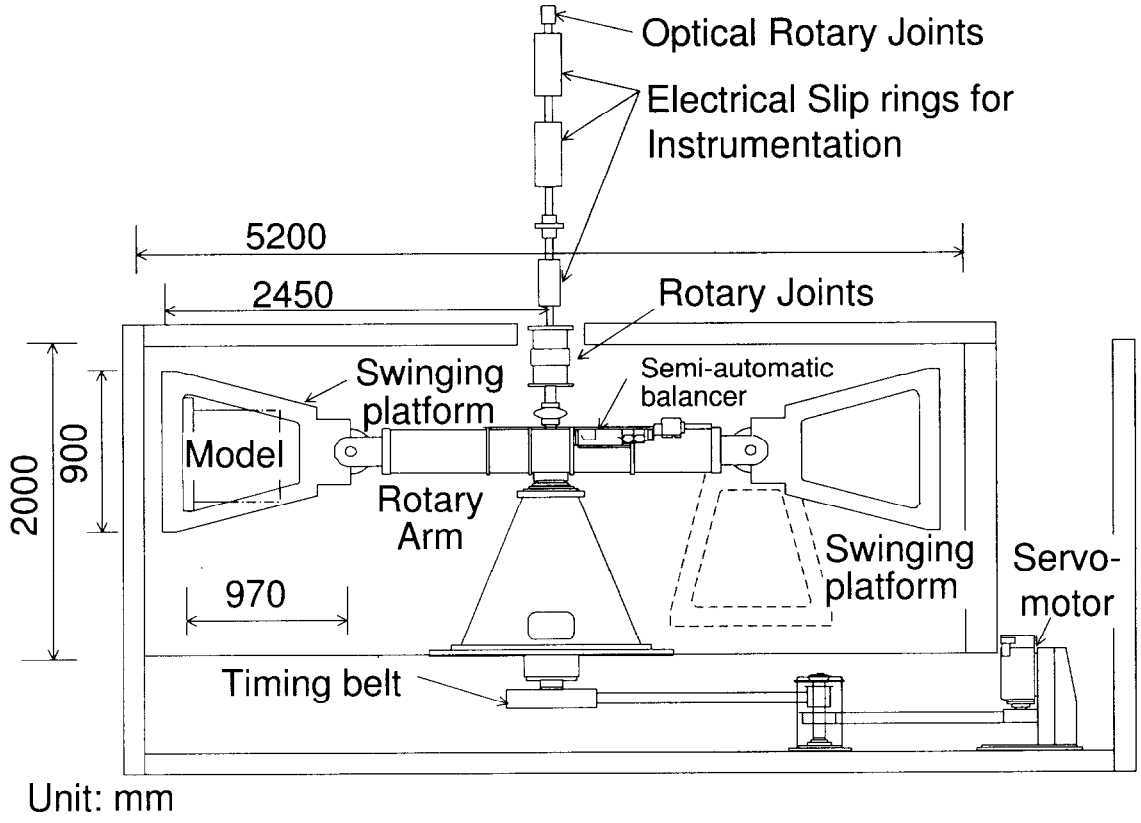

Figure A.3: Section view of the Tokyo Tech Mark III Centrifuge.

Table A.3: Specifications of the Tokyo Tech Mark III Centrifuge.

Radius	Platform radius	2.45m
	Effective radius	2.0–2.2m
Platform dimensions	Width	0.9m
	Depth	0.9m
	Maximum height	0.97m
Capacity	Maximum payload	50g.ton
	Maximum number of rotation	300rpm
	Maximum payload at 80g	600kg
Electrical slip rings	For instrumentation	72 channels
	For operation	18 channels
Optical rotary joint	Number of ports	4
Rotary joint	Number of ports for air and water	2
	Working pressure for air and water	1MPa
	Number of ports for oil	2
	Working pressure for oil	21MPa

connected to signal conditioners on the centrifuge. Analog signals from the transducers are amplified there and then are converted to digital signals by A/D converters. Gains and the other conditions of the signal conditioners can be controlled by a PC on the laboratory floor. The digital signals are transferred to a PC on the lab. floor through the optical rotary joint.

A hydraulic rotary joint with a maximum pressure of 20.5MPa mounted on the centrifuge is used for charging and discharging oil to the centrifuge during spinning of the centrifuge. Two four-liter hydraulic accumulators are mounted on the centrifuge to satisfy the required flow rate of pressurized oil for the active type shear box and a horizontal–vertical 2D shaker.

Appendix B

Similitude in centrifuge model tests

The most important feature of centrifuge modeling is the application of centrifugal acceleration to a model. In physical model tests, maintenance of the same stress level as that in the corresponding prototype is important for soil behavior, as the stress–strain relation of soil is highly dependent on the stress level and the strain-history. In order to ensure similarity between model and prototype, the scaling laws for centrifuge modeling are examined based on the governing equations.

Let us suppose that the same soil is used in the model as in the corresponding prototype and they are subjected to similar stress histories. If the model is subjected to a centrifugal acceleration of N times Earth's gravity, the vertical stress at a depth of h^M in the model will be identical to that in the prototype at a depth of h^P, where $h^P = Nh^M$*, where superscript 'M' denotes the model scale, and 'P' denotes the corresponding prototype. Basically, a linear length of x_i^M in the model is scaled by

$$x_i^M = x_i^P / N \tag{B.1}$$

where x_i^P is the linear length in the prototype.

B.1 Static problem

If the dynamics of the problem are so slow that all accelerations are seen to be negligible, $\ddot{u}_i$ and $\ddot{w}_i$ can be omitted. The momentum balance relation for the solid–fluid mixture (equation (5.8)) can be written as

$$\frac{\partial \sigma_{ij}^M}{\partial x_j^M} + \rho^M b_i^M = 0 \tag{B.2}$$

$$\frac{\partial \sigma_{ij}^P}{\partial x_j^P} + \rho^P b_i^P = 0. \tag{B.3}$$

If we assume that the density of the mixture in the model is equal to that in the corresponding prototype, i.e. $\rho^M = \rho^P$, and the stress level is maintained equally in both the model and the prototype, i.e. $\sigma_{ij}^M = \sigma_{ij}^P$, body force per unit mass, b_i, must satisfy

$$b_i^M = N b_i^P. \tag{B.4}$$

* Taylor, R.N. 1995. Centrifuges in modelling: principles and scale effects, R.N.Talyor (eds), *Geotechnical Centrifuge Technology*, 19–33, Blackie Academic & Professional, London.

Substituting equation (5.12) into (5.11), the momentum balance of fluid can be written as

$$\frac{\partial p}{\partial x_i} - \frac{\rho_f g}{k}\dot{w}_i + \rho_f b_i = 0. \tag{B.5}$$

The integrated flow conservation equation (equation (5.9)) in time can be written as

$$\int_0^t \frac{\partial \dot{w}_i}{\partial x_i}dt + \int_0^t \dot{\varepsilon}_{ii}dt - \int_0^t \frac{n\dot{p}}{K_f}dt = 0 \tag{B.6}$$

$$\frac{\partial w_i}{\partial x_i} + \varepsilon_{ii} - \frac{np}{K_f} = \left.\frac{\partial w_i}{\partial x_i}\right|_{t=0} + \varepsilon_{ii}|_{t=0} - \left.\frac{np}{K_f}\right|_{t=0} = C \tag{B.7}$$

$$p = \frac{K_f}{n}\left(\frac{\partial w_i}{\partial x_i} + \varepsilon_{ii} - C\right) \tag{B.8}$$

$$\frac{\partial p}{\partial x_i} = \frac{K_f}{n}\left(\frac{\partial^2 w_i}{\partial x_i^2} + \frac{\partial \varepsilon_{ii}}{\partial x_i} - \frac{\partial C}{\partial x_i}\right). \tag{B.9}$$

where C is an integration constant. Substituting equation (B.9) into (B.5), the momentum balance of fluid becomes

$$\frac{K_f^M}{n^M}\left(\frac{\partial^2 w_i^M}{\partial x_i^{2M}} + \frac{\partial \varepsilon_{ii}^M}{\partial x_i^M} - \frac{\partial C^M}{\partial x_i^M}\right) - \frac{\rho_f^M g}{k^M}\dot{w}_i^M + \rho_f^M b_i^M = 0 \tag{B.10}$$

$$\frac{K_f^P}{n^P}\left(\frac{\partial^2 w_i^P}{\partial x_i^{2P}} + \frac{\partial \varepsilon_{ii}^P}{\partial x_i^P} - \frac{\partial C^P}{\partial x_i^P}\right) - \frac{\rho_f^P g}{k^P}\dot{w}_i^P + \rho_f^P b_i^P = 0. \tag{B.11}$$

If we assume that the density and the compressibility of the fluid in the model are equal to those in the corresponding prototype, i.e. $\rho_f^M = \rho_f^P$ and $K_f^M = K_f^P$, and the soil used in the model has the same characteristics as in the prototype, i.e. $\varepsilon_{ii}^M = \varepsilon_{ii}^P$, $k^M = k^P$ and $n^M = n^P$, the ratio of each term in equation (B.10) to that in equation (B.11) is required to satisfy

$$\frac{K_f^M}{n^M}\left(\frac{\partial^2 w_i^M}{\partial x_i^{2M}} + \frac{\partial \varepsilon_{ii}^M}{\partial x_i^M} - \frac{\partial C^M}{\partial x_i^M}\right) \Big/ \frac{K_f^P}{n^P}\left(\frac{\partial^2 w_i^P}{\partial x_i^{2P}} + \frac{\partial \varepsilon_{ii}^P}{\partial x_i^P} - \frac{\partial C^P}{\partial x_i^P}\right) = \frac{\rho_f^M b_i^M}{\rho_f^P b_i^P} = N. \tag{B.12}$$

$$\begin{aligned}\frac{\rho_f^M g}{k^M}\dot{w}_i^M &= N\frac{\rho_f^P g}{k^P}\left(\frac{\dot{w}_i^M}{N}\right) \\ &= N\frac{\rho_f^P g}{k^P}\dot{w}_i^P\end{aligned} \tag{B.13}$$

Thus, rearranging this relation of equation (B.13), the following equation is obtained:

$$\dot{w}_i^M = N\dot{w}_i^P. \tag{B.14}$$

Considering that the linear length in the prototype is the length N times that in the model (equation (B.1)) and the relation in the average Darcy velocity of the percolating water (equation (B.14)), time in the model, t^M, is scaled by

$$t^M = t^P/N^2 \tag{B.15}$$

where t^P is the time in the prototype. This relation implies that a consolidation event lasting one year in the prototype can be simulated within an hour in the centrifuge at 100g.

B.2 Dynamic problem

In dynamic events, all accelerations must be considered (unlike static events). The momentum balance relation for the solid–fluid mixture (equation (5.8)) can be written as

$$\frac{\partial \sigma_{ij}^M}{\partial x_j^M} - \rho^M \ddot{u}_i^M + \rho^M b_i^M = 0 \tag{B.16}$$

$$\frac{\partial \sigma_{ij}^P}{\partial x_j^P} - \rho^P \ddot{u}_i^P + \rho^P b_i^P = 0. \tag{B.17}$$

If we assume that the density of the mixture in the model is equal to that in the corresponding prototype, i.e. $\rho^M = \rho^P$, and the stress level is maintained equally in both the model and the prototype, i.e. $\sigma_{ij}^M = \sigma_{ij}^P$, then the acceleration, $\ddot{u}_i$, and body force per unit mass, b_i, are required to satisfy

$$\ddot{u}_i^M = N\ddot{u}_i^P, \tag{B.18}$$

$$b_i^M = Nb_i^P. \tag{B.19}$$

Considering that the linear length in the protype is the length N times that in the model (equation (B.1)) and the relation in the acceleration (equation (B.18)), then time in the model, t^M, is scaled by

$$\underline{t^M = t^P/N} \tag{B.20}$$

where t^P is the time in the prototype†. This relation is different from that in static events (equation (B.15)).

The flow conservation equation coupled with the momentum balance of fluid (equation (5.14)) can be written as

$$\frac{k^M}{\rho_f^M g}\frac{\partial}{\partial x_i^M}\left(\frac{\partial p^M}{\partial x_i^M} + \rho_f^M b_i^M\right) + \dot{\varepsilon}_{ii}^M - \frac{n^M \dot{p}^M}{K_f^M} = 0 \tag{B.21}$$

$$\frac{k^P}{\rho_f^P g}\frac{\partial}{\partial x_i^P}\left(\frac{\partial p^P}{\partial x_i^P} + \rho_f^P b_i^P\right) + \dot{\varepsilon}_{ii}^P - \frac{n^P \dot{p}^P}{K_f^P} = 0. \tag{B.22}$$

If we assume that (1) the density and the compressibility of the fluid in the model are equal to those in the corresponding prototype, i.e. $\rho_f^M = \rho_f^P$ and $K_f^M = K_f^P$, (2) the soil used in the model has the same characteristics of that in the prototype, i.e. $\dot{\varepsilon}_{ii}^M = \dot{\varepsilon}_{ii}^P$ and $n^M = n^P$, and (3) the pore pressure level is maintained equally in both the model and the prototype, i.e. $p^M = p^P$, then the ratio of each term in equation (B.21) to that in equation (B.22) is required to satisfy

$$\dot{\varepsilon}_{ii}^M / \dot{\varepsilon}_{ii}^P = \frac{n^M \dot{p}^M}{K_f^M} \Big/ \frac{n^P \dot{p}^P}{K_f^P} = N. \tag{B.23}$$

$$\frac{k^M}{\rho_f^M g}\frac{\partial}{\partial x_i^M}\left(\frac{\partial p^M}{\partial x_i^M} + \rho_f^M b_i^M\right) = \frac{k^M}{\rho_f^P g}\frac{\partial}{\partial (x_i^P/N)}\left(\frac{\partial p^P}{\partial (x_i^P/N)} + \rho_f^P (N b_i^P)\right)$$

† Zienkiewicz, O.C., Chan, A.H.C., Pastor, M., Schrefler, B.A. & Shiomi, T. 1999. Validation of prediction by centrifuge, *Computional geomechanics – with special reference to earthquake engineering*, 217–251, John Wiley & Sons, Chichester.

$$= N\frac{(Nk^M)}{\rho_f^P g}\frac{\partial}{\partial x_i^P}\left(\frac{\partial p^P}{\partial x_i^P}+\rho_f^P b_i^P\right)$$
$$= N\frac{k^P}{\rho_f^P g^P}\frac{\partial}{\partial x_i^P}\left(\frac{\partial p^P}{\partial x_i^P}+\rho_f^P b_i^P\right). \quad \text{(B.24)}$$

Thus, rearranging this relation of equation (B.24), the following equation is obtained:

$$\underline{k^M = k^P/N.} \quad \text{(B.25)}$$

Equation (B.25) indicates that if we accept equation (B.20), i.e. $t^M = t^P/N$, we are required to reduce the hydraulic conductivity of the soil by $1/N$ when the centrifugal acceleration is Ng. This requirement cannot be achieved if we use the same soil and fluid in both the model and the prototype. One solution is to use higher viscosity fluid to replace the water and reduce the hydraulic conductivity. With N centi-stokes viscosity fluid at Ng, the hydraulic conductivity meets the requirement[‡]. Another solution is to use a smaller hydraulic conductivity soil to satisfy the requirement[§]. The former technique was adopted in Chapters two, three and five, while the latter was adopted in Appendix E in this study.

[‡] Sakemi, T., Tanaka, M., Higuchi, Y., Kawasaki, K. & Nagura, K. 1995. Hydraulic conductivity of pore fluids in the centrifuge field, *Proceedings of the 10th Asian Regional Conference on Soil Mechanics and Foundation Engineering*, 481–484.

[§] Kimura, T., Takemura, J., Hiro-oka, A., Okamura, M. & Matsuda, T. 1995. Countermeasures against liquefaction of sand deposits with structures, *Proceedings of the 1st International Conference on Earthquake Geotechnical Engneering (IS-Tokyo 95)*, Vol.3, 1203–1224.

Appendix C

Discretization of governing equations in space and time

C.1 Discretization of equations in space

The set of coupled equations (equations (5.8) and (5.14)) in u–p formulation can be written in vectorial notation as

$$\mathbf{L}^{\mathrm{T}}\sigma - \rho\ddot{\mathbf{u}} + \rho\mathbf{b} = \mathbf{0} \tag{C.1}$$

$$\frac{k}{\rho_f g}\nabla^{\mathrm{T}}\left(\nabla p + \rho_f \mathbf{b}\right) + \mathbf{m}\dot{\varepsilon} - \frac{n}{K_f}\dot{\mathbf{p}} = 0 \tag{C.2}$$

where $\mathbf{L}$ is defined as $\mathrm{d}\dot{\varepsilon} \equiv \mathbf{L}\mathrm{d}\dot{\mathbf{u}}$ and $\mathbf{m} \equiv [1\ 1\ 1\ 0\ 0\ 0]^{\mathrm{T}}$. The variables $\mathbf{u}$ and $\mathbf{p}$ can be spatially discretized by shape functions $\mathbf{N}^u$ and $\mathbf{N}^p$ respectively and can be written as

$$\mathbf{u} \approx \mathbf{N}^u\bar{\mathbf{u}} \tag{C.3}$$

$$\mathbf{p} \approx \mathbf{N}^p\bar{\mathbf{p}} \tag{C.4}$$

where $\bar{\mathbf{u}}$ and $\bar{\mathbf{p}}$ are the displacement and pore water pressure at nodes, respectively. To obtain the equations (C.1) and (C.2) discretized in space, the equations are premultiplied by transposed shape functions $(\mathbf{N}^u)^{\mathrm{T}}$ and $(\mathbf{N}^p)^{\mathrm{T}}$ respectively and are integrated with boundary conditions. The discretized equations are given as

$$\rho\left[\int_\Omega (\mathbf{N}^u)^{\mathrm{T}}\mathbf{N}^u d\Omega\right]\ddot{\bar{\mathbf{u}}} + \int_\Omega \mathbf{B}^{\mathrm{T}}\sigma' d\Omega + \left[\int_\Omega \mathbf{B}^{\mathrm{T}}\mathbf{m}\mathbf{N}^p d\Omega\right]\bar{\mathbf{p}} = \rho\int_\Omega (\mathbf{N}^u)^{\mathrm{T}}\mathbf{b}d\Omega + \int_{\Gamma_t}(\mathbf{N}^u)^{\mathrm{T}}\bar{\mathbf{t}}d\Gamma \tag{C.5}$$

$$\left[\int_\Omega \mathbf{B}^{\mathrm{T}}\mathbf{m}\mathbf{N}^p d\Omega\right]\dot{\bar{\mathbf{u}}} - \frac{n}{K_f}\left[\int_\Omega (\mathbf{N}^p)^{\mathrm{T}}\mathbf{N}^p d\Omega\right]\dot{\bar{\mathbf{p}}} - \frac{k}{\rho_f g}\left[\int_\Omega (\nabla\mathbf{N}^p)^{\mathrm{T}}\nabla\mathbf{N}^p d\Omega\right]\bar{\mathbf{p}} = \frac{k}{g}\int_\Omega (\nabla\mathbf{N}^p)^{\mathrm{T}}\mathbf{b}d\Omega \tag{C.6}$$

where $\mathbf{B}$ is given as $\mathbf{B} \equiv \mathbf{L}\mathbf{N}^u$.

These equations (C.5) and (C.6) can be written as

$$\begin{bmatrix} \mathbf{M} & \mathbf{O} \\ \mathbf{O} & \mathbf{O} \end{bmatrix}\begin{Bmatrix} \ddot{\bar{\mathbf{u}}}|_t \\ \ddot{\bar{\mathbf{p}}}|_t \end{Bmatrix} + \begin{bmatrix} \mathbf{C} & \mathbf{O} \\ \mathbf{Q}^{\mathrm{T}} & -\mathbf{S} \end{bmatrix}\begin{Bmatrix} \dot{\bar{\mathbf{u}}}|_t \\ \dot{\bar{\mathbf{p}}}|_t \end{Bmatrix} + \begin{bmatrix} \mathbf{K} & \mathbf{Q} \\ \mathbf{O} & -\mathbf{H} \end{bmatrix}\begin{Bmatrix} \bar{\mathbf{u}}|_t \\ \bar{\mathbf{p}}|_t \end{Bmatrix} = \begin{Bmatrix} \mathbf{f}_u|_t \\ \mathbf{f}_p|_t \end{Bmatrix} \tag{C.7}$$

where

$$\mathbf{M} = \rho\int_\Omega (\mathbf{N}^u)^{\mathrm{T}}\mathbf{N}^u d\Omega \tag{C.8}$$

$$\mathbf{Q} = \int_\Omega \mathbf{B}^{\mathrm{T}}\mathbf{m}\mathbf{N}^p d\Omega \tag{C.9}$$

$$\mathbf{S} = \frac{n}{K_f}\int_\Omega (\mathbf{N}^p)^{\mathrm{T}}\mathbf{N}^p d\Omega \tag{C.10}$$

$$\mathbf{H} = \frac{k}{\rho_f g}\int_\Omega (\nabla \mathbf{N}^p)^{\mathrm{T}}\nabla \mathbf{N}^p d\Omega \tag{C.11}$$

$$\mathbf{f}_u|_t = \rho\int_\Omega (\mathbf{N}^u)^{\mathrm{T}}\mathbf{b}|_t d\Omega + \int_{\Gamma_t} (\mathbf{N}^u)^{\mathrm{T}}\bar{\mathbf{t}}|_t d\Gamma - \left\{\int_\Omega \mathbf{B}^{\mathrm{T}}\sigma'|_{t-\Delta t} d\Omega - \mathbf{K}\bar{\mathbf{u}}|_{t-\Delta t}\right\} \tag{C.12}$$

$$\mathbf{f}_p|_t = \frac{k}{g}\int_\Omega (\nabla \mathbf{N}^p)^{\mathrm{T}}\mathbf{b}|_t d\Omega. \tag{C.13}$$

Though $\mathbf{K}\bar{\mathbf{u}}$ is not shown explicitly in equation (C.5), $\int_\Omega \mathbf{B}^{\mathrm{T}}\sigma'|_t d\Omega$ can be rewritten as

$$\int_\Omega \mathbf{B}^{\mathrm{T}}\sigma'|_t d\Omega \equiv \int_\Omega \mathbf{B}^{\mathrm{T}}\sigma'|_{t-\Delta t} d\Omega + \mathbf{K}(\bar{\mathbf{u}}|_t - \bar{\mathbf{u}}|_{t-\Delta t}) \tag{C.14}$$

$$\mathbf{K} \equiv \int_\Omega \mathbf{B}^{\mathrm{T}}\mathbf{D}^{ep}\mathbf{B} d\Omega \tag{C.15}$$

where $\mathbf{D}^{ep}$ is an elastoplastic stiffness matrix.

In addition, the term of $\mathbf{C}\dot{\bar{\mathbf{u}}}$ is introduced to the equation of the solid phase to describe a system damping. In this study, $\mathbf{C}$ is assumed as the 'Rayleigh damping matrix'* and defined as

$$\mathbf{C} = \alpha\mathbf{M} + \beta\mathbf{K} \tag{C.16}$$

where α and β are constants. A relationship between the damping ratio for the n-th mode of free vibration h_n and these constants can be written as

$$h_n = \frac{\alpha}{2\omega_n} + \frac{\beta\omega_n}{2} \tag{C.17}$$

where ω_n is n th free vibration frequency and should be the fundamental frequency of the system.

C.2 Discretization of equations in time

To obtain a numerical solution of the equation (C.7), the differential equations are integrated in time. A general numerical approach to step-by-step dynamic response analysis makes use of integration to step forward from the initial to the final conditions for each time step. An essential concept is represented by the following equations:

$$\dot{u}|_{t+\Delta t} = \dot{u}|_t + \int_t^{t+\Delta t} \ddot{u}|_\tau d\tau \tag{C.18}$$

$$u|_{t+\Delta t} = u|_t + \int_t^{t+\Delta t} \dot{u}|_\tau d\tau$$

where $u|_t$ is a displacement at the time of t. In this method, it is necessary to assume how the acceleration varies during the time step of Δt.

* Clough, R.W. & Penzien, J. 1993. *Dynamics of structures*, 2nd ed., 234–245.

One of the step-by-step formulations proposed by Newmark[†] is adopted in this study. The relationship between the values at time t and $t+\Delta t$ can be written as

$$\begin{aligned}
\ddot{\bar{\mathbf{u}}}^i|_{t+\Delta t} &= \frac{1}{\beta\Delta t^2}\Delta\bar{\mathbf{u}}^{i-1} - \frac{1}{\beta\Delta t}\dot{\bar{\mathbf{u}}}|_t + \left(1-\frac{1}{2\beta}\right)\ddot{\bar{\mathbf{u}}}|_t \\
\dot{\bar{\mathbf{u}}}^i|_{t+\Delta t} &= \frac{1}{2\beta\Delta t}\Delta\bar{\mathbf{u}}^{i-1} + \left(1-\frac{1}{2\beta}\right)\dot{\bar{\mathbf{u}}}|_t + \left(1-\frac{1}{4\beta}\right)\ddot{\bar{\mathbf{u}}}|_t\Delta t \\
\bar{\mathbf{u}}^i|_{t+\Delta t} &= \Delta\bar{\mathbf{u}}^{i-1} + \bar{\mathbf{u}}|_t
\end{aligned} \tag{C.19}$$

where $\Delta\bar{\mathbf{u}}$ is an increment of the displacement in Δt and β is a weighting parameter. Setting $\beta = 1/4$, the variation of acceleration in Δt becomes constant, and this method, i.e. Newmark $\beta = 1/4$ method, is referred to as the constant average acceleration method.

For the pore water pressure, a first order differential scheme is adopted, as the order of the differential equation is one, i.e.

$$\begin{aligned}
\dot{\bar{\mathbf{p}}}^i|_{t+\Delta t} &= \frac{1}{\theta\Delta t}\Delta\bar{\mathbf{p}}^{i-1} - \frac{1-\theta}{\theta}\dot{\bar{\mathbf{p}}}|_t \\
\bar{\mathbf{p}}^i|_{t+\Delta t} &= \Delta\bar{\mathbf{p}}^{i-1} + \bar{\mathbf{p}}|_t
\end{aligned} \tag{C.20}$$

where $\Delta\bar{\mathbf{p}}$ is an increment of the pore water pressure in Δt and θ is a weighting parameter. Adopting the parameter $\theta = 1/2$, this scheme becomes the well known central differential scheme. When the acceleration is negligible, i.e. when 'static' analysis is assumed, this scheme is also applied to the displacement.

[†] Newmark, N.M. 1959. A method of computation for structural dynamics, *Proc. of ASCE*, Vol.8, 67–94

Appendix D

Method for solving non-linear equations

In order to solve non-linear systems, the modified Newton Raphson iterative procedure, i.e. the Newton Raphson procedure using the 'constant stiffness matrix,' is adopted. To obtain a first iteration step solution, i.e. a displacement $\Delta\bar{\mathbf{u}}^0$ and a pore water pressure $\Delta\bar{\mathbf{p}}^0$, substituting equations (C.19) and (C.20) into the equation (C.7) at the time of '$t+\Delta t$', the following equations are obtained:

$$\left\{ \begin{array}{c} \Delta\bar{\mathbf{u}}^0 \\ \Delta\bar{\mathbf{p}}^0 \end{array} \right\} = [\hat{\mathbf{K}}]^{-1} \left\{ \begin{array}{l} \mathbf{f}_u|_{t+\Delta t} - \mathbf{M}\left\{ -\frac{1}{\beta\Delta t}\dot{\bar{\mathbf{u}}}|_t + \left(1-\frac{1}{2\beta}\right)\ddot{\bar{\mathbf{u}}}|_t \right\} \\ \quad -\mathbf{C}\left\{ \left(1-\frac{1}{2\beta}\right)\dot{\bar{\mathbf{u}}}|_t + \left(1-\frac{1}{4\beta}\right)\ddot{\bar{\mathbf{u}}}|_t \Delta t \right\} - \int_\Omega \mathbf{B}^{\mathrm{T}}\sigma'|_t d\Omega - \mathbf{Q}\bar{\mathbf{p}}|_t \\ \mathbf{f}_p|_{t+\Delta t} - \mathbf{Q}^{\mathrm{T}}\left\{ \left(1-\frac{1}{2\beta}\right)\dot{\bar{\mathbf{u}}}|_t + \left(1-\frac{1}{4\beta}\right)\ddot{\bar{\mathbf{u}}}|_t \Delta t \right\} \\ \quad -\frac{1-\theta}{\theta}\mathbf{S}\dot{\bar{\mathbf{p}}}|_t + \mathbf{H}\bar{\mathbf{p}}|_t \end{array} \right\} \tag{D.1}$$

where

$$\hat{\mathbf{K}} = \left[\begin{array}{cc} \frac{1}{\beta\Delta t^2}\mathbf{M} + \frac{1}{2\beta\Delta t}\mathbf{C} + \mathbf{K} & \mathbf{Q} \\ \frac{1}{2\beta\Delta t}\mathbf{Q}^{\mathrm{T}} & \frac{1}{\theta\Delta t}\mathbf{S} + \mathbf{H} \end{array} \right] \tag{D.2}$$

and the constant stiffness matrix, i.e. the initial stiffness matrix, $\mathbf{K}$ is defined as

$$\mathbf{K} \equiv \int_\Omega \mathbf{B}^{\mathrm{T}}\mathbf{D}^e\mathbf{B}d\Omega. \tag{D.3}$$

Solving this equation, the displacement and the pore water pressure are updated using equations (C.19) and (C.20). With the updated displacement and pore water pressure, a residual force $\mathbf{r}$ in the $(i-1)$th iteration can be calculated by equation (D.4), and the increment of the displacement and the pore water pressure in the i-th iteration can be obtained by equation (D.5):

$$\mathbf{r}^{i-1} = \left\{ \begin{array}{l} \mathbf{f}_u|_{t+\Delta t} - \left(\mathbf{M}\ddot{\bar{\mathbf{u}}}^{i-1}|_{t+\Delta t} + \mathbf{C}\dot{\bar{\mathbf{u}}}^{i-1}|_{t+\Delta t} + \int_\Omega \mathbf{B}^{\mathrm{T}}\sigma'^{i-1}|_{t+\Delta t} d\Omega + \mathbf{Q}\bar{\mathbf{p}}^{i-1}|_{t+\Delta t} \right) \\ \mathbf{f}_p|_{t+\Delta t} - \left(\mathbf{Q}^{\mathrm{T}}\dot{\bar{\mathbf{u}}}^{i-1}|_{t+\Delta t} - \mathbf{S}\dot{\bar{\mathbf{p}}}^{i-1}|_{t+\Delta t} - \mathbf{H}\bar{\mathbf{p}}^{i-1}|_{t+\Delta t} \right) \end{array} \right\} \tag{D.4}$$

$$\left\{ \begin{array}{c} \Delta\hat{\mathbf{u}}^i \\ \Delta\hat{\mathbf{p}}^i \end{array} \right\} = [\hat{\mathbf{K}}]^{-1}\mathbf{r}^{i-1} \tag{D.5}$$

$$\left\{ \begin{array}{c} \Delta\bar{\mathbf{u}}^i \\ \Delta\bar{\mathbf{p}}^i \end{array} \right\} = \left\{ \begin{array}{c} \Delta\bar{\mathbf{u}}^{i-1} \\ \Delta\bar{\mathbf{p}}^{i-1} \end{array} \right\} + \left\{ \begin{array}{c} \Delta\hat{\mathbf{u}}^i \\ \Delta\hat{\mathbf{p}}^i \end{array} \right\}. \tag{D.6}$$

With equation (D.6), the increment of the displacement and the pore water pressure in this time step by the i-th iteration can be calculated. The energy norm at the i-th iteration step, ξ^i, is defined as

$$\xi^i \equiv \left\{ \begin{array}{c} \Delta\hat{\mathbf{u}}^i \\ \Delta\hat{\mathbf{p}}^i \end{array} \right\}^{\mathrm{T}} \mathbf{r}^{i-1}. \tag{D.7}$$

The iteration procedure from equation (D.4) to (D.6) will be repeated until ξ^i achieves a certain tolerance. At convergence, the displacement and the pore water pressure in this time step are updated and the calculation moves to the next time step.

Appendix E

Liquefaction remediation for mitigation of structure damage

E.1 Remediation of liquefiable soils

When there is liquefaction potential in the foundation of a structure, remediation is often necessary. Though many liquefaction remediation methods have been proposed, they are essentially based on two principles, i.e. soil improvement and structural design. The former involves the improvement of the soil so that liquefaction will not occur, and the latter involves strengthening the structure so that it will bear up against liquefaction of its foundation and/or surrounding soil. Soil improvement has the possibility of application to existing structures, while structure strengthening techniques have difficulties and may only be applicable to newly built structures.

The former method, i.e. soil improvement, can be classified into three categories based on the liquefaction mechanism as follows:

(1) Dissipation enhancement of excess pore water pressure in the soil,
(2) Increase of liquefaction strength of the soil,
(3) Reduction of cyclic shear deformation of the soil induced by earthquake motion.

Examples for each these techniques are listed in table E.1. Details of these methods are provided in the handbook on liquefaction remediation edited by the Port and Harbour Research Institute in Japan*.

The Tokyo Tech Soil Mechanics group has worked on the evaluation of countermeasures against liquefaction using a shaking table in a centrifuge†. Before and after the 1995 Hyogo-ken Nambu Earthquake, the soil improvement techniques of (1) and (3) in Table E.1, i.e. a gravel drain method and a shear strain restraint method with sheet pile walls, were investigated mainly for an existing oil tank and an existing underground utility tunnel. Additionally, a combination method, i.e. a shear strain restraint method with drainage capable sheet pile walls, was examined. Figure E.1 shows the model setups for the centrifuge tests on the liquefiable foundations improved by the gravel drains and the sheet pile walls, respectively. Silica sand No.8, uniformly graded sand (D_{50}=0.09mm) was used

* Port and Harbour Research Institute. 1997. *Handbook on Liquefaction Remediation of Reclaimed Land*, A.A.Balkema, Rotterdam.

† Kimura, T., Takemura, J., Hiro-oka, A., Okamura, M. & Matsuda, T. 1995. Countermeasures against liquefaction of sand deposits with structures, *Proceedings of the 1st International Conference on Earthquake Geotechnical Engneering (IS-Tokyo 95)*, Vol.3, 1203–1224.

Table E.1: Types of liquefaction remediation with soil improvement

(1) Dissipation enhancement of excess pore water pressure in soil.
Gravel or plastic drain method
Replacement of liquefiable soil with high hydraulic conductivity soil
(2) Increase of liquefaction strength of soil.
Compaction of soil using sand compaction pile method, vibrofloatation method, etc.
Solidification of soil using deep mixing method, premix method or chemical grouting.
Preload with a surcharge embankment.
Lowering of ground water level.
(3) Reduction of cyclic shear deformation of soil induced by earthquake motion.
Shear strain restraint with underground wall that surrounds structure foundation.

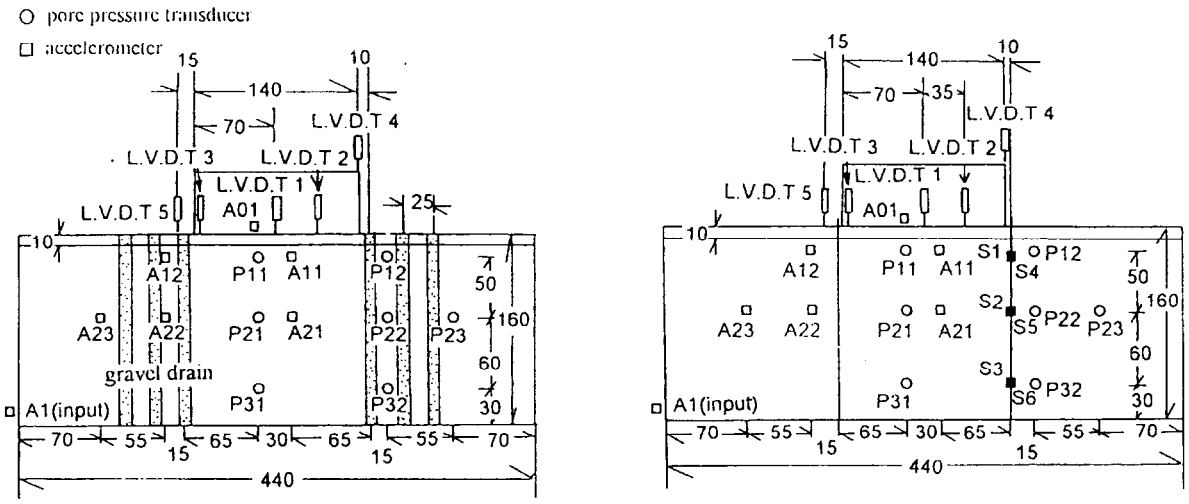

(a) Gravel drain method

(b) Shear strain restraint method

Figure E.1: Model setups for centrifuge tests on liquefiable foundations improved by gravel drains and sheet pile walls (Kimura *et al.*, 1995).

for the model ground. The ground was prepared by air pluviation to achieve a relative density of 40%. It was saturated up to the ground surface with de-aired water and subjected to a negative pressure of 98kPa in a large tank by applying a vacuum. A 49kPa pressure acted on the ground surface by a model oil tank. Horizontal shaking was applied to the model by sinusoidal waves with a frequency of 100Hz and a maximum acceleration of approximately 10g under 50g centrifugal acceleration. Observed distributions of the tank settlement caused by the earthquake motions are illustrated in Fig. E.2. Settlement of the structure arises from two mechanisms; compression and lateral deformation of the subsoil. An increase of lateral deformation gives rise to an increase in total settlement as well as differential settlement. In order to avoid excessive settlement and differential settlement of

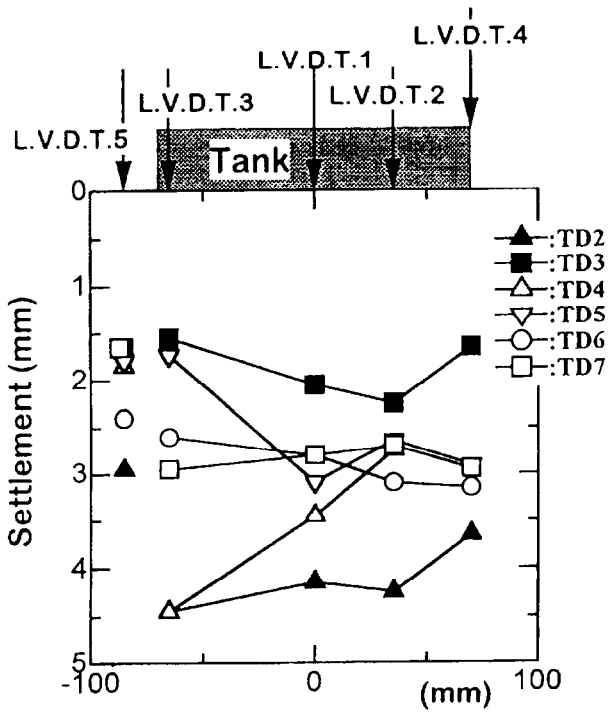

TD2: Without countermeasure TD3: Foundation soil was not fully saturated.
TD4: With gravel drain of one row TD5: With gravel drain of three rows
TD6: With sheet pile walls TD7: With drainage capable sheet pile walls

Figure E.2: Observed oil tank settlement distributions (Kimura *et al.*, 1995).

the structure on the foundation ground, suppression of lateral deformation is necessary. Kimura *et al.* concluded that the countermeasures of the sheet pile walls and the gravel drain were effective in suppression of total and differential settlement.

Though these remediation methods effectively restrain ground deformation due to liquefaction, they require a large working space and heavy equipment for construction. Consequently, these techniques have been rarely applied to existing oil tanks located in crowded reclaimed areas, while they have been applied to existing river dikes. Other alternatives involve cementation or solidification of the liquefiable soils, as these methods enable construction within a small working space and relatively small equipment. Some contractors in Japan have developed small chemical grouting machines as shown in Fig. E.3[‡]. They are altered boring machines and can operate in small working spaces and supply grouting beneath existing structures. The workability of the technique has been examined in-situ, and tests at the sites revealed that the unconfined compressive strength of the improved sand,

[‡] Raito Kogyo Co. 1998. Macs palm method,
http://www.raito.co.jp/html/eigyo/jiban/macspa.html.
Nishimatsu Co. 1998. Development of countermeasures against liquefaction of existing oil tank foundation by chemical ground method,
http://www.nishimatsu.co.jp/tech/newtech/tech14.htm.
Kajima Co. 2001. Soil improvement using universal boring machine,
http://www.kajima.co.jp/news/press/200106/21c1fo-j.htm.

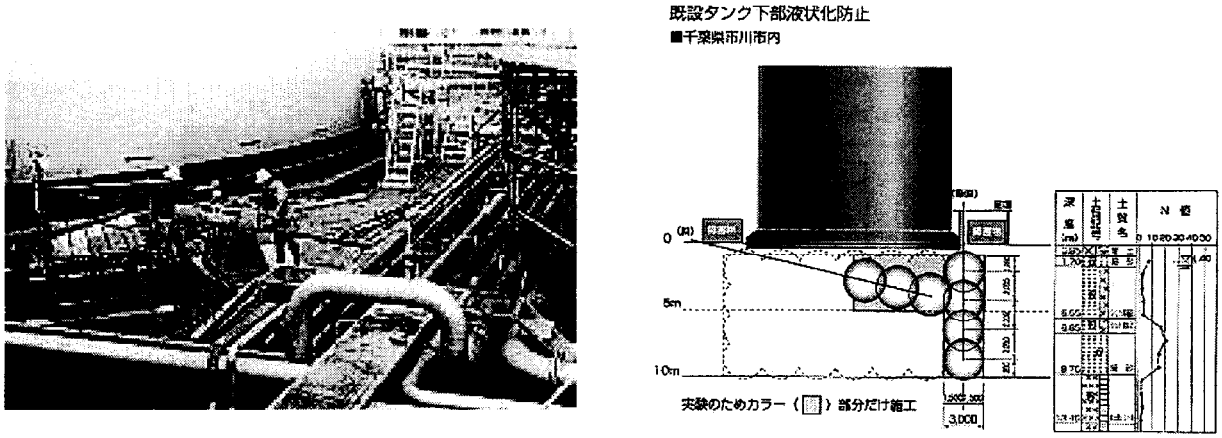

(a) Raito Kogyo Co. & Nishimatsu Co. (1998)

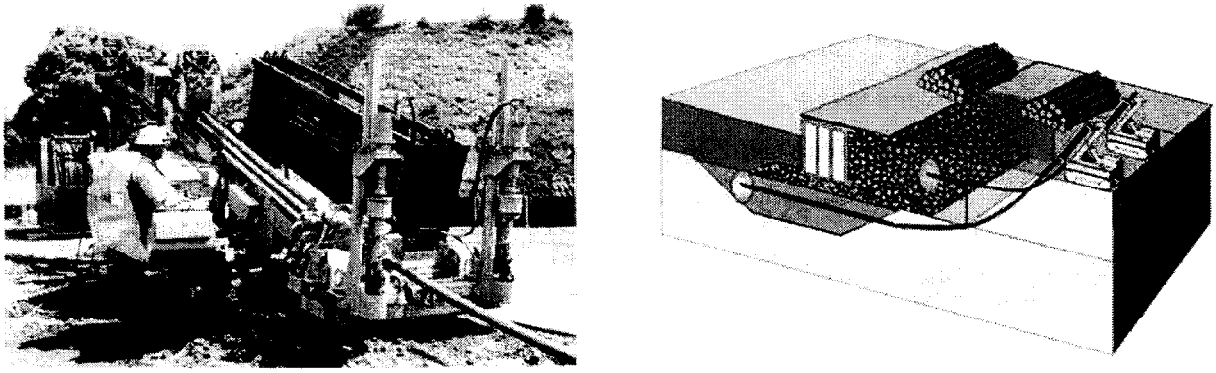

(b) Kajima Co. (2001)

Figure E.3: Chemical grouting machines developed by the Japanese contractors (after Raito Kogyo Co. & Nishimatsu Co., 1998, Kajima Co., 2001).

q_u, archived 100kPa with such grouting methods.

E.2 Motivations for physical and numerical model tests

As mentioned in the previous section, solidification of liquefiable soils by chemical grouting can be performed in small working spaces and beneath existing structures. However, it is no yet clear the extent to which an existing structure with such an improved foundation will perform in an earthquake. In order to understand the behavior of the treated soil during an earthquake, the soil improvement techniques of (2) in Table E.1, i.e. the solidification of soil by chemical grouting, was investigated using the centrifuge[§]. Numerical analyses were also conducted to simulate structure/treated soil/liquefiable

[§] Mizoguchi, A., Takemura, J. & Takahashi, A. 2000. Effects of chemical grouting on settlement of existing oil tank as countermeasure against liquefaction, *Proceedings of the 35th Japan National Conference on Geotechnical Engineering*, Vol.2, 1671–1672 (in Japanese).
Takemura, J., Mizoguchi, A. & Takahashi, A. 2000. Dynamic behavior of oil tank on sandy ground improved by chemical grouting, *Proceedings of the 35th Japan National Conference on Geotechnical Engineering*, Vol.2, 1669–1670 (in Japanese).

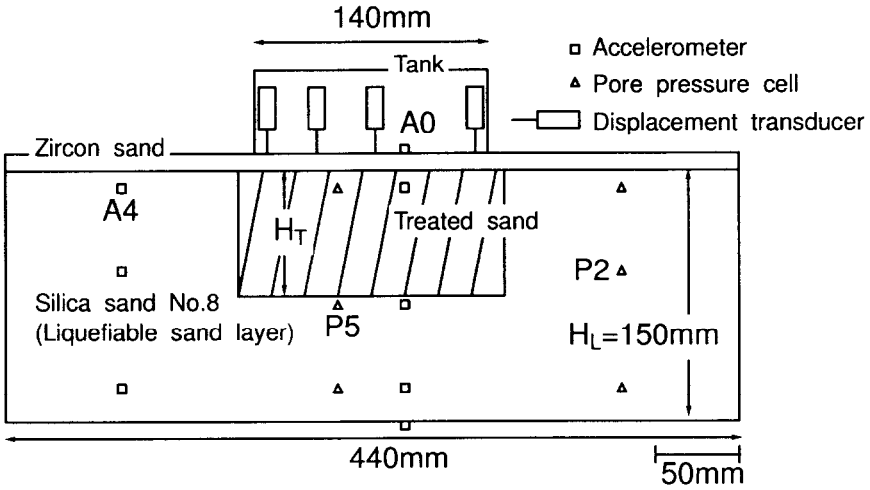

Figure E.4: Model setup for centrifuge model tests on oil tank on grouted ground

Table E.2: Material properties of Silica sand No.8

Specific gravity	2.65
Mean grain size D_{50}	0.09mm
Uniformity coefficient U_c	2.93
Maximum void ratio e_{max}	1.333
Minimum void ratio e_{min}	0.703

soil interaction during an earthquake[¶].

E.3 Outline of physical and numerical model tests

E.3.1 Centrifuge model tests

The centrifuge used in the tests was the Tokyo Tech Mark II Centrifuge (cf. Appendix A). The model setup used in this study is shown in Figure E.4. Due to the limitation of the model size, a two dimensional model oil tank was used in the tests. The model ground was placed in a laminar box made of aluminum with inner size 440mm in width, 150mm in breadth, and 220mm in height (Fig. E.5). Silica sand No.8, uniformly graded sand (D_{50}=0.09mm) was used for the model ground. The material properties of Silica sand No.8 are summarized in Table E.2. The ground was prepared by air pluviation to achieve a relative density of 50%. The thickness of the sand was 150mm. Lead shots were placed in the sand to measure the displacements of ground by radiographs taken before and after the centrifuge tests. Zircon sand was placed on the surface to obtain a 10mm thick surcharge layer that gives a surcharge pressure of 10kPa at 50g. After laying zircon sand, the model tank was placed. The model oil tank was essentially a box made of 0.7mm–thickness aluminum with a rubber membrane

[¶] Takahashi, A., Takemura, J. & Mizuguchi, A. 2001. Settlement of oil tank on liquefiable sandy ground improved by chemical grouting during earthquake, *Proceedings of the 26th JSCE Earthquake Engineering Symposium*, Vol.1, 697–700 (in Japanese).

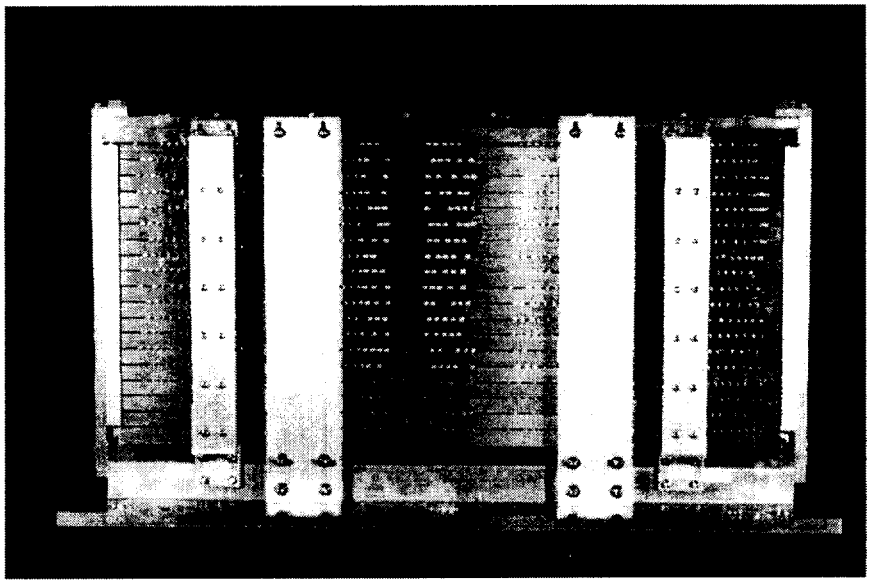

Figure E.5: Laminar box for centrifuge model test.

base that represented a flexible base of an actual oil storage tank. The width of the model tank was 140mm, which corresponded to 7m in the prototype scale when the centrifuge tests were conducted at 50g. Lead shots were put into the model tank so that a pressure of 100kPa could be applied to the ground surface at 50g. The completed model was put into a vacuum tank, and the sand was saturated by de-aired water from the bottom of the box under a negative pressure of 98kPa.

When the soil improvement was applied to the liquefiable soil, a ready grouted sand block was placed beneath the model tank. The grouting material used in the tests was a liquid glass from which sodium was eliminated by ion exchange method for long-term stabilization of the material[‖]. The unconfined compressive strength of the improved sand, q_u, achieved 150kPa. The width of the improvement was 160mm in all the cases.

The shaking tests were conducted under 50g by applying sinusoidal waves with a frequency of 100Hz and a maximum acceleration of approximately 17g that corresponded to 0.34g in the prototype scale. Typical time history of the input sinusoidal waves is given in Fig. E.6. In the tests, the thickness of the improved soil layer, H_T, was taken as the test parameter, while the width of the improved soil was kept at 1.15 times larger than that of the tank in all the cases. The test conditions are summarized in Table E.3. Here, the ratio of the improved soil layer thickness, H_T, to the initial liquefiable layer thickness, H_L, is defined as the improvement ratio, H_T/H_L.

E.3.2 Numerical analyses

In order to simulate the centrifuge model tests and to qualitatively study the effect of the countermeasure against liquefaction on the permanent settlement of the structure, two dimensional finite element analyses were conducted under the plane strain condition. The constitutive equations used in the analyses were the extended subloading surface model with rotational hardening employing an

[‖] Raito Kogyo Co. 1998. Macs palm method,
http://www.raito.co.jp/html/eigyo/jiban/macspa.html.

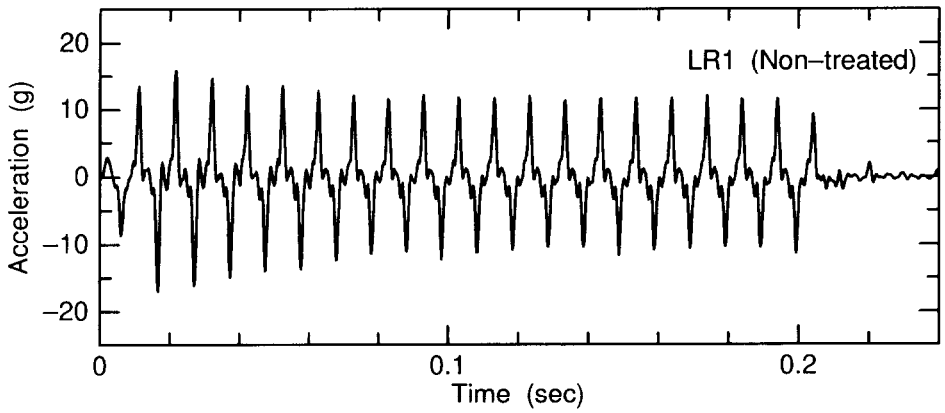

Figure E.6: Time history of input sinusoidal waves (LR1)

Table E.3: Test conditions in existing oil tank series.

Case	Improvement ratio H_T/H_L	Maximum acceleration of input waves (g)
LR1 (Non-improved)	0.00	17.0
LR2	0.25	17.1
LR3	0.50	17.7
LR4	1.00	13.3

Improvement ratio ≡ Improved layer thickness H_T/Initial liquefiable layer thickness H_L

ellipsoid type yield surface, which was proposed by Hashiguchi *et al.*** The geomaterial parameters used in the analyses are summarized in Table E.4. κ and λ were obtained by oedometer tests, and the hydraulic conductivity, k, was determined by constant head permeability tests. The other parameters were determined by trial and error so as to fit consolidated-undrained triaxial test results. Figure E.7 shows typical calculated stress–strain relations and stress paths in undrained cyclic triaxial tests for isotropically consolidated non-treated and treated sand. The liquefaction resistance curve is illustrated in Fig. E.8, where σ_d is a deviator stress. Though the calculated liquefaction resistances at the smaller number of load cycles are larger than those of the laboratory test results, the calculated curve is close to that found in the laboratory in gross. Modeling of the treated sand, i.e. the soil improved by chemical grouting, will be described in the following section. Zircon sand placed on the surface was modeled as the non-treated sand with specific gravity of 5.06.

The size of the element was 10×10mm. Fluid flow velocities were set to zero at all the boundaries

** Hashiguchi, K., Ueno, M. & Chen, Z.P. 1996. Elastoplastic constitutive equation of soils based on the concepts of subloading surface and rotational hardening, *Journal of Geotechnical Engineering, JSCE*, III-36, No.547, 127–144 (in Japanese).
Hashiguchi, K. & Chen, Z.P. 1998. Elastoplastic constitutive equation of soils with the subloading surface and the rotational hardening. *International Journal for Numerical and Analytical Methods in Geomechanics*, Vol.22, 197–277.

Table E.4: Soil parameters for numerical analysis on oil tank on grouted ground.

		G_s	e_0	κ	λ
Liquefiable sand *1		2.65	1.03	2.9×10^{-3}	1.5×10^{-2}
Treated sand *2		2.65	1.03	2.9×10^{-3}	1.5×10^{-2}
ν	ϕ	ϕ_d	μ	ϕ_b	b_r
0.33	35	27	1.0	27	1.0×10^2
0.33	35	27	1.0	27	1.0×10^2
u_1	m_1	c	k (m/s)	$F_0/(-\sigma'_{m0})$	s_{ij0}
8.0	1.0	30.0	1×10^{-3}	1.2	$0.2\ \sigma'_{ij0}$
8.0	1.0	30.0	1×10^{-4}	12.0	$0.2\ \sigma'_{ij0}$

*1: Liquefaction strengths were R_5=0.25, R_{20}=0.11 at ε_{DA}=5%.

*2: Double amplitude of axial strain, ε_{DA}, did not reach 5%.

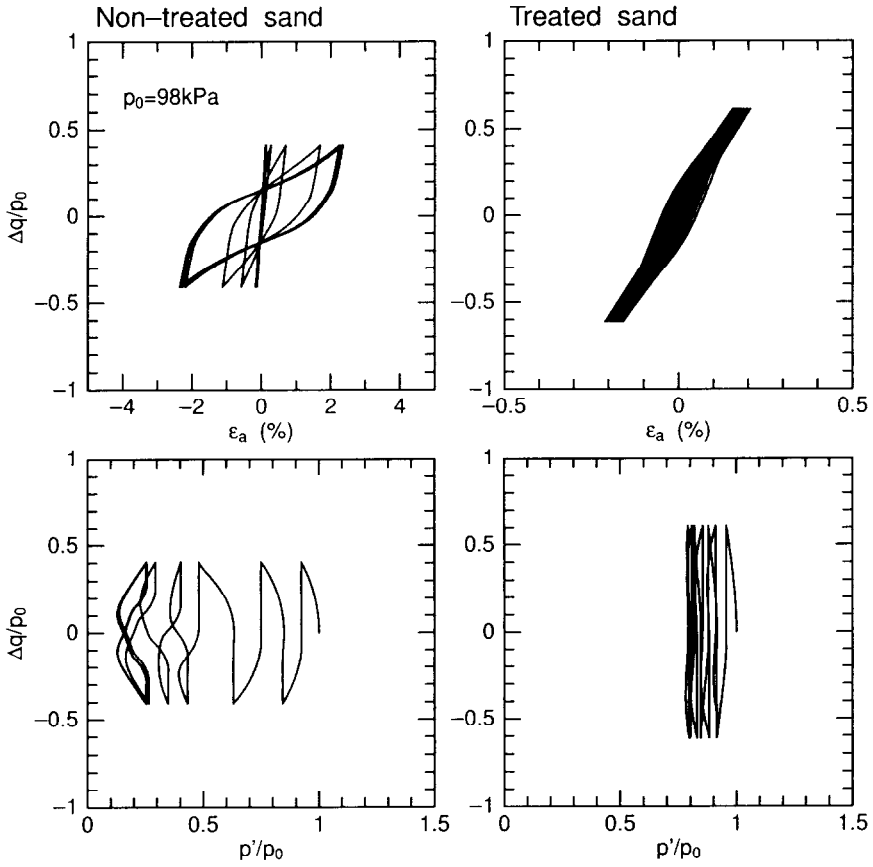

Figure E.7: Typical calculated stress–strain relations and stress paths in undrained cyclic triaxial test for isotropically consolidated non-treated and treated sands.

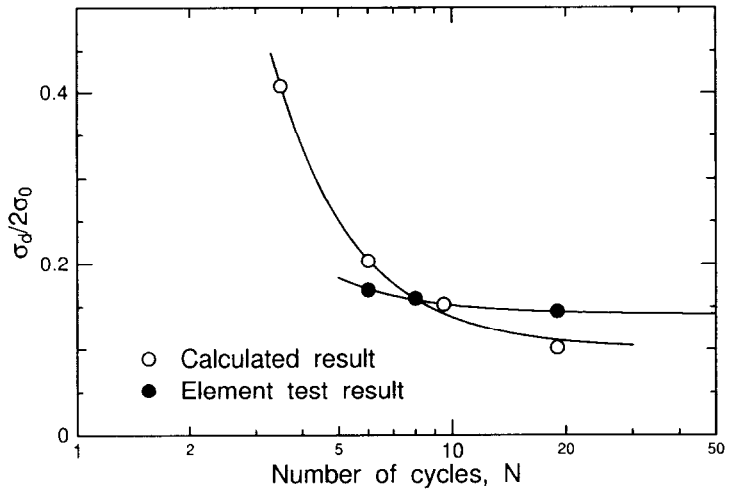

Figure E.8: Liquefaction resistance curves for non-treated sand.

except at the surface of the ground. The nodes on the side boundaries were tied to each other at each depth, i.e. a periodic boundary at the ends of the box was assumed to simulate the model ground in the laminar box. The applied earthquake motions were similar to the waves obtained in the centrifuge tests. In order to obtain the numerical solution, the differential equations are integrated with respect to time. The integration scheme used was the Newmark's β method (cf. Appendix C), and the time step for the integration was Δt=0.0002sec. System damping was represented by Rayleigh damping, and the damping ratio was 0.1% in the first mode of free vibration of the system. The first vibration frequency of the system was 0.0142sec, 0.71sec in the prototype scale. Analyses conditions were essentially the same as those in the centrifuge tests. The condition of H_T/H_L=0.75 was also conducted. Although the maximum acceleration of the input waves in LR4 was smaller than that in the other centrifuge test cases, the maximum acceleration of the input waves in the numerical analyses was set to 17g in all the cases.

E.3.3 Modeling of chemically grouted sand in numerical analyses

The structure of grouted soil, i.e. the arrangement of soil particles, is thought to be essentially the same since that of non-treated soil, as the pore water of the soil is merely replaced by the grouting material. In other words, the soil parameters that characterize the behavior of the soil skeleton in the constitutive model should be the same as that of non-treated soil.

The ductile behavior of soil under cyclic loading is one of the most important characteristics of the grouted soil, though it will degrade with cyclic loading. As a result, the grouting material ceases to resist against cyclic loading, and the treated soil will behave as *non-treated soil* in the end. This assumption is similar to that by Asaoka *et al.*[††].

In the sense that there is no difference between the treated and the non-treated soils in soil skeleton characteristics, and since the treated soil will be transformed to non-treated soil with cyclic loading, then the number of parameters that require modification from non-treated to treated soil are quite lim-

[††] Asaoka, A., Nakano, M. & Noda, T. 2000. Superloading yield surface concept for highly structured soil behavior, *Soils and Foundations*, Vol.40, No.2, 99–110.

ited, e.g. compressibility of pore filling material, K_f; overconsolidation ratio, $F_0/(-\sigma_{m0})$; hydraulic conductivity, k; and normal yield surface rotation characteristics, s_0 and c.

The ductile behavior of treated soil seems to be modeled by soil whose pore pressure accumulation rate is smaller than that of non-treated soil. As mentioned in Section 5.3.2, the rate of excess pore water pressure accumulation during a cyclic loading can be controlled by the parameters s_0 and F_0 in the extended subloading surface model.

s_0: After the start of normal yield surface rotation, the stress path rapidly approaches the origin of the stress space in the case of the larger s_{ij0}/σ_{ij0}, while it gradually approaches the origin in the case of the smaller s_{ij0}/σ_{ij0} as shown in Fig. 5.19.

F_0: The stress path ceases to move toward the origin of stress space once the rotation of normal yield surface starts. After certain duration, the stress path begins to approach the origin again. The overconsolidation ratio, $F_0/(-\sigma_{m0})$, influences the period of this delay as shown in Figs. 5.20 and 5.21.

These parameters only affect the development of excess pore water pressure before the appearance of cyclic mobility around the origin of stress space. Regarding ductile behavior of the treated soil and the degradation of treatment during a cyclic loading, the larger F_0 is seen to be suitable for modeling treated soil as shown in Figs. 5.20 and 5.21. Based on these facts, the treated soil is modeled by the larger F_0 soil, and its value is assumed to be one-tenth of that for the non-treated soil in this study. The hydraulic conductivity is also reduced and assumed to be a tenth of that for the non-treated soil as shown in Table E.4.

E.4 Physical and numerical model test results and discussions

E.4.1 Acceleration and excess pore water pressure responses

Figure E.9 shows observed acceleration responses at A0 and A4, at the base of the tank and at a depth of 1m in the surrounding soil respectively, in LR1 (H_T/H_L=0) and LR3 (H_T/H_L=0.5). Solid lines represent the responses in the numerical analyses, and dotted lines represent the responses in the centrifuge model tests. In the centrifuge tests, the amplitudes of the recorded acceleration response at the base of the tank and in the surrounding soil were almost constant in both cases. In the numerical analyses, the responses at the tank base were almost the same in amplitude as those in the physical tests, while the acceleration response ceased at the middle of the shaking in the surrounding ground. The attenuation of the acceleration response of the ground nearby the tank in LR3 was faster than that in LR1.

Observed excess pore water pressure responses at P2 and P5 at the depth of 70mm in the surrounding soil and at the depth of 90mm below the tank respectively, are shown in Fig. E.10. Initial over burden pressures at those points are plotted in the figure. Excess pore water pressure at P2 reached σ'_{v0} and leveled off, showing liquefaction in the middle of the shaking in both the physical and the numerical model tests. The achievement of the pore pressure at P2 to σ'_{v0} in LR3 was relatively faster than that in LR1. However, pore pressure at P5, beneath the tank, gradually increased in the centrifuge tests, while they increased in the early stage of shaking and then gradually decreased in the numerical model tests. At the end of the shaking, pore pressure at P5 remained small compared to the initial effective over burden pressure in both the physical and the numerical model tests. Though minor

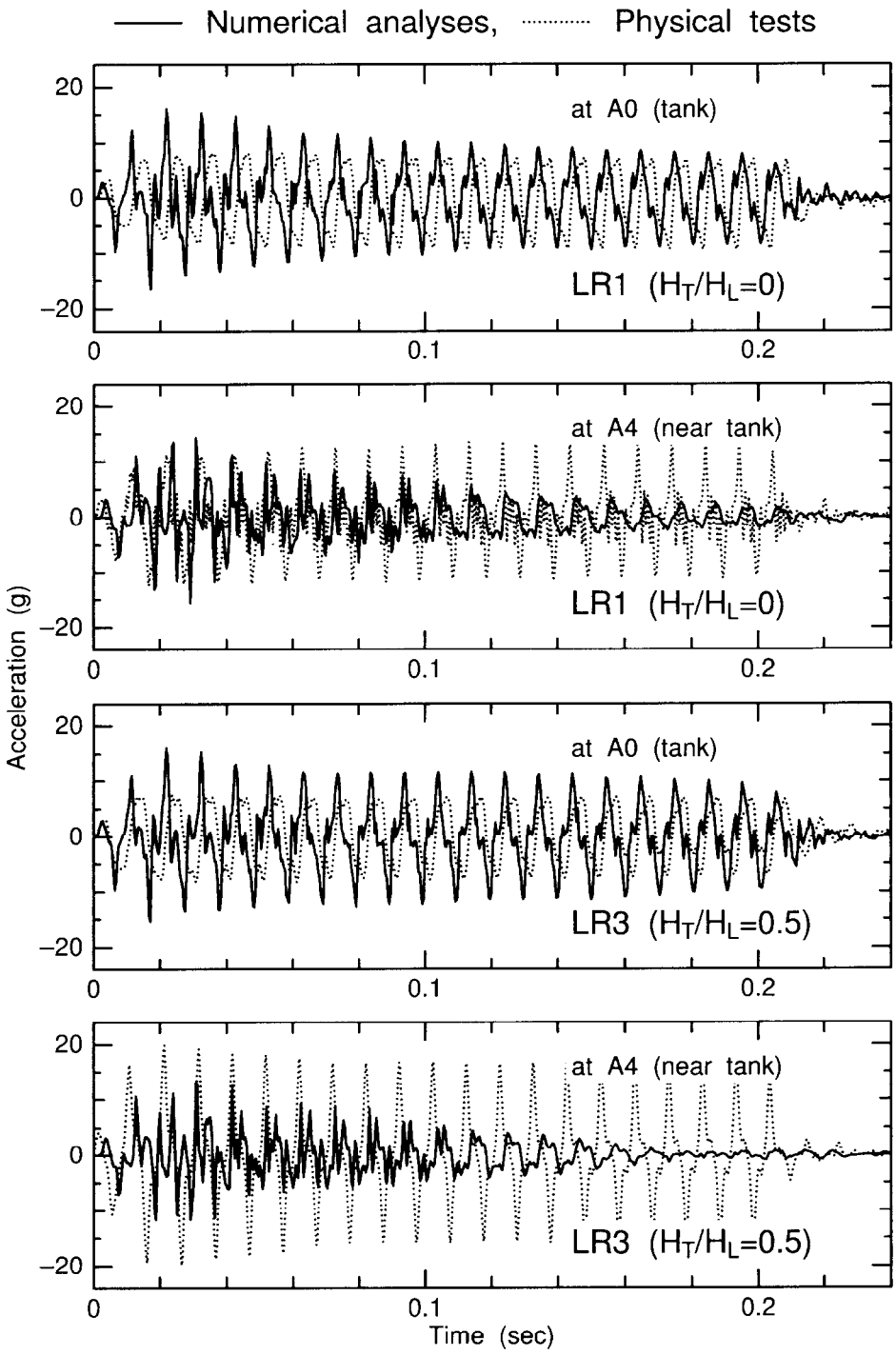

Figure E.9: Time histories of accelerations at A0 (tank) & A4 (nearby tank) in LR1 & 3.

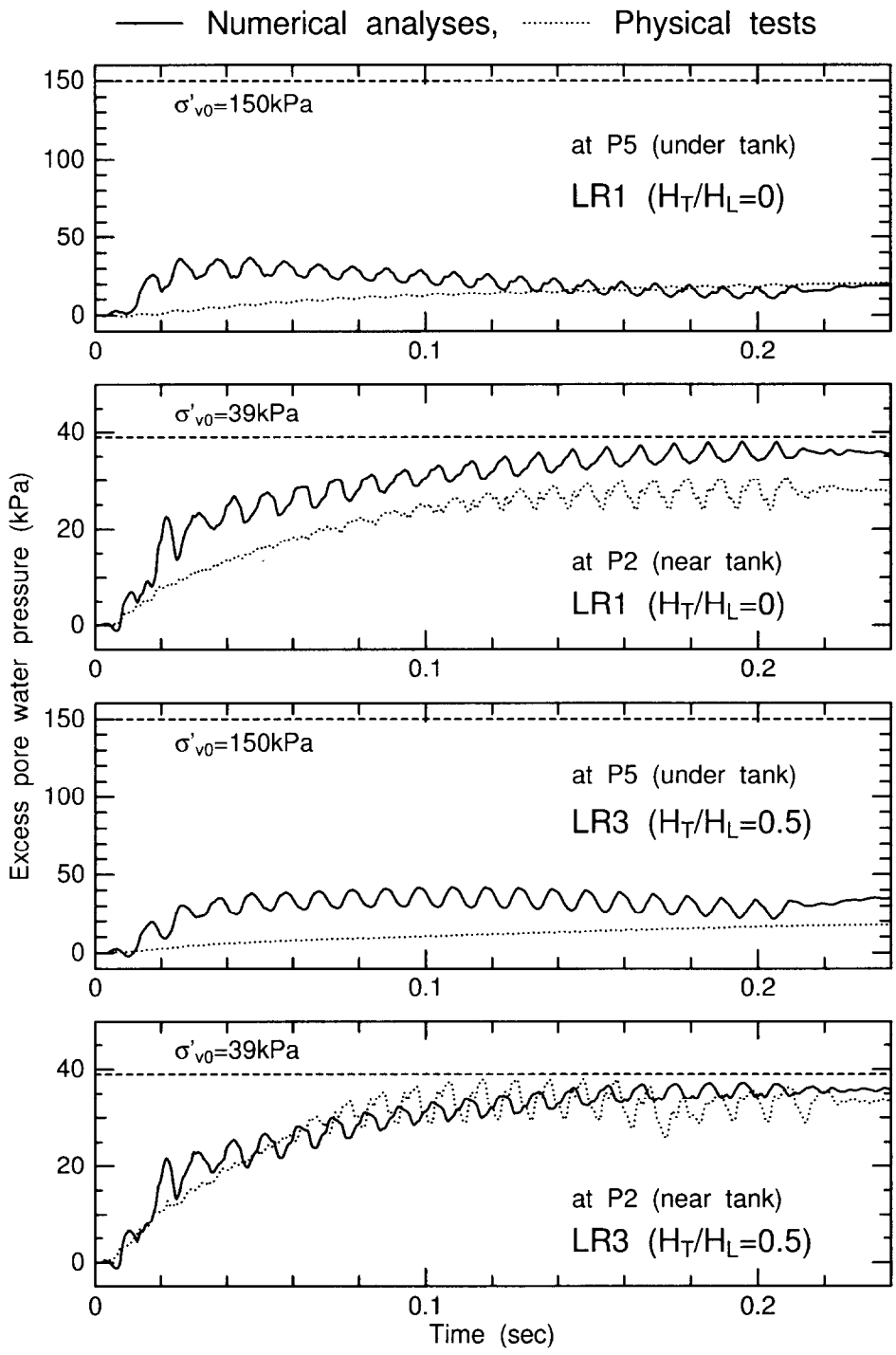

Figure E.10: Time histories of excess pore water pressures at P5 (under tank) & P2 (nearby tank) in LR1 & 3.

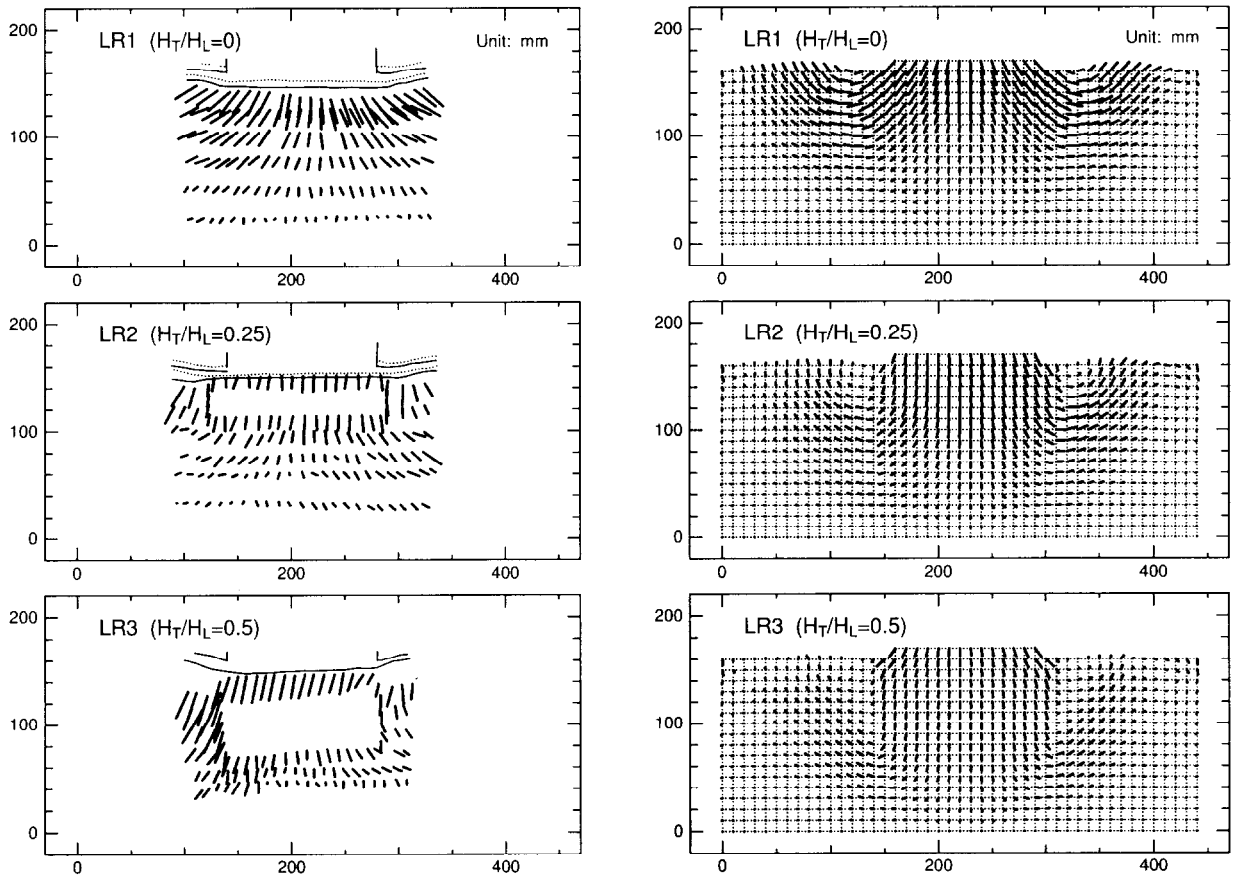

(a) Physical tests (b) Numerical analyses

Figure E.11: Permanent deformations of ground just after shaking in LR1, 2 & 3, where displacement scale is magnified by a factor of five.

differences were observed in the excess pore water pressure responses, it can be said that the numerical analysis has the capability of predicting the pore pressure generation in the ground on which the shallow foundation of the structure exists.

E.4.2 Settlement of the oil tank

Figure E.11 illustrates the permanent deformations of the ground in LR1, LR2, and LR3. The deformations of the ground in the physical tests were obtained by measuring the displacements of the lead shots placed in the ground by the X-ray photographs taken before and after the centrifuge tests. The displacement scale is magnified by a factor of five. As the specific gravity of the lead shot was larger than that of the soil, the lead shots showed larger settlement than that of the soil. Deformation patterns were seen to be essentially the same in both the physical and the numerical model tests. Since the ready grouted sand block beneath the tank was placed on a slant from the start in the centrifuge test LR3, large differential settlement was observed.

In the case without any improvement, LR1, a large lateral deformation of the ground just below the tank was observed, while no deformation of the treated portion could be seen, and there was small lateral deformation of the liquefiable soil just below the improved soil in the other cases. This result

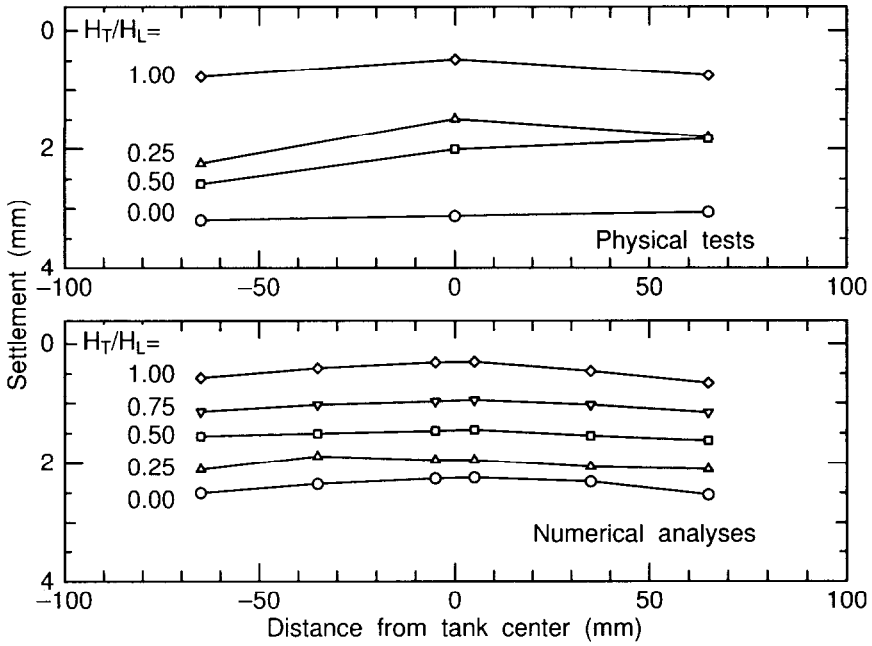

Figure E.12: Oil tank settlement distributions

indicates that the improved ground beneath the tank suppressed ground movements beneath the tank, and the liquefiable ground nearby the structure was separated from it, i.e. the stress condition of the ground near the tank was uninfluenced by the initial shear stress component of the initial stress induced by the dead load of the structure. Consequently, the liquefiable ground nearby the tank behaved like a free field, i.e. a level ground, and showed comparatively faster liquefaction as shown in Figs. E.9 and E.10.

Observed settlement distributions of the tank are illustrated in Fig. E.12 for all the cases. Settlements decreased with the increasing of the improvement ratio, H_T/H_L. At the edges of the tank, the settlements were relatively larger than those at the center of the tank in all the cases. Time histories of the tank settlement at the center are shown in Fig. E.13. Settlement of the tank increased with shaking and no substantial displacement could be seen after shaking. However post-shaking settlement increased by about 10% of that during the shaking due to the consolidation of the subsoil.

The permanent settlement at the center of the tank is plotted against $\frac{H_L-H_T}{H_L}$ in Fig. E.14. This ratio, $\frac{H_L-H_T}{H_L}$, represents the proportion of the thickness of the non-treated sand layer to the initial liquefiable layer thickness and is here defined as the non-improvement ratio. The tank-center settlement was almost proportional to the non-improvement ratio in both the physical and the numerical model tests. As the settlement of the tank takes place due to the compression and the lateral deformation of the non-treated soil beneath the tank, the average settlement of the tank can be predicted when the deformation of the improved area was comparatively small and the deformation of the non-treated soil below the treated soil can be estimated.

In this study, all the areas of the liquefiable soil beneath the tank were improved. In order to obtain an optimum improvement pattern for the existing oil tank, a variety of patterns should be examined.

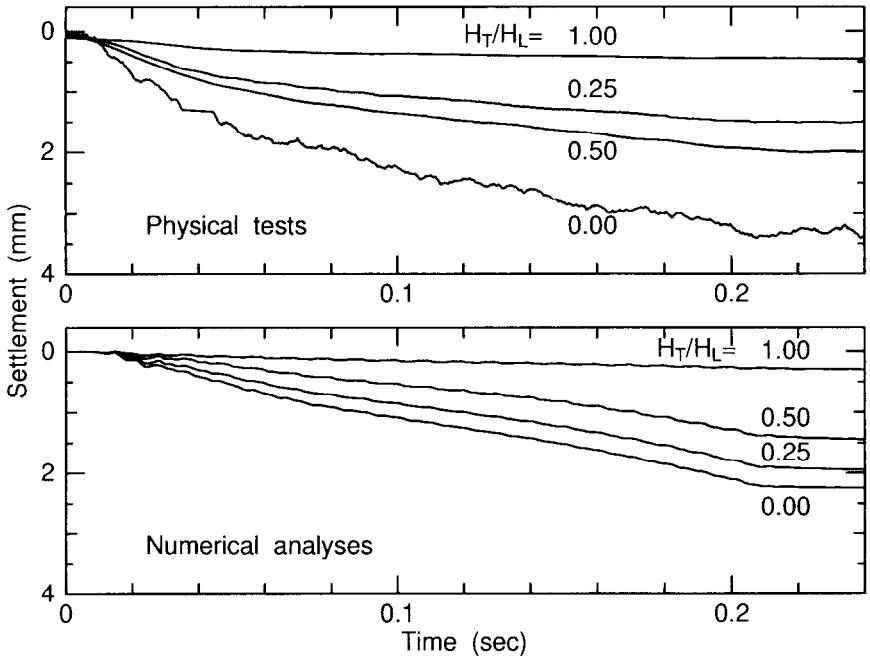

Figure E.13: Time histories of settlement at center of the tank.

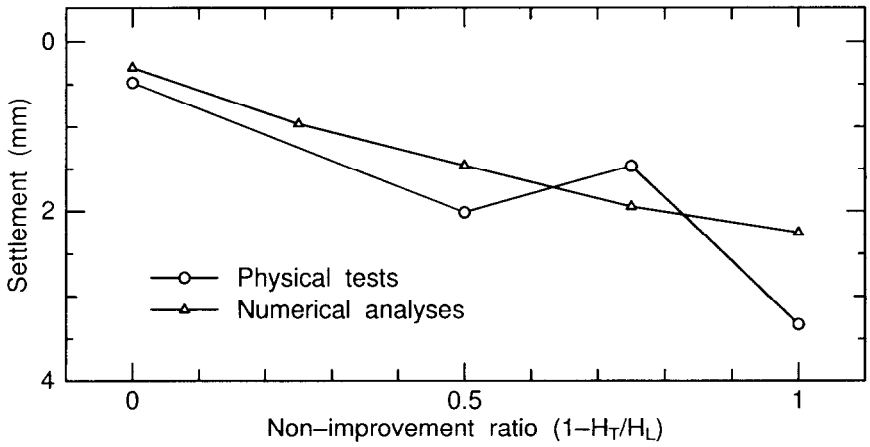

Figure E.14: Settlements against non-improvement ratio at center of tank.

Imamura *et al.*[‡‡] showed that the existing oil tank still performs well during an earthquake when the improvement was adopted only to the subsoil beneath the ring footing. The shape of the improved mass assumed the likeness of a hollow cylinder. This type of improvement can be adopted when the

[‡‡] Imamura, S., Hirato, T., Sato, Y., Hosoi, T., Hagiwara, T. & Takemura, J. 2000. 3-D dynamic centrifuge model tests on countermeasure against liquefaction on existing oil tanks by chemical grouting, *Proceedings of the Geotech – Year 2000, Developments in Geotechnical Engineering*, 531–540.
Imamura, S., Hirano, T., Sato, Y., Hagiwara, T. & Takemura, J. 2001. Proposal of contermeasures against liquefaction of existing oil tank foundation by chemical ground method, *Tsuchi-To-Kiso*, Vol.45, No.5, 28–30 (in Japanese).

diameter of the existing oil tank is large.

In the practical design of the soil improvement area for the existing oil tank, the width of the improved area is very large compared with that of the oil tank, considering the failure of the improved soil at the ring foundation and at the interface between the treated and the liquefiable soils. Though the width of the improved area was almost the same as that of tank, i.e. the width of the improved area was 1.15 times larger than that of the tank in this study, the soil improvement performed well in suppression of the permanent settlement of the oil tank when the appropriate depth of the liquefiable sand layer was improved.

E.5 Summary

Solidification of liquefiable soils by the chemical grouting has capabilities of being constructed in small working spaces and improving the soil beneath existing structures. Physical and numerical model tests were carried out to investigate the effect of this countermeasure against liquefaction on the permanent settlement of an existing oil tank. The following conclusions are drawn;

- The improvement of soil beneath the tank had an instant effect on the settlement prevention even if the width of the improved area was nearly the same as that of tank when the appropriate depth of the liquefiable sand layer was improved.

- The improved ground beneath the tank suppressed movements of the ground beneath the tank, and the liquefiable ground nearby the structure was separated from it. In other words, the stress condition of the ground nearby the tank was uninfluenced by the initial shear stress component of the initial stress induced by the dead load of the structure. Consequently, the liquefiable ground nearby the tank behaved like a free field and could easily liquefy during an earthquake.

- The tank settlement was almost proportional to the non-improvement ratio, $\frac{H_L - H_T}{H_L}$. As the settlement of the tank takes place due to the compression and the lateral deformation of the non-treated soil beneath the tank, the average settlement of the tank can be predicted when the deformation of the improved area was comparatively small and the deformation of the non-treated soil below the treated soil can be estimated.

- Though minor differences were observed between the physical and the numerical model tests, it can be said that the numerical analysis has the capability of predicting the pore pressure generation in the ground on which the shallow foundation of the structure exists and the settlement of the structure whose foundation was improved by chemical grouting.